Secondary flows and inlet skew in axial flow turbine cascades

Joseph Anthony Walsh

SECONDARY FLOWS AND INLET SKEW IN AXIAL FLOW TURBINE CASCADES

JOSEPH ANTHONY WALSH

School of Engineering and Applied Science
University of Durham

A thesis submitted for the degree of
Doctor of Philosophy of the University of Durham

May 1987

DECLARATION

The work contained in this thesis has not been submitted elsewhere for any other degree or qualification and that unless otherwise referenced it is the authors own work.

For my mother

SECONDARY FLOWS AND INLET SKEW IN AXIAL FLOW TURBINE CASCADES

J.A. WALSH

ABSTRACT

This thesis presents a detailed experimental investigation of the effects of inlet skew on the secondary flows and losses in a linear cascade of high turning turbine rotor blades. The blade that was used was modified from its original design to give aerodynamic similarity in the cascade flow conditions. Three levels of inlet skew were investigated using pressure probe instrumentation and the surface oil flow technique of flow visualisation. The results have shown that inlet skew has a profound effect on the secondary flows and on the magnitude of the secondary losses.

The flowfield of the cascade was modelled using several computer models. Although reasonable results were obtained with a fully viscous three-dimensional code the other models were unable to predict accurately the magnitude of the losses or even the relative effect of inlet skew on the losses.

This thesis also presents measurements of the turbulent flowfield of a similar linear cascade. It was found that regions of high turbulent kinetic energy were associated with regions of high total pressure loss. It was also found that the mass averaged total pressure loss and turbulent kinetic energy followed similar distributions in the cascade.

ACKNOWLEDGEMENTS

I have appreciated the capable guidance and the encouragement of my supervisor Dr. David Gregory-Smith. His enthusiasm and interest have been inspiring, particularly during the difficult times.

The technical staff of the Engineering Department have played an important role in the design, manufacture and maintainance of the experimental facilities. Particular mention must be made of Bill Roscamp (Departmental Superintendant), Ian Glassford and Frank Emery. I am grateful for the time and interest of the academic staff and my fellow postgraduates. Particular thanks are due to Dr. Chris King for the many useful discussions, and to Miss Marion Hawkins for sending on my computer output.

I would like to thank Dr. John Denton of the Whittle Laboratory at Cambridge University for giving me a copy of his computer model and also for loaning me the motor and controller to drive the moving belt. I would like to thank Professor John Moore (and Dr. Peter Stow of Rolls-Royce Ltd) for allowing me to use his computer model. I would also like to thank Thames Polytechnic for allowing me to use their computer to communicate with the Durham computer, and my current employers Logica SDS Ltd who have allowed me to use my spare time 'gainfully'. The financial support of Rolls-Royce Ltd and the Science and Engineering Research Council is gratefully acknowledged.

The skills of Miss Lesley Graham who typed my manuscript are clearly evident.

Lastly, but by no means least, I am so grateful to Jenny for her constant encouragement - and for putting up with me!

CONTENTS

NOMENCLATURE

A	area
C	blade chord
C_{ax}	blade axial chord
C_L	coefficient of lift
d	trailing edge thickness
f	frequency
H	boundary layer shape factor
n	power law index
P	pressure
Re	Reynolds number
s	pitch
S_n	Strouhal number
U	belt velocity
u',v',w'	fluctuating air velocity components
V	air velocity
W	relative air velocity
Y_s	secondary loss
Z_{TE}	penetration height at the trailing edge
α	rotor air angle
β	stator air angle, or blade angle
δ	boundary layer thickness
δ^*	displacement thickness
ϵ	yaw angle
θ	momentum thickness
ξ	total pressure loss coefficient $= \dfrac{P_{01} - P_{OLOCAL}}{1/2\ \rho\ V_1^2}$

ξ_N	normal vorticity
ξ_S	streamwise vorticity
ρ	density

Subscripts

ax, x	axial
G	gross
m	mean
N	net
rad	radial
tan, θ	tangential
u	upstream
t	throat
0	stagnation
1	upstream or inlet
2	downstream or exit

LIST OF FIGURES

CHAPTER 1: INTRODUCTION

The recent popularisation of the jet engine has resulted in a greater awareness of its role as a propulsive unit for aircraft. However, apart from its role in aircraft power plant the gas turbine engine has found important applications in marine propulsion systems and electrical power generation. Although the basic concept of the gas turbine engine is simple, in practice the designs of all of its components are highly complex. At a simplistic level the mechanical arrangement consists only of two rotating components (the compressor and the turbine) and a combustion chamber. The role of the turbine is to provide power to drive the compressor, and to provide shaft power for a propellor or fan if required, by extracting power from the hot gases released from the combustion system. This extraction is achieved by expanding the gases to a lower pressure and temperature. When high pressure ratios are required in one axial compressor it is mechanically separated into two or three sections that can be run at different rotational speeds. Since they are separate each compressor will require its own turbine to drive it. A typical design for a multi-stage turbine with a triple shaft arrangement is shown in Figure 1.1. An additional problem due to this particular arrangement is that the blade height for the high pressure turbine is limited by the presence of the shaft which passes through the centre of the disc. An overview of all of the components of a modern gas turbine is given in an excellent

anonymous publication 'The Jet Engine' (1973). Some aspects of gas turbine theory have been reviewed by Cohen et al (1972).

Due to the complexities of the fluid flow processes in a turbomachine the components are often studied in isolation so that the test conditions can be carefully controlled. A linear cascade, which is in effect formed by unwrapping the blades from their disc, is the simplest of a range of tools that can be used to investigate blade row fluid flow phenomena and loss generation mechanisms. The primary flow direction in a linear cascade may be defined as the flow direction that results from a two-dimensional uniform flow at inlet to the cascade. This definition is often used by workers using low aspect ratio cascades. An alternative definition which is sometimes used is that the primary flow direction is the same as the camber line angle. The secondary flow may be thought of, in the classical sense, as being produced by the streamwise vorticity in the flowfield, which is itself produced as a result of the vorticity at inlet to the cascade. This secondary flow appears as transverse velocity components and causes the production of the secondary losses. These so called secondary losses may in fact be a major proportion of the total losses within the blade row of a low aspect ratio turbine. Most of the reported experimentations contain the results of measurements made outside of the blade passage. Qualitative results for the flow in the blade passage have tended to be derived from flow visualisation results. However the linear cascade does allow detailed measurements to be made relatively easily in the blade passage, without the complexities of the

radial pressure gradients that are found in annular cascades. A good introductory review of cascade research has recently been given by Gostelow (1984).

The work presented in this thesis is part of an ongoing experimental research programme at Durham University. The overall aim of the programme is to obtain detailed experimental data to aid the understanding of the fundamental processes associated with secondary flows and losses in axial flow turbines. A large amount of data had been collected from the large scale linear cascade prior to the start of the research reported in this thesis. This earlier work, which has been reported by Graves (1985), concentrated on collecting detailed data throughout the cascade using pressure probe instrumentation. In addition limited measurements were made with hot-wire probes. An objective of the research reported in this thesis is to answer the questions posed by Graves' results. It was therefore decided to determine whether an increased number of measurement points in the wake region downstream of the cascade would lead to improved repeatability and thereby increased confidence in the measured levels of loss. A flow visualisation study was proposed so that a better qualitative understanding of the physical structure of the flowfield in the blade passage could be obtained. A further objective was to traverse more of the cascade flowfield with hot-wire probes so that the connection between the regions of high total pressure loss and high turbulent kinetic energy could be investigated. A spectral study was proposed to attempt to determine the source of the high levels of turbulence intensity in the cascade. However,

the main objective of the research reported here is the study of the effect of inlet skew. The skew is introduced into the flowfield in a real machine by a change in frame of reference as the working fluid goes from the stationary hub to the rotating blade row. This research required a new purpose built rig and in addition a new blade profile was used that was based on a typical HP turbine blade section. The profile was redesigned for aerodynamic similarity in the low speed cascade environment. The main experimental results were obtained using pressure probe instrumentation and flow visualisation. It had been hoped that there would be sufficient time to carry out some measurements using hot-wires but this was not possible. A subsidiary objective of this work was to use the experimental results to validate commonly used correlations for the secondary losses and also several state of the art computer models. There is a need to validate models and the relative simplicity of the geometry of the linear cascade appears to make it a valuable tool for providing good test results.

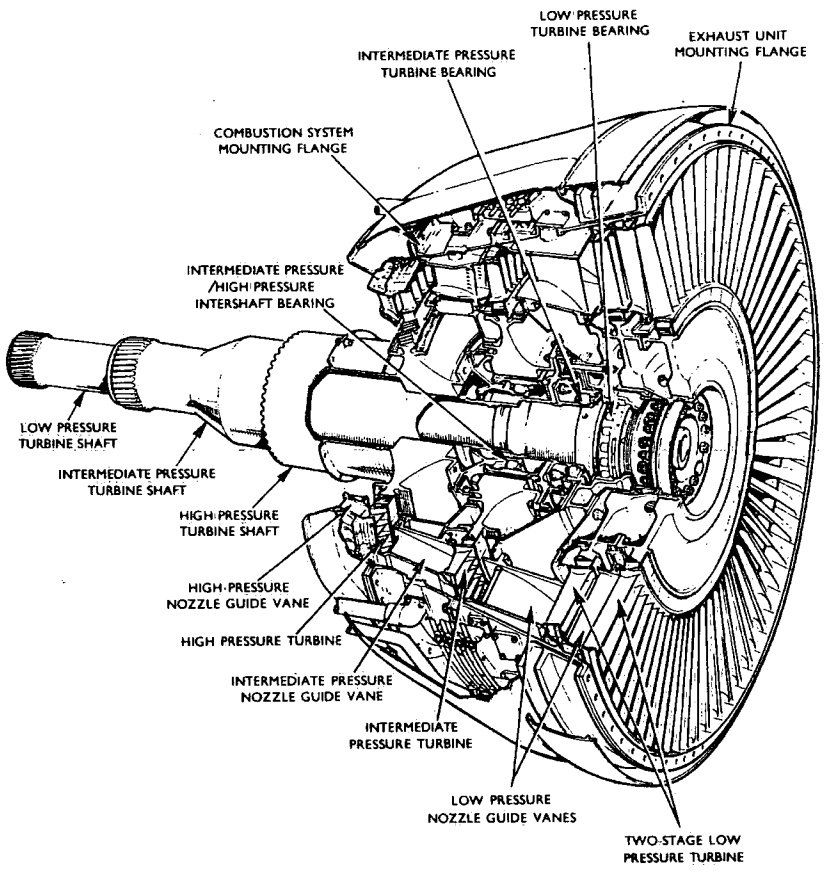

(After Anonymous (1973))

FIGURE 1.1: Typical Multi-Stage Turbine

With a Triple Shaft

CHAPTER 2: LITERATURE REVIEW

This chapter reviews the results of experimental investigations in order to present a complete picture of the flowfield within a turbine blade passage. The effects of various parameters on the secondary flows and losses are discussed. The modelling of secondary losses and the new approaches to general turbomachinery modelling presented.

2.1 INTRODUCTION

Secondary flows are transverse velocity components produced when a non-uniform flow is turned. An equivalent classical definition is that secondary flows are produced when a streamwise component of vorticity is developed from the turning of an initially sheared flow. In a turbine cascade secondary flows are often considered to be the difference between the primary, or ideal, flow direction and that measured in the cascade.

The reason for studying secondary flows is that they produce a spanwise variation of outlet angle in a cascade and that secondary losses, due to the action of the secondary flows, may constitute a major portion of the losses within a blade row. Belik (1972) has stated that for low aspect ratio blading the secondary losses may be as large as the profile losses. Furthermore in steam turbines secondary flows are the source of undesirable concentrations of wetness and water film. Gaugler and Russell (1984) show by a comparison of flow visualisation and heat transfer measurements that local peaks in heat transfer correspond

to secondary flow regions. The motivation for studying secondary flows is to improve the design of turbomachinery and these improvements can only come from a deeper understanding of the fluid dynamics involved.

The last thirty years have seen a large amount of research undertaken into various aspects of this field. Since there are some excellent reviews of the earlier work available it is intended to review in depth only those papers of historical significance or of particular relevance.

2.2 EXPERIMENTAL SECONDARY FLOWS

Experimental secondary flows have been the subject of a number of reviews (Lakshminarayana and Horlock (1963), Dunham (1970), Horlock and Lakshminarayana (1973), Chauvin (1975), Tall (1977), and Sieverding (1985)). All of these reviews charted the progress that had been made towards obtaining an understanding of the basic fluid flow processes involved and their effects on the losses that are generated in blade rows. The reviewers, however, have not always been fully in agreement. Dunham (1970) felt that the flow processes associated with secondary flows were adequately understood. Whereas seven years later Tall (1977) found that the research he had reviewed showed major gaps in the understanding of secondary flows and their effects on the flowfield, particularly within the blade passage.

From an experimental point of view the early NACA studies of Herzig and Hansen (1955), and Herzig et al (1953), had clearly identified the passage vortex as one of the main features of the

flow in a blade passage. They used flow visualisation techniques, such as surface oil flow and smoke, in linear and annular cascades. They identified the passage vortex as a three-dimensional rollup of the endwall boundary layer in a region near to the suction surface of the blade. The size and tightness of the passage vortex was seen to depend on the angle through which the mainstream fluid was turned. They also showed that the passage vortex moved away from the endwall as it moved downstream. Most other researchers who have carried out flow visualisation studies and measurements have also detected the presence of the passage vortex. Senoo (1958) made measurements in a linear cascade of turbine nozzles and, in addition to detecting the passage vortex, found that the endwall boundary layer at the throat was laminar and highly skewed irrespective of the inlet boundary layer thickness. Turner (1957) traversed the exit plane of a geometrically similar cascade with and without an endwall boundary layer at inlet. It was found that even without an inlet boundary layer the endwall flow was swept onto the suction surface in the usual manner. A notable exception was Denton and Johnson (1975) who took measurements in a model turbine and did not find the usual type of flow structure. The low energy fluid was seen to be shed gradually from the blade into the wake rather than being formed into a loss core. It was suspected that the cause was the very high turbulence intensity levels that were detected in the inlet boundary layer.

When a shear layer has a bluff body, such as a cylinder, placed perpendicularly in it the flow rolls up into a vortex ahead

of the bluff body. This vortex has two legs which go either side of the body and its name, the horseshoe vortex, is taken from the shape of the endwall flow pattern generated in the case of a cylinder. The earliest recognition of the presence of the horseshoe vortex in turbomachinery was probably given by Klein (1966). On the basis of surface flow visualisation a remarkable picture of the flow was produced (Figure 2.1) with virtually no comment. The passage vortex was shown to sweep the endwall flow onto the suction surface of the blade. A stagnation point vortex (the suction-side leg of the horseshoe vortex) was shown travelling up the suction surface of the blade and was, presumably, dissipated by the opposing effect of the much stronger passage vortex. The pressure-side leg of the horseshoe vortex was not shown but the blade was seen to have a laminar separation bubble on the suction surface.

It was realised that the cascade volume approach, where measurements were only taken upstream and downstream of the cascade, was inadequate. From 1975 onwards detailed studies of the passage flows were therefore undertaken. Sjolander (1975) detected separation around the leading edge of a turbine cascade which extended across the blade passage to the suction surface. This separation appeared to have the effect of removing the endwall boundary layer by sweeping it towards the suction surface. A newly formed endwall boundary layer was detected downstream of the cross-passage separation line. This new boundary layer appeared to be independent of the inlet boundary layer and it was thought to be made up of re-attached freestream fluid. By using a

combination of surface oil flow and a laser sheet technique, Marchal and Sieverding (1977) produced excellent flow visualisation of the flow in linear cascades of nozzles and of rotor blades. The legs of the horseshoe vortex were seen to go around the two sides of the leading edge of the blades. The suction-side leg was seen to be partially dissipated by a passage vortex, since the two vortices opposed each other. It was also seen to be pushed on to the suction surface where it remained on the midspan side of the passage vortex. The pressure-side leg of the horseshoe vortex was thought to initiate the passage cross-flow and develop into the passage vortex. The main effect of the passage vortex was that it removed the endwall boundary layer and allowed high momentum freestream fluid to be convected from the pressure side of the passage to form a new endwall boundary layer. The only drawback of the laser sheet technique, and most other flow visualisation techniques, is that it only provides a two-dimensional image of an instant in time and does not give any direct information about the three-dimensional nature of the flow. However, the flow visualisation in this case was complemented by five-hole pressure probe measurements which verified the qualitative flow visualisation results. Langston et al (1977) carried out tests in a large scale linear cascade, geometrically similar copies of which have been used by other researchers. The measurement techniques used were five-hole pressure probes in the blade passage and hot-wire anemometry in the endwall boundary layer. A flow visualisation technique of injecting indian ink into the endwall flow was used to indicate

the paths of the limiting streamlines. The most striking feature of the flow visualisation results was the presence of a separation saddle point upstream of the leading edge of the blade. This was due to the separation, and rolling up into the horseshoe vortex, of the inlet boundary layer. The pressure-side leg of the horseshoe vortex was again thought to be the initiator of the passage vortex. The new relatively thin boundary layer that was formed behind the cross-passage separation line, from fluid originating near to the pressure surface, was also detected. Langston (1980) suggested that the suction-side leg of the horseshoe vortex remained in the suction surface endwall corner. The endwall flow was examined using a cross-flow boundary layer approach and its qualitative behaviour was correlated by a simple expression. Denton and Usui (1981) developed an ingenious technique for detecting injected ethylene in order to study the mixing of fluid in a single blade row and in a complete stage of a turbine. It was found that there was very little mixing of fluid at the midspan position of the blades but much more intense mixing in the endwall regions. Much of the endwall boundary layer was seen to appear in the core of the passage vortex. Hunter (1982) presented results for the flow behind a stator and behind a rotor placed at two different axial distances behind the stator. It was observed that the stator endwall flows were consistent with those observed in linear cascades and that the spanwise pressure gradient, due to the annular geometry, promoted a migration of the boundary layer fluid towards the hub. In the rotor the passage vortex and loss accummulation were affected by the unsteady nature

of the flow at its inlet. Sieverding and Van Den Bosche (1983) used coloured smoke to obtain qualitative pictures of the evolution of the passage and horseshoe vortices. They detected the roll-up of the vortices and the cross-passage movement of the pressure-side leg of the horseshoe vortex before it became part of the passage vortex. Bario et al (1982) showed that in a cascade of highly loaded turbine blades the passage vortex was formed inside the blade passage near to the leading edge of the blades. The accummulation of low momentum fluid, in and around the passage vortex core, was suggested as having been convected by the vortex from low energy regions near to the endwall, or by the merging of the suction-side leg of the horseshoe vortex with the passage vortex, or by a combination of both effects. Gregory-Smith and Graves (1983) took measurements in a large scale, low speed, linear cascade and found that the passage vortex and loss core centres did not coincide. Turbulence measurements showed that very high levels of turbulence intensity are associated with the loss core. Generally there have been very few detailed turbulence studies reported in the literature. Binder and Romey (1983) measured losses at several axial stations downstream of an annular stator row. The suction-side leg of the horseshoe vortex was clearly detected as having remained on the midspan side of the passage vortex. The averaged losses were seen to continue to grow downstream of the trailing edges of the blades. Sieverding et al (1984) investigated the flow in an annular nozzle guide-vane of low aspect ratio with a colateral inlet boundary layer. The blade profile was the same as that used by Marchal and Sieverding (1977)

in their linear cascade tests. Using the laser sheet flow visualisation technique the passage vortex and the suction-side leg of the horseshoe vortex were detected. The pressure-side leg of the horseshoe vortex was not detected but at the blade tip a cyclic variation of the flow was detected. Moore and Smith (1984) used a geometrically similar cascade to Langston et al (1977), and the ethylene injection technique, to show that fluid from the pressure-side leg of the horseshoe vortex was distributed throughout the passage vortex. It was also shown that fluid that had originated in the suction-side leg of the horseshoe vortex appeared to be convected around the centre of the passage vortex. In an experimental investigation of the flows in a one and a half stage high pressure turbine, Sharma et al (1985) found that the flow at exit from the stator was steady and unaffected by the presence of a downstream rotor. The flow in the rotor was however highly unsteady. When the rotor leading edge interacted with the upstream stator wakes, the stator wakes were seen to merge with the rotor wakes to give an overall flow field pattern that was very similar to that usually found in high turning linear cascades. When the rotor leading edge did not interact with the upstream stator wakes, the upstream stator wakes passed straight through the rotor row without interacting with the rotor wakes. This changed the flowfield dramatically and appeared to inhibit the formation of the secondary flow patterns. Moustapha et al (1985) traversed upstream and downstream of a linear cascade and an annular cascade, both using the same blade profiles. The low aspect ratio of the cascades meant that the hub and tip passage

vortices interacted on the suction surface of the blade. In the annular cascade the effect was to merge the two loss cores into a single high loss core in the centre of the blade passage. However, the two passage vortices were seen to remain separate. Ishii and Honami (1986) created and analysed a horseshoe vortex. They found low frequency fluctuations in the separation region.

A composite picture of the flow in a turbine blade passage can now be formed. As many research workers have found the main features of the flowfield are the passage and horseshoe vortices. There may additionally be a number of smaller vortices that have a minor effect on the flowfield.

The passage vortex is undoubtably associated with regions of high loss but the centre of the loss core does not coincide with the centre of the passage vortex. Some researchers (Marchal and Sieverding (1977), Langston et al (1977)) have proposed that the passage vortex is initiated by the pressure-side leg of the horseshoe vortex. This is unlikely since the passage vortex has been detected (Turner (1957), Bailey (1980)) in the absence of an inlet boundary layer. Rather, the presence of the passage vortex is due to the cross-passage pressure gradient and the turning of the mainstream fluid by the curvature of the blade passage. Undoubtably the presence of the horseshoe vortex system affects the passage vortex. In a recent flow visualisation study using a water table, Pernet (1986) clearly showed that fluid from the pressure-side leg of the horseshoe vortex travelled up the centre of the passage vortex. This then is the reason that researchers have been unable to detect the presence of the pressure side leg

of the horseshoe vortex using surface flow visualisation techniques such as surface oil flow and the injection of indian ink. This may also be a qualitative reason for the centres of the passage vortex and loss core not coinciding. There is no disagreement however about the fact that the pressure-side leg of the horseshoe vortex crosses the blade passage on its way to the centre of the passage vortex. The resulting separation is a characteristic feature of the endwall flow. Downstream of this separation line a new highly skewed boundary layer is formed from high momentum freestream fluid convected from near to the pressure surface of the blade. A small corner vortex may be formed in the suction surface endwall corner with an opposite sense of rotation to that of the passage vortex. A vortex of this type was detected and reported by Gregory-Smith and Graves (1983). It is unlikely that this vortex is the suction-side leg of the horseshoe vortex as reported by Langston (1980). This would imply that the suction-side leg of the horseshoe vortex would have to be wrapped around the passage vortex (Figure 2.1) for which there is no experimental evidence. Rather, there is evidence (Marchal and Sieverding (1977), Binder and Romey (1983)) to suggest that the suction-side leg of the horseshoe vortex remains on the midspan side of the passage vortex. The suction-side leg of the horseshoe vortex is likely to be at least partially dissipated by the much stronger passage vortex that has an opposite sense of rotation. This may explain why Langston et al (1977) were unable to locate the suction-side leg of the horseshoe vortex. Furthermore the horseshoe vortex has been shown to have a low frequency cyclic

variation (Sieverding et al (1984), Ishii and Honami (1986), Pernet (1986)). This unsteadiness will not be detected by two dimensional surface flow visualisation techniques.

2.3 GROWTH OF LOSSES

The averaged growth of losses through a cascade has been presented by several researchers. Langston et al (1977) and Marchal and Sieverding (1977) found that the losses remained fairly constant up to the axial position of maximum suction surface velocity. In the deceleration region to the trailing edge it was found that the losses increased significantly. Gregory-Smith and Graves (1983) showed that the losses grew through the cascade with a large increase at the trailing edge. This difference may be explained by the presence of a tripwire on both the Marchal and Sieverding, and the Langston et al blades. This was used to ensure that a fully attached turbulent boundary layer was present on the suction surface of the blade. This was to overcome the suction surface diffusion effect, which may lead to separation, due to placing blades designed for transonic operation into an incompressible flow. The profile used by Gregory-Smith and Graves was not tripped and flow visualisation results, to be presented in this thesis, show the presence of a laminar separation bubble on the suction surface of the blade. The growth of losses early in the passage may therefore be due to an increase in profile loss as a result of the transition of the suction surface boundary layer from a laminar to a turbulent state. The losses associated with the rapid deceleration region were none-the-less found to be significant.

Downstream of the cascade most researchers have found that the losses continued to grow due to the action of the cascade endwall shear stresses (Binder and Romey (1983), Marchal and Sieverding (1977), and Gregory-Smith and Graves (1983)). Moore and Adhye (1985) traversed four downstream planes of a linear cascade that was geometrically similar to that of Langston et al (1977). It was found that the increase in total pressure loss was balanced by a corresponding decrease in secondary kinetic energy. It was therefore suggested that the increase in total pressure loss was caused by the dissipation of secondary kinetic energy. The decay of the spanwise component of the secondary kinetic energy was identified as being the largest contributor to the increase in total pressure loss. Moore et al (1986) traversed one downstream plane of the same cascade with twin hot-wires. The Reynolds stress measurements were combined with the mean velocity measurements obtained with the five-hole probe. This allowed the turbulent deformation work terms in the equations for the generation of total pressure loss and the decay of the components of mean kinetic energy to be evaluated. Two mechanisms were identified that could act to produce total pressure loss. There was a deformation work term that acted to produce mean kinetic energy from turbulence kinetic energy and there was a reversible pressure work term which could exchange mean kinetic energy between its three components. The combined effect of these two mechanisms was found to offset the loss production rate caused by the shear of the primary flow in the endwall boundary layer. Chen and Dixon (1986) found that the losses continued to grow downstream of their high turning, high aspect ratio cascade. They were

able to apply a simple correlation that was independent of inlet boundary layer thickness.

2.4 INLET BOUNDARY LAYER

There is a large literature concerning the effect of varying inlet boundary layer thickness on the secondary flows and losses in cascades. Klein (1966) found that within the range of boundary layer thicknesses used the losses did not alter. Graziani et al (1980) carried out surface heat transfer measurements in a cascade with the same geometry as that used by Langston et al (1977). It was found that the size of the passage vortex was dependent on the inlet boundary layer thickness. When the inlet boundary layer was thinned the separation saddlepoint was seen to move further back into the blade passage and closer to the suction surface. The strength of the cross-flow velocities were also reduced. Bailey (1980) used Laser Doppler Anemometry and hot-wire anemometry in a large scale linear cascade with the leading edge horseshoe vortex suppressed to show that a reduction of inlet boundary layer thickness reduced the cross-flow velocities and left the passage vortex closer to the endwall. Gregory-Smith and Graves (1983) varied the inlet boundary layer thickness at inlet to a large scale, low speed, linear cascade of high turning rotor blades. It was shown that the growth of loss through the cascade was independent of inlet boundary layer thickness. Chen and Dixon (1986) also found that the increase in the net loss was invariant with inlet boundary layer thickness. It was seen that the positions of the loss peaks, in the

pitch-averaged sense, were also independent of inlet boundary layer thickness but their magnitude was proportional to δ_1^*. Govardhan et al (1986) took measurements in an annular cascade of high turning turbine impulse blades. It was found that as the hub inlet boundary layer thickness was increased the passage vortex was convected towards midspan. It was also found to be larger in size since there was more entry boundary layer fluid being fed into its core. When the casing inlet boundary layer was thickened the hub passage vortex still grew and was convected towards midspan, whilst the casing passage vortex remained unchanged. In a pitch-averaged sense the magnitude of the hub loss core was increased with increased inlet boundary layer thickness but its position was unchanged. The casing loss core was however seen to move away from the endwall. In his review Dunham (1970) quotes results obtained by Wolf (1961) for the systematic variation of inlet boundary layer thickness. It had been concluded that thickening a thin inlet boundary layer had an important effect, whereas thickening an already thick one had little effect. This statement may go some way towards explaining the negligible difference in losses seen for changes in inlet boundary layer thickness by some researchers.

Another important inlet boundary layer effect, that has received little attention from researchers, is that of skewing. Three studies have been reported using linear cascades. Moore and Richardson (1957) used air jets to produce a cross-flow profile in order to simulate the effect of skewing the inlet boundary layer in compressors. They were unable to report on the effect of skew

on the secondary losses since they did not take measurements in the exit plane. It was, however, reported that in the skewed case the cascade showed a smaller reduction of the blade pressure force near to the endwall. It would be expected that inlet skew would not be so important in compressors since the skew would oppose the transverse pressure gradient in the blade passage, whereas in turbines the skew would reinforce the transverse pressure gradient. Carrick (1977) investigated the effect of inlet skew in a cascade of turbine impulse blades using a moving belt upstream of the cascade to simulate the skew. It was shown that the secondary flows were intensified and that the secondary losses were significantly increased by the skew. Much of the flow measurement in the blade passage was undertaken with three-hole pressure probes which did not allow the spanwise movement of the flow to be recorded. Kingcombe (1976) attempted to assess the effect of skew in a linear cascade of turbine impulse blades without the effect of shear. A Beltrami flow, in which the stagnation pressure is constant but a vorticity component may be present in the direction of the streamlines, was generated at inlet to the cascade. The flowfield was measured at two downstream planes using a three-hole pressure probe. For very low levels of skew ($\pm 10^0$) it was found that secondary flow theory could be adapted to adequately describe the behaviour of Beltrami flow through a cascade. Bindon (1979, 1980) attempted to measure the effect of inlet skew in Sjolander's annular cascade of low aspect ratio, low turning, turbine blades. It was shown that the effect of skew was to decrease the losses. The traversing was

limited to only part of the blade span and was carried out with a three-hole pressure probe. It is difficult to judge the effect of skew alone in the results presented due to the geometry of the cascade. The tunnel was not speed controlled and therefore considerable drift in operating point and inlet velocity resulted. The rotating hub extended to a slot immediately upstream of the leading edge of the blades. The slot was shown, using flow visualisation, to have a greater effect than the skew since the inlet boundary layer was effectively sucked off. Duncan et al (1960) have shown that as well as removing the boundary layer the slot modifies the pressure distribution in its vicinity. The result may be to form a completely new boundary layer downstream of the slot and to change the local pressure gradient from unfavourable to favourable for some distance upstream and downstream. Lawrenz (1984) used a similar cascade to measure the effect of inlet skew on nozzle guide vanes. However, it was clear that the effect of the slot ahead of the cascade was significant since even at inlet to the blade row there was no evidence of skew. Klein (1966) conducted a series of tests in an annular configuration to determine the effect of tip clearance. The case of zero clearance at the hub was a similar case to those of Bindon and of Lawrenz. The cascade, which consisted of steam turbine blades of 66^0 turning with a very thick leading edge and a thin trailing edge, was traversed with a three-dimensional conical probe. The full effect of the skew is difficult to ascertain since only the lower half span of the flow field was measured. The losses were however seen to increase with skew. All of the

above annular cascade studies limited their measurements to locations upstream and downstream of the cascade. Boletis et al (1983) and Boletis (1984) present the results of a major investigation of the flow field in annular cascades. The effect of inlet skew was measured in an annular cascade of low aspect ratio, high turning turbine nozzle guide vanes. Two cases of inlet skew were investigated by having different upstream conditions. To produce the required inlet conditions the first case used a rotating hub and the second a complete stage. It was found that the effect of skew was significant. The suction surface endwall flows were reinforced and a radial movement of the fluid towards midspan was seen to counteract the movement from tip to hub usually seen in annular configurations. It was also shown that the simple entrainment approach, produced by the rotating hub upstream of the blade row, was not a good model for the flow downstream of a complete stage. This result is not surprising since the flow would be highly unsteady downstream of a stage and the flow field at inlet to the blade row would be very complex. An additional study is required in this case using more sophisticated instrumentation in order to obtain more detail than can be obtained from circumferential averaging of the flow field.

2.5 OTHER EFFECTS

In the review of cascade data Dunham (1970) identified various factors that appeared to affect secondary losses. It was clear that the losses were inversely proportional to aspect ratio. More recently Atkins (1985) confirmed this result and showed that

it held for aspect ratios as low as 0.3. Jilek (1986) found that as long as the secondary flow regions did not interact the downstream flow pattern was also unaffected by aspect ratio.

Moore and Ransmayr (1984) used a geometrically similar cascade to that of Langston et al (1977) to investigate two different leading edge profiles (circular and wedged). They found that the static pressure distributions around the throat of the passage were independent of the shape of the leading edge. It was concluded that since the size of the horseshoe vortex was small compared to the thickness of the inlet boundary layer it did not significantly influence the passage vortex as far as the local wall static pressure distribution was concerned. A traverse with a five-hole pressure probe downstream of the cascade showed only minor differences in the flowfield due to the change in shape of the leading edge. It was therefore concluded that the shape of the leading edge and the details of the flow close to it may have only a relatively small influence on the production of loss in some cascades.

The shape of the endwall has received some attention. Morris and Hoare (1975) showed that meridional wall profiling can significantly reduce the secondary losses in linear cascades. Atkins (1985), however, found that endwall profiling had surprisingly little effect on the secondary flows and losses. Boletis (1984) had some success with tip endwall contouring.

Sieverding and Wilputte (1981) attempted to investigate the effect of Mach number and, although they detected losses increasing with increasing Mach number, they were unable to

ascertain whether they were looking at a Mach number or a Reynolds number effect. They also showed that the injection of cooling fluid may have a significant effect on the endwall flow field.

2.6 SECONDARY LOSS CORRELATIONS

In order to use experimental data obtained from cascades in the design of turbomachines a number of correlations have been developed. Methods of correlating the secondary losses were reviewed by Dunham (1970) who found a disturbing lack of agreement between the various correlations in common use.

Blade row secondary loss is generally represented by a single figure

$$Y_s = \frac{\text{Averaged Stagnation Pressure Loss}}{\text{Outlet Dynamic Head}}$$

Experimentally the gross secondary loss is found by subtracting the profile loss, usually taken as the midspan loss, from the total loss. This is a technique that is valid for high aspect ratio blades only. A technique used for low aspect ratio blading would be to calculate the profile loss using a two-dimensional model. The net secondary loss is found by subtracting the inlet loss from the gross secondary loss. Dunham found that the best correlation for the secondary loss was given by an expression based on the Ainley and Mathieson (1951) blade loading parameter

$$Y_s = \frac{C}{h}\left(\frac{\cos\alpha_2}{\cos\beta_1}\right)\left(\frac{C_L}{S/C}\right)^2 \frac{\cos^2\alpha_2}{\cos^3\alpha_m} f\left(\frac{\delta_1^*}{C}\right)$$

where $\alpha_m = \tan^{-1}(1/2\ (\tan\alpha_1 + \tan\alpha_2))$

and $f\left(\frac{\delta_1^*}{C}\right) = 0.0055 + 0.078\left(\frac{\delta_1^*}{C}\right)^{1/2}$

Dunham did not specify whether the above formula was for net or gross secondary loss. The function of inlet boundary layer displacement thickness has itself been the subject of review and correction. Dunham and Came (1970) suggested the relationship

$$f\left(\frac{\delta_1^*}{C}\right) = 0.0334$$

when the inlet boundary layer displacement thickness is not known. This result was based on losses measured in real machines as opposed to cascades. Came (1973) corrected the earlier results of Dunham and suggested that the relationship

$$f\left(\frac{\delta_1^*}{C}\right) = 0.008 + 0.64\left(\frac{\delta_1^*}{C}\right)$$

be used to give the gross secondary loss. Morris and Hoare (1975) suggested an ammended form for the gross secondary loss

$$f\left(\frac{\delta_1^*}{C}\right) = 0.011 + 0.294\left(\frac{\delta_1^*}{C}\right)$$

More recently Chen and Dixon (1986) have suggested that the net secondary loss is correlated by the equation

$$Y_{SN} = 0.0055\ \frac{C}{h}\left(\frac{\cos\alpha_2}{\cos\beta_1}\right)\left(\frac{C_L}{S/C}\right)^2\left(\frac{\cos^2\alpha_2}{\cos^3\alpha_m}\right)$$

$$+\ \frac{2\theta/h}{(3n+1)\left(\frac{1}{2n}+\frac{1}{2}-\frac{\theta}{h}\right)}$$

where

$$\frac{\theta}{h} = 0.379\left(\frac{x}{h}\right)Re_x^{-0.2},$$

x is the distance downstream from the exit plane in the flow direction and n is the index for a power law fitted to the velocity profile at inlet.

These correlations highlight what may be considered to be the most important parameters affecting the magnitude of the losses. Aspect ratio, blade loading, inlet boundary layer thickness and blade geometry appear to be important parameters for incompressible flows.

There are numerous other correlations that have been critically reviewed by Hirch and Denton (1981) and by Sieverding (1984). In reality all correlations rely on blade profile

similarity and their application is therefore limited. The necessity of adjusting correlations to obtain agreement between cascade and real machine results is a clear indication of their lack of generality.

2.7 THEORETICAL SECONDARY FLOWS

Gregory-Smith (1984) has recently given a review of secondary flow theory. The theoretical solution for the increase in streamwise vorticity through a curved duct, also applied to a cascade, was given by Squire and Winter (1951). The solution has been generalised using the equations of vorticity and vector analysis. Particular contributors were Hawthorne (1955), Smith (1955) and Lakshminarayana and Horlock (1973). Came and Marsh (1974) presented an alternative simpler approach that used vortex tracing in conjunction with Kelvin's circulation theorem. The equations for the components of vorticity (trailing filament, trailing shed and distributed secondary) were given for a many bladed cascade. Marsh (1974) extended this approach to take account of the axial velocity ratio in cascades. This effect may be caused by non-parallel endwalls, or blockage due to endwall boundary layer growth, or streamline shift due to non-free vortex design. Marsh (1976) further extended the theory to compressible flows and showed that for accelerating flows in turbines the effect was negligible within a given range of incidence. Glynn and Marsh (1980) presented an analysis for the secondary flow in an annular cascade. The analysis was in terms of a secondary flow stream function that was defined in the trailing edge plane. The

technique was used to simplify the analysis for annular configurations having non-constant primary exit flow angles along the span of the blades. Glynn (1982) presented a method to take into account the effect of Bernoulli surface distortion in linear cascades. A Bernoulli surface is one of constant stagnation pressure.

An interesting application of secondary flow theory of particular relevance has been given by Kingcombe (1976). A factor, K, was derived to show the relative effect of skewing the inlet boundary layer on the secondary vorticity at exit from a cascade. It was shown that

$$K = \frac{\xi_{S2}}{(\xi_{S2})_{colat}} = \cos(\alpha_1 - \beta_2) - \frac{\sin(\alpha_1 - \beta_2)}{2\tan\alpha_1 - \tan\alpha_2\left(1 + \frac{\cos^2\alpha_2}{\cos^2\alpha_1}\right)}$$

where α_1 is the rotor air inlet angle, α_2 is the rotor air exit angle and β_2 is the upstream stator air exit angle. However this result is not appropriate to the case in which we shall be interested. It was assumed that in the colateral case the normal vorticity was given by

$$\xi_{n1} = \frac{\partial V}{\partial Z}$$

and therefore that the freestream velocity was not the same in the colateral case as in the skewed case. To compare the

colateral and skewed cases we require the relative flow to the cascade to be the same, i.e. we require W and ξ_{n1} to be unchanged but $\xi_{s1} = 0$ for the colateral case. This requires a simple correction to the Kingcombe formula

$$K_{new} = \frac{K}{\cos(\alpha_1 - \beta_2)}$$

This result is for skew alone and since ξ_{n1} is unchanged takes no account of the effect of shear which may be important. For an impulse cascade with $\alpha_1 = -\alpha_2 = 40^o$ and $\beta_2 = 60^o$ it is found that $K_{new} = 1.11$. For a high turning rotor blade with $\alpha_1 = 42.75$, $\alpha_2 = -68.8$ and $\beta_2 = 70^o$ it is found that $K_{new} = 1.10$. These results show that inlet skew in the absence of shear increases the secondary vorticity at exit from the cascade by about 10%. The relationship between blade speed and K_{new} is shown in Figure 2.2. This result shows that the level of increase of exit streamwise vorticity does, as would be expected, depend on the blade speed.

2.8 FLOW MODELLING

The more challenging problem is to move away from correlations and to produce models that can be used in the design process to predict losses. As has been described above, the flow phenomena are very complex and there are therefore very few simple models available.

By considering the physics associated with secondary flows Gregory-Smith (1982) has produced a simple method for the prediction of secondary flows and losses. The secondary flow angles are calculated from secondary velocities that are obtained using a secondary flow stream function with the secondary vorticity at exit from the blade row. The secondary losses, which are obtained using the secondary flow angles, are divided into three components. The first component is assumed to be due to the upstream boundary layer which is shed as a loss core. This loss core is assumed to be triangular in shape and to have the same mass flow and kinetic energy deficit as the upstream boundary layer. The second component is assumed to be due to the new endwall boundary layer that is formed downstream of the cross-passage separation line. This new boundary layer is assumed to be turbulent and to start at the passage throat. The third component is an extra secondary loss that is assumed to be equal to the secondary kinetic energy calculated using classical secondary flow theory. The three components are simply summed to give the total estimated loss. Reasonable results were reported for several turbine blade rows.

Modelling of the endwall boundary layer flows is complementary to the modelling of secondary flows. A number of researchers have investigated compressor endwall boundary layers and, due to the simplicity of the method, have proposed models based on a momentum-integral approach. Mager (1954), Taylor (1959), Johnston (1960), Dring (1971), Horlock (1973) and Booth (1975) are amongst the classical works. The most well known model

for small cross flows was the triangular polar plot proposed by Johnston. This model did not however allow for crossover cross-flow behaviour as would be found in a cascade. These simple endwall flow modelling techniques give reasonable results for compressors where the endwall boundary layers can be considered to be a small perturbation of the main flow. However, they are unable to cope with turbines where the endwall boundary layer rolls up to form a loss core. Moreover, Langston (1980) quotes Johnston (1976) concluding that there was no general universal cross-flow profile, and that the flow in three-dimensional boundary layers is dependent in each case on the boundary conditions and flow history. This lack of generality has led to the abandonment of the momentum-integral based techniques in favour of the differential techniques.

The advent of high speed digital computers with increased storage capacity has encouraged the development of many new three-dimensional models. A review by Japikse (1976) of computational methods used for turbomachinery analysis concentrates almost entirely on two-dimensional methods, such as streamline curvature and stream function methods, for the meridional (S2) and blade-to-blade (S1) surfaces. Very little space was given to three-dimensional methods since it was felt that they were rarely, if ever, used for even inviscid turbomachinery designs. However, the inviscid three-dimensional models described were really quasi-three-dimensional in that they iterated between the S1 and S2 surfaces rather than solved the full equations. Less than ten years later McNally and Sockol

(1985) produced a review of computational methods for analysing turbomachinery flows. The emphasis of this review was completely different. The majority of it was taken up by reviews of fully three-dimensional models. It contained 144 references which was a clear indication of the interest and research effort that had been applied in the intervening period.

The eventual aim of the modellers must be to solve the full Navier-Stokes equations. However this is not yet possible and so simplifications have to be made. Models fall nautrally into one of two classes. They are either inviscid, in which case the Euler equations are solved, or they are viscous, in which case the time-averaged Navier-Stokes equations are solved. The full solution of these equations is an elliptic problem.

Although the Euler equations allow entropy, total pressure, and total temperature to be varied in the flow field they do not allow the generation of losses. A number of algorithms exist for marching the time-dependent Euler equations to a steady state solution but in general they require large numbers of iterations and thus computer time. Another disadvantage is the amount of storage required since up to five variables may have to be stored for each grid point in the flow field. An example of an explicit method, one in which the derivatives are calculated using results from an earlier time step, has been given by Denton (1975) for modelling turbomachinery flow fields. Although the model has been extensively used, Bryce and Litchfield (1975), most of the reported examples are for two-dimensional transonic flow. Denton

(1983) has revised the model in order to improve its accuracy and speed of convergence.

The basic equations that are solved are those for the conservation of mass, momentum (in each coordinate direction), and energy. For two-dimensional modelling the energy equation is often replaced by an assumption of isentropic flow. A better assumption is that the stagnation enthalpy is constant since this condition is exact for adiabatic steady flow. A similar condition of constant rothalpy along streamlines may not be feasible for three-dimensional flows that have significant variation of flow properties in the spanwise direction. The energy equation is therefore usually solved directly for three-dimensional flows.

In order to ensure the stability of the model upwind differencing was used in the streamwise direction for the fluxes of mass and momentum whilst downwind differencing was used for pressure. Central differencing was used for all quantities in the pitchwise direction. The stability of this "opposed difference" scheme was found to depend only on the axial Mach number rather than on the absolute Mach number. A major disadvantage of timemarching is that errors in the finite differencing lead to entropy changes that appear as stagnation pressure changes in the flow. These errors do not remain localised but appear to affect the whole downstream flowfield. The revised scheme (Denton (1983)) uses a non-overlapping grid in order to reduce differencing errors and thus improve the conservation of entropy. Another disadvantage is the amount of computer time required to obtain a converged solution. The revised scheme introduced a

simple multigrid system that allows the overall flow pattern to be developed quickly on a coarse grid, with the fine detail being resolved on one or more finer grids. This had the effect of considerably improving the speed of convergence. A disadvantage of the opposed difference scheme is that reverse flows cause the scheme to become unstable. This problem is overcome, at the expense of accuracy, by using upwinded values of convected velocity when the meridional velocity is negative. Experience of using the revised method for two-dimensional transonic flows has been reported by Sato et al (1986a, 1986b).

In the case of viscous flows the time-averaged Navier-Stokes equations pose formidable problems. For three-dimensional flow there may be five variables, two turbulence properties, and nine or more metric derivatives. Each of these quantities needs to be stored for each grid point which, for a reasonable grid size, indicates that a large amount of computer storage will be required. However, simplifying assumptions can be made. A partially parabolic approximation can be produced if the primary flow direction can be assumed. A sequence of marching followed by a pressure update is repeated until convergence is obtained. Moore and Moore (1979) have produced a method that uses a pressure equation derived from the divergence of the momentum equations. Another approximation can be made by assuming, in addition to the partially parabolic assumption, that there is negligible transmission upstream of pressure disturbances. This then is the fully parabolic approximation and only a single pass is required for solution. However, the effects of flow separation

and reversal can only be adequately modelled by fully elliptic codes. There are few of these codes available and their status is currently that of a research tool.

Recently Moore and Moore (1985) have presented results of using an elliptic method for three-dimensional viscous flows. The conservation equations for mass, momentum and energy were coupled with a Prandtl mixing length model for viscosity. The velocity components were obtained from the momentum equation and rothalpy from the energy equation. This model is a pressure correction method that solves the continuity equation for pressure and the equation of state is then used to obtain density. Timemarching methods generally solve the continuity equation for density and then use the equation of state for pressure. An advantage of using the pressure correction technique is that it can be made to converge in very few iterations. Important features of the model are the use of central differencing in order to eliminate numerical mixing and upwinded control volumes are used to ensure the stability of the scheme. This overcomes the effect of numerical viscosity imposed by upwind differencing that is often used to force stability on schemes. The drawbacks of this model are that its use is limited to steady, subsonic flows and that there is no transition model programmed. However, regions of the flowfield can be designated to be either laminar or turbulent. This model has been used by Moore and Moore (1985) for the flowfield in the Langston et al (1977) cascade. Remarkably good results for the turbulent flow were obtained with only sixteen iterations. However, the 7000 grid points used required over one

hour of CPU time on an IBM 3081 mainframe computer and 3 Mbytes of storage.

Undoubtably the bulk of the data required for three-dimensional flow programs consists of the geometry description. The further development of the three-dimensional codes will be hampered by the difficulty of setting up the required geometry definition until the process is automated. Furthermore, the amount of computer storage and operator involvement required for modelling just a single component is a clear indication that running the codes is not a routine matter. And further, that the full three-dimensional design of turbomachinery using these codes is still a long way off.

There still remains a requirement for simple models, maybe based on secondary flow theory, that can be used in the initial design optimisation stages. The validation of the design may then be carried out using three-dimensional codes. In order to ensure the validity of these three-dimensional codes test cases are required. The work reported in this thesis is intended to at least partially fill that requirement.

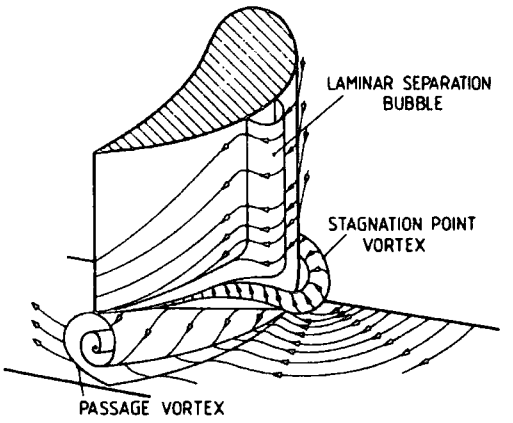

Klein (1966)

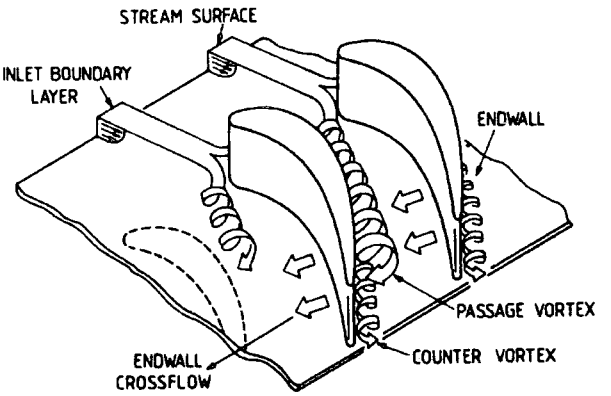

Langston (1980)

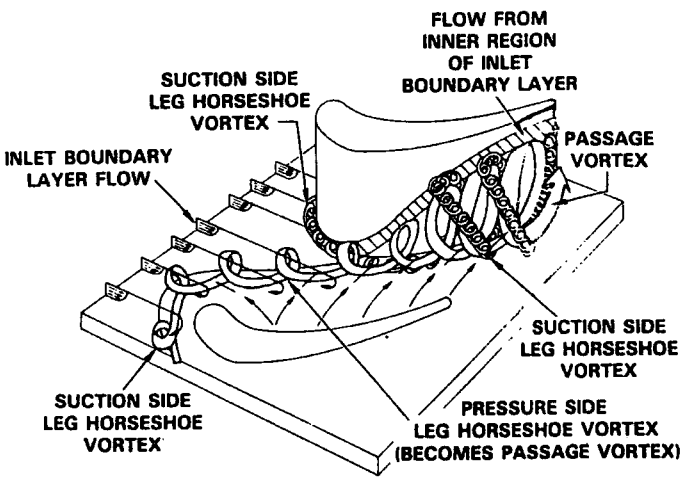

Sharma and Butler (1986)

FIGURE 2.1: Cascade Flow Models

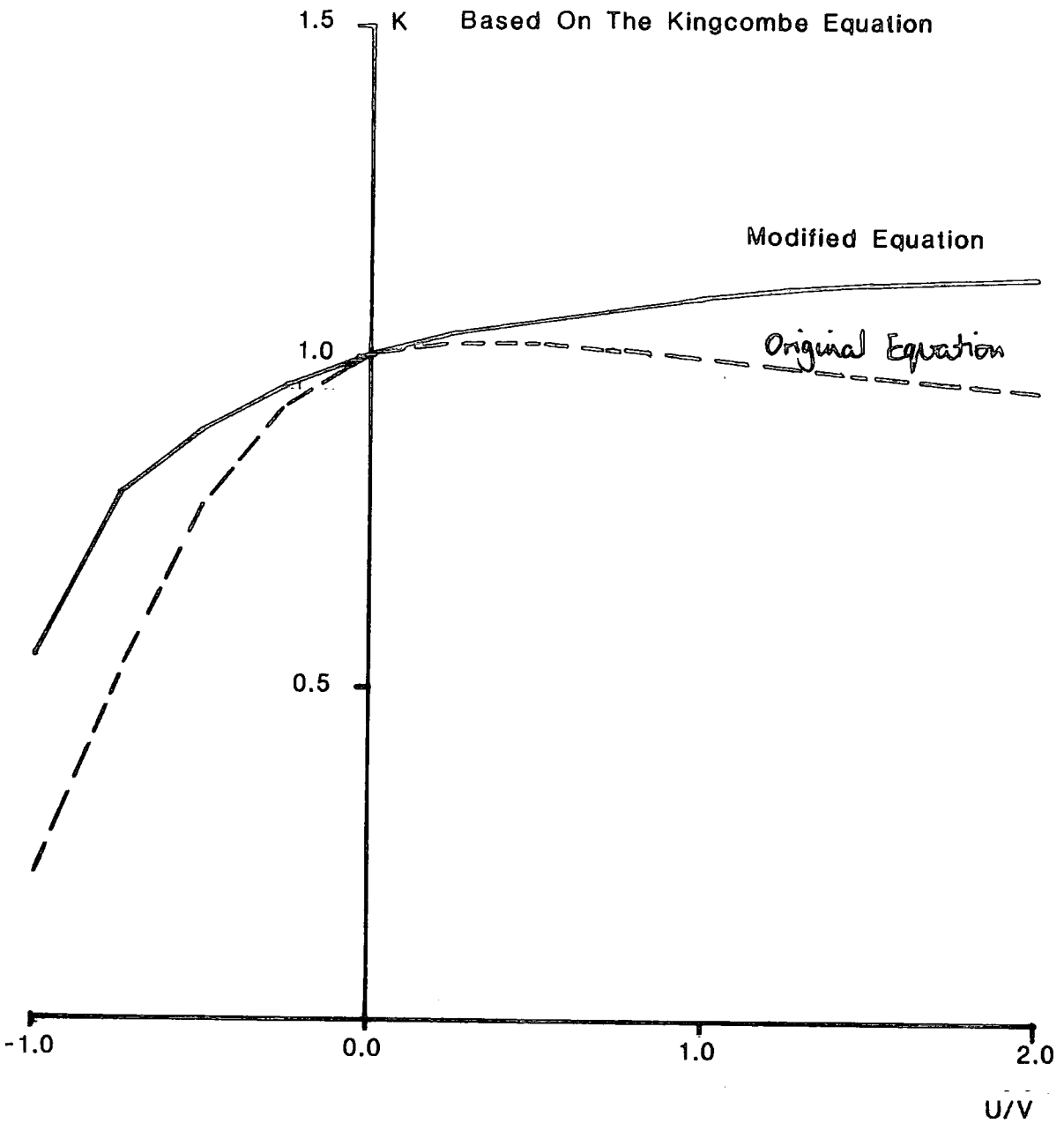

FIGURE 2.2: The Effect Of Blade Speed On Streamwise Vorticity

CHAPTER 3 : EXPERIMENTAL APPARATUS AND TECHNIQUES

This chapter reviews the experimental apparatus and techniques that were used to collect data from two large scale, low speed, rectilinear cascades. The first cascade and much of the instrumentation was already in existence at the start of this research project. The second cascade was specifically designed and built to measure the effect of a skewed inlet boundary layer. The design details and construction techniques of this cascade are discussed. The data collection methodology and a brief analysis of the experimental accuracy are also discussed. The flow visualisation technique that was used is presented.

3.1 AIR SUPPLY

The cascade of blades is mounted on the exit of a blowing wind tunnel that exhausts to atmosphere. The air for the wind tunnel is diffused from a double entry centrifugal fan through gauze screens into a large settling chamber. The air is then accelerated through a contraction and enters, via a honeycomb flow straightener, the parallel walled working section. In an effort to cut down the contamination of hot-wire anemometry sensors by airborne grease and dust particles, the fan was completely enclosed in a timber and plywood housing. Three of the walls each contained six 18" square Vokes general purpose filter elements in a panel.

3.2 CASCADES

The early part of this research was carried out on a large-scale low speed rectilinear cascade that was already in existence. Since the constructional details have been fully documented by Graves (1985) only brief details will be given here. This cascade will be referred to as the CPG cascade.

The CPG cascade consisted of seven blades that were suitably scaled from a midspan high pressure turbine reaction blade design. The blades were cast in epoxy resin, using a technique similar to that of Gregory-Smith and Marsh (1971), and held in a framework of timber and plywood at the correct stagger angle by studs and locating dowels. Two of the blades were instrumented with surface static pressure tappings. A large portion of one endwall was constructed from perspex to form a window in order to allow flow visualisation. The opposite endwall, which was made from plywood, was slotted at the appropriate axial planes for traversing with the probes (Figure 3.1). Unfortunately the construction methods employed prevented the removal of the perspex window and the blades without destroying the cascade box.

It was decided to construct a new facility that would allow the investigation of the effect of skewing the inlet boundary layer. The rig design was to incorporate features to overcome the practical problems associated with the CPG cascade. Other features that were required included a cantilever blade mounting so that the rig could be used at a later date to

investigate the effects of over tip leakage flows and a more representative inlet boundary layer thickness.

The blade profile needed modification for operation at low speed. When a blade designed to operate at transonic Mach numbers is placed into a low speed incompressible flow there is a large amount of suction surface diffusion. This adversely affects the phenomena under investigation and so removes the test further from reality. The reason for the suction surface diffusion may be explained by the effect of compressibility in the accelerating region up to the throat of the blade passage. Consider R where

$$R = \frac{\text{Mean velocity across passage upstream of throat}}{\text{Velocity at throat}}$$

$$= \frac{(\rho A)\ \text{throat}}{(\rho A)\ \text{upstream}}$$

where ρ is density and A is the cross-sectional area in the passage. Since for incompressible flow $\rho \simeq$ constant and for compressible flow $\rho_t < \rho_u$ then $R_{incompressible} > R_{compressible}$.

Hence in incompressible conditions the suction surface peak velocity would be expected to be greater relative to the throat velocity. The resulting diffusion will alter the profile loss and also probably affect the secondary flows.

When designing the new cascade, which will be referred to as the JAW cascade, it was decided to modify the profile of the adopted blade section in order to reduce the suction surface diffusion at low speed. This would also delay the onset of the

laminar separation bubble which was found in the CPG cascade. Thus the profile that was used was designed to give aerodynamic similarity rather than geometric similarity to a typical high pressure turbine blade section. The model turbine blade profile that had been used as the basis for the CPG cascade had undergone a redesign since that cascade was built. Since the effect of inlet skew was to be investigated it was decided to base the JAW cascade on the root section of the redesigned blade.

The modification of the blade profile for use in the JAW cascade was carried out using a quasi-three-dimensional computer program based on the streamline curvature technique. Details of the design process and model have been presented by Morgan (1984) and by Jennions and Stow (1985a, 1985b). The static pressure coefficient distributions (Figure 3.2) clearly show the effect of modifying the profile. The aim was to reduce the predicted suction surface diffusion level of 44% in the low speed conditions to the design conditions predicted level of 14%. However, this was found to be impossible to achieve since to alter the lift coefficient the pitch to chord ratio would have to be changed. A predicted suction surface diffusion of 28% was achieved by reducing the throat opening by 8% and the flow inlet angle by about 7^{o}. A laminar separation bubble was predicted to occur at about 70% of an axial chord from the leading edge of the blade and its position is predicted to be virtually insensitive to variation in incidence because of the relatively large radius used for the leading edge. It was found that the modification of the blade

profile reduced the Zweifel blade loading coefficient from the design value of 1.09 to 0.97.

The blades were cast in epoxy resin from an aluminium master using a technique similar to that reported by Gregory-Smith and Marsh (1971). In order to ensure that the blades were accurately mounted into the cascade box a full size computer plot of the blades at the correct stagger angle was produced and fixed to the endwall. The two blades that form the central passage were instrumented with surface static pressure tappings by casting hypodermic tubing under the surface running in the spanwise direction. The locations of the tappings are shown in Figure 3.4. The tappings were drilled at appropriate spanwise distances from one endwall and when not in use the holes on the surface of the blade were covered with thin plastic tape to preserve their integrity. The hypodermic tubing was led out through the endwall on which the blades were mounted, and could then be connected via plastic tubing to an inclined multitubed manometer. A steel spine was also cast into the blades in order to give stiffness to the blades since a cantilever mounting was being used. A stud was fitted into the end of each blade after it had been cut to size and this was the fixing to the solid endwall. In order to ensure that the blades always went into the cascade box at the correct orientation a 'D'-washer arrangement was used with the studs being cut appropriately (Figure 3.3). Since the blades are effectively supported by only one endwall it was constructed from 1.75" hardwood cored blockboard. The rest of the cascade box was manufactured from timber and 0.75" plywood. A perspex window,

large enough to allow the removal of the two instrumented blades for flow visualisation documentation purposes, was fitted into the plywood endwall. The endwall on which the blades were mounted had slots cut at appropriate axial planes for traversing with the probes (Figure 3.4).

As with the CPG cascade, the JAW cascade was manufactured with seven blades in the cascade box although only six were used in this research to form five passages in the flow. The seventh blade could be used at a later date to study the effect of an incidence change. The design parameters of both cascades are summarised below:-

TABLE 3.1: CASCADE DESIGN DATA

	CPG	JAW
Flow inlet angle	42.75°	42.75°
Blade inlet angle	52.25°	47.6°
Flow exit angle	-66.6°	-68.8°
Blade exit angle	-67.5°	-68.6°
Blade chord	216 mm	224 mm
Axial chord	175 mm	181 mm
Span	457 mm	400 mm
Blade pitch	191 mm	191 mm
Zweifel loading coefficient	1.07	0.97
Cascade Re	4×10^5	4×10^5

A right handed axis system is defined for the cascades in the usual way by the axial, tangential and spanwise (or radial) directions (Figure 3.5).

3.3 SKEWED INLET BOUNDARY LAYER RIG

It was decided to investigate the effect of skewing the inlet boundary layer separately from the effects of radial pressure gradients and other effects that may be found in annular cascades. The existing low speed facility was therefore modified by placing a moving belt 15% of an axial chord upstream of the cascade box to produce the required skewing effect. This technique can be justified by considering the boundary layer developed on the belt to be the kinematic equivalent of the boundary layer from a stator passing through a cascade of moving blades. Carrick (1977) used a similar design to study the effect of inlet skew in a linear cascade of impulse blades.

It can be deduced from the velocity triangle (Figure 3.6) that the ratio of belt speed to air speed is a function of the stator outlet angle, β, and the rotor inlet angle, α. In modern practice a typical value for β is 70° and for the design conditions in the JAW cascade it can be shown that the required ratio of belt speed to air speed is 1.339. The width of the belt can be approximately determined from the required thickness of the boundary layer. If it is assumed that there is no pressure gradient in the working section of the tunnel, and thus across the belt, the well known flat plate approximation for boundary layer thickness can be used:

$$\delta = 0.371x \, Re_x^{-0.2}$$

where δ is the boundary layer thickness

x is the distance along the belt

and Re_x is the Reynolds number based on x.

The required belt width is then given by

$$w = x \cos\alpha$$

For an 800mm wide belt, the size that was eventually selected, one would expect a boundary layer thickness of about 42mm. The cascade and moving belt system were supported by a framework in a twin goalposts arrangement constructed from steel section 50mm square by 4mm thick (Figure 3.7). The two pulleys were turned from hardened steel with a maximum diameter of 150mm on the crown and they were dynamically balanced. The upper pulley was mounted in plummer blocks and driven by a 4kW thyristor controlled motor via a timing belt. A smaller motor was initially used to drive the system but, in conjunction with its associated controller, it was unable to provide sufficient torque to overcome the inertia of the system at startup. The timing belt drive was geared to step up from the motor and give a maximum pulley speed of about 3,400 rev/min. The lower pulley was mounted on takeup units that were fitted onto sliding rails to allow the belt to be tensioned and tracked.

The belt was mounted so that it formed one endwall of the working section of the tunnel upstream of the cascade box (Figure 3.8). The belt used was a Habasit type SNB-8E, 800mm wide by 5892mm long, and it was made from polyester with a pvc covering.

Since the tunnel pressure was above atmospheric pressure it was found that the belt ran flat against the formica covered backboard. In an attempt to reduce friction compressed air was injected between the belt and backboard to provide an air bearing. This produced no noticeable change in the performance so that all the tests were done without the air bearing. Seals that were made from Melinex were designed to be used at the upstream and downstream edges of the belt. At the upstream edge of the belt the air flow helped to maintain the contact between the edge of the seal and the belt surface whereas at the downstream edge the action of the flow was to lift the edge of the seal away from the belt surface. Thus at the downstream edge of the belt, for the non-stationary cases, it was difficult to get the balance right between the seal pressing hard enough to remain in contact with the belt surface but not so hard as to damage the belt. Flow visualisation (Figure 3.9) showed that the seals were only necessary for the stationary belt case since when the belt was not tensioned it had a tendancy to curl slightly at the edge.

Upstream of the belt there was a short length of false wall the backface of which led into a bleed opening (Figure 3.10). To ensure that the tunnel was balanced a static pressure tapping was embedded into each side of this wall and connected to a differential pressure transducer. The bleed opening was set to give a reading of near to zero and it was found that the setting did not need to be altered. A disc with six vanes cut into it was mounted on the shaft of the drive pulley and was used as an interupter for an opto-electronic device. This enabled the shaft

speed of the belt pulley to be kept constant. The relationship between belt speed and shaft speed was calibrated with a hand held digital tachometer with surface wheel. The calibration was checked from time to time to ensure that the belt was not slipping.

Although the design specification and manufacture of most of the skewed boundary layer rig were completed within the Engineering Department, the production of the detailed design drawings was put out to contract.

3.4 INSTRUMENTATION

The instrumentation used in this research was already in existence and since full details are given by Graves (1985) only brief details will be given here except where techniques or equipment have changed.

The experiments were run by a Cifer microcomputer programmed in Fortran. The Cifer read data from up to eight channels of analogue to digital converter that input data from the positional transducers and the differential pressure transducers or hot wire anemometers. The Cifer also controlled a unit that operated solenoid valves to select the appropriate pressure combinations from the pressure sensing probes for connection to the differential pressure transducer.

Limited analysis of the data was carried out by the Cifer before the data was transferred via a floppy disk to the mainframe computer where a full analysis and presentation of results was carried out.

Data from the blade's surface static pressure tappings was recorded manually from an inclined multi-tubed manometer.

Probe traverse slots were cut into one endwall, at appropriate axial positions, parallel to the tangential plane (Figures 3.1 and 3.4). The probe traversing gear, which had been designed to accept both pressure sensing and hot-wire probes, was aligned with the required slot by adjusting the whole assembly on T-slotted rails that were bolted to the cascade endwall. The traverse gear consisted of flat sliders in the tangential and spanwise directions and a calibrated rotary table (Figure 3.11). The tangential and spanwise slider assemblies were fitted with potentiometers that acted as positional transducers.

Three-hole and five-hole pressure sensing probes of the cobra type (see Graves (1985)) were used to traverse the cascade flowfield. The sensing heads were constructed of 0.5 mm bore hypodermic tubing and had been designed so that the measuring volume remained fixed in cascade coordinate space as the probe was rotated. A pitot-static tube was placed upstream and was used for reference purposes. Data was recorded simultaneously from both the multi-tubed probe and the reference probe.

The calibration of the five-hole pressure sensing probe was carefully checked before each series of tests to ensure that it was still valid. The probe was placed in a calibration position in the working section of the tunnel mounted on a compound mount formed from two rotary mounts and a pair of angle brackets. The probe was set at various twist and tilt angles at which data was recorded and then later run through the analysis

programs to recover the turret setting angles from the calibration maps. Since the calibration was found not to have altered the probe did not require recalibration.

The three-hole pressure sensing probe was recalibrated several times since it was easily damaged. The probe was only calibrated for varying twist angle since it does not record pitch angle (i.e. spanwise) variation.

The CPG cascade flowfield was also traversed with two miniature twin hot-wire sensors (DISA 55P53 and 55P54). The measuring plane of the two sensor types differed by 90^{o} relative to the sensor support (DISA 55H24). A probe stem had been constructed to ensure that the measuring planes for both types of hot-wire sensor were invariant with probe rotation. The instrumentation used for hot-wire anemometry is very complex and a great deal of care has to be taken in order to obtain good quality results. The two wires of the sensor being used were analysed separately. Each wire was led into a constant temperature bridge circuit (DISA 55M01). The output of the bridge was fed into a linearisor (PROSSER 6130) which was calibrated to provide a direct relationship between the bridge output voltage and the air velocity. The linearisor output was taken to a signal conditioner (PROSSER 6141). In order to increase accuracy the difference between the mean and rms values of the signal was maximised by removing a large amount of DC and amplifying the remaining portion. This ensured that the full range of the analogue to digital converters was used. This output was then fed into a unit that separated the mean and rms portions of the signal and also

into a turbulence processor (DISA 52B25) to provide correlation data. The results of these processes were input to the analogue to digital converters for collection by the Cifer microcomputer. An upstream pitot-static tube was used for reference purposes and to check that the tunnel conditions did not change.

Hot-wire sensors need to be calibrated in a region of flow in which the velocity can be varied over the range that is to be measured. Graves (1985) calibrated his sensors in a jet of compressed air. However, it is sufficient if not preferable to calibrate the sensors at a low turbulence position in the rig in which the measurements will be taken (Perry (1982)). Therefore the calibration was carried out in a downstream slot (slot 10) of the cascade between the blade wakes. Each wire of each sensor was individually calibrated. After the cable resistance was balanced out and the overheat ratio set, the sensor was placed into the flow and its response to a 3kHz square wave optimised. With the sensor aligned with the flow, and a pitot-static tube placed downstream of it on the same stream surface but slightly displaced in the spanwise direction to avoid interference effects, the bridge output voltage and the flow velocity were recorded for different fan speeds (typically fifteen). Wire sensitivity and linearisers settings were then calculated using a fourth order polynomial fitted by least squares. The performance of the linearisers were checked using an external voltage source.

3.5 EXPERIMENTAL TECHNIQUE

Since the data collection and the control of the experiments were carried out by the microcomputer most of the experimental technique was embedded in the computer programs that were used. Much of the actual process of collecting the data has been described by Graves (1985) but the software was further developed during this project to cope with the skewed inlet boundary layer experiments.

To ensure the consistency of the results the experiments were always carried out at the same Reynolds number defined by the exit velocity and blade chord. In a question and answer approach the atmospheric conditions were input into the microcomputer and using a standard day set of conditions the dynamic head for setting the tunnel was calculated. In the case of inlet skew the required belt velocity was calculated from this dynamic head to maintain the consistency.

The probe that was being used to traverse the cascade flowfield was placed through the endwall at the appropriate slotted axial postion (Figures 3.1 and 3.4). The probe was traversed away from the opposite endwall in the spanwise direction for each of a series of pre-determined tangential positions (usually twelve in the case of a traverse inside the blade passage). At each tangential position the portions of the slot not being used were taped over to ensure that there was no bulk inflow or outflow of air. Slots not being used had T-shaped fillers that were manufactured to present a smooth endwall surface to the flow.

In the case of pressure sensing probe measurements Graves (1985) described a method of conditional sampling to be used for the data collection. This scheme was appropriate when an earlier research fan was used which did not give steady flow conditions. The removal of the conditional sampling criteria was accomplished without a major rewrite of the software by making the acceptance band of the scheme much wider. This had the effect of speeding up the traversing whilst still giving good results. A statistical test was retained to ensure that sufficient data was collected at each traverse point in the flow to give a 99% confidence that the mean was within 1% of the value of each pressure reading. At the start of each traverse the probe was set to the approximate midspan flow angle. With the development of the skewed inlet boundary layer rig it was expected that flow directions would change rapidly. A facility was therefore introduced to allow the turret setting angle to be changed during the run. This ensured that the flow angle was always within the central part of the probe calibration region. This modification meant that there were significantly fewer occasions on which results had to be extrapolated for data lying outside of the calibration region.

When traversing with hot-wire sensors the flowfield had to be traversed separately by each of the two types of sensor. The probe was inserted, very carefully, into the flowfield as described above. At each position at which data was required the probe was aligned with the yaw angle found by the pressure sensing probes (usually the five-hole probe). Hot-wire anemometry is very user intensive and requires a great deal of effort and care for

successful traversing. The signals from the sensors were continuously monitored with an oscilloscope to ensure that the whole input range of the analogue to digital converters was used in an effort to maximise sensitivity and accuracy. Care had to be taken to avoid clipping the signals by over-amplification. At the start of a traversing session a calibration check position was selected. At the end of each tangential traverse the probe was returned to that position to check that its performance was not significantly altered due for example to wire contamination. The filtering of the air at inlet to the fan greatly reduced the occurrence of this phenomenon. If the wire characteristics had changed slightly the anemometer probe was cleaned and rechecked. If the wire characteristics had changed significantly the traverse was redone with a fresh probe. At several points in the flowfield data was recorded on a four channel instrumentation tape recorder for later spectral investigation.

3.6 DATA ANALYSIS

For the pressure sensing probes the data collected for each traverse position consisted of the positional coordinates, the turret setting angle and a set of pressures in units of millimetres of water gauge. For the hot-wire sensors the equivalent data collected consisted of the positional coordinates and the direct voltages with the gain and offset settings.

For the pressure sensing probes the local velocity, V_L, the flow angles (pitch and for the five-hole probe yaw), and the total and static pressures were obtained from calibration maps.

The non-nulling technique that was used was described by Schaub et al (1964) for incompressible flows. The total pressure loss coefficient is defined as:

$$\xi = \frac{P_{01} - P_{0L}}{1/2\ \rho\ V_1^2}$$

where V_1 is the upstream velocity and is defined as

$$V_1^2 = \frac{2\ (P_{01} - P_1)}{\rho}$$

A similar expression is used for the static pressure loss coefficient. Pitchwise averaged values were obtained by integrating in the tangential direction across the pitch

$$\bar{\xi} = \frac{\int V_{ax}\ \xi\ dT}{\int V_{ax}\ dT}$$

and for the yaw angle

$$\bar{\epsilon} = \tan^{-1}\left(\frac{\bar{V}_{tan}}{\bar{V}_{ax}}\right) = \tan^{-1}\left(\frac{\int V_{ax}\ V_{tan}\ dT}{(\int V_{ax}\ dT)^2}\right)$$

An area average was obtained for the axial plane by integrating the pitch averaged values in the spanwise direction. The streamwise component of vorticity was calculated from the velocity measurements by fitting a least squares bicubic spline surface to the data. This allowed the gradients of the local velocity to be calculated in the tangential and spanwise directions. Due to the relatively wide spacings of the axial

measurement planes the incompressible Helmholtz equation was used to obtain an expression for the axial gradients. Details of the technique are given by Gregory-Smith et al (1987).

For the hot-wire sensors the data was converted to mean and fluctuating components of velocity using the sensitivities obtained at calibration. The analysis has been described by Graves (1985). The data from the separate traverses of the two types of hot-wire sensor were analysed in parallel. Redundancy in the equations was used to provide an average value for the mean and fluctuating velocities in the axial direction.

The data obtained by traversing with the probes was transferred via a floppy disk to the University's mainframe computer for full analysis. The results of the data analysis will be presented as contour or vector plots for each axial plane. Where appropriate the results will also be mass averaged across the pitch using a four point quadrature integration scheme.

3.7 EXPERIMENTAL ACCURACY

It is impossible to estimate the cumulative effect of experimental errors even though steps were taken to ensure that the errors were minimised at each link in the chain that formed the experiments. The probes were positioned relative to the windowed endwall and the trailing edge plane of the blade to within 0.5 mm. The differential pressure transducers were regularly recalibrated to ensure that pressures were read as accurately as possible. An indication of the accuracy to which the pressures were recorded is given by the pressure sensing probe

calibration checks that were regularly carried out. The turret setting angles that were recovered by the analysis program were generally within 0.2 of a degree of the value actually set. For hot-wire probes the turret angle was set to within five minutes of the angle required at each traverse position. The dynamic head and velocity of the moving belt were both set to within 1% of the value required for constant Reynolds number operation and continuously monitored and adjusted when necessary. The calibration of all of the electronic circuitry associated with the hot-wire anemometry was carefully checked before it was used. The accuracy of the analogue to digital converters was continuously monitored by comparing the reading obtained by voltmeters, oscilloscopes and digital micromanometers, as appropriate, to the result obtained and displayed by the microcomputer.

Although it has been shown that reasonable care has been taken to minimise errors whilst running the experiments it is necessary to attempt to determine the uncertainty of the results. Because of the complexity of carrying out an analysis such a statement of uncertainty is in itself likely to be uncertain. A number of possible physical errors for pressure sensing probes have been identified by Blake (1983) for incompressible flows. There are alignment errors such as between the probe axis and the flow velocity vector, or between the probe axis and the cascade axis. The former is not appropriate since a non-nulling technique was used. However this technique required the probe to be calibrated and therefore introduced other errors such as those that are implicit in fitting a surface to the calibration data.

Another error that can be identified is due to the presence of turbulence which will have the effect of increasing the sensed value of the mean total pressure. However the error in the difference between the total and static pressures will probably be less than that in each pressure separately and may even by negligable. Another error may be due to wall proximity effects that arise when the probe head approaches the endwall and causes the deflection of the streamlines. In the case of the five-hole pressure probe the minimum distance of the probe axis from the endwall was greater than the suggested minimum of two probe diameters. Another possible error is due to the influence of the probe support stem but the cobra design that was used minimised this error.

The non-nulling technique that was used for the pressure sensing probes does not fully take into account the variation of flow parameters with respect to Reynolds number. Schaub et al (1964) show that the error in ignoring the Reynolds number effect is likely to be $\pm 4\%$. This would indicate a maximum error of approximately $\pm 1^{o}$ for the flow angle measurements assuming perfect alignment of the probe axis and cascade axis systems. However a finer calibration grid was used than that suggested by Schaub et al (1964) so that the actual error is likely to be smaller. The results for the total pressure loss coefficient showed an unexpected zero shift resulting in non-zero values in the midspan low loss region (between the blade wakes for slot 10). This zero shift could not be satisfactorily explained and the values were therefore corrected. The absolute levels of total pressure loss

may therefore be in error by as much as the correction that was applied. The gradients and relative levels of total pressure loss should be more accurate. Because of the potential importance of the corrections they are tabulated below. The values were obtained by integrating the total pressure loss coefficient in a region that would be expected to have a zero value (e.g. between the wakes at a midspan position for slot 10). The values in the table were subtracted from the measured values of total pressure loss, and to maintain consistency from the static pressure coefficient as well. These values represent a possible error of up to 6% of the maximum measured value of the total pressure loss.

TABLE 3.2: CORRECTIONS FOR TOTAL PRESSURE LOSS

	INLET SKEW TYPE		
SLOT	NEGATIVE	COLATERAL	POSITIVE
1	0.0103	0.0197	0.0172
3	0.0408	0.0431	0.0403
5	0.0399	0.0576	0.0491
8	0.0982	0.1000	0.0962
10	0.0933	0.0964	0.0959

(NB: Correction assumed constant over the slot area)

In the case of the hot-wire results there is very little in the literature to help determine their uncertainty. Yavuzkurt (1984) identified the largest source of calibration error as being due to inaccurate reading of the micromanometer at low velocities. It was also shown that 5% is a reasonable estimate of the uncertainty for the velocity and second order correlations for a slant wire in a two-dimensional flat plate boundary layer. In the

absense of any other data the level of uncertainty for the hot-wire results will be assumed to be limited to 5% although in regions of large pitch angle this may be an underestimate of the errors.

3.8 FLOW VISUALISATION

Many techniques of flow visualisation have been reviewed by Merzkirch (1974) and by Settles (1986). Most of the techniques are not appropriate for this application due to the speed of the air through the cascade. Surface flow visualisation studies were carried out on both cascades using a method described by Maltby and Keating (1962). Diesel oil was mixed with 'Dayglo' pigment in a ratio of three to one by weight for painting onto the surface of interest. 'Dayglo' pigment is particularly good for this purpose since fine patterns can be produced, without the need for additives to control the size of the floc. The patterns that are produced are clearly visible in daylight and photograph very well under ultraviolet illumination.

The endwall and blade surfaces were first coated with a thin sheet of self adhesive plastic film. The oil and dye mixture was then painted on to the covered surfaces and the tunnel run. The resulting patterns were photographed in situ. In the case of the CPG cascade the plastic film was carefully removed for further photographs to be taken trying to minimise the damage to the patterns. In the case of the JAW cascade the perspex endwall and blades were removed with the plastic film intact for further photographs to be taken.

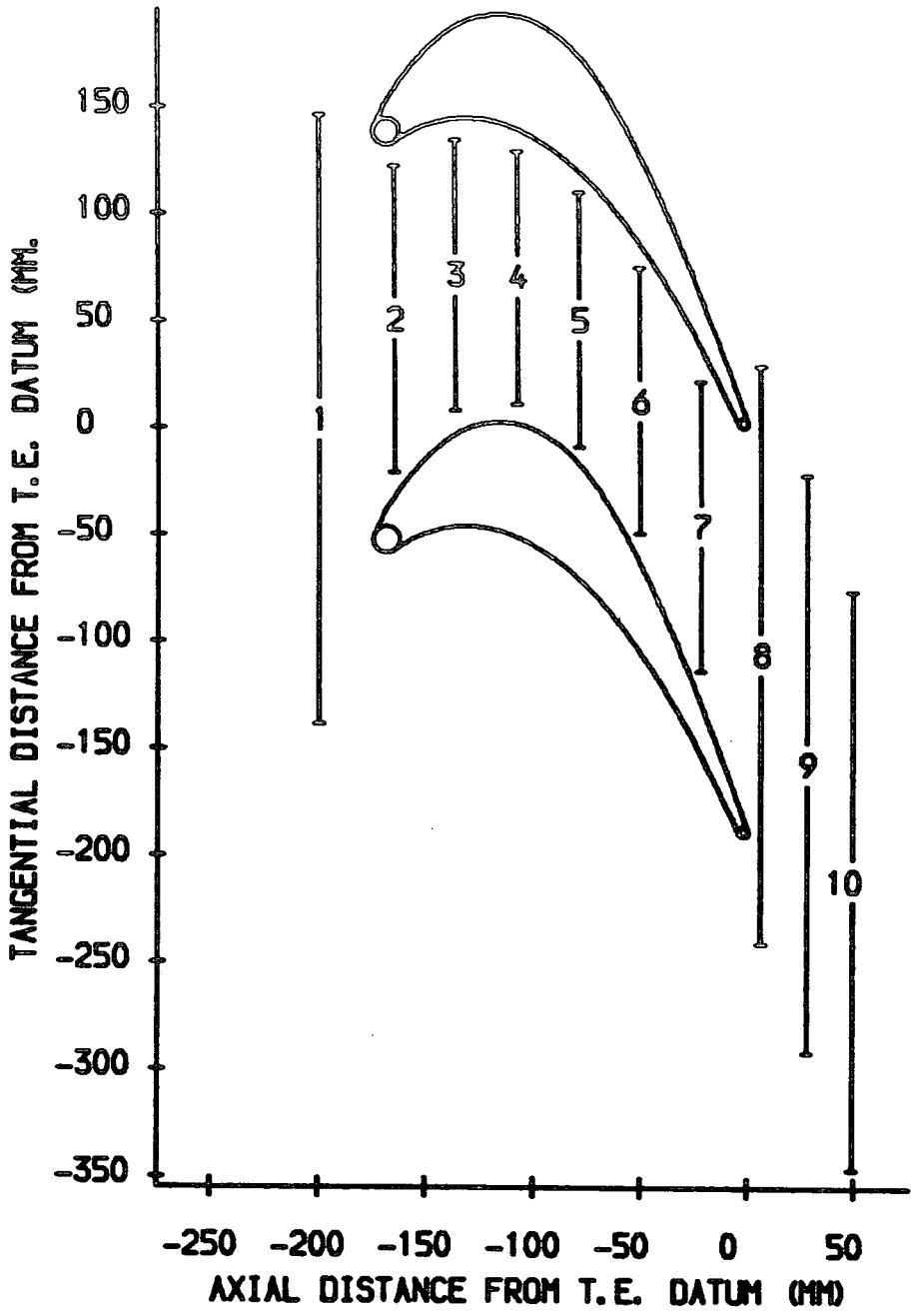

FIGURE 3.1: Location Of Measurement Planes (CPG Cascade)

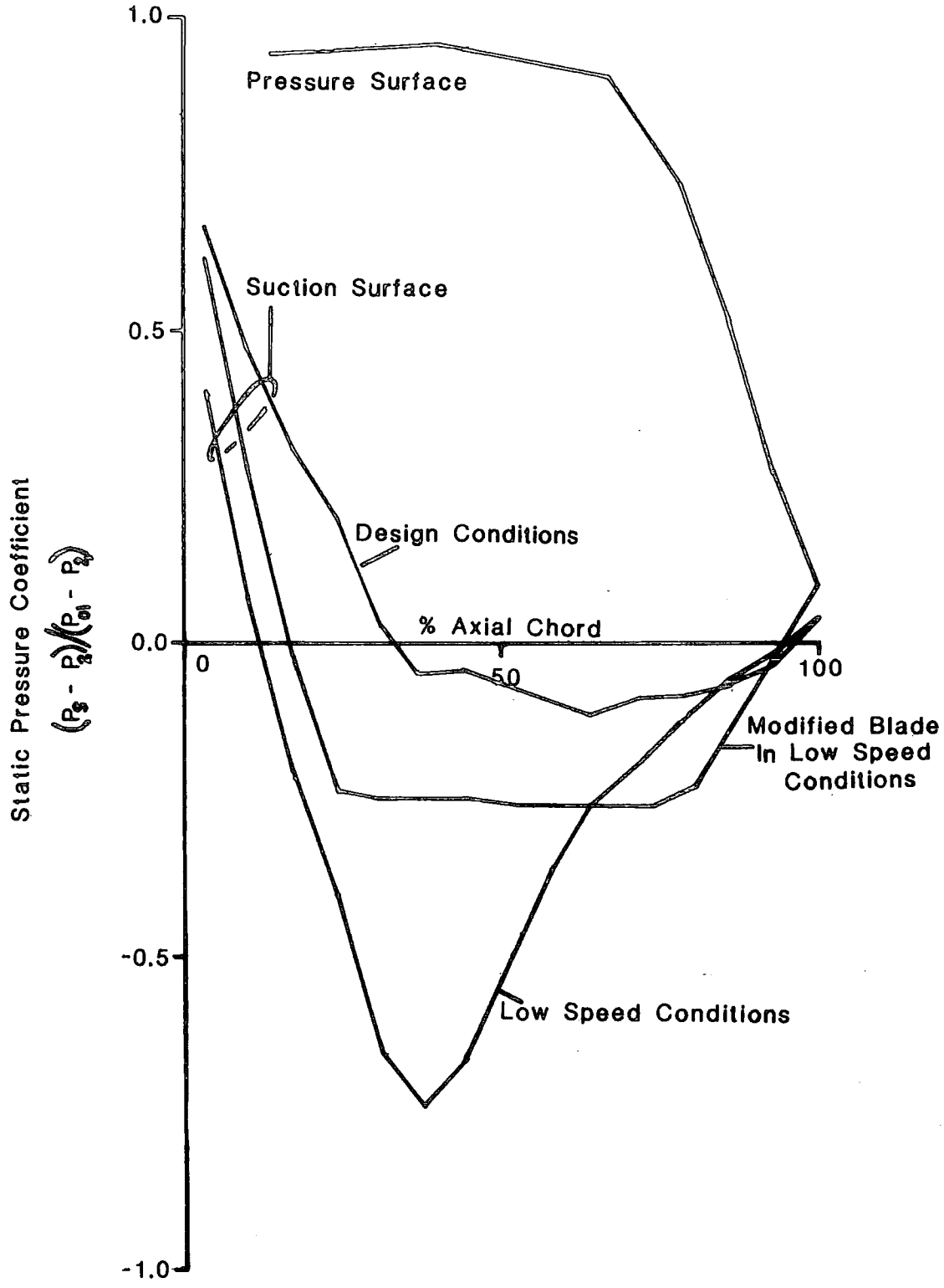

FIGURE 3.2: The Effect Of Redesigning The JAW Blade Profile

Not To Scale

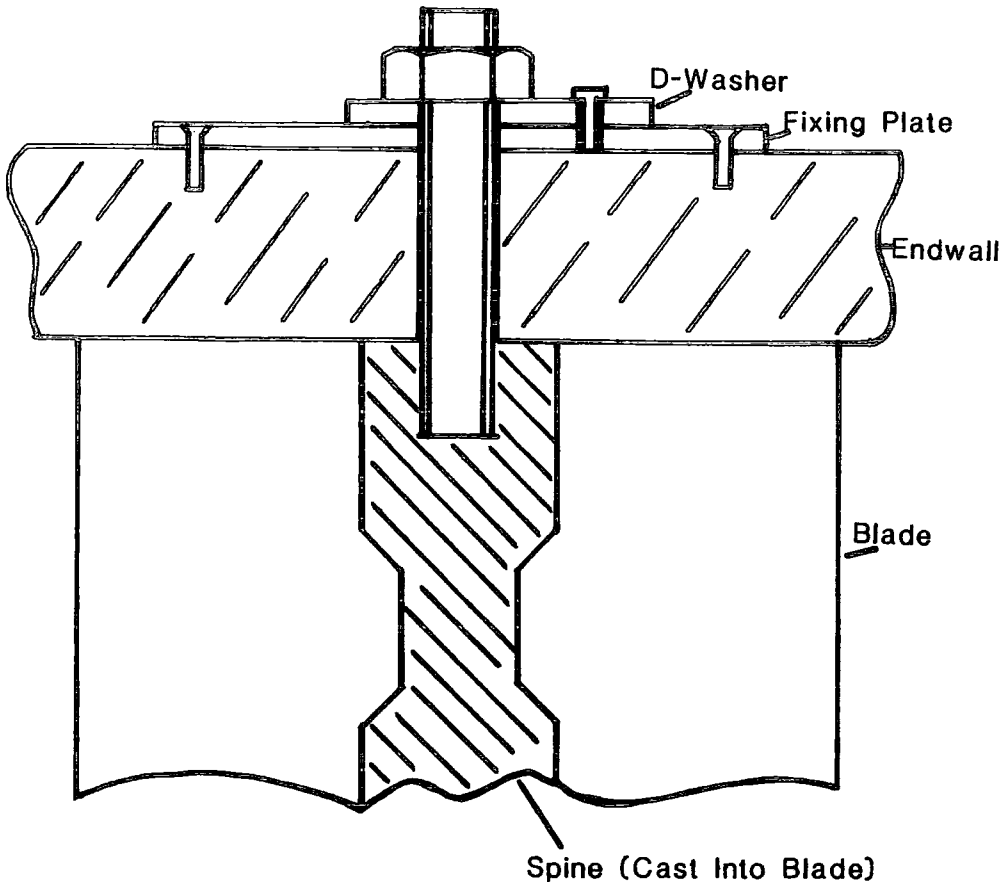

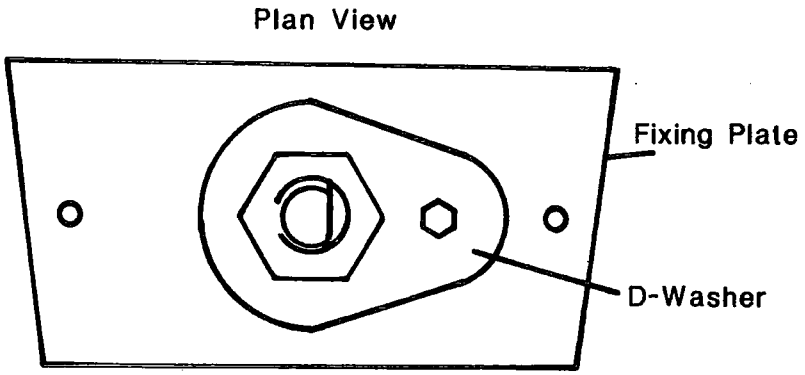

FIGURE 3.3: Blade Mounting Onto Cascade Endwall

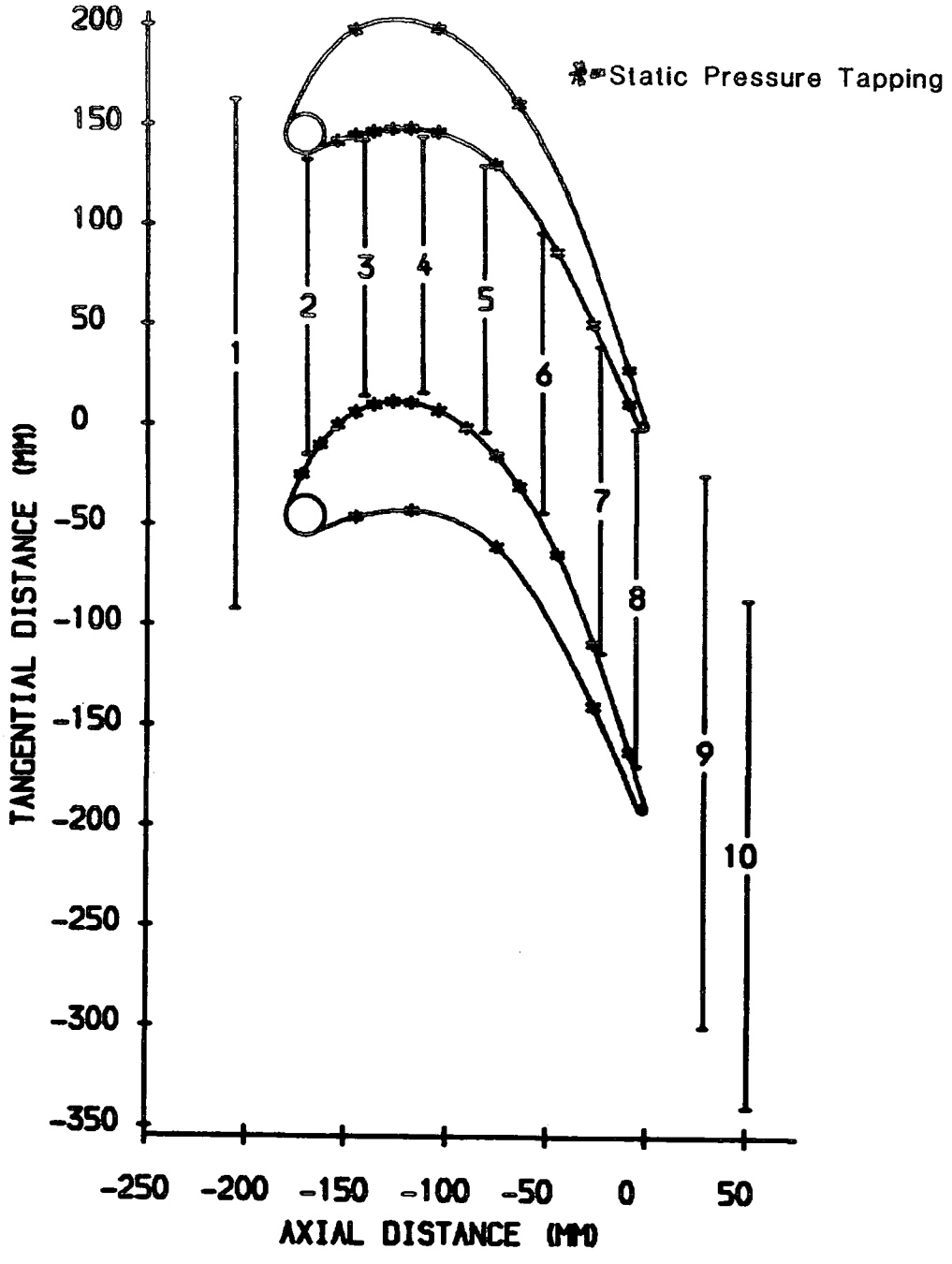

FIGURE 3.4: Location Of Measurement Planes (JAW Cascade)

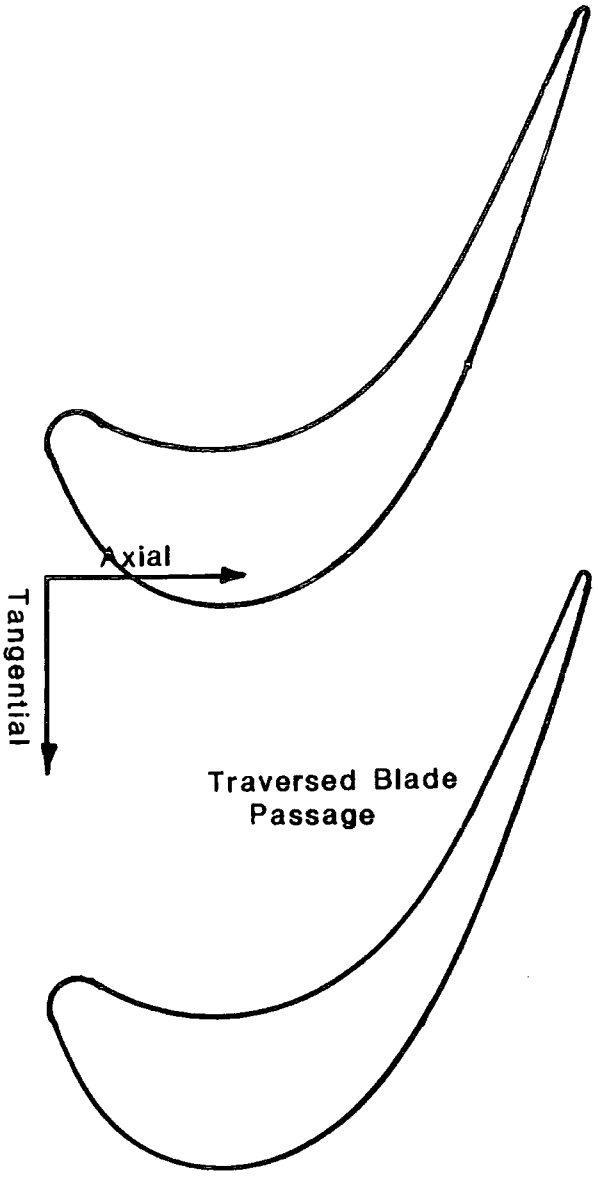

Spanwise Distances Measured From Perspex Endwall

FIGURE 3.5: Cascade Axis System

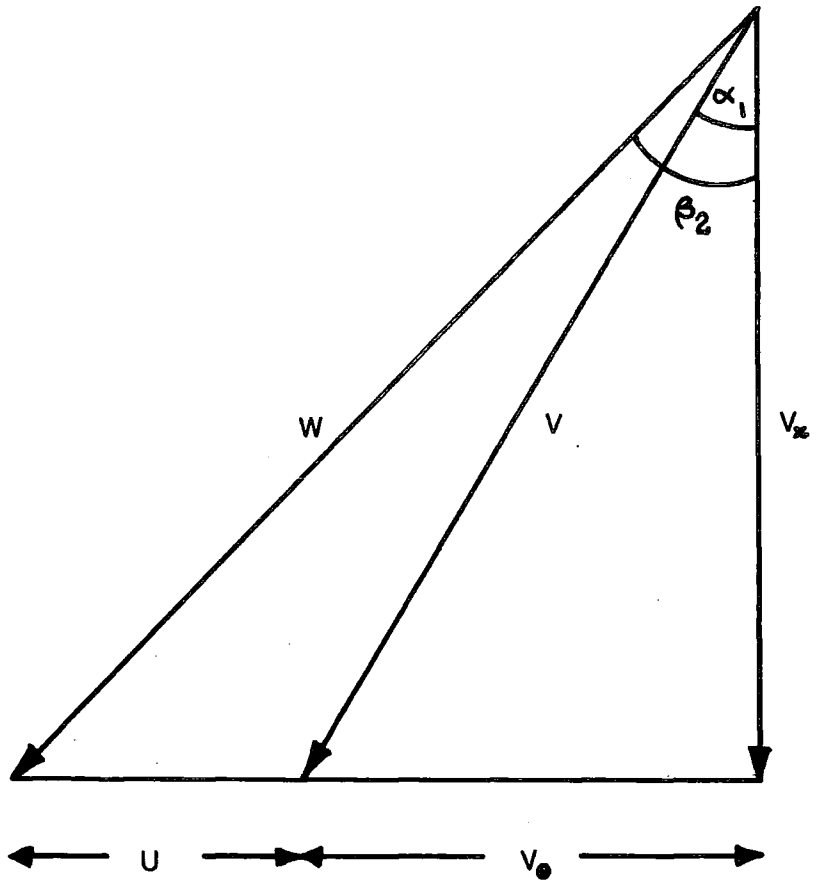

α_1 = Rotor Inlet Angle

β_2 = Stator Outlet Angle

U = Belt Velocity

V = Air Velocity

V_x = Axial Velocity Of Air

V_θ = Tangential Velocity Of Air

W = Relative Velocity Of Air To Belt

FIGURE 3.6: Velocity Triangle

FIGURE 3.7: Moving Belt Support Framework

FIGURE 3.8: Moving Belt Mounted Into Tunnel

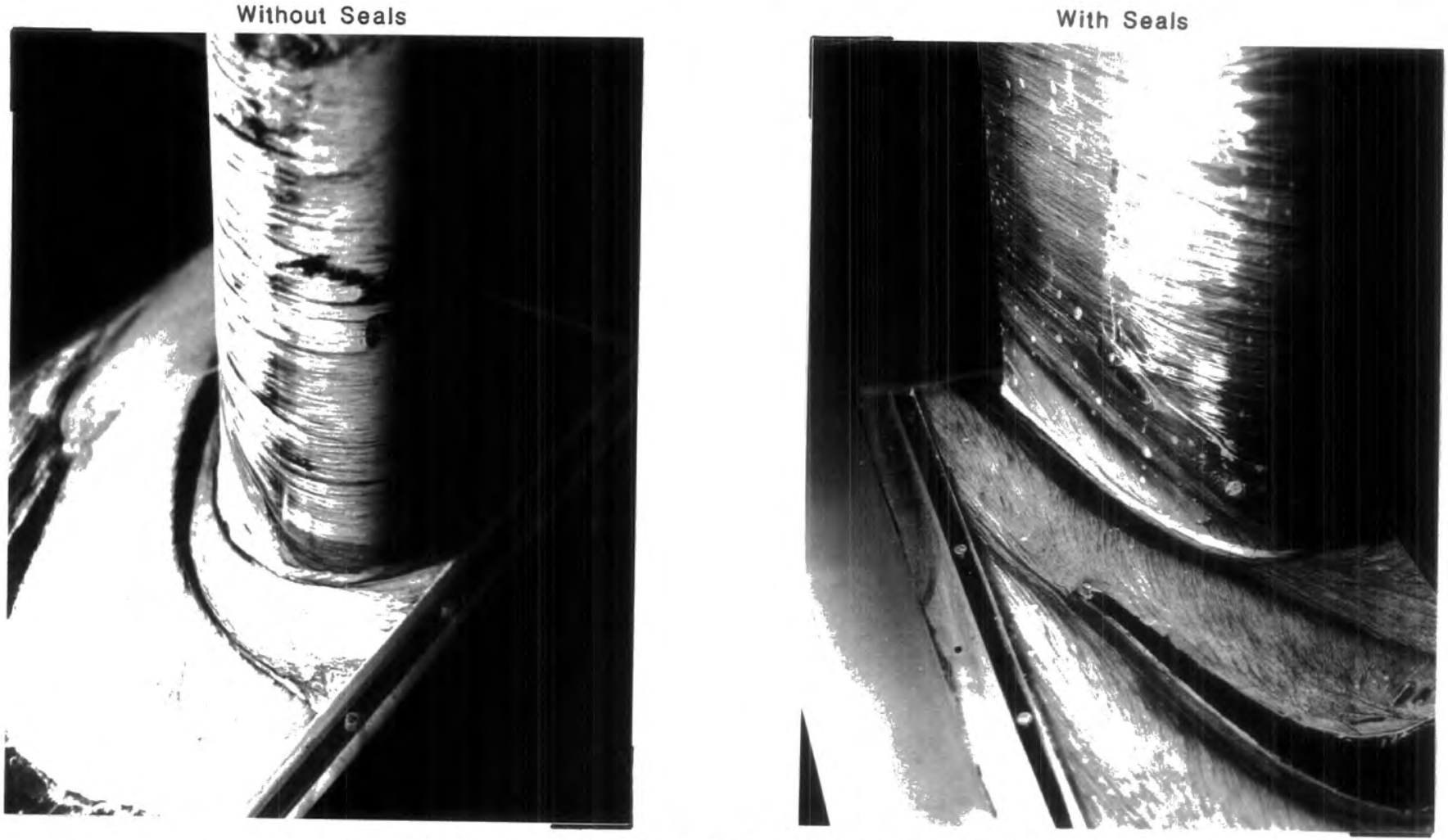

FIGURE 3.9: The Effect Of Belt Seals

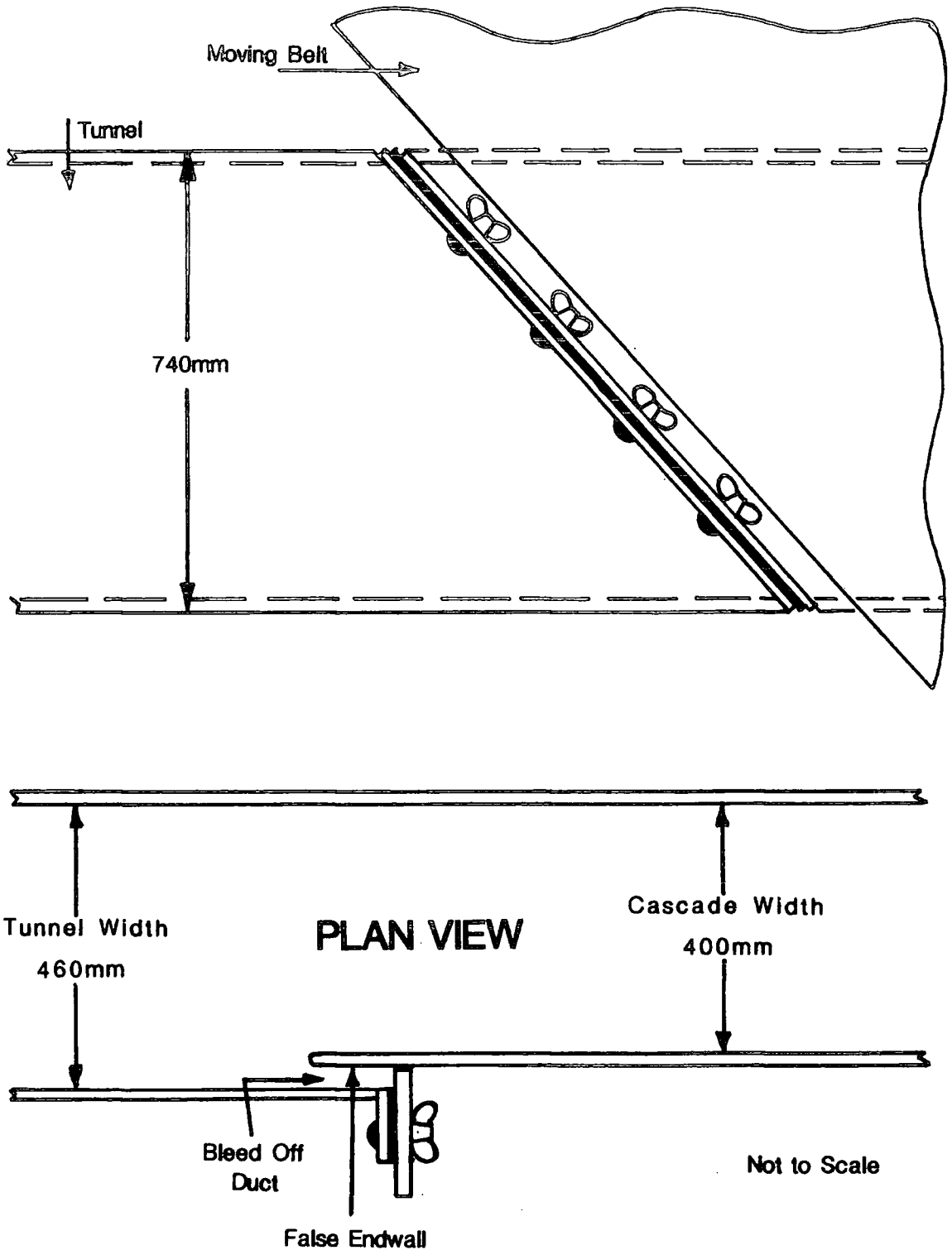

FIGURE 3.10: Details of Bleed Off Duct

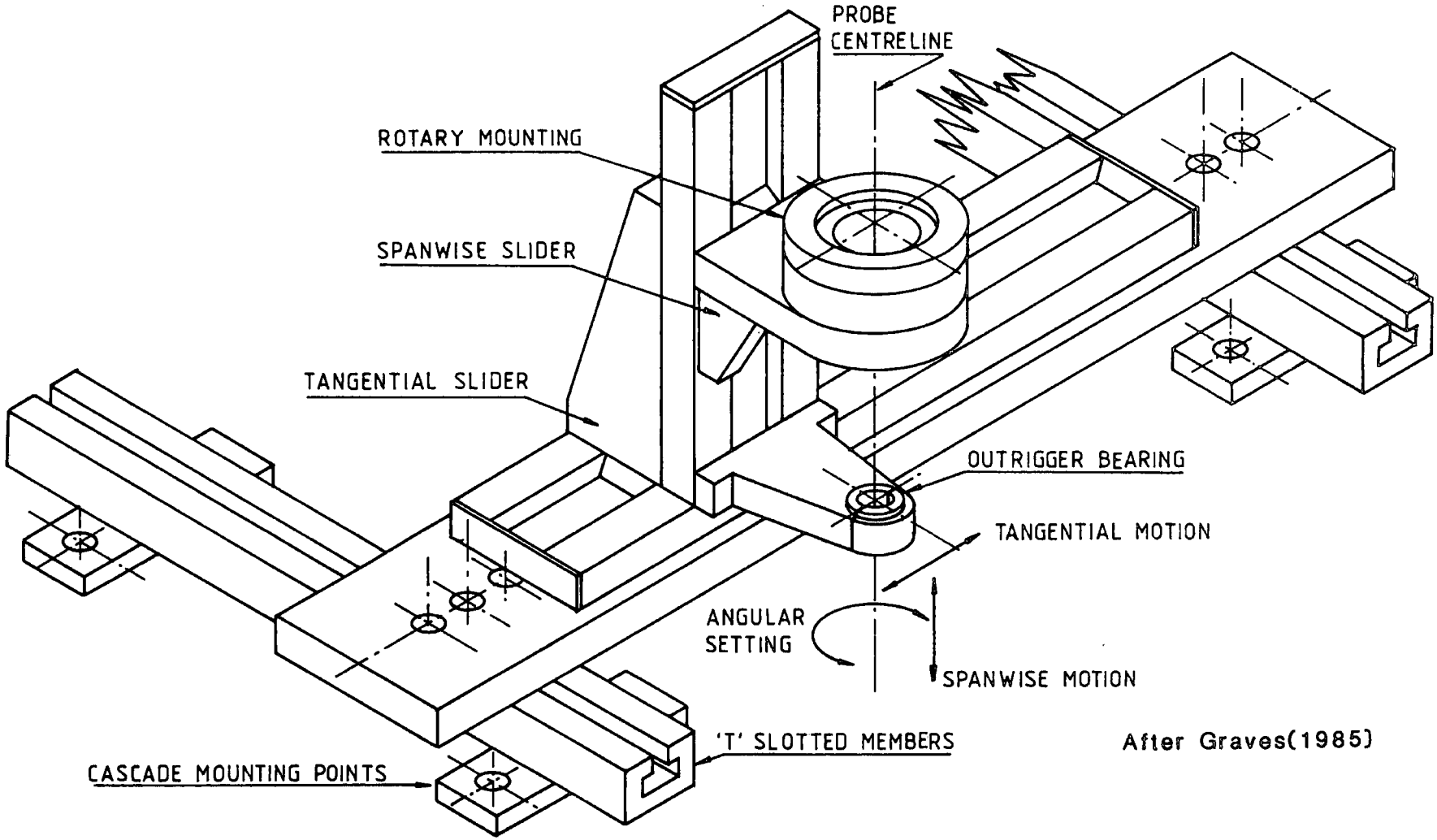

FIGURE 3.11: Traverse Gear

CHAPTER 4 : EXPERIMENTAL RESULTS (CPG CASCADE)

This chapter reviews the experimental results that were obtained using the CPG cascade. The results of traversing downstream of the cascade at slot 10 with a five-hole pressure sensing probe, and the results of traversing at slots 5, 6 and 10 with hot-wire anemometry, are presented. The results of a brief spectral study to determine the nature of the turbulence in the cascade and the results of a flow visualisation study are also discussed.

4.1 FIVE-HOLE PRESSURE PROBE RESULTS FOR SLOT 10

This was the first piece of experimental work that was undertaken and it was used to gain familiarisation with both the instrumentation techniques and the data analysis methodology. The flow was measured at Slot 10 which is 28% of an axial chord downstream of the cascade (see Figure 3.1). The flow at this downstream plane had previously been measured by Graves (1985). It was found that the sparse distribution of measurement points used in the blade wake regions was the cause of poor repeatability. Extra tangential traverses (a total of 27 instead of 19) were therefore concentrated in the wake regions and the measurement grid was also refined in the spanwise direction. Problems were encountered with the integration routines that had been written assuming equally spaced tangential traverse positions. The use of a numerical quadrature integration

technique both increased the accuracy and simplified the computer programs.

The results of traversing with a five-hole pressure probe are presented in Figure 4.1. The results are qualitatively similar to those reported by Graves but there are however slight quantitative differences. Figure 4.1(a) shows the location of the measurement positions that were used within the axial plane. In Figure 4.1(b) the yaw angle contours show more underturning associated with the loss core although this may have been as a result of the finer definition. However, the general shape of both the pitch (Figure 4.1(c)) and the yaw angle contours has remained very similar to those reported by Graves. The total pressure loss coefficient contours, Figure 4.1 (d), clearly show the two blade wakes with improved repeatability and values of the coefficient were found to be similar to those reported by Graves. Evidence of counter vortices were seen on the endwall where there were skewed regions of high loss. The values of loss coefficient were corrected to ensure that the low loss region at midspan between the blade wakes had a value of zero. This technique was used but not reported by Graves. Other researchers (eg. Sharma et al (1985)) have also found it necessary to apply a similar correction. The correction is discussed more fully in Chapter 3. The secondary velocity vectors, Figure 4.1(e), where the primary flow direction is defined as being the midspan flow direction, clearly show the passage vortex and indicate the existence of the counter vortices on the endwall. A weak counter vortex was apparent on the midspan side of the passage vortex. A comparison

of the total pressure loss contours and the secondary velocity vectors clearly shows that the centres of the passage vortex and the loss core do not coincide. The streamwise vorticity contours, Figure 4.1(f), also support the existence of the vortices that have been identified. In the figure the solid lines represent negative (clockwise rotation) vorticity. The positive region of vorticity extending to midspan was formed from vorticity that had been shed from the blades and there was also a contribution from the endwall counter vortices. Figure 4.2 presents pitch averaged quantities. The yaw angle plot, Figure 4.2(a), presents a typical example of the underturning and overturning of the flow due to the action of the secondary flows. The maximum underturning corresponded to the position of the loss core and the maximum overturning to the region of low total pressure loss between the loss core and the endwall high loss zone. The pitch averaged total pressure loss and secondary kinetic energy plots, Figure 4.2(b), also show the loss core and the high loss zone which was associated with the counter vortices near to the endwall. The pitch averaged streamwise vorticity plot, Figure 4.2.(c), indicates some interesting features of the flow field. In the spanwise direction, until the first zero value of vorticity, the effect of the endwall counter vorticity can be seen. At about the midpoint of this region the graph goes close to zero at a point coinciding with the centres of the loss cores that were associated with the counter vortices. In the region bounded by the two zero vorticity values the influence of the passage vortex was clear. The location of the peak negative vorticity value corresponded to

the position of the centre of the passage vortex, whereas the centre of the loss core was marked by the upper zero crossing point of the graph. The table below presents the mass averaged measured losses. Since the data was collected over more than a pitch in the tangential direction the data was analysed twice. Firstly over a region to incorporate fully the left-hand wake, and secondly over a region to incorporate fully the right hand wake. All of the results shown in the table are an average of the two values obtained by this procedure. The results of a mixed-out loss calculation are also presented as an attempt to remove the dependence of the results on the distance downstream of the cascade. The technique used was to calculate the loss far downstream, ignoring viscous effects, by applying a momentum balance. The gross secondary loss was calculated by subtracting the mixed out profile loss from the mixed out loss coefficient. The profile loss was assumed to be equal to the midspan loss. The net secondary loss was calculated by subtracting the inlet loss coefficient, obtained from Graves (1985), from the gross secondary loss. For comparative purposes results are shown that were based on the data collected by Graves for the natural inlet boundary layer case.

TABLE 4.1: SLOT 10 LOSSES

	WALSH	GRAVES
Measured Loss Coefficient Measured Profile Loss	0.237 0.097	0.287 0.115
Mixed-Out Loss Coefficient Mixed-Out Profile Loss	0.293 0.104	0.321 0.099
Gross Secondary Loss	0.189	0.222
Inlet Loss	0.084	0.084
Net Secondary Loss	0.105	0.138

4.2 HOT-WIRE RESULTS FOR SLOT 5

Results of traversing with a five-hole pressure probe, taken from Graves (1985) and Gregory-Smith et al (1987), are shown in Figure 4.3. The results of traversing with the hot-wires are presented in Figure 4.4. Figure 4.4(a) shows the grid of measurement points which were used and, due to the probe dimensions, contains eleven tangential traverses compared to the twelve used for the five-hole pressure probe (Figure 4.3(a)). The results obtained from the hot-wire mean velocity data show good qualitative agreement with the corresponding five-hole pressure probe results. In detail there are, however, quantitative differences. In particular the five-hole pressure probe produced negative pitch angles that were approximately 5^{o} lower than those measured by the hot-wire probes. The positive values of pitch angle compare fairly well. The lack of agreement was probably due

to the hot-wires not being aligned with the flow direction with respect to the pitch angle and that there was large pitch angle variation. This situation should be compared to that for the yaw angles where excellent agreement was obtained between the hot-wire probe and pressure probe results. However, the hot-wires were accurately aligned with the flow direction with respect to yaw angle and the assumption of only a small variation of the flow direction from the sensing plane was therefore correct in this case. The secondary velocity vectors obtained using both types of instrumentation also compare well. The turbulent kinetic energy, which has been normalised by the upstream velocity (Figure 4.4(f)) may be compared to the total pressure loss shown in Figure 4.3(d). This is an interesting comparison since the production of turbulence is the first step in losing energy from the (steady) flow. It can be seen that the centre of the loss core and the position of peak turbulent kinetic energy did not coincide. The centre of the loss core appeared further from the suction surface but at the same spanwise distance from the endwall. The peak turbulent kinetic energy position did however appear very close to the vortex centre as shown in Figure 4.4(e). The turbulence intensity levels, Figure 4.4(i-k), appeared to be similar for each of the velocity components indicating a fair degree of isotropy. The w' component was however slightly larger than the other two components. The shear stresses are important since they give an indication of the dissipation of the kinetic energy of the mean flow by conversion to turbulent kinetic energy. This loss of mean flow kinetic energy also depends on the relevant velocity

gradient. It is difficult to describe other than qualitative features of the shear stress contours shown in Figure 4.4(f-g). The u'w' contours appear to have a number of local peaks which may be an indication of numerical error. The two shear stresses appear to undergo a sign change in the region corresponding to the centre of the loss core. Of the two shear stresses that were measured the u'v' would appear to be the largest. However, the shear stress that was not measured, v'w', was found at a downstream plane by Moore et al (1986) to be at least twice as big as the other two. They concluded that the v'w' shear stress was therefore the main dissipator of the mean flow kinetic energy. The pitch averaged results, Figure 4.5, show that the peak turbulent kinetic energy and total pressure loss values occured at the same spanwise distance from the endwall. The location of peak vorticity did not coincide with the other two peaks but was found to be nearer to the endwall.

4.3 HOT-WIRE RESULTS FOR SLOT 6

Results of traversing with a five-hole pressure probe, taken from Graves (1985) and Gregory-Smith et al (1987), are shown in Figure 4.6. Corresponding results obtained with hot-wire probes are shown in Figure 4.7. Figure 4.7(a) shows the location of the measurement positions within the axial plane. The probe dimensions meant that only ten tangential positions were traversed compared to the twelve traversed with the five-hole pressure probe (Figure 4.6(a)). Good qualitative agreement was again obtained between the pressure probe and hot-wire results that were derived

from the mean velocity data. Similar quantitative differences in pitch angle measurements to those found at Slot 5 were again detected. The yaw angle was seen to dip lower in the hot-wire results. The combined effect of the differences in both pitch and yaw angles can be seen in a comparison of the secondary velocity vector plots. In the hot-wire results, Figure 4.7(e), a significant spanwise velocity was detected even out at midspan near to the suction surface that was not detected by the five-hole pressure probe. A comparison of the turbulent kinetic energy contours, Figure 4.7(f), and the total pressure loss contours, Figure 4.6(d), again show the non-coincidence of the peak values. Rather, the peak turbulent kinetic energy was to be found on the pressure surface side of the loss core. This is to be compared to slot 5 where the peak turbulent kinetic energy appeared on the suction surface side of the total pressure loss core. Both of the peak values have, however, moved further from the endwall. The turbulent kinetic energy contours do not show evidence of the suction-side leg of the horseshow vortex that was seen in the total pressure loss contours. This was probably due to the hot-wire probe being unable to traverse sufficiently close to the suction surface of the blade. Although the turbulence intensity contours, Figure 4.7(i-k), show similar qualitative features for each of the velocity components, the w' component (spanwise direction) has the largest peak value. The shear stress contours, Figure 4.7(g-h), again show the u'v' shear stress to be the larger of the two measured. The pitch averaged results, Figure 4.8, highlight some of the above features. The turbulent kinetic

energy and total pressure loss coefficient peak values occured at the same spanwise distance from the endwall. These peak values coincided with a dip in the vorticity. The pitch averaged turbulent kinetic energy did not decrease towards midspan in the same way as was seen in slot 5. There appeared to be a mechanism generating sufficient turbulent kinetic energy to delay the decrease. The pitch averaged vorticity shows that this effect coincided with the presence of a significant vorticity with the same sense of rotation as the passage vortex. A possible explanation might be the presence of the laminar separation bubble on the surface of the blade. This effect was not seen at slot 5, because it is just upstream of the separation bubble. The pitch averaged total pressure loss distribution is seen to broaden, compared to slot 5, which may indicate greater loss production. The major effect of a separation bubble is to increase loss. The increase in turbulent kinetic energy may be accounted for by the unsteady nature of the separation bubble (see section 4.7).

4.4 HOT-WIRE RESULTS FOR SLOT 10

The results of traversing with hot-wires are shown in Figure 4.9. These results may be compared to the five-hole pressure probe results that were presented earlier in Figure 4.1. It can be seen that there is good qualitative agreement between the pressure probe results and the results that have been derived from the hot-wire mean velocity data. The discussion concerning the quantitative differences between the pitch and yaw angles

using the two types of instrumentation in slots 5 and 6 is also appropriate for this slot. The negative pitch angles were consistently lower in the hot-wire case than in the pressure probe case. The yaw angles and secondary velocity vectors showed very good agreement for both types of instrumentation. The comparison between the total pressure loss contours, Figure 4.1(d), and the turbulent kinetic energy contours, Figure 4.9(f), is interesting since within the loss core the positions of the peak values coincide. There were also regions of high turbulent kinetic energy due to the presence of the endwall counter vortices. The turbulence intensity contours, Figure 4.9(i-k), showed a high degree of isotropy since all three fluctuating components of velocity have very similar intensity levels and features. The shear stress contours, Figure 4.9(g-h), can only be commented on from a qualitative point of view. In particular the u'v' contours have a number of local peaks that make interpretation difficult. However, there were sign changes that cut across the loss core region coinciding with changes in sign of the gradient of the velocity contours. The u'v' contours showed an altogether much sparser picture without sign changes dividing the loss core region. The pitch averaged results, Figure 4.10, showed a remarkable similarity between the total pressure loss and the turbulent kinetic energy. The approximate proportions of turbulent kinetic energy, contained in the regions characterised by the various elements of streamwise vorticity, are presented in the table below.

TABLE 4.2: SLOT 10 TURBULENT KINETIC ENERGY

Vorticity Region	Proportion of Area Averaged Turb. K.E.
Endwall Counter Vortex	0.37
Passage Vortex	0.34
Shed Vorticies	0.29

This result shows that at this downstream location the largest proportion of turbulent kinetic energy is concentrated into the small region associated with the endwall counter vortex. In the more general sense this result shows that the regions of high streamwise vorticity were associated with high turbulent kinetic energy.

4.5 SPECTRAL ANALYSIS

Because such high levels of turbulence were detected further work was carried out in order to determine its nature. The signal from the XZ hot-wire probe was recorded for several positions in various slots on an instrumentation quality tape recorder. A limited spectral analysis of the data was carried out and typical results obtained for slots 1, 6 and 10 are shown in Figure 4.11. At both slots 1 and 6 it was difficult to identify any dominant frequencies in the range analysed. The spectra for these two slots, Figure 4.11(a-b), showed that the turbulence activity was equally spread over all frequencies and was therefore random in nature. However, it is evident from the results for slot 10, Figure 4.11(c), that the frequency containing the most

energy in the spectrum is in the band 27.5Hz to 32.5Hz. This is a surprising result and cannot be due to vortex shedding from the trailing edge. For a trailing edge thickness of 5mm, an exit velocity of 30m/s, and a Strouhal number, S_n, of 0.2 where

$$S_n = \frac{fd}{v}$$

a frequency, f, of 1200 Hz would be expected as a result of the shedding of trailing edge vortices. Working back the other way by fixing the frequency at 30 Hz, a "thickness" of 200 mm is obtained which is close to the pitch. This result would appear to indicate a bulk unsteadiness of the fluid within the blade passage. It was initially thought that the unsteadiness was due to the presence of a laminar separation bubble on the suction surface of the blade. However, this explanation is unlikely since the frequency was not detected at slot 6 which is downstream of the location of the separation bubble (Figure 4.13). Recently Pernet (1986) has reported the results of using the same profile in a very low speed water flow visualisation experiment. It was found that there was a low frequency oscillation of the fluid at the leading edge of the blade. However, once again the spectral analysis results do not indicate the presence of the low frequency at slot 1. It may be that slot 1 is too far upstream to detect this effect which is likely to be associated with the presence of the horseshoe vortex. This does not however explain why the effect is not seen at slot 6. Although the two effects discussed above may have contributed to the unsteadiness within the cascade, it is probable that the

dominant frequency that was detected is a result of the the passage vortex being shed from the passage. It may be that this shedding frequency is a unique feature that could be used for identifying vortices.

4.6 DEVELOPMENT THROUGH THE CASCADE

Additional hot-wire results have been presented by Graves (1985) for slots 1 and 8 and by Fulton (1983) for slot 7. The hot-wire results in conjunction with the five-hole pressure probe results have allowed the growth of total pressure loss, turbulent kinetic energy and vorticity through the cascade to be compared (Figure 4.12). The error bands given for slots 1, 8 and 10 were obtained by integrating over different regions of the plane for pitch averaging. The error bands give a measure of repeatability and in the case of slot 8 the poor repeatability was due to the sparseness of traverse points in the wake regions. The total pressure loss was seen to grow throughout the cascade with a jump at the trailing edge. This is different to Langston et al (1977) and to Marchal and Sieverding (1977) who found that the losses did not start to grow until well into the passage, followed by a large increase in loss at the trailing edge. This was probably due to both of these experiments being carried out with trip wires attached to the blades in order to avoid the formation of a laminar separation bubble on the suction surface of the blade. It is therefore probable that the profile loss in the CPG cascade increased in the blade passage due to the transition of the boundary layer from laminar to turbulent following the separation

bubble. However, the loss continued to grow downstream of the cascade due to the presence of the endwall. The turbulent kinetic energy was seen to grow in the same way as the total pressure loss. The value at slot 6 seems to be too high since it would not seem possible for the difference between the total pressure loss and turbulent kinetic energy to decrease at all. The rest of the plot would appear to indicate that the growth in total pressure loss appeared as an increase in turbulent kinetic energy thus implying only small direct viscous action. The vorticity was seen to grow more negative through the cascade up to slot 4. An unexpected large increase in the negative direction was seen at slots 6 and 7 followed by a jump towards zero at the trailing edge. This jump towards zero was due to the presence of positive vorticity that had been shed from the trailing edge of the blade. The vorticity then continued towards a zero value.

4.7 FLOW VISUALISATION

Typical surface flow visualisation results are shown for the endwall and the suction surface of the blade in Figure 4.13. The pictures show that the flow was very complicated and had a strong three-dimensional nature. Figure 4.13(a) shows the flow pattern that occurred on the endwall. Unfortunately the blade profile is not clear due to the ragged edges of the plastic film. The flow pattern clearly shows the cross-passage separation line, that divides the passage, due to the presence of the pressure-side leg of the horseshoe vortex and the passage vortex. There were clearly strong cross-passage flows on the downstream side of this

separation that fed low momentum endwall fluid into the passage vortex. The separation line did not quite meet the suction surface of the blade but was displaced a small distance from it due to the presence of a counter vortex in the suction surface endwall corner. The facilities used did not allow the flow visualisation to extend far enough upstream to detect a saddle point near to the leading edge of blades as reported by other workers (Langston et al (1977), Carrick (1977), Marchal and Sieverding (1977)). Figure 4.13(b) shows a developed view of the flow pattern that occurred on the suction surface of the blade. The flow visualisation was dominated by the presence of a laminar separation bubble. Initially the presence of the bubble was marked by a gathering of the oil and dye mixture which was slowly dispersed by the unsteady nature of the bubble. Also clearly seen was a separation line that marked the path of the passage vortex. This separation line was seen to move further from the endwall as the passage vortex grew in size and there was evidence of strong spanwise flows away from the endwall within the passage vortex. The separation line due to the presence of the suction-side leg of the horseshoe vortex was seen to attach to the surface of the blade on the midspan side of the passage vortex separation line. The separation line due to the suction-side leg of the horseshoe then disappeared, presumably swallowed by the laminar separation bubble. This phenomena has not been observed by other workers who used a boundary layer trip to avoid the formation of a separation bubble on the suction surface of the blade, e.g. Langston et al (1977), Marchal and Sieverding (1977). Downstream of the

separation bubble the mainstream flow was seen to re-attach and to remain attached until the trailing edge.

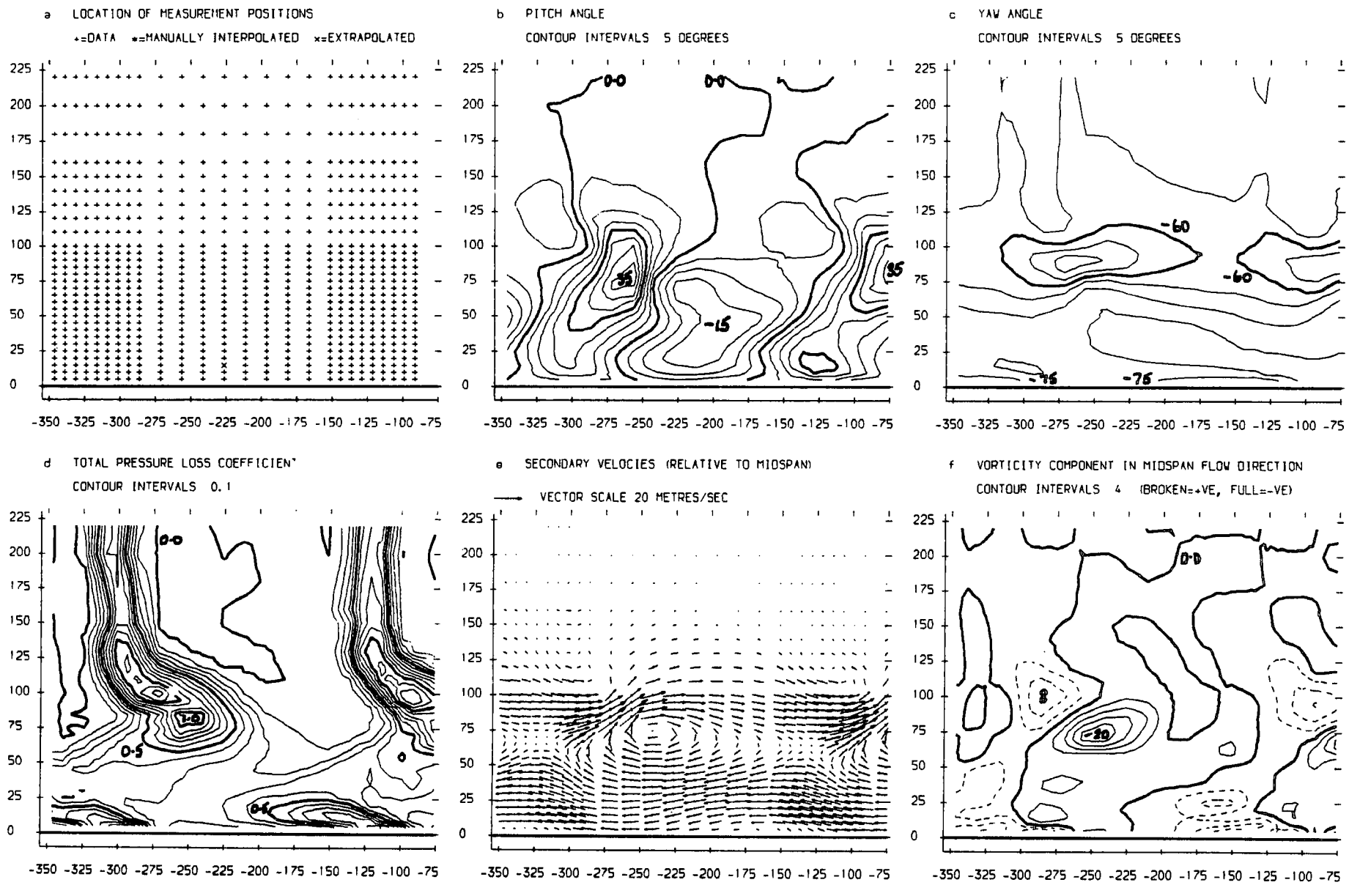

FIGURE 4.1 (a-f) : Five-Hole Probe Results For Slot 10

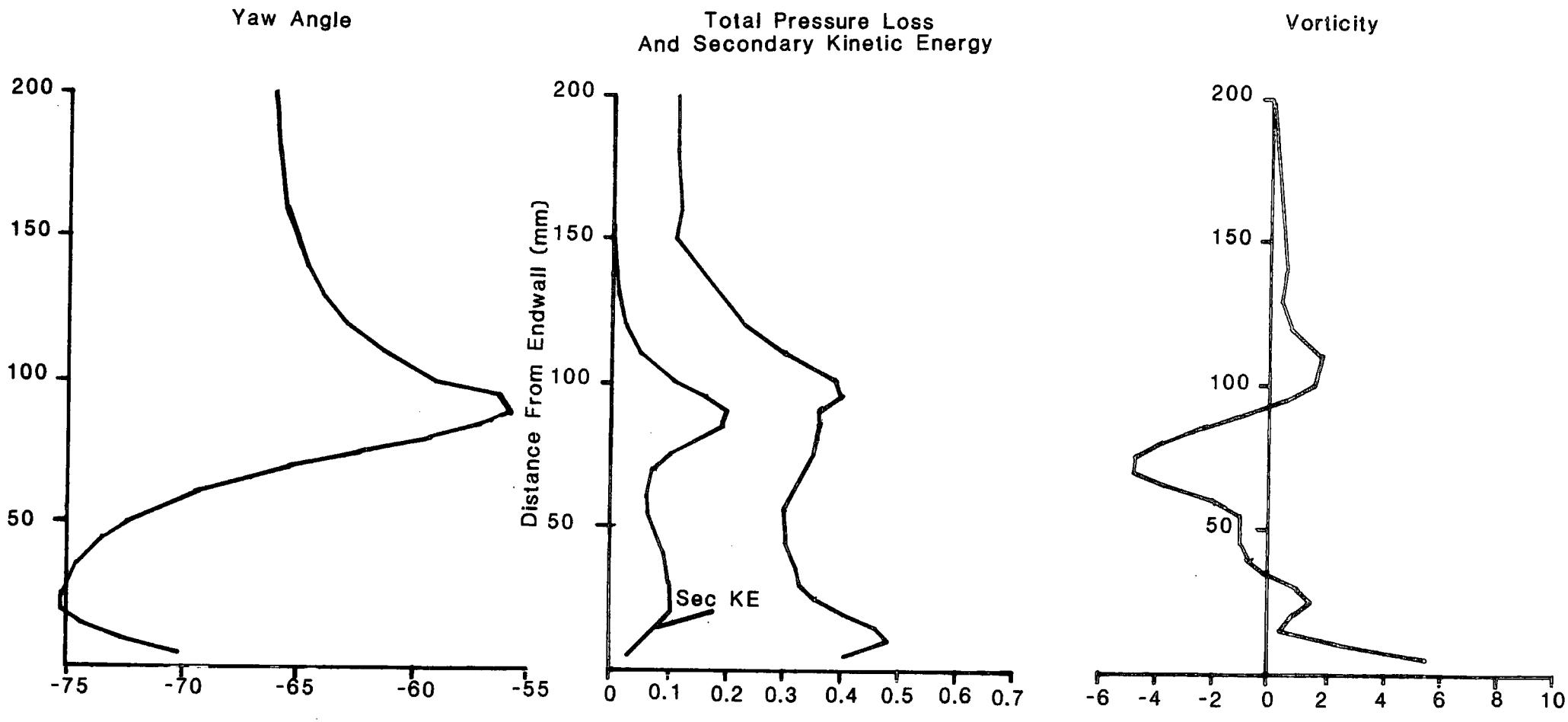

FIGURE 4.2: Pitch Averaged Results For Slot 10

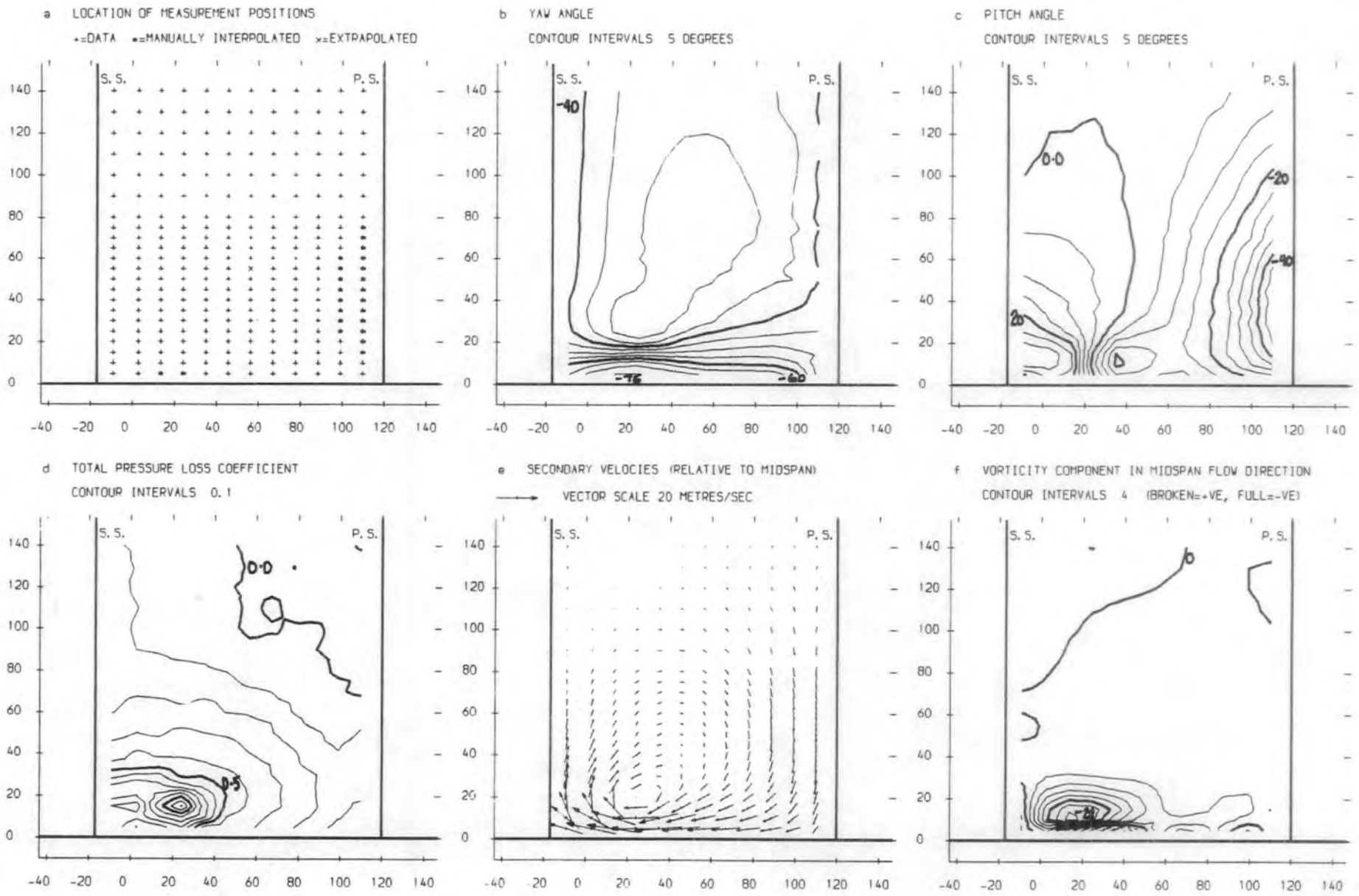

FIGURE 4.3(a-f) : Five-Hole Probe Results For Slot 5

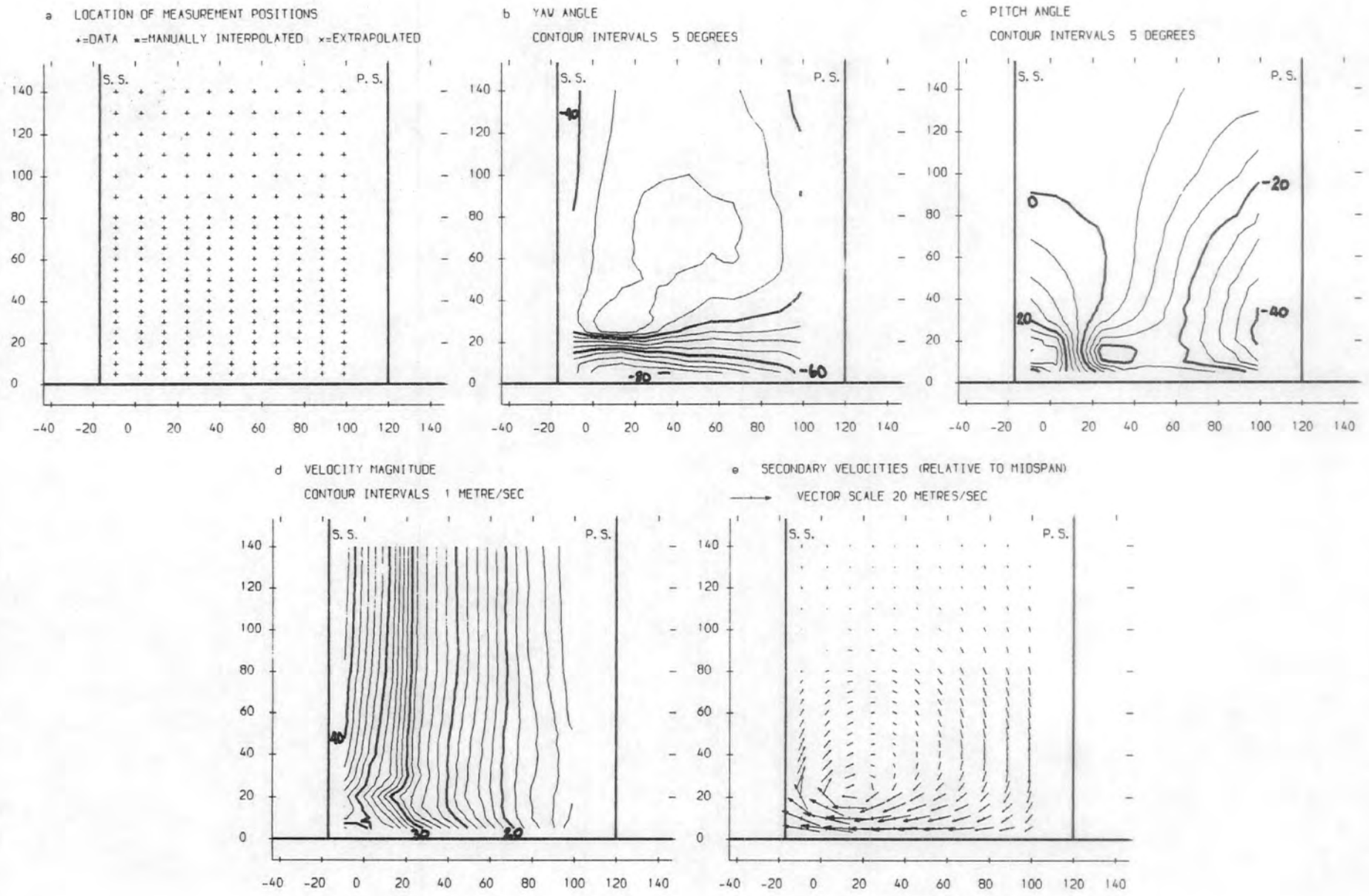

FIGURE 4.4 (a-e) : Hot-Wire Anemometry Results For Slot 5

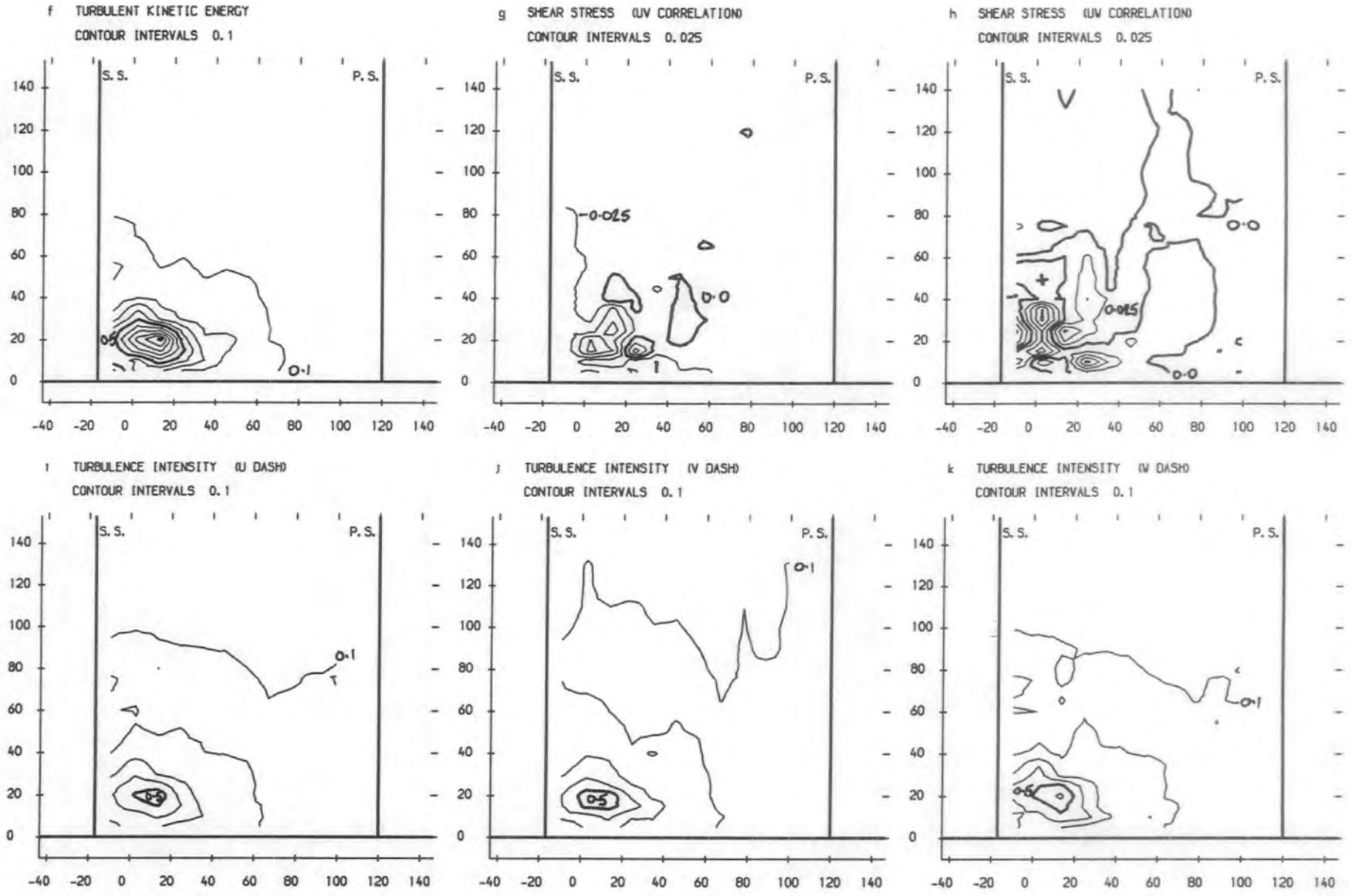

FIGURE 4.4(f-k): Hot-Wire Anemometry Results For Slot 5

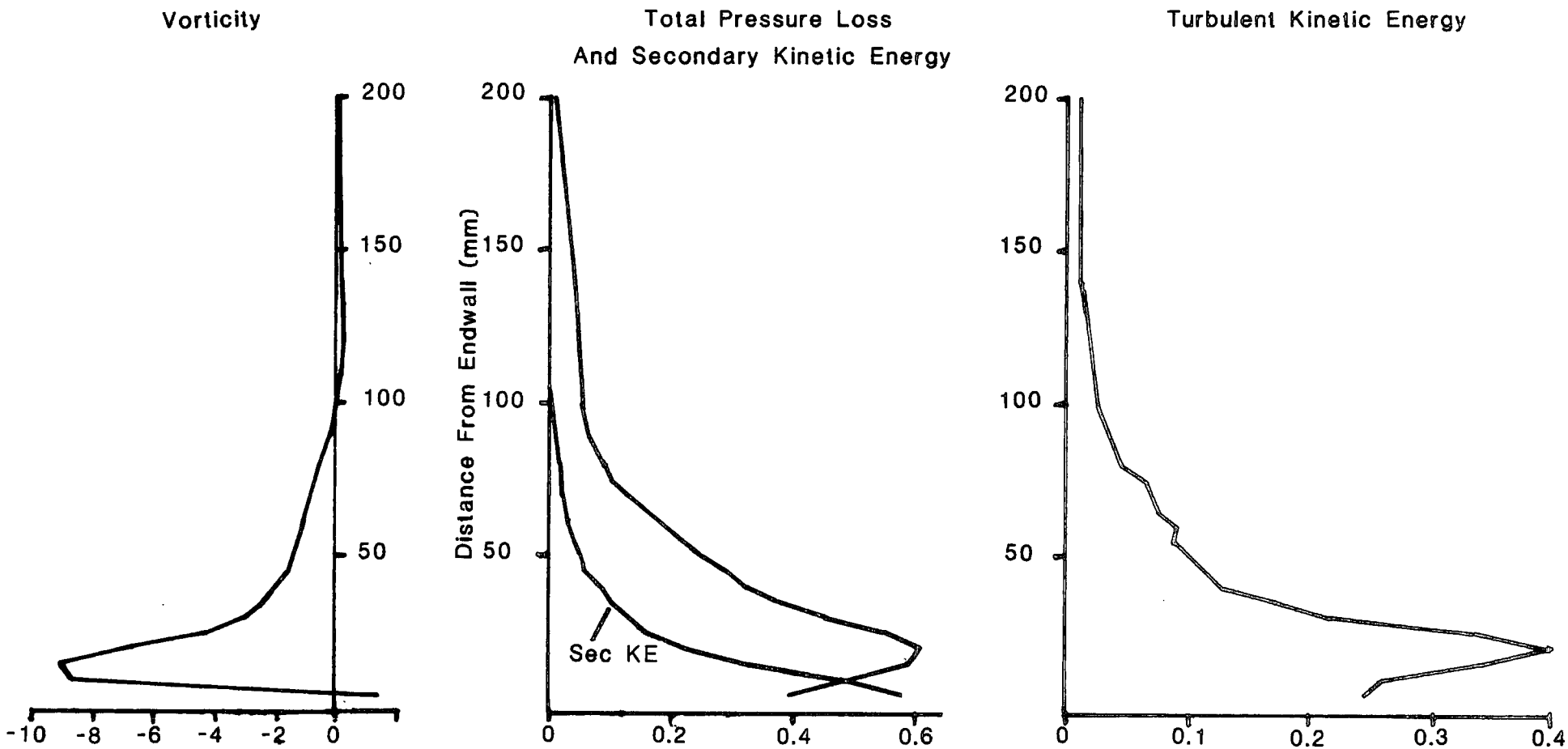

FIGURE 4.5: Pitch Averaged Results For Slot 5

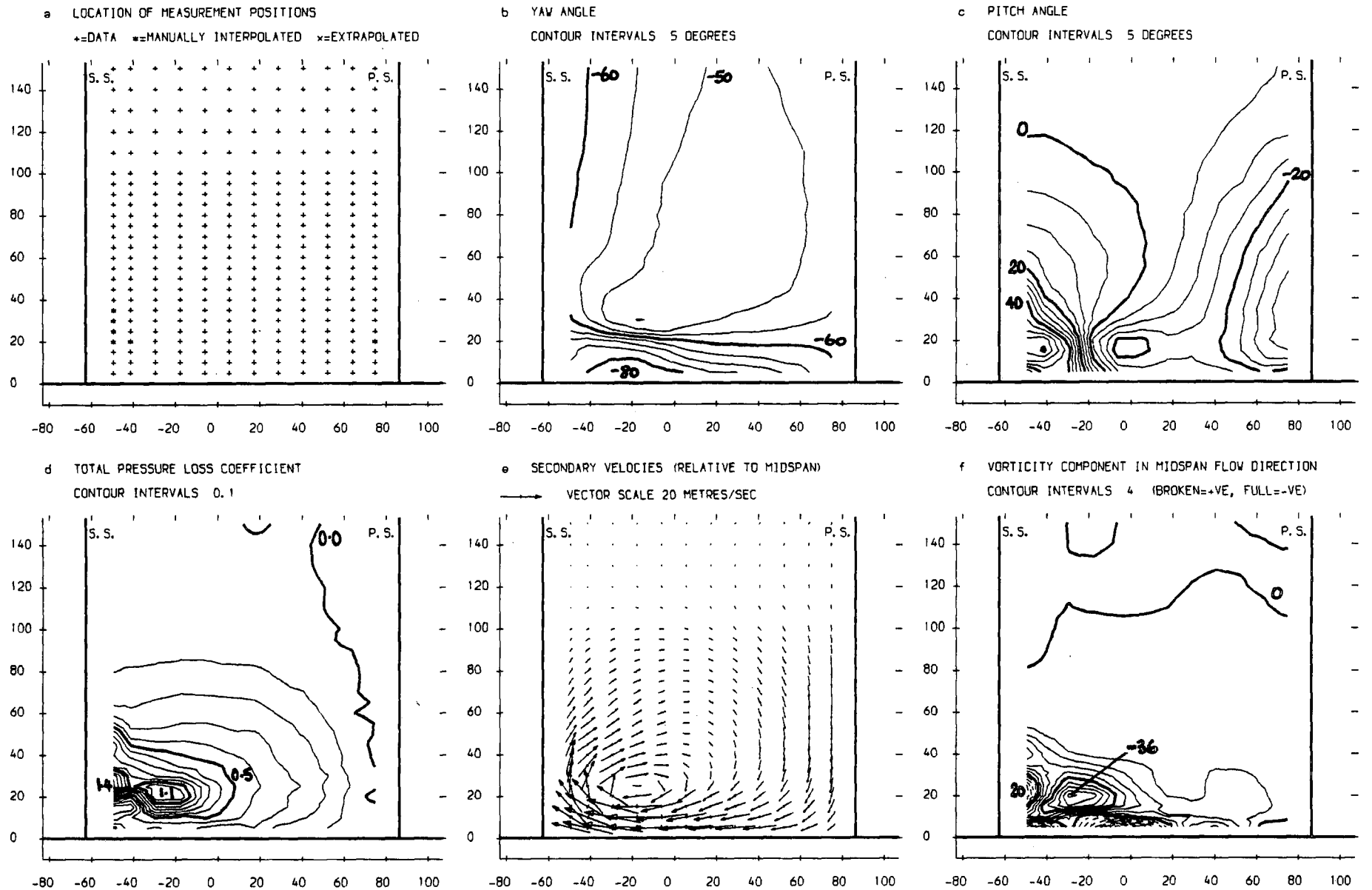

FIGURE 4.6(a-f) : Five-Hole Probe Results For Slot 6

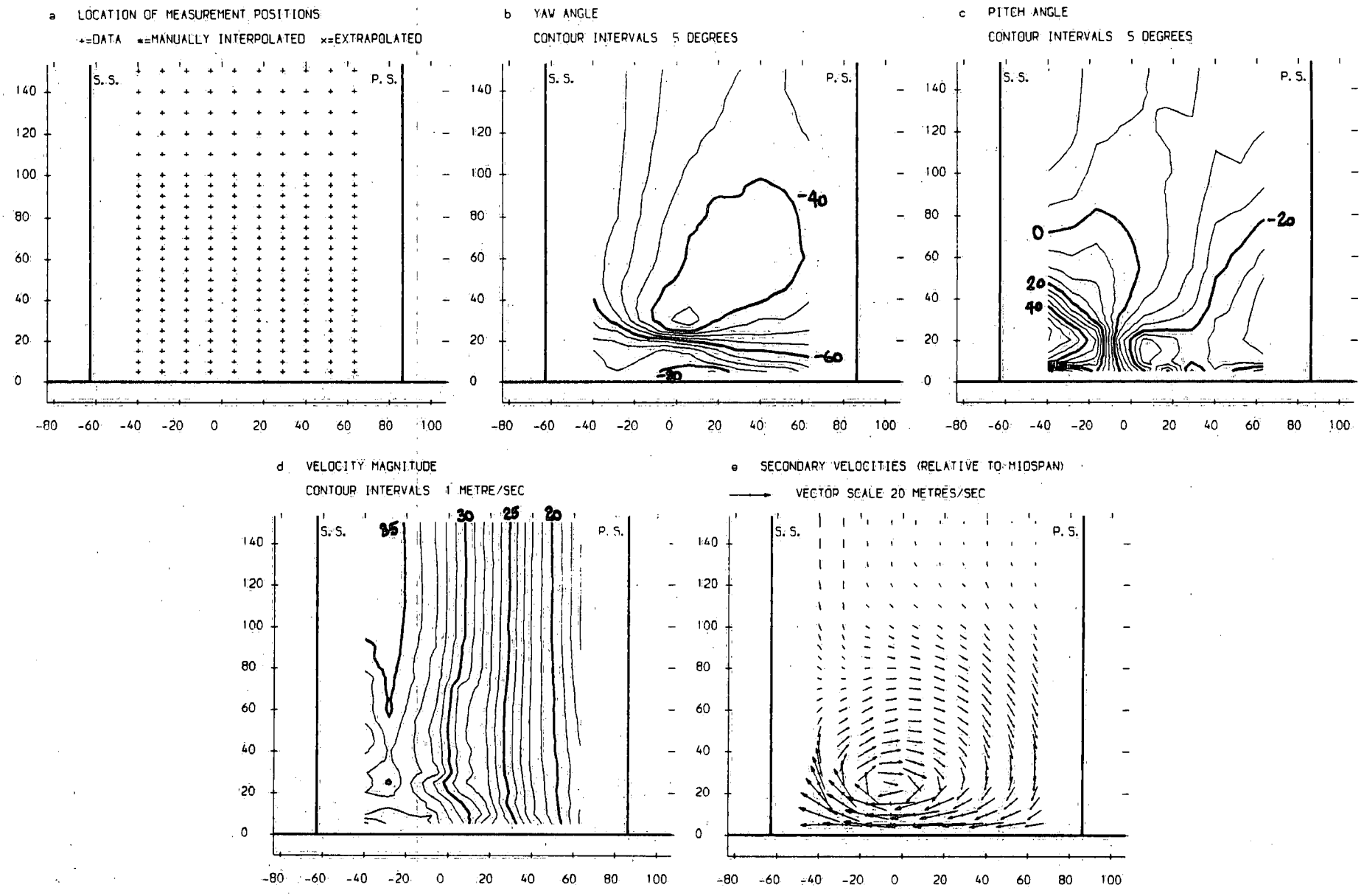

FIGURE 4.7(a-e): Hot-Wire Anemometry Results For Slot 6

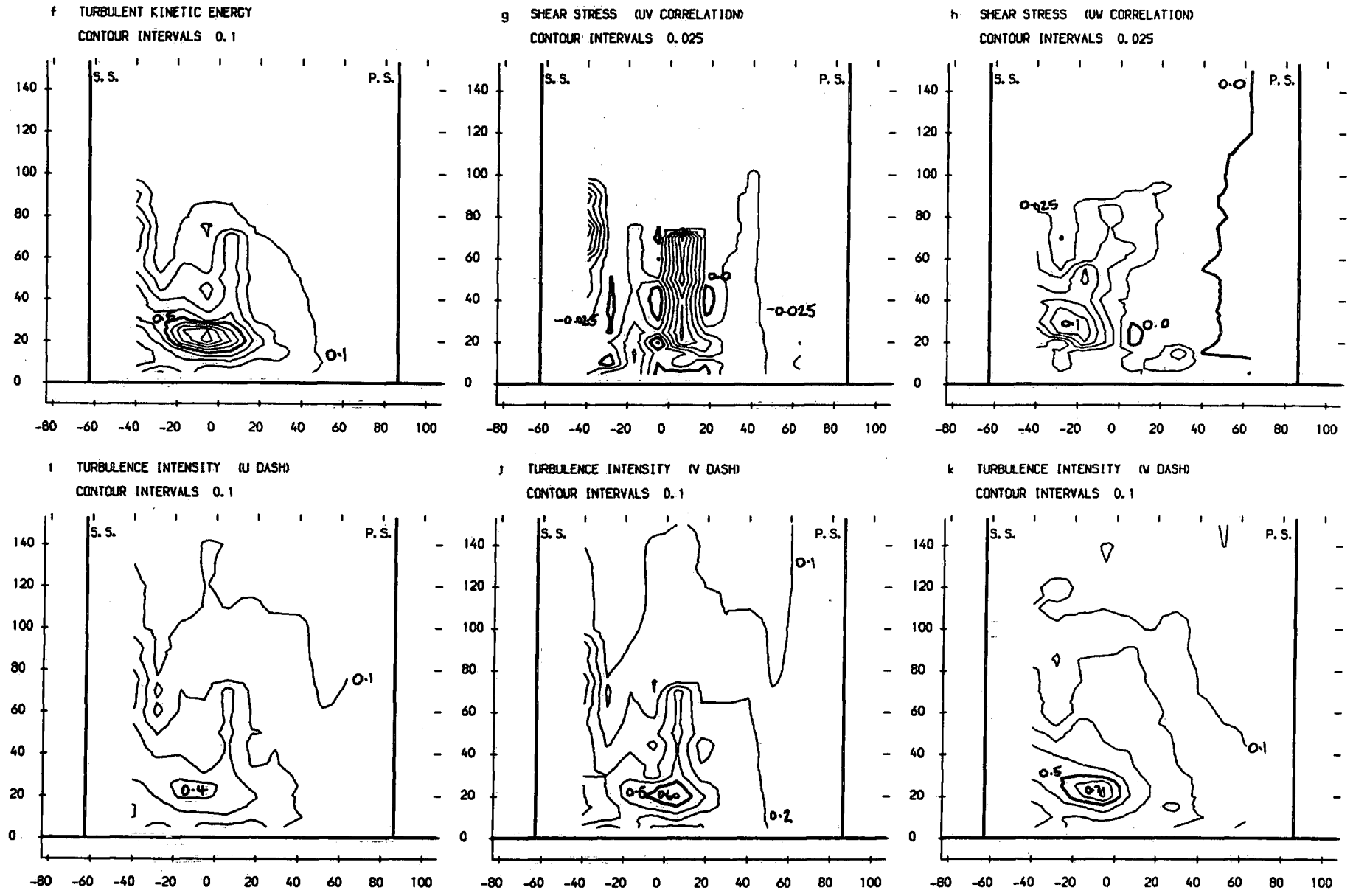

FIGURE 4.7(f-k): Hot-Wire Anemometry Results For Slot 6

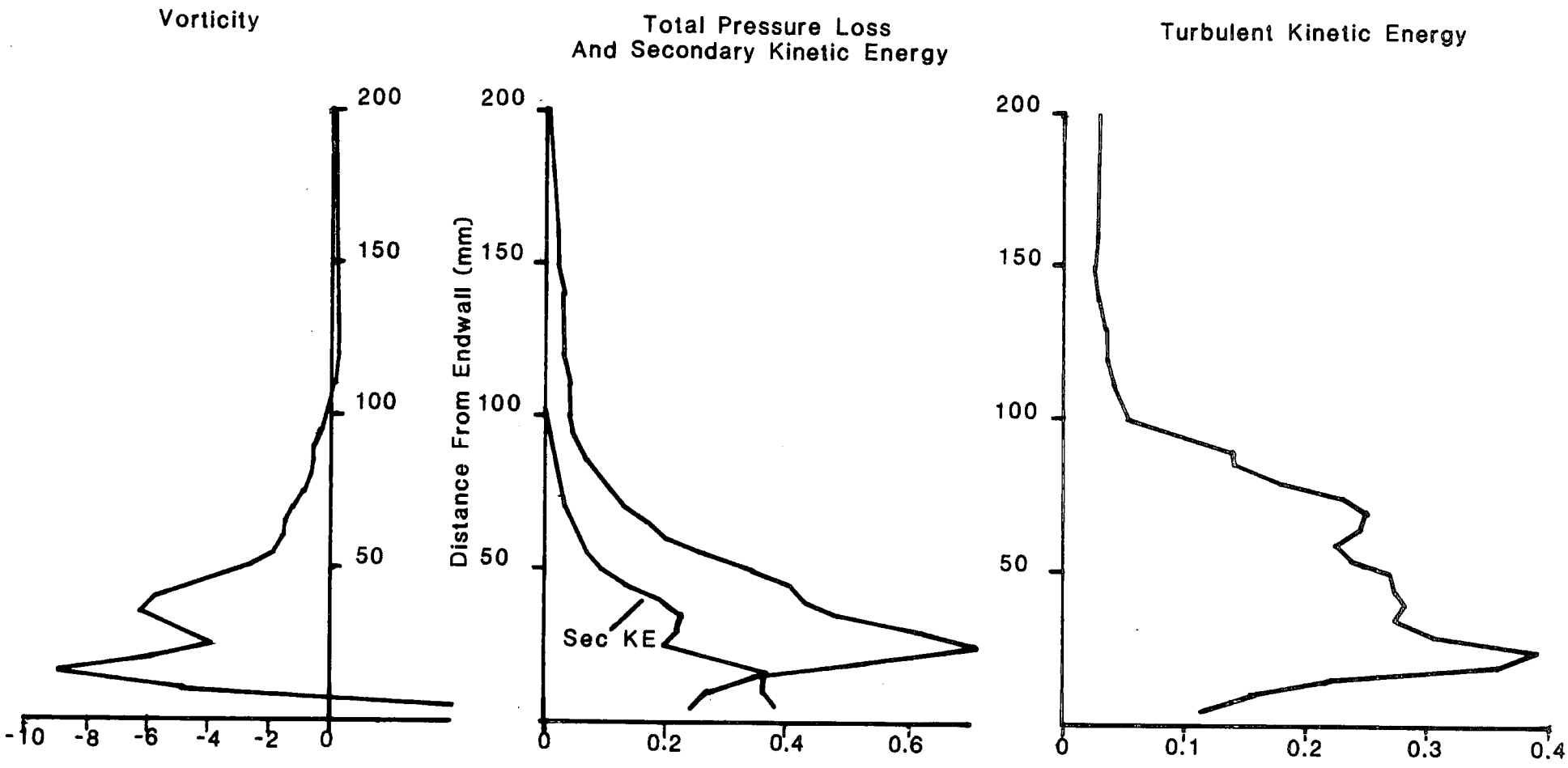

FIGURE 4.8: Pitch Averaged Results For Slot 6

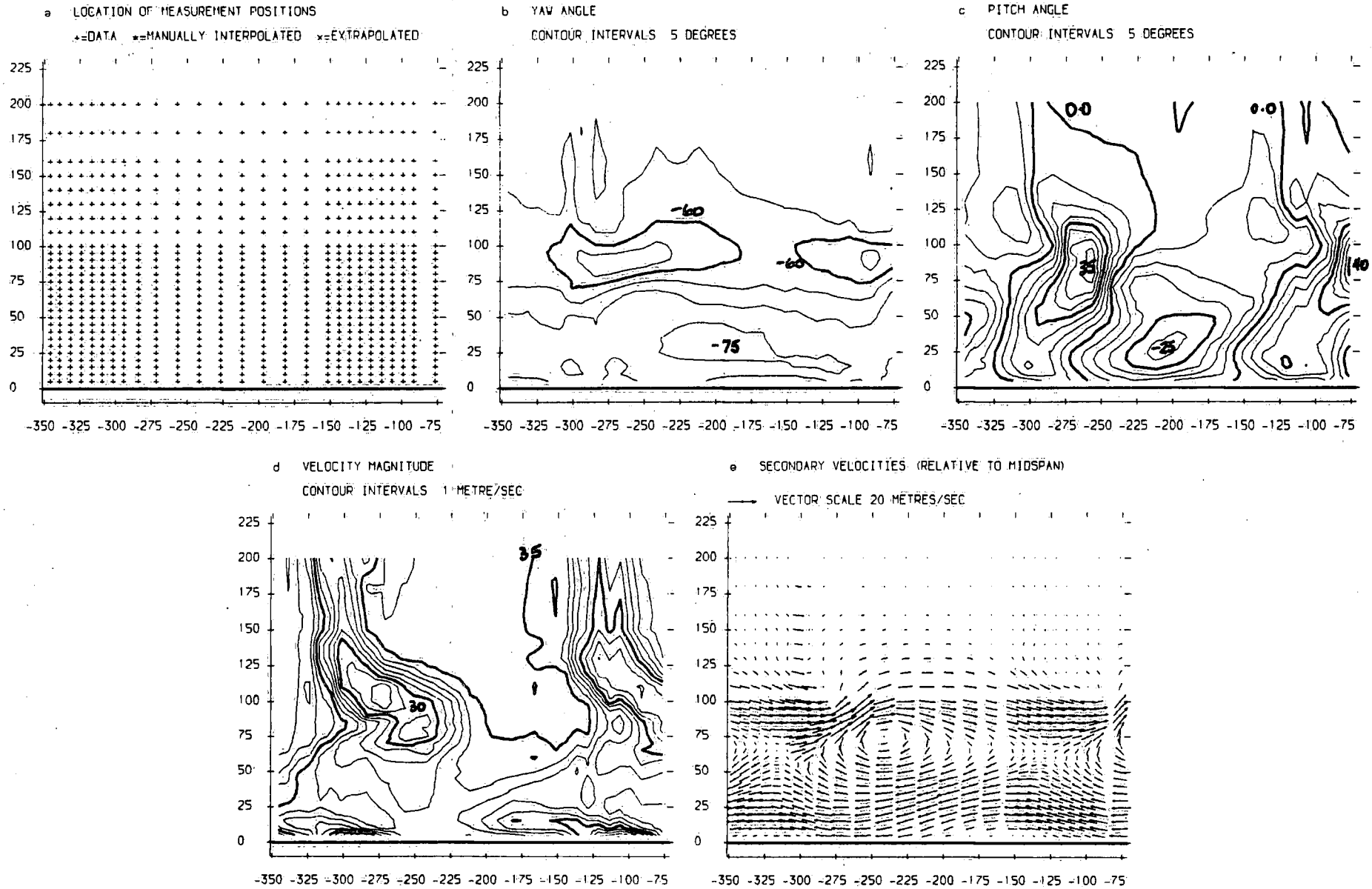

FIGURE 4.9(a-e): Hot-Wire Anemometry Results For Slot 10

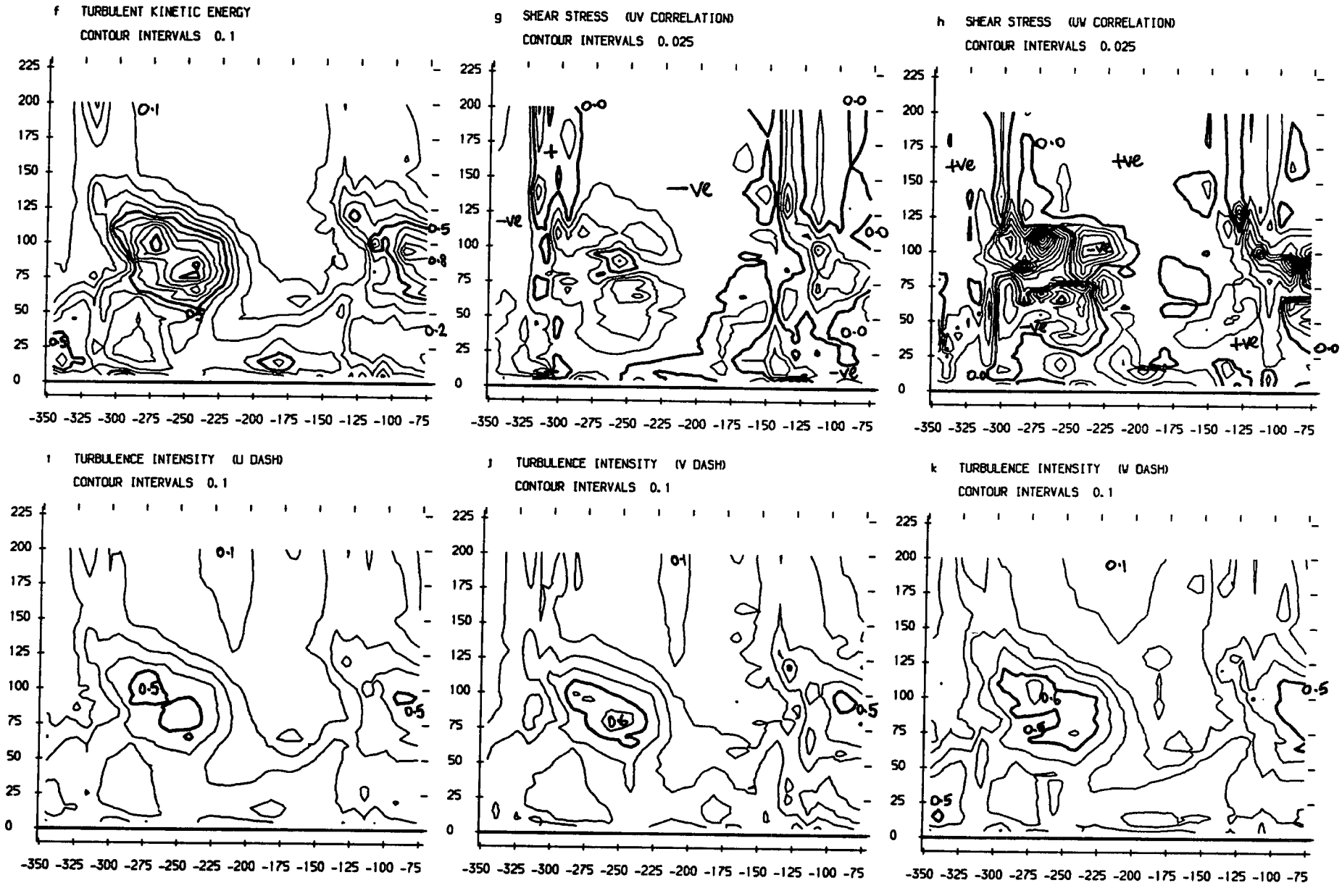

FIGURE 4.9(f-k): Hot-Wire Anemometry Results For Slot 10

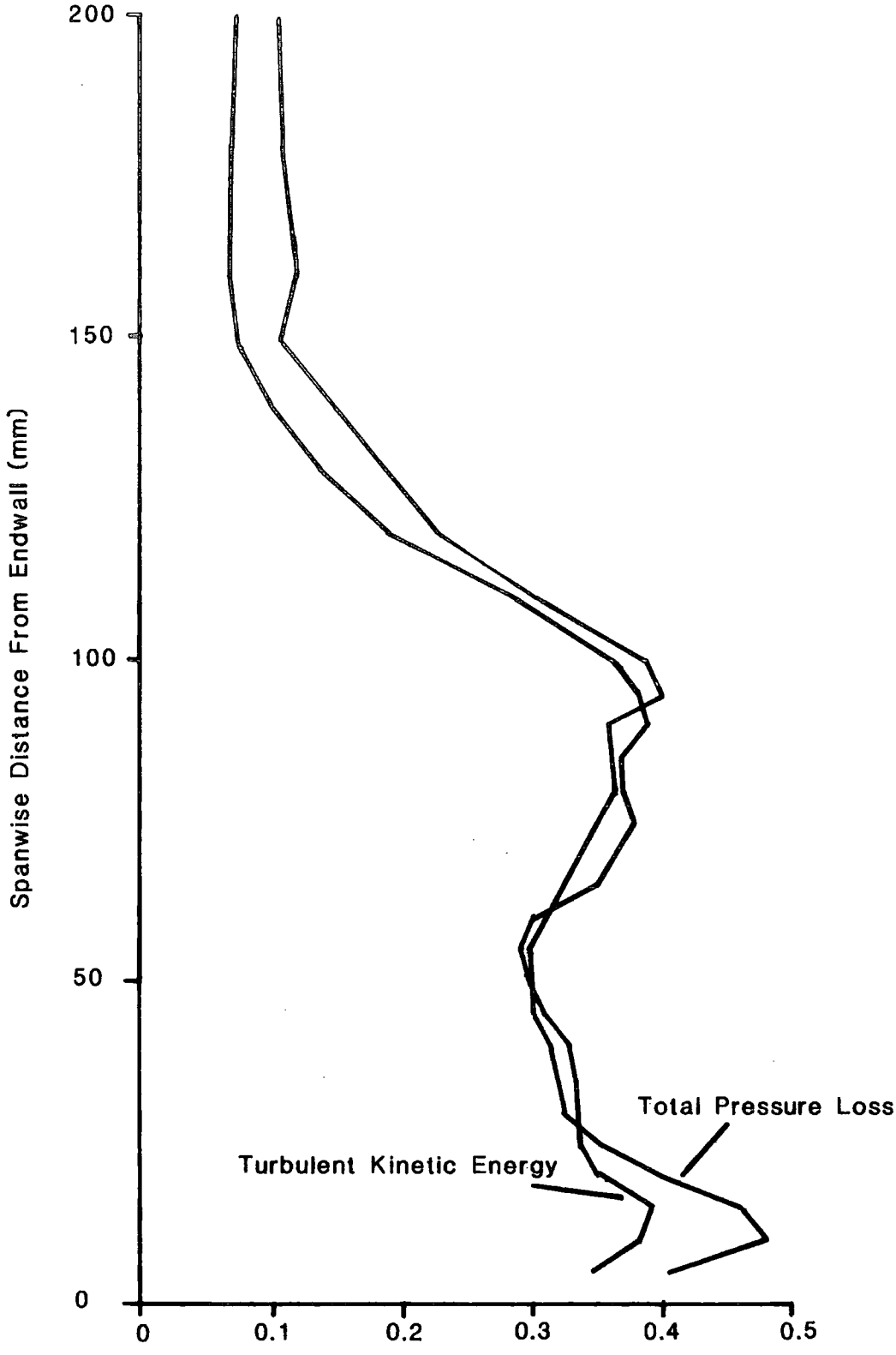

FIGURE 4.10: Slot 10 Turbulent Kinetic Energy

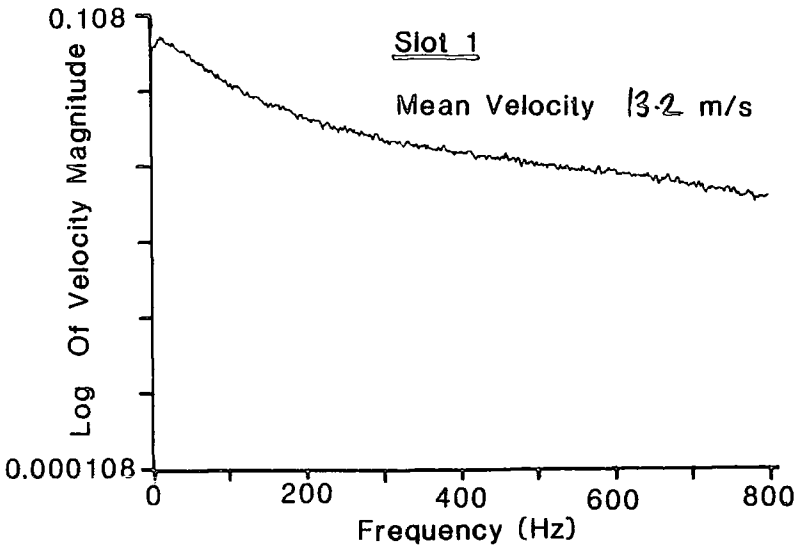

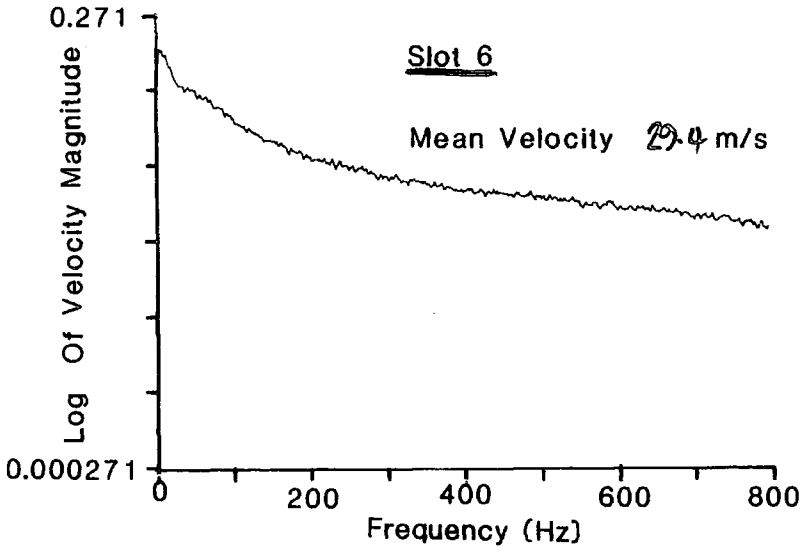

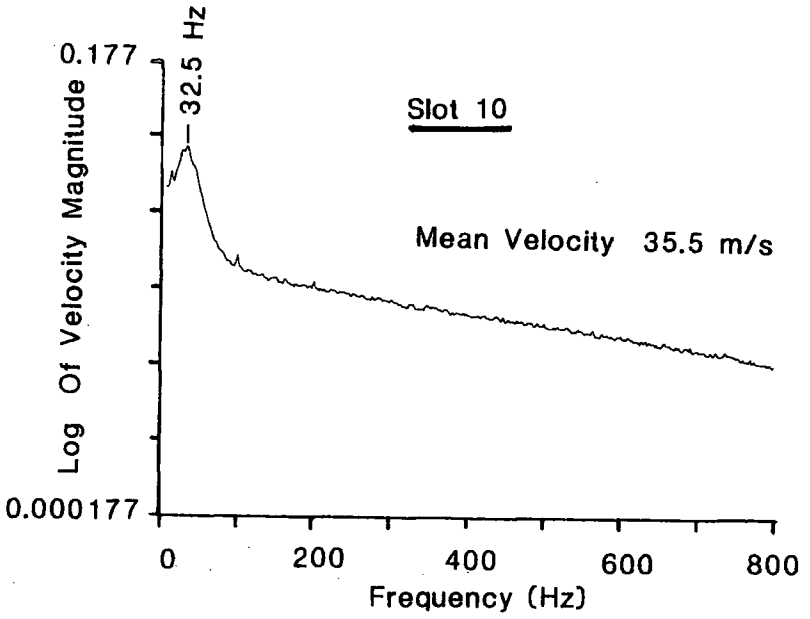

FIGURE 4.11: Spectral Analysis Results

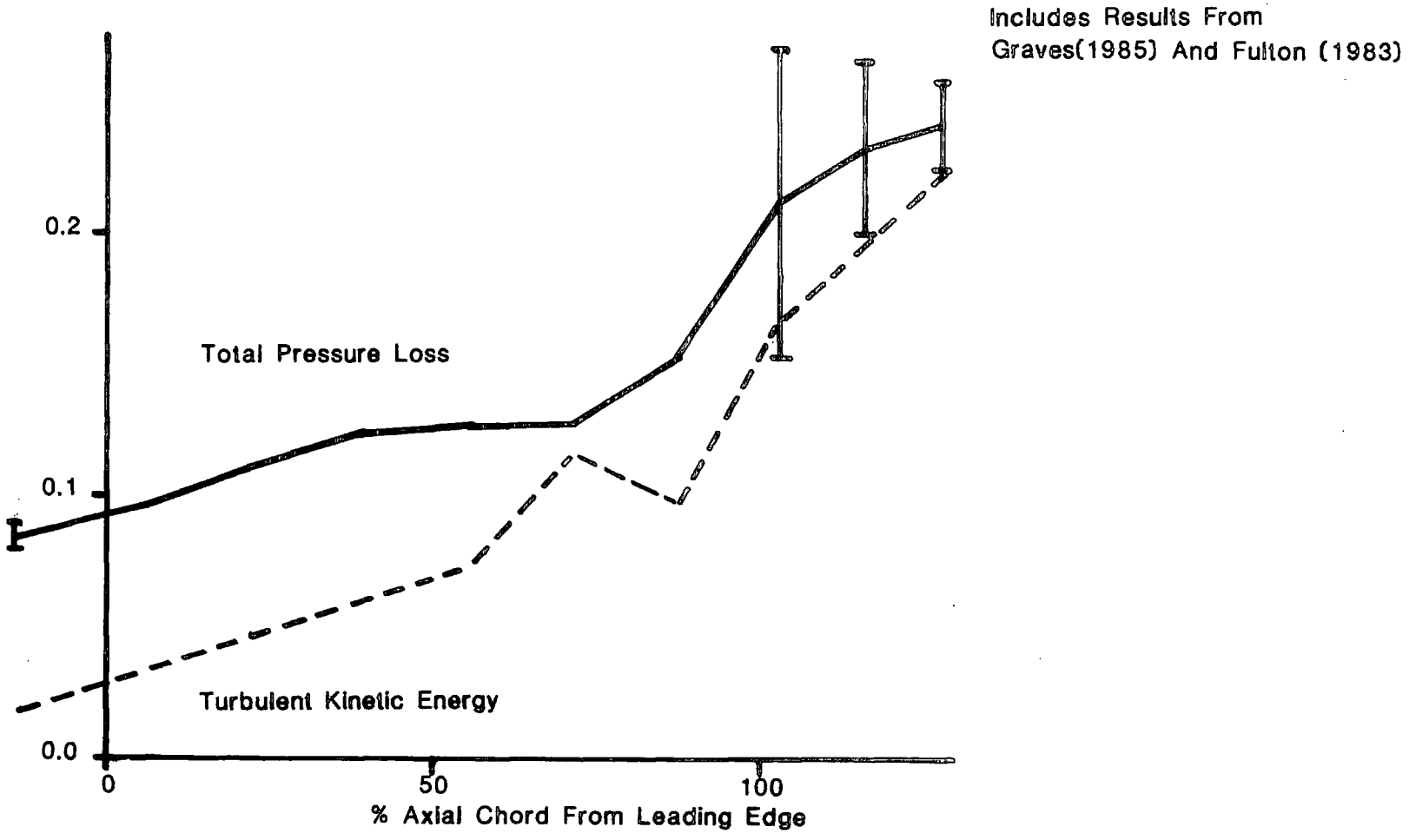

FIGURE 4.12: Development Of Loss And Turbulent Kinetic Energy

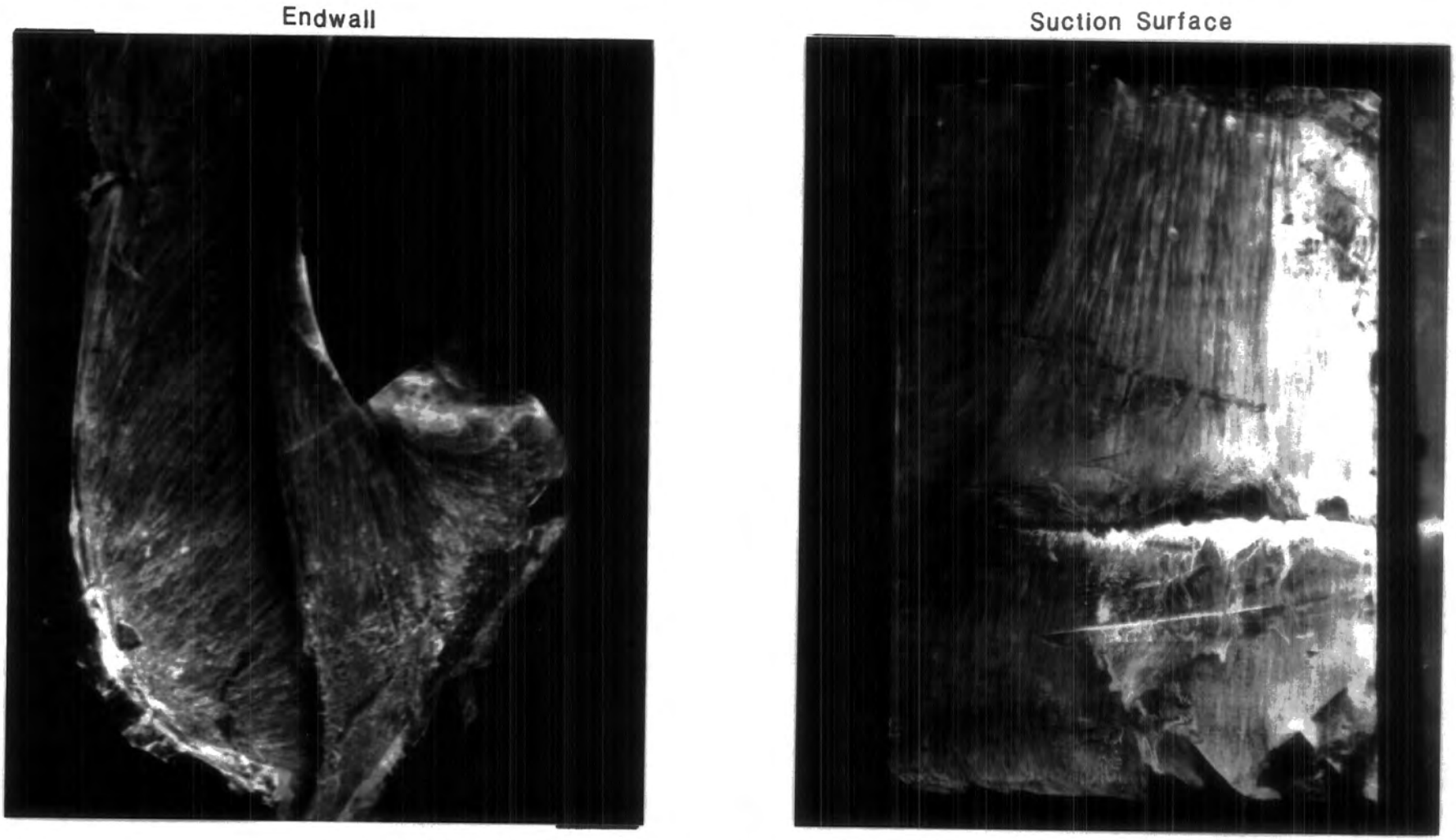

FIGURE 4.13: Flow Visualisation Results

CHAPTER 5 : EXPERIMENTAL RESULTS (JAW CASCADE)

This chapter reviews the experimental results that were obtained using the JAW cascade. Results were obtained for three levels of inlet skew using three-hole and five-hole pressure sensing probes at five axial locations in the cascade. The surface static pressure distributions and flow visualisation results are also presented.

5.1 INTRODUCTION

In linear cascade testing it is usual to present uniform flow conditions at inlet to the cascade. However, when the flow enters a rotor row in a real machine the wall boundary layer will be skewed relative to the blades. In a compressor the direction of skew would be such as to act to reduce the secondary flows. The direction of skew in a turbine would be such that the secondary flows in the blade passage would be reinforced. An important reason for studying the effect of skew in a linear cascade is that it is possible to make very detailed measurements that will enhance the understanding of the fundamental flow structure. A new low speed facility was therefore constructed with a moving belt upstream of a cascade of blades to produce the required skewing effect. Details of the construction of the cascade and the moving belt facility are given in Chapter 3. The technique of using a moving belt upstream of the cascade is justified since the boundary layer passing from the moving belt

through a stationary cascade is the kinematic equivalent of the boundary layer passing from a stationary wall through a row of moving blades. The belt was approximately 800mm wide and its downstream edge was located at 15% of an axial chord upstream of the cascade.

From a velocity triangle, Figure 3.6, it can be deduced that the ratio of belt speed to air speed is a function of the upstream stator air exit angle, β, and the rotor air inlet angle, α. In modern practice a typical value for β is 70^{o}, and for the JAW cascade the design value for α is 42.75^{o}. Then

$$\tan \alpha = \frac{V_\theta}{V_x} \qquad \text{and} \qquad \tan \beta = \frac{W_\theta}{V_x}$$

and therefore

$$\frac{U}{V} = \frac{\tan \beta - \tan \alpha}{\sec \alpha}$$

where U is the belt velocity and V is the air velocity. For the specified conditions the magnitude of negative skew, which occurs in a turbine, is produced by a ratio of belt velocity to air velocity of -1.34. It was also decided to test the effect of applying positive skew to the cascade. This would partially simulate the effects of secondary flows that are produced by an upstream stator and give some increased incidence onto the rotor row. Predictions showed (Chapter 6) that a positive skew produced by an equal and opposite belt speed all but eliminated the

secondary flows in the cascade. A lower belt speed was therefore used resulting in a ratio of belt velocity to air velocity of 0.68 for the positive skew case.

The experimental results are presented for the three skew cases (negative, zero (colateral) and positive) side by side for each of the slots to enable easy comparison. The plots are presented in three columns on each page and unless otherwise stated the left hand column contains the negative skew results, that centre column the colateral results, and the right hand column the positive skew results. In the blade passage, for reasons of clarity only, the area plots are not presented right out to midspan although the measurements were made. Where appropriate, such as for loss, the reference condition is taken as being the upstream condition and the primary flow direction is assumed to be the same as the midspan flow direction.

5.2 SLOT 1

Slot 1 is located at 14% of an axial chord upstream of the cascade and is thus very close to the downstream edge of the moving belt. For the five-hole pressure probe the locations of the measurement positions within the axial plane were the same for all three skew cases and are shown in Figure 5.1(a). In the case of the three-hole pressure probe the locations used for the colateral case are shown in Figure 5.1(f), and for the other two skew cases in Figure 5.1(g). The results that were obtained with the five-hole pressure probe are presented in Figure 5.2, and those obtained with three-hole probe close to the endwall are

presented in Figure 5.3. Pitch averaged results are presented for the five-hole pressure probe in Figure 5.4.

It is clear that in the case of positive skew the results close to the endwall are in some doubt. This was due to being unable to rotate the probe sufficiently to bring the flow direction within the probe measurement cone without the edge of the belt interfering with the probe. For the five-hole probe the results at 5mm from the endwall were therefore mainly obtained by extrapolation and must be treated with caution.

The five-hole probe results show similar general features for all three skew cases. The total pressure loss coefficient contours are presented in Figure 5.2(a-c). In a colateral boundary layer the surfaces of constant total pressure, or Bernoulli surfaces, would be expected to be parallel to the endwall. In all three skew cases the contours in the outer portion of the endwall boundary layer were approximately parallel. The upstream effect of the blades was indicated by the presence of the horseshoe vortex which is marked by the slight indentations in the contours close to the endwall. The contours clearly show that the effect of skew was confined to within 40mm of the endwall in the spanwise direction. Another effect seen in these contours is that negative skew appeared to thicken the inlet boundary layer whereas positive skew appeared to thin it. In addition the lower levels of total pressure loss detected in the case of positive skew indicate that a re-energisation of the inlet boundary layer had occurred. The secondary velocity vectors, presented in Figure 5.2(d-f), show almost zero values for most of the axial plane.

However in the case of negative skew the upstream effect of the blades reinforced by the skew produced relatively large secondary flows close to the endwall. In the case of positive skew the vectors close to the endwall clearly indicate the uncertainty of the results in this region since unlikely pitchwise flows were detected. The pitch angle contours are presented in Figure 5.2(g-i). The increasingly negative angles as the endwall was approached indicate that the flow direction was towards the endwall and that high energy freestream fluid was being moved into the endwall region. The effect was most clearly seen in the case of negative skew. Similarly the yaw angles, Figure 5.2(j-l), were found to be increasing on the endwall which indicated that the flow was rotating in the opposite sense to that in which the subsequently formed passage vortex will rotate. It was clear that the combined pitch and yaw angle results were pointing to the presence of the horseshoe vortex. The static pressure coefficient contours, Figure 5.2(m-o), show positive values in the region corresponding to an upstream projection of the blade passage. This indicates that the velocity was increased in this region relative to the upstream reference velocity. There was no sign of a stagnation point in any of the three skew cases. At such a point the local static pressure would be equal to the upstream total pressure and the static pressure coefficient would take a value of -1. The reason for not detecting a stagnation point was probably that the measurement plane was too far upstream of the leading edge of the blade. The streamwise vorticity contours are presented in Figure 5.2(p-r) and negative values indicate rotation

in a clockwise direction. The contours indicate the formation of positive vorticity close to the endwall in the colateral and negative skew cases. Although the contours for the positive skew case also show positive vorticity close to the endwall this was probably due to errors in the numerical differentiation of the extrapolated data. It is therefore doubtful as to whether this was a real effect.

The results that were obtained with the three-hole probe are presented in Figure 5.3(a-f). The total pressure loss coefficient contours, Figure 5.3(a-c), show similar patterns with comparable magnitudes of loss to those obtained with the five-hole probe. In the non-zero skew cases the loss on the endwall that would usually be associated with the horseshoe vortex was smeared over a large portion of the endwall. This may have been as a result of the closeness of the slot to the edge of the belt. The yaw angle contours, Figure 5.3(d-f), show a reasonable level of agreement with the corresponding five-hole probe results apart from the region very close to the endwall. The rapidly changing flow direction, coupled with the limitation on the rotation of the probe due to presence of the belt, meant that there was a lot of extrapolation from the calibration surfaces in this region particularly for the non-zero skew cases.

The results of averaging the measurements made with the five-hole probe across the blade pitch are presented in Figure 5.4. The pitch averaged results are particularly important at slot 1 since they define the inlet conditions for the cascade and therefore find particular application for modelling purposes. The

pitch averaged mass meaned midspan yaw angle was not found to be the same as the design inlet flow angle of 42.75^{o}. For the negative skew case the pitch averaged angle was found to be 43.9^{o}, for the colateral case it was 45.7^{o} and for the positive skew case it was 44.3^{o}. The discrepancy is an indication of the accuracy of the construction of the cascade and of the accuracy of the alignment of the probe and cascade axis systems. The plots of pitch averaged yaw angle, Figure 5.4(a-c), clearly show the effect of skew. The negative skew case, Figure 5.4(a), shows an overturning of the flow in the lower part of the span compared to the underturning produced in the case of positive skew (Figure 5.4(c)). The validity of the endwall point must however be questionable in both of these skew cases. The slight overturning of the flow in the colateral case, Figure 5.4(b), is an indication of the extent of the upstream influence of the blade. The results of pitch averaging the total pressure loss coefficient are presented in Figure 5.4(d-f) and the vorticity in Figure 5.4(g-i). An effect that was seen in the case of negative skew, Figure 5.4(g), was that negative streamwise vorticity was introduced into the flow. Similarly in the case of positive skew, Figure 5.4(i), positive streamwise vorticity was introduced into the flow. It can also be seen that the skew significantly modified the distribution of the normal component of vorticity at inlet. These results can be tied in with those obtained for the total pressure loss coefficient. The increase in loss in the case of negative skew, Figure 5.4(d), was seen to correspond to an increase in normal vorticity. Similarly in the case of positive skew, Figure

5.4(f), the reduction in loss was seen to correspond to a decrease in normal vorticity. Vorticity is defined as the gradient of the velocity so that as the loss increases the velocity falls faster and the gradient, and thus the vorticity, will increase.

For each of the skew cases an effective velocity profile was deduced from the pitch averaged total pressure loss coefficient by assuming that there was no gradient of static pressure coefficient within the working section of the tunnel. This assumption implied that the velocity was affected only by the friction and would therefore lead to the correct value of loss. The boundary layer thicknesses that are presented in Table 5.1 were defined in the streamwise direction which was taken to be the midspan flow direction. To obtain the thicknesses the endwall point in the colateral and positive skew cases was smoothed. The table of results is presented in three sections. The first section contains the experimental results for the flow characteristics defined relative to the cascade frame of reference. The second section contains the experimental results for the flow characteristics after transformation to the moving belt frame of reference. These results are useful for modelling purposes and indicate whether the flow may be considered to be colateral to the belt. The third section contains results that were obtained by assuming that the velocity profile relative to the cascade could be represented by a simple power law of the form

$$\frac{u}{u_\infty} = \left(\frac{y}{\delta}\right)^n$$

to give the experimentally determined values of displacement thickness and inlet total pressure loss. These values of n and δ are required for one of the loss predictions in Chapter 6.

TABLE 5.1 : INLET BOUNDARY LAYER DATA

		INLET SKEW TYPE		
		NEGATIVE	COLATERAL	POSITIVE
1	n	0.430	0.147	0.093
	δ (mm)	41.7	39.6	43.5
	δ^* (mm)	12.6	6.0	5.1
	θ (mm)	6.4	3.6	3.1
	H	2.0	1.7	1.6
	Y	0.077	0.041	0.031
2	n	0.153	0.147	0.126
	δ (mm)	43.3	39.6	41.3
	δ^* (mm)	5.9	6.0	5.7
	θ (mm)	4.6	3.6	3.5
	H	1.3	1.7	1.6
3	n	0.249	0.204	0.229
	δ (mm)	63.2	37.8	27.4
	θ (mm)	8.4	4.5	3.5
	H	1.5	1.4	1.5

The slight increase in boundary layer thickness detected in the non-zero skew cases was a result of the extra distance that the fluid had to travel due to the movement of the belt. The effect of the increase in inlet boundary layer thickness on the secondary loss was probably not significant (Atkins (1985) and Graves (1985)). The effect of skew was however significant as far as all the other boundary layer parameters were concerned. In particular the change in the index n shows that the shape of the boundary layer velocity profile was changed, and the loss coefficients show the re-energisation of the boundary layer as a

result of positive skew. The results relative to the belt show that the assumption of colateral flow on the belt was probably reasonable. When the inlet loss is taken into consideration it is clear that a power law assumption is not valid for any of the skew cases.

5.3 SLOT 3

Slot 3 is located inside the blade passage 22% of an axial chord from the leading edge. The locations of the measurement positions were the same for all three skew cases. They are shown for the five-hole pressure probe in Figure 5.1(b) and for the three-hole probe in Figure 5.1(h). The results that were obtained with the five-hole probe are presented in Figure 5.5 and those obtained with the three-hole probe close to the endwall in Figure 5.6. Pitch averaged results are presented for the five-hole probe in Figure 5.7.

The total pressure loss coefficient contours are presented in Figure 5.5(a-c). A comparison with the flow visualisation results presented in Figures 5.19 to 5.20 has allowed the regions of loss to be identified. In the colateral case Figure 5.5(b), the contours indicate little Bernoulli surface distortion beyond 20mm from the endwall. The slight indentation in the contours at an approximate tangential coordinate of 40mm was probably due to the presence of the pressure-side leg of the horseshoe vortex. In the negative skew case, Figure 5.5(a), the flow appeared to have undergone a significant winding up of the Bernoulli surfaces. The resulting loss core appeared to have moved closer to the suction

surface side of the blade passage and away from the endwall. This structure was seen to have affected the flowfield further out towards midspan. In the positive skew case a small loss core was seen in a midpitch position close to the endwall. This loss core was associated with the pressure-side leg of the horseshoe vortex which, because of the reduced normal vorticity at inlet, had not completed its cross-passage migration. The secondary velocity vectors are presented in Figure 5.5(d-f). These vectors indicate the flow features that were associated with the loss cores. In the negative skew case, Figure 5.5(d), a relatively strong rotational flow was detected. This vortex feature was closer to the suction side of the passage and further from the endwall than the corresponding feature that was detected in the colateral case (Figure 5.5(e)). The positive skew case, Figure 5.5(f), showed the rotational flow centred on the pressure-side leg of the horseshoe vortex close to a midpitch position and near to the endwall. The pitch angle contours are presented in Figure 5.4(g-i). The progression from negative skew to positive skew shows that the zero contour moved towards the pressure surface side of the passage although it appeared to meet the endwall at approximately the same point in all three skew cases. A change of sign of pitch angle is evidence of the flow winding up and may indicate the formation of the passage vortex. This effect was most marked in the negative skew case, Figure 5.5(g), where the pitch angles were of a significantly larger magnitude than those measured in either of the other two skew cases. This was a result of the larger spanwise velocities. In the negative skew case the

zero contour appeared to run along a midpitch line for a large portion of the span. Near to the suction surface endwall corner there was a bunching of contours corresponding to the position of the pressure-side leg of the horseshoe vortex. However it is not clear how the pressure-side leg of the horseshoe vortex and the passage vortex merge together so that it is difficult to determine which was the driving phenomenon. The positive skew contours, Figure 5.5(i), showed a spanwise and pitchwise variation of pitch angle that was confined to a midpitch region close to the endwall associated with the small vortex that was detected. The yaw angle contours are presented in Figure 5.5(j-l). A clear progression through the skew cases is again detectable. Going from negative skew to positive skew there is a reduction in the level of overturning near to the endwall with the effect extending less in the spanwise direction. In the colateral case, Figure 5.5(k), the effects were confined to within 20mm of the endwall in the spanwise direction. In the negative skew case, Figure 5.5(j), this region extended to about 30mm from the endwall in the spanwise direction. The presence of the pressure-side leg of the horseshoe vortex, or the passage vortex, was marked by the deviation of the contours from their midpitch direction. In the case of positive skew, Figure 5.5(l), the contours appeared to be confined to a region even closer to the endwall resulting in an apparently steeper endwall gradient. The static pressure coefficient contours are presented in Figure 5.5(m-o). In all three skew cases there was a cross-passage static pressure gradient at midspan. From the pressure surface side of the

passage to the approximate midpitch position all three skew cases showed a similar picture. As the suction surface side of the passage was approached the contours show that there was a rapid increase in the coefficient and therefore the local velocity. The values obtained from the static pressure tappings on the blade surface have been annotated onto the plots. The probe dimensions did not allow traversing to be carried out close to the surfaces of the blade so that it is difficult to tie the two sets of results together particularly on the suction surface. On the pressure surface there was a reasonable level of agreement between the two sets of values. On the suction surface the values obtained from the tappings showed that the static pressure coefficient, and thus the velocity, continued to increase close to surface of the blade. The streamwise vorticity contours are presented in Figure 5.5(p-r). In all three skew cases the major portion of the axial plane was found to have a zero value of vorticity. In the colateral case, Figure 5.5(q), there was a small amount of negative vorticity on the endwall. There was a small peak of negative vorticity in the suction surface endwall corner which was probably due to the pressure-side leg of the horseshoe vortex. In the negative skew case, Figure 5.5(p), there was negative vorticity spread along the whole of the endwall and also up the lower part of the blade to about 40mm in the spanwise direction. The contour plot for positive skew, Figure 5.5(r), shows a region of negative vorticity on the endwall that was associated with the pressure-side leg of the horseshoe vortex. There was an additional region of negative vorticity on the

suction surface of the blade and also a region of positive vorticity on the endwall. It was unclear whether these regions marked real effects or whether, since there was no supporting evidence in any of the other plots, they were errors generated as a result of the surface fitting and numerical differentiation that were used to obtain the streamwise vorticity.

The results that were obtained with the three-hole probe are presented in Figure 5.6. The total pressure loss contours, Figure 5.6(a-c), showed the same qualitative features that had been detected by the five-hole probe. The magnitude of the losses that were detected were similar for both types of probe although the losses were slightly higher for the three-hole probe. In both the negative skew (Figure 5.6(a)) and the colateral (Figure 5.6(b)) cases the endwall flow appeared to be swept towards the loss core associated with the pressure-side leg of the horseshoe vortex or the passage vortex. The effect was most clearly seen in the case of negative skew where the contours close to the endwall appeared to be pulled back towards the loss core. In the positive skew case, Figure 5.6(c), the loss core associated with the pressure-side leg of the horseshoe vortex was seen to extend all the way to the endwall. It was not clear whether the small region of endwall loss on the suction surface side of the loss core was a real effect. The yaw angle contours, Figure 5.6(d-f), also show good qualitative agreement with the five-hole probe results. In the colateral case, Figure 5.6(e), the results close to the endwall are of a poorer quality than for the other two skew cases. This was because the facility that allowed the probe

turret angle to be varied during traversing was not introduced until the effect of skew was being investigated. Even in the colateral case there was too much variation of the flow angle for the probe calibration to cope. However the other two skew cases proved the value of the modification to the traversing technique since apparently good results were obtained even in the regions of rapidly changing flow angle.

The results of averaging the five-hole probe measurements across the blade pitch are presented in Figure 5.7. The pitch averaged mass meaned yaw angles, Figure 5.7(a-c), clearly show that the presence of inlet skew had a significant effect on the flow. The introduction of negative skew at inlet resulted in an increased level of overturning of the flow when compared to that produced in the colateral case. The introduction of positive skew at inlet resulted in the apparent removal of the overturning to give the appearance of a uniform flow. The results of pitch averaging the total pressure loss coefficient and the secondary kinetic energy are shown in Figure 5.7(d-f). With the exception of a slight increase in the secondary kinetic energy the results for the colateral case remained unchanged from the results obtained for slot 1. With the exception of the endwall point, the validity of which was in any case found to be uncertain for slot 1, the same comment can be applied to the results that were obtained for the case of positive skew. However the results that were obtained in the negative skew case show that a substantial development of the flowfield had occurred since slot 1. The growth of loss was seen to fall away close to the endwall and

there was a corresponding substantial increase in the secondary kinetic energy consistent with the rolling up of the Bernoulli surfaces as the passage vortex developed. The results of pitch averaging the streamwise vorticity are presented in Figure 5.7(g-i). For comparative purposes the theoretical streamwise vorticity, calculated using the formula of Came and Marsh (1974), has also been plotted. The comparison between the experimental and the theoretical results is discussed in Chapter 6. In all of the skew cases the positive vorticity detected at slot 1 was masked by the increase in negative vorticity. In the case of negative skew the vorticity associated with the passage vortex was clearly identifiable. In the colateral case there was also a significant region of negative vorticity closer to the endwall that was associated with the pressure-side leg of the horseshoe vortex or the passage vortex. In the case of positive skew there was a very intense region of negative vorticity that extended very close to the endwall. However the validity of this result must be in some doubt due to the presence of high velocity gradients in this region that may have adversely affected the numerical differentiation.

5.4 SLOT 5

Slot 5 is located inside the blade passage at 55% of an axial chord from the leading edge. The locations of the measurement points were the same for all three skew cases. They are shown for the five-hole probe in Figure 5.1(c) and for the three-hole probe in Figure 5.1(i). The results that were obtained

with the five-hole probe are presented in Figure 5.8 and those obtained with the three-hole probe close to the endwall in Figure 5.9. Pitch averaged results are presented for the five-hole probe in Figure 5.10.

The main feature of the five-hole probe results was that they showed the continued development of the passage vortex. The total pressure loss contours are presented in Figure 5.8(a-c). In the colateral case, Figure 5.8(b), significant Bernoulli surface distortion was detected which suggested that the flow had started winding up to produce a loss core. In the negative skew case, Figure 5.8(a), a fully developed loss core was already present with significantly greater levels of loss than was detected in either of the other two skew cases. Although the positive skew case, Figure 5.8(c), exhibited a similar maximum value of loss to that detected in the colateral case the general distribution of loss within the passage was very different. In the positive skew case the Bernoulli surfaces appeared to have wrapped around the high loss core that was associated with the pressure-side leg of the horseshoe vortex. The secondary velocity vectors are presented in Figure 5.8(d-f). Going from negative to positive skew there are several progressions that are clearly identifiable. Firstly the distance of the passage vortex from the endwall was greatest in the case of negative skew (Figure 5.8(d)) and least in the case of positive skew (Figure 5.8(f)). Secondly the distance of the passage vortex from the suction surface side of the passage was least in the case of negative skew and greatest in the case of positive skew. Finally the extent to which the passage vortex

affected the freestream flow was greatest in the case of negative skew and least in the case of positive skew. The pitch angle contours, Figure 5.8(g-i), showed two features common to all three skew cases. Firstly the passage vortex appeared to have migrated towards the suction surface side of the passage. Secondly the magnitude of the velocity in the spanwise direction was much increased which would imply a much stronger passage vortex. This was probably due to the acceleration of the flow that occurred between slots 3 and 5. The negative skew case (Figure 5.8(g)) again showed a more developed flow picture than that seen for the colateral case (Figure 5.8(h)). The positive skew case, Figure 5.8(i), appeared to have remained influenced by the pressure-side leg of the horseshoe vortex as in slot 3. The yaw angle contours, Figure 5.8(j-l), showed the high overturning of the flow that occurred near to the endwall. For the negative skew case, Figure 5.8(j), the flow features were seen to extend further into the blade passage in the spanwise direction. The flow features were also seen to appear closer to the suction surface side of the passage. Both of these effects were seen to be less significant in the other two skew cases. The static pressure coefficient contours, Figure 5.8(m-o), again showed the cross-passage gradient out to midspan for all three skew cases. There was also a similarity in the pictures from the pressure surface side of the passage to the midpitch position. From the midpitch position to the suction surface side of the passage the effect of the loss core was seen, particularly in the suction surface endwall corner. The results that were obtained from the static pressure tappings

on the surface of the blade have been annotated onto the plots. The tappings show a uniform static pressure gradient over the pressure surface for all of the skew cases with a negative value indicating low velocities. On the suction surface the two sets of results in the negative skew case, Figure 5.8(m), are the easiest to tie together due to the relatively developed flow picture. In general the values obtained from the tappings on the suction surface for all of the skew cases did not appear to be inconsistent with the probe results. The contours of streamwise vorticity, Figure 5.8(p-r), also showed the continued development of the passage vortex. The negative skew case, Figure 5.8(p), showed a more developed flowfield picture than was apparent in either of the other two skew cases. In the colateral case, Figure 5.8(q), the vorticity appeared to be concentrated on the endwall rather than on the suction surface of the blade as in the negative skew case. In the positive skew case, Figure 5.8(r), the erroneous regions of positive vorticity that were detected in slot 3 have disappeared. The contours still indicate that the flowfield was dominated by the pressure-side leg of the horseshoe vortex. This feature was seen to have remained in the centre of the passage.

The results that were obtained with the three-hole probe are presented in Figure 5.9. The total pressure loss coefficient contours, Figure 5.9(a-c), showed similar gross features to those that had been detected with the five-hole probe. The magnitude of the losses that were detected was similar for both types of probes in the colateral case (Figure 5.9(b)). However in the other two

cases the losses detected with the three-hole probe were higher than those detected with the five-hole probe. This may be due to the relative fineness of the measurement grid used for the three-hole probe. In the negative skew case, Figure 5.9(a), the contours show that the endwall flow was being swept into the loss core. In the suction surface endwall corner there was a small additional region of loss that may have been associated with a counter vortex. A similar picture was detected in the colateral case; the endwall flow being swept into a developing loss core, and a possible endwall counter vortex. In the positive skew case, Figure 5.9(c), the picture was dominated by the pressure-side leg of the horseshoe vortex. On the endwall there was a small region of loss that may have been associated with an endwall counter vortex. The yaw angle contours, Figure 5.9(d-f), showed good agreement with the corresponding results that were obtained with the five-hole probe. However the results showed the high level of overturning of the flow that occurred close to the endwall. In all of the skew cases the endwall counter vortex was seen to cause the contours to appear to bend back on themselves.

The results of averaging the five-hole probe measurements across the blade pitch are presented in Figure 5.10. The pitch averaged mass meaned yaw angles, Figure 5.10(a-c), show that there was significant overturning of the flow in all three skew cases. In the negative skew case, Figure 5.10(a), the region of overturning extended further in the spanwise direction than in the other two skew cases. In the negative skew case there appeared to be more underturning of the flow than was detected in the

colateral case (Figure 5.10(b)). The positive skew case, Figure 5.10(c), showed a lower level of overturning than had been detected in both of the other two skew cases, and also showed virtually no underturning of the flow. The results of pitch averaging the total pressure loss coefficient and the secondary kinetic energy are presented in Figure 5.10(d-f). All three skew cases showed that the loss decreased close to the endwall. This was as a result of the loss core moving away from the endwall in the spanwise direction. In the case of negative skew, Figure 5.10(d), the loss distribution had a second peak close to the endwall that was associated with the endwall counter vortex. The secondary kinetic energy was seen to grow as the endwall was approached. The negative skew and colateral cases were seen to have similar maximum values of secondary kinetic energy. The positive skew case, Figure 5.10(f), showed the same trend as in the other two skew cases but had a significantly lower maximum value. The overall distribution of secondary kinetic energy was very different in the colateral and negative skew cases. The negative skew case had significantly more secondary kinetic energy in the spanwise region associated with the passage vortex which was consistent with the higher secondary velocities that were detected. The results of pitch averaging the streamwise vorticity are presented in Figure 5.10(g-i). The cases of positive and negative skew both showed regions of high negative vorticity at approximately the same spanwise distance from the endwall. The peak value in the case of negative skew (Figure 5.10(g)) was however approximately twice the peak value detected in the case of

positive skew (Figure 5.10(i)). In the colateral case, Figure 5.10(h), the close proximity of the passage vortex to the endwall, and thus the high velocity gradients, caused problems for the numerical calculation of the differentials required to determine the vorticity. The magnitude of the vorticity on the endwall must in this case be in some doubt.

5.5 SLOT 8

Slot 8 is located just upstream of the trailing edge of the blade at 97% of an axial chord from the leading edge. The location of slot 8 is slightly different for the JAW cascade compared to the location used for the CPG cascade. The locations of the measurement positions were the same for all three skew cases. They are shown for the five-hole probe in Figure 5.1(d) and for the three-hole probe in Figure 5.1(j). The results that were obtained with the five-hole probe are presented in Figure 5.11 and those obtained with the three-hole probe close to the endwall in Figure 5.12. Pitch averaged results are presented for the five-hole probe in Figure 5.13.

The results that were obtained with the five-hole probe show that the flowfield had continued to develop and that in all three skew cases it was dominated by the presence of strong streamwise vorticity in the blade passage. The total pressure loss coefficient contours, Figure 5.11(a-c), show that the flowfield had undergone significant changes since slot 5. In all three skew cases the pressure surface side of the passage was covered by low loss freestream fluid. A comparison with the flow

visualisation results, Figures 5.19 and 5.20, has allowed the regions of loss to be identified. In the colateral case, Figure 5.11(b), there were three regions of loss. Close to the endwall there was a region of loss that was associated with an endwall counter vortex. Further from the endwall there was a region of loss that had developed as a consequence of the action of the passage vortex. The contours also show that the endwall flow was being swept into this loss core. Further from the endwall was a region of loss that was attached to the region associated with the passage vortex. This region of loss was caused by the presence of the suction-side leg of the horseshoe vortex. Nearly half of the suction surface of the blade in the spanwise direction was seen to be covered by low loss freestream fluid. In the negative skew case, Figure 5.11(a), a similar but more developed picture of the flowfield was obtained. The loss core associated with the passage vortex was seen to have grown as most of the endwall fluid was swept into the core. As a consequence the loss core had extended further across the passage towards the pressure surface side. This region appeared to have two peaks and gave the impression of the loss core breaking into two, with one half staying close to the suction surface of the blade and the other moving out into the passage. As in the colateral case there was a region of loss close to the suction surface of the blade attached to the midspan side of the loss core associated with the passage vortex. The flow visualisation results showed that the suction-side leg of the horseshoe vortex was dissipated before it could appear on the suction surface of the blade. This loss region must therefore

have been associated with a loss core that had developed, in the absence of the suction-side leg of the horseshoe vortex to counterbalance the passage vortex. In the case of positive skew, Figure 5.11(c), the regions of high loss were seen to be almost separate. Close to the endwall there was a region of loss that was associated with the endwall counter vortex that was of a lower level than had been detected in either of the other two skew cases. There was a loss core close to the suction surface of the blade that was identified from the flow visualisation results as being associated with the separation line that marked the edge of the passage vortex. There was also a loss core close to the midpitch position which was associated with the passage vortex as it grew out of the pressure-side leg of the horseshoe vortex. The secondary velocity vector plots are presented in Figure 5.11(d-f). In all of the skew cases they show a fully developed passage vortex that had expanded to its boundaries in the pitchwise direction. In particular for the positive skew case the vectors showed the effect of the midpitch vortex extending to the suction surface side of the passage. This then accounted for the presence of the separation line running along the suction surface of the blade and its associated region of loss. The pitch angle contours are presented in Figure 5.11(g-i). The differences between the skewed cases appeared less marked than had been noticed in the earlier slots. The passage vortex appeared closer to the suction surface side of the passage in the colateral case (Figure 5.11(h)) than in the negative skew case (Figure 5.11(g)). In the latter case the movement of the passage vortex away from the suction

surface of the blade was probably due to its increased size. However the yaw angle contours, Figure 5.11(j-l), showed that the distance of the passage vortex from the endwall was very similar in both the colateral and negative skew cases. In the case of positive skew, Figure 5.11(l), the central flow feature appeared to be significantly closer to the endwall. In all three skew cases the static pressure coefficient contours, Figure 5.11(m-o), showed virtually no cross-passage gradient consistent with being close to the trailing edge of the blade. Locally high values of the coefficient were detected within the passage vortex in the colateral and negative skew cases. In the case of positive skew, Figure 5.11(o), the peak value of the coefficient coincided with the centre of the loss core associated with the pressure-side leg of the horseshoe vortex. In the other two skew cases the peak value of the coefficient did not coincide with the peak value of the total pressure loss coefficient although it did coincide with a high value of total pressure loss. In these two skew cases the peak static pressure coefficient value also coincided with the centre of the passage vortex as shown by the secondary velocity vectors. The values of static pressure coefficent obtained from the tappings on the suction surface of the blade have been annotated onto the plots. There were no tappings on the pressure surface since the thickness of the blade at this axial location did not allow it. It is not easy to tie the two sets of results together since the probe dimensions did not allow traversing to occur any close to the suction surface of the blade. However the values that were obtained from the tappings do not appear to be

unreasonable when compared to those obtained with the probe. The streamwise vorticity contours are presented in Figure 5.11(p-r). In both the colateral and negative skew cases the passage vortex was marked by the negative contours. In the case of positive skew, Figure 5.11(r), the negative vorticity was concentrated around the pressure-side leg of the horseshoe vortex which had taken on the role of the passage vortex. In the positive skew case there appeared to be some positive vorticity on the endwall at tangential coordinates of -80 to -30 that did not correspond to any identifiable flow feature. This error was probably due to the presence of large velocity gradients very close to the endwall that caused problems for the numerical differentiation. The region of positive vorticity close to the suction surface of the blade corresponded to the separation line detected in the flow visualisation that marked the edge of the passage vortex. This region was also present in the colateral case, Figure 5.11(q), where there were additional regions of positive vorticity. These regions marked the presence of the counter vortex in the suction surface endwall corner and also the suction-side leg of the horseshoe vortex on the midspan side of the passage vortex. These regions of positive vorticity were seen even more clearly in the case of negative skew (Figure 5.11(p)). However in this case the region of positive vorticity on the midspan side of the passage vortex was probably generated, in the absence of the suction-side leg of the horseshoe vortex, to counterbalance the opposing vorticity of the passage vortex. An important additional feature

was that the regions of positive vorticity had developed further into the flowfield away from the suction surface of the blade.

The results that were obtained with the three-hole probe are presented in Figure 5.12. The total pressure loss coefficient contours, Figure 5.12(a-c), showed the same gross features that had been detected with the five-hole probe. For example in the case of positive skew, Figure 5.12(c), the midpitch loss core was detected at the same location albeit with a marginally lower level of loss. The three-hole probe results also showed that there was loss spread along much of the endwall in all three skew cases. The results for the positive skew case showed the endwall counter vortex loss core and the passage vortex loss core to be separate. This is to be compared in particular with the colateral case, Figure 5.12(b), where the two loss cores appeared to mix. The yaw angle contours, Figure 5.12(d-f), again showed good agreement with those obtained using the five-hole probe.

The five-hole probe measurements were averaged across the pitch and the results are presented in Figure 5.13. The pitch averaged mass meaned yaw angles, Figure 5.13(a-c), showed that the development of the flowfield was dominated by the passage vortex in all three skew cases. The levels of overturning and underturning of the flow were generally increased. The underturned region had developed into a distinct peak which had moved away from the endwall consistent with the movement of the passage vortex. The peak was furthest from the endwall in the case of negative skew (Figure 5.13(a)) and closest to the endwall in the case of positive skew (Figure 5.13(c)). The results of

pitch averaging the total pressure loss coefficient and the secondary kinetic energy are presented in Figure 5.13(d-f). The magnitude of the main peak of the total pressure loss had remained virtually unchanged since slot 5, however it had moved away from the endwall in the spanwise direction. In the colateral (Figure 5.13(e)) and negative skew (Figure 5.13(d)) cases the loss was seen to increase on the endwall as the counter vortex continued to developed. All three skew cases appeared to have developed double peaks in the distribution of loss. The peak on the midspan side was associated with a region of positive vorticity. In the negative and positive skew cases this region was a result of the separation line that marked the edge of the passage vortex on the suction surface of the blade. The colateral and negative skew cases also showed a peak of secondary kinetic energy. In the case of negative skew the growth of secondary kinetic energy on the endwall that had been detected at slot 5 was no longer present. In the colateral and positive skew cases the endwall growth of secondary kinetic energy was present although at a reduced level. The results of pitch averaging the streamwise vorticity are presented in Figure 5.13(g-i). In the cases of positive skew (Figure 5.13(i)) and negative skew (Figure 5.13(g)) there was a large peak of negative vorticity associated with the passage vortex. The colateral case, Figure 5.13(h), showed two smaller peaks separated by a region of positive vorticity as a result of the positive vorticity near to the suction surface of the blade as seen in the area plots. On the midspan side of the negative peak there was a small peak of positive vorticity due, in the colateral

case, to the suction-side leg of the horseshoe vortex. In the other two skew cases this region of positive vorticity coincided with the separation line marking the edge of the passage vortex.

5.6 SLOT 10

Slot 10 is located downstream of the trailing edge of the blade, 28% of an axial chord from the trailing edge. The locations of the measurement positions were the same for all three skew cases and are shown in Figure 5.1(e). The results that were obtained with the five-hole probe are presented in Figure 5.14 and the pitch averaged results in Figure 5.15.

The results obtained with the five-hole probe show the unbounded development of the flow features downstream of the cascade. The total pressure loss coefficient contours are presented in Figure 5.14(a-c). The presence of the blade wakes is immediately apparent in all three skew cases. Additionally the width of the wake is similar at midspan, as might have been expected, for all three skew cases. The positive and negative skew cases had the same tangential coordinate for the wake centreline whereas in the colateral case, Figure 5.14(b), the centreline appeared to be approximately 10mm further over in the negative tangential direction. In the negative skew case, Figure 5.14(a), the loss associated with the suction surface endwall counter vortex was seen to be highly skewed. In the colateral case, Figure 5.14(b), the skewed region was seen to have been pulled around to point at the wake centreline. In the positive skew case, Figure 5.14(c), this region appeared in a relatively

unskewed condition on the endwall. The development of the counter vortex may in this case have been inhibited by the flow features associated with the other loss cores that were also present. In both the negative skew and colateral cases there appeared to be two distinct peaks within the loss core. The negative skew case had marginally higher values of loss. The positive skew case also exhibited two peaks within the loss core. The peak that was in line with the wake centreline had a similar value to that found in the negative skew and colateral cases. The other peak had a significantly lower value. There was also another separate loss core that was associated with the passing of the pressure-side leg of the horseshoe vortex through the cascade. The secondary velocity vectors are presented in Figure 5.14(d-f). In all skew cases there was a clearly defined passage vortex with a region of counter vorticity on the midspan side of it. Close to the endwall the effect of the endwall counter vortex could be seen on the secondary flows. The pitch angle contours, Figure 5.14(g-i), show a progression through the skew cases. It was apparent that in the case of negative skew, Figure 5.14(g), the contours extended further in the spanwise direction and had larger values than those obtained for the colateral case (Figure 5.14(h)). The contours obtained for positive skew, Figure 5.14(i), extended less in the spanwise direction than those obtained for the colateral case. The yaw angle contours, Figure 5.14(j-l), also showed this progression within what otherwise might have been described as typical pictures of the overturning and underturning of the flow. The static pressure coefficient contours, Figure 5.15(m-o), showed

that significant mixing had occurred in all three skew cases. The contours defining the regions associated with the vortices were no longer as distinct as they were in the earlier slots. The result was most clearly illustrated in the case of positive skew (Figure 5.14(o)). In the other two cases the presence of the passage vortex was the most clearly marked feature. In the case of negative skew, Figure 5.14(m), the endwall counter vortex was also apparent. The streamwise vorticity contours, Figure 5.14(p-r), clearly show the regions of positive vorticity on the endwall and in the blade wakes for all three skew cases. The region closest to the endwall and extending into the wakes in all three skew cases was associated with the endwall counter vortex. The core of positive vorticity that appeared above this region in the spanwise direction in all three skew cases was the shed vorticity. This region corresponds to the trailing filament and trailing shed vorticity of classical secondary flow theory. In both the negative skew (Figure 5.14(p)) and the colateral (Figure 5.14(q)) cases the passage vortex was marked by the presence of high negative vorticity. In the case of positive skew, Figure 5.14(r), there appeared to be a small peak of negative vorticity at the point where the passage vortex might have been expected to be centred. However this region was swamped by the attached stronger region of negative vorticity that was associated with the pressure-side leg of the horseshoe vortex. The positive vorticity detected between this region and the endwall was probably not a real effect.

The results of averaging the five-hole probe measurements across the blade pitch are presented in Figure 5.15. The pitch averaged mass meaned yaw angles, Figure 5.15(a-c), show the continued development of the flowfield in all three skew cases. The negative skew case, Figure 5.15(a), showed a typical picture of the overturning and underturning of the flow due to the action of the secondary flows. The distributions for the colateral and positive skew cases were found to have remained similar to the distributions detected at slot 8. However a peak of underturning had developed close to the endwall in both of these cases. In all three skew cases the overturning peak was found to have moved further from the endwall consistent with the movement of the passage vortex. The results of pitch averaging the total pressure loss coefficient and the secondary kinetic energy are presented in Figure 5.15(d-e). The plots show that in all three skew cases there had been a significant reduction in secondary kinetic energy since slot 8. This was particularly noticable close to the endwall. The total pressure loss results showed that the loss associated with the blade wakes had appeared within the distribution. It was also apparent that the loss on the endwall had continued to grow since slot 8. The results of pitch averaging the streamwise vorticity are presented in Figure 5.15(g-i). In general these results confirm the reduced strength of the passage vortex since the levels of vorticity were lower than for at slot 8. In the case of positive skew, Figure 5.15(i), the value of vorticity for the endwall point seems to be a little uncertain since the other two skew cases indicated a reduction in

vorticty on the endwall. All three skew cases showed an increase in positive vorticity on the midspan side of the passage vortex due to the presence of the trailing shed and trailing filament vorticity components. The table below presents the mass averaged losses defined with respect to the inlet dynamic pressure. The results of a mixed-out loss calculation are also presented in the table to remove the dependence of the results on the distance of the measurement plane downstream of the cascade. The gross secondary loss was calculated by subtracting the mixed-out profile loss (assumed to be equal to the mixed-out midspan loss coefficient) from the mixed-out loss coefficient. The net secondary loss was calculated by subtracting the inlet loss coefficient from the gross secondary loss.

TABLE 5.2: SLOT 10 SECONDARY LOSSES

	INLET SKEW TYPE		
	NEGATIVE	COLATERAL	POSITIVE
Measured Loss Coefficient	0.272	0.211	0.168
Measured Profile Loss	0.090	0.094	0.091
Mixed-Out Loss Coefficient	0.352	0.249	0.206
Mixed-Out Profile Loss	0.096	0.102	0.110
Gross Secondary Loss	0.256	0.147	0.096
Inlet Loss	0.077	0.041	0.031
Net Secondary Loss	0.179	0.106	0.065

(NB: Correction applied as shown in Table 3.2)

The results given in this table show that inlet skew has a very significant effect on the magnitude of the secondary losses. In the case of negative skew the net secondary loss was increased by a factor of 1.7 and in the case of positive skew it was reduced by a factor of 0.6.

5.7 AREA AVERAGED RESULTS

The area averaged results for total pressure loss and secondary kinetic energy are presented in Figure 5.16. For comparative purposes results based on data reported by Graves (1985) are also plotted. It is not strictly fair to compare the two sets of results since they are for different spans. However important comparisons can be made concerning the shapes of the plots if not their magnitudes. The total pressure loss, Figure 5.16(a), showed the colateral and positive skew cases to have a similar level of loss at inlet. In the negative skew case the inlet loss was much higher. However in the case of positive skew the inlet boundary layer appeared to be re-energised resulting in a reduced value of loss. In the colateral and positive skew cases the loss was seen to remain almost constant in the first half of the blade passage. In the negative skew case there was a slight increase in the loss to the halfway point. In all three skew cases the loss was then seen to increase to the trailing edge of the blades with a further increase downstream of the cascade. The results based on the data of Graves (1985) show the loss increasing right through the passage with a further increase at the trailing edge. The growth of loss for the skewed cases has a

similar pattern to that reported by Langston et al (1977) and Marchal and Sieverding (1977) where tripped blade profiles were used. The secondary kinetic energy results, Figure 5.16(b), showed that there was growth right through the passage. The secondary kinetic energy was then dissipated downstream of the cascade. The negative skew case appeared to have higher levels of secondary kinetic energy than the other two cases. The results based on Graves' data showed a similar distribution of secondary kinetic energy growth and dissipation.

It is interesting to plot the mass flow rate calculated at each slot since this gives an indication of the accuracy of the experimental method and of the integration techniques. The mass flow rates normalised by the mass flow rate at inlet to the cascade are presented in Figure 5.17. A possible explanation for the scatter, particularly in the early part of the passage, is that it was not possible to traverse close enough to the blades to include the fluid that was in the surface boundary layers. The mass flow rates calculated by Graves (1985) have also been plotted and they show a similar level of scatter.

5.8 MOVEMENT OF THE PASSAGE VORTEX

An appreciation of the complex three-dimensional nature of the flowfield in the cascade can be obtained by tracking the movement of the centre of the passage vortex and the movement of the peak value of its associated loss core. The passage vortex centre was defined as being the point of intersection of the primary flow angle contour and the zero crossflow angle contour in

the probe traverse plane. The loci of the position of the vortex centre and the peak value in its associated loss core are presented in Figure 5.18. The arrows show the direction of movement starting at slot 3 and finishing at slot 10. In all skew cases the passage vortex, or at this stage the pressure-side leg of the horseshoe vortex, initially moved towards the suction surface of the blade and in the colateral case towards the endwall. As the passage vortex grew in size it moved away from both the suction surface of the blade and the endwall. Downstream of the cascade the unbounded passage vortex headed back towards the wake centreline. This effect was most marked in the non-zero skew cases. In the colateral and negative skew cases the peak value in the loss core stayed on the suction surface side of the passage vortex while in the blade passage. Downstream the peak value and the passage vortex centre were at approximately the same distance from the wake centreline, but the peak value of loss was further from the endwall. In the positive skew case the picture appeared to be very compressed in that all of the movement occurred within a region closer to the endwall. In this case the peak value of total loss appeared to be much more mobile relative to the passage vortex. Results produced by Graves (1985) were similar to the colateral case, as would be expected.

5.9 FLOW VISUALISATION

The results of a flow visualisation study are presented in Figures 5.19 and 5.20. The surface flow technique that was used has been described in Chapter 3. The main feature of the endwall

flow, Figure 5.19(a-c), was the cross-passage separation line due to the movement of the pressure-side leg of the horseshoe vortex and the passage vortex. In the colateral case, Figure 5.19(b), this separation line was separated from the suction surface of the blade by the relatively weak counter vortex in the suction surface endwall corner. On the pressure surface side of the cross-passage separation line there was evidence of strong secondary flows as a result of the endwall flow being swept into the passage vortex. On the suction surface side of the cross-passage separation line the flow appeared to be swept onto the suction surface of the blade. In particular the suction-side leg of the horseshoe vortex was seen to be swept on to the suction surface of the blade. The flow visualisation did not extend far enough upstream of the cascade to detect the stagnation region that is associated with the horseshoe vortex. In the case of negative skew, Figure 5.19(a), there were some important differences in the flow visualisation results. When compared to the colateral case the cross-passage separation line was seen to have moved closer to the suction surface side of the passage earlier in the passage. On the pressure surface side of the cross-passage separation line there was evidence of stronger secondary flows than had been detected in the colateral case. On the suction side of the cross-passage separation line there was a separation line that marked the presence of the suction-side leg of the horseshoe vortex. This separation line did not go onto the surface of the blade but appeared to merge with the cross-passage separation line. This would appear to indicate that the suction-side leg of

the horseshoe vortex was dissipated by the action of the passage vortex. There was evidence of the suction surface endwall corner counter vortex. In the case of positive skew, Figure 5.19(c), the cross-passage separation line moved closer to the pressure surface side of the passage then for the colateral case. The separation line appeared to follow a midpitch position for much of the passage before moving close to the suction surface of the blade. The secondary flows on the pressure surface side of the cross-passage separation line appeared to be weaker than in the other two skew cases. On the suction surface side of the cross-passage separation line there was evidence of the endwall counter vortex. The suction-side leg of the horseshoe vortex was not at all clear and if it was present in this case it was in a much reduced form. The results for the flow visualisation on the suction surface of the blade are shown in Figure 5.20(a-c). The main features in all three skew cases were the presence of a laminar separation bubble, with its upstream edge at about 80% of an axial chord from the leading edge of the blade, and the separation line marking the edge of the passage vortex on the suction surface of the blade. In the colateral case, Figure 5.20(b), there was a second separation line on the midspan side of the passage vortex that was associated with the suction-side leg of the horseshoe vortex. These two separation lines remained apart all the way to the trailing edge of the blade. Within the passage vortex the flows appeared highly skewed. In the case of negative skew, Figure 5.20(a), the suction-side leg of the horseshoe vortex did not go on to the suction surface of the

blade. The separation line on the midspan side of the passage vortex must therefore have marked the presence of a counter vortex that developed to counterbalance the passage vortex. In the case of positive skew, Figure 5.20(c), it was not possible to detect the suction-side leg of the horseshoe vortex or a balancing counter vortex. However the passage vortex appeared much reduced in size compared to the other two skew cases.

Recently Sharma and Butler (1986) attempted to correlate Z_{TE} the penetration height of the passage vortex separation line at the trailing edge of the blade. They proposed the following empirical realtionship

$$Z_{TE} = C_{ax} \left\{ 0.15\ (\alpha_1 - \alpha_2) \left(\frac{U_1}{U_2} \right)^{1/2} + f\left(\frac{\delta_1}{h} \right) \right\}$$

where

$$f\left(\frac{\delta_1}{h} \right) = 1.4 \left(\frac{\delta_1}{h} \right) - 2.73 \left(\frac{\delta_1}{h} \right)^2 + 1.77 \left(\frac{\delta_1}{h} \right)^3$$

A value of 58mm is obtained for all three skew cases using this formula. However measurements taken from the flow visualisation results give the approximate penetration height as 85mm for the negative skew case, 64mm for the colateral case, and 45mm for the positive skew case. It is not surprising that the correlation gives reasonable results only for the colateral case since it was empirically based on linear cascade results for uniform inlet flow conditions (a particular cascade test used to derive the correlation was that of Graves (1985)). However for the skewed cases presented here the inlet boundary layer thickness

was constant and therefore was not a good indicator of the changing flow conditions.

5.10 SURFACE STATIC PRESSURE DISTRIBUTION

The static pressure distribution was measured on the surface of the blade at six spanwise distances from the endwall for each of the skew cases. The locations of the tappings are shown in Figure 3.4 and the results are presented in Figure 5.21 and 5.22.

In Figure 5.21 it can be seen that in all cases the distribution of the coefficient on the pressure surface of the blade was similar. The distribution of the coefficient on the suction surface of the blade showed a reduction in loading at the leading edge as the endwall was approached. This reduction was most marked in the case of negative skew and least noticable in the case of positive skew. A slight loading effect was also seen at the trailing edge of the blade. Negative skew appeared to slightly reduce the blade loading, and positive skew increase it, relative to the colateral case. The position of the peak suction surface velocity was found to approximately correspond to the position of the laminar separation bubble that was detected in the flow visualisation results. Figure 5.22 compares the midspan static pressure coefficient distribution with that obtained using a two-dimensional streamline curvature calculation for the design blade profile. Within experimental limits there was fair

agreement. The results obtained from the tappings have been compared with the results obtained with pressure sensing probes and discussed earlier in this chapter.

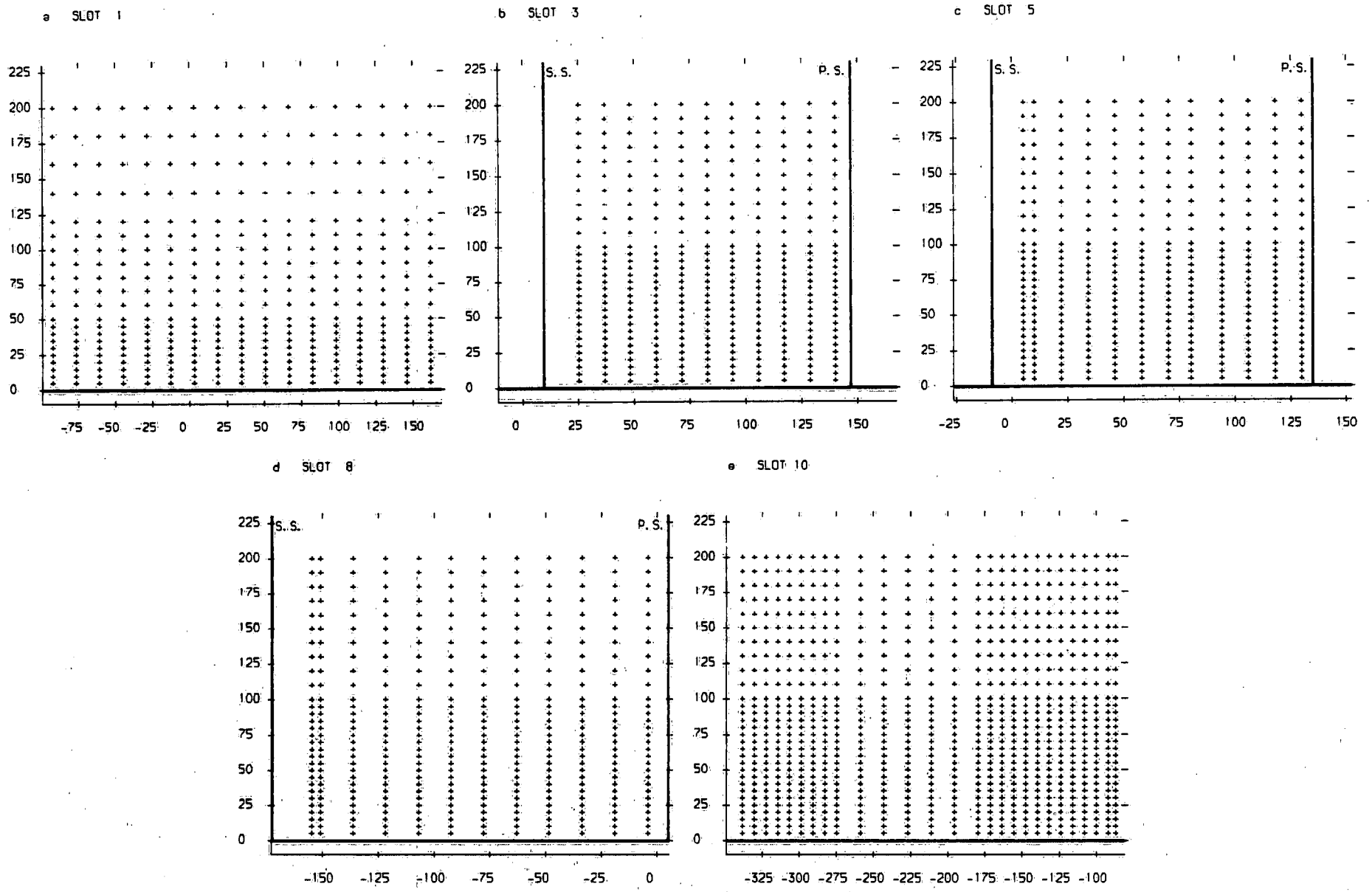

FIGURE 5.1 (a-e) : Pressure Probe Measurement Positions

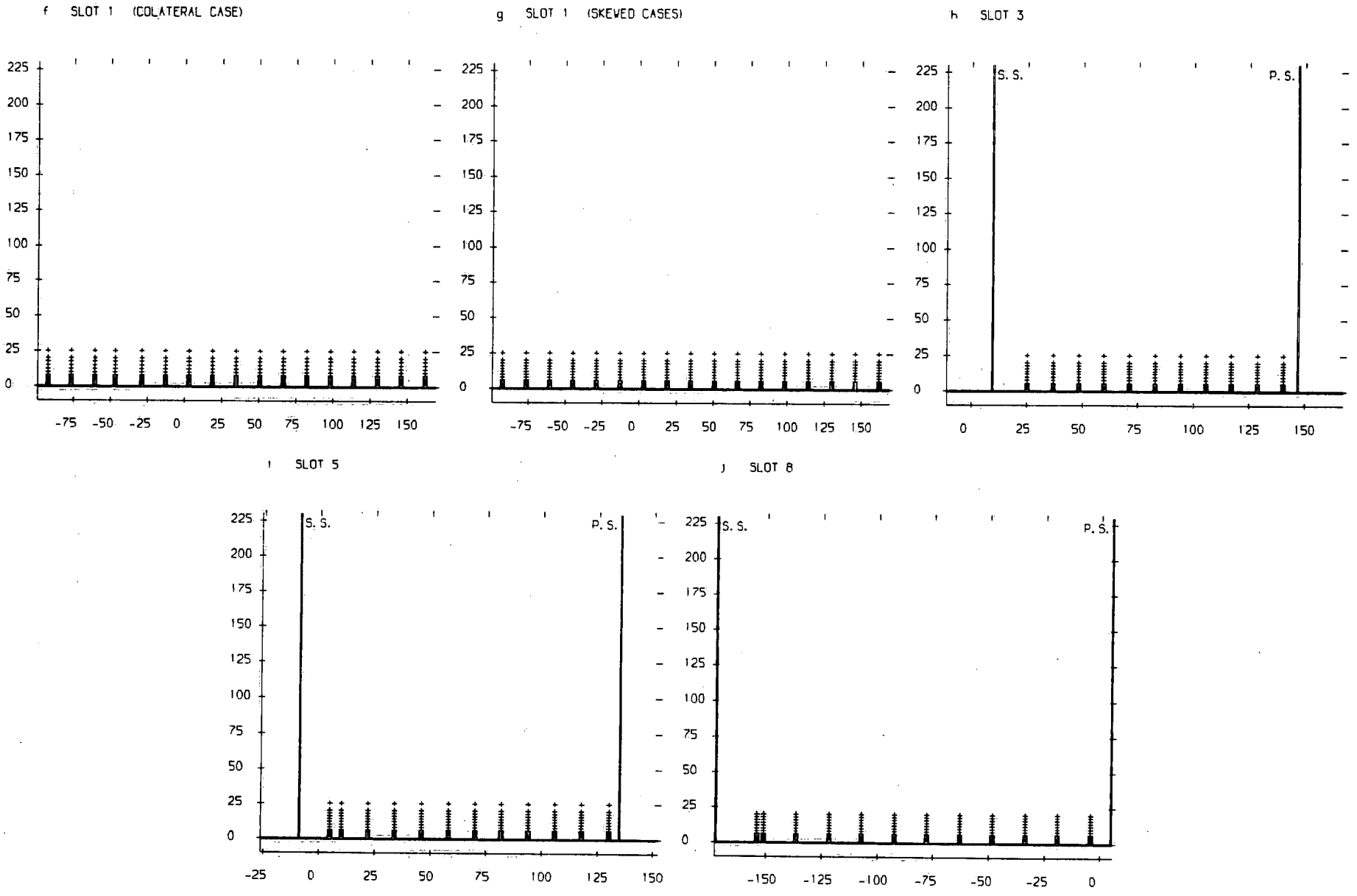

FIGURE 5.1 (f-j): Pressure Probe Measurement Positions

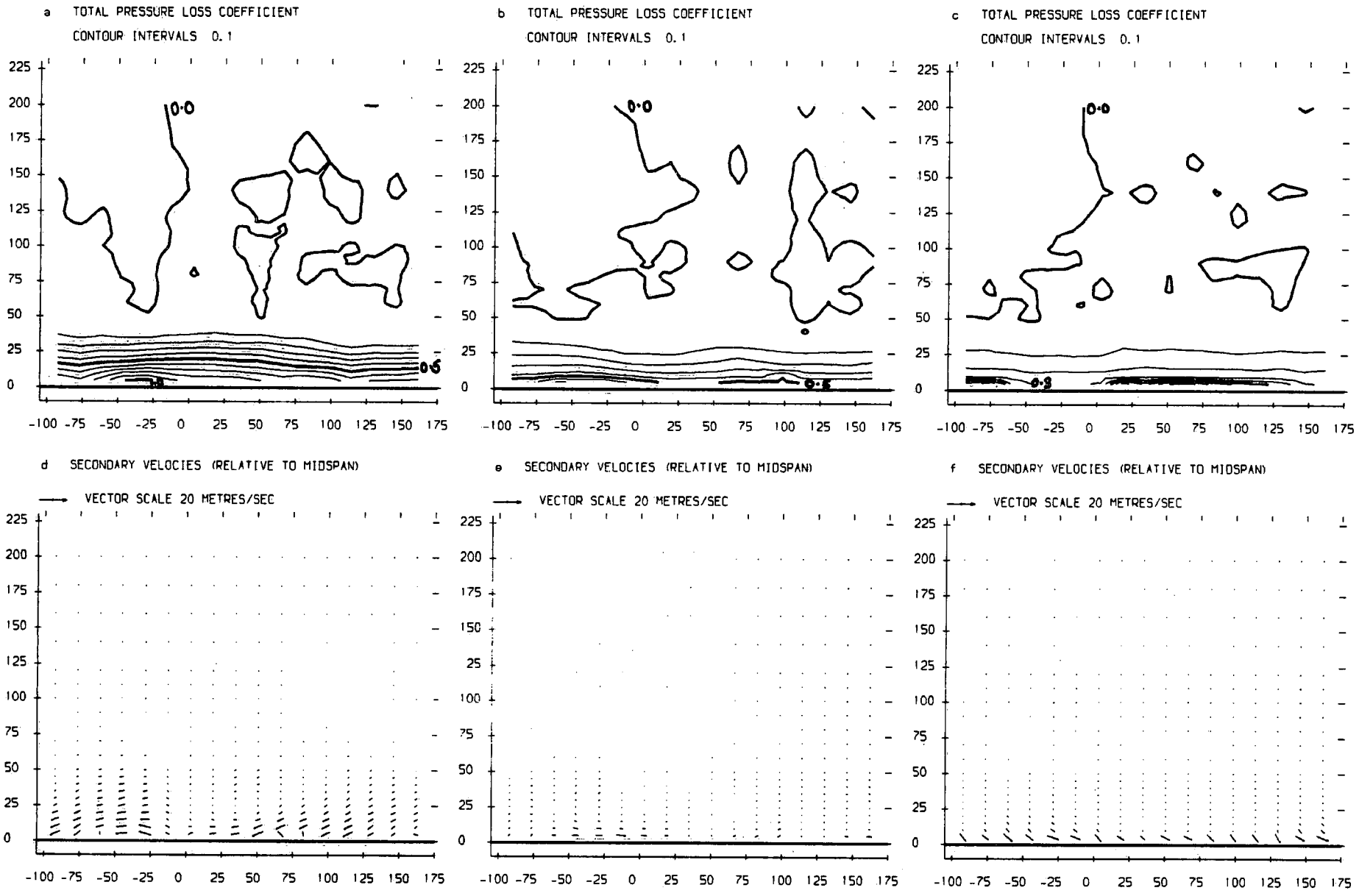

FIGURE 5.2(a-f) : Five-Hole Probe Results For Slot 1

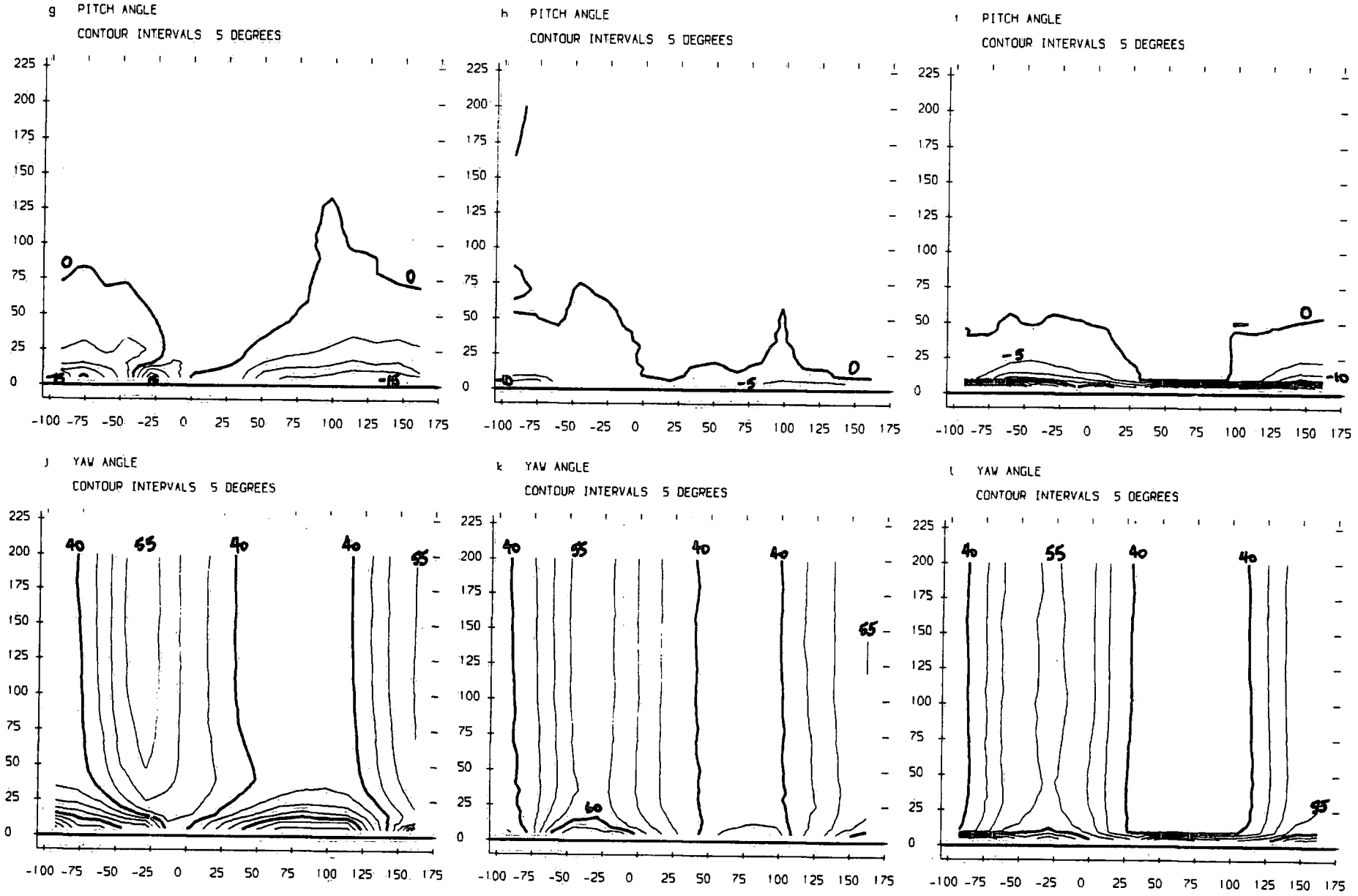

FIGURE 5.2(g-l): Five-Hole Probe Results For Slot 1

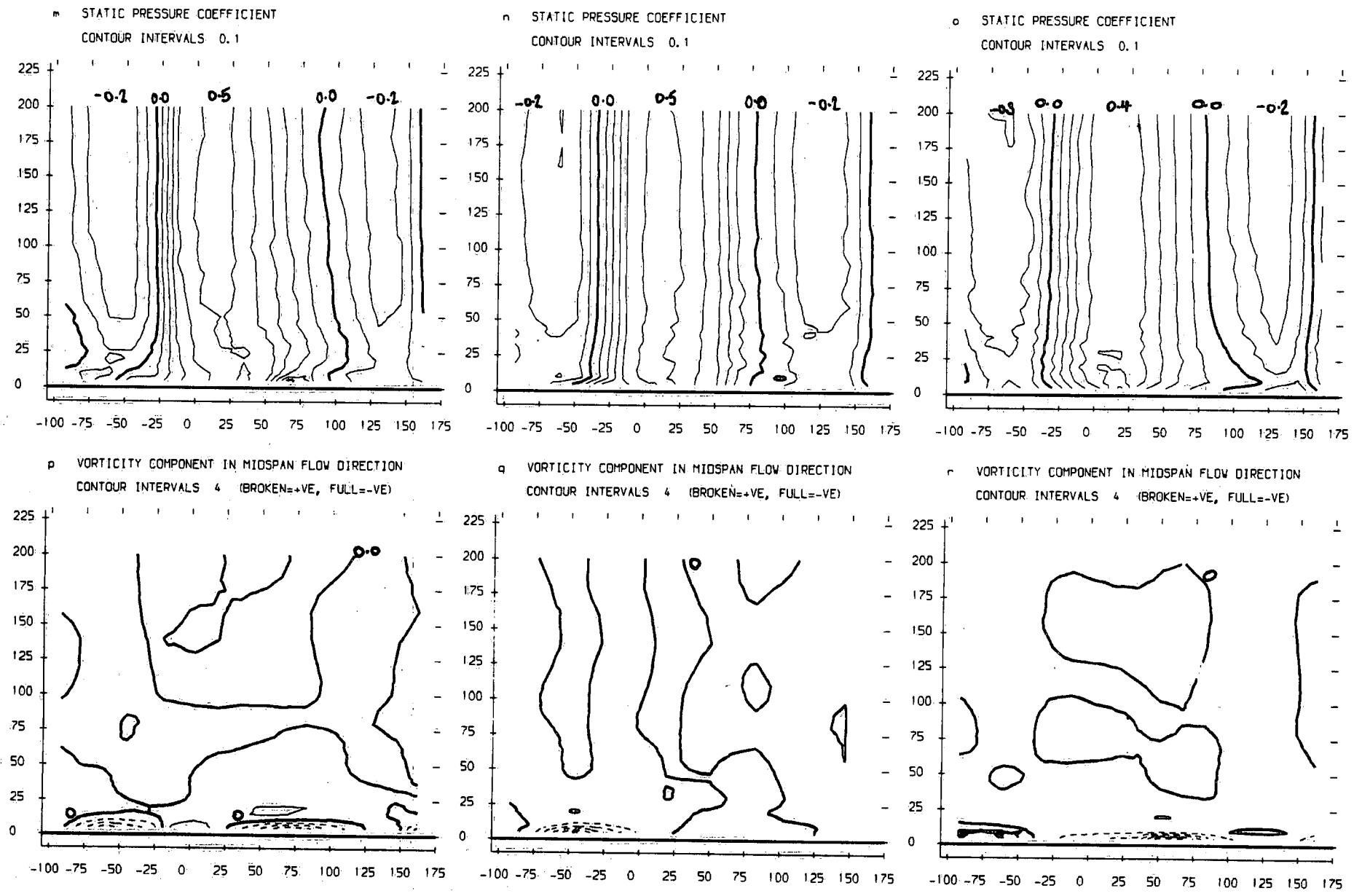

FIGURE 5.2(m-r): Five-Hole Probe Results For Slot 1

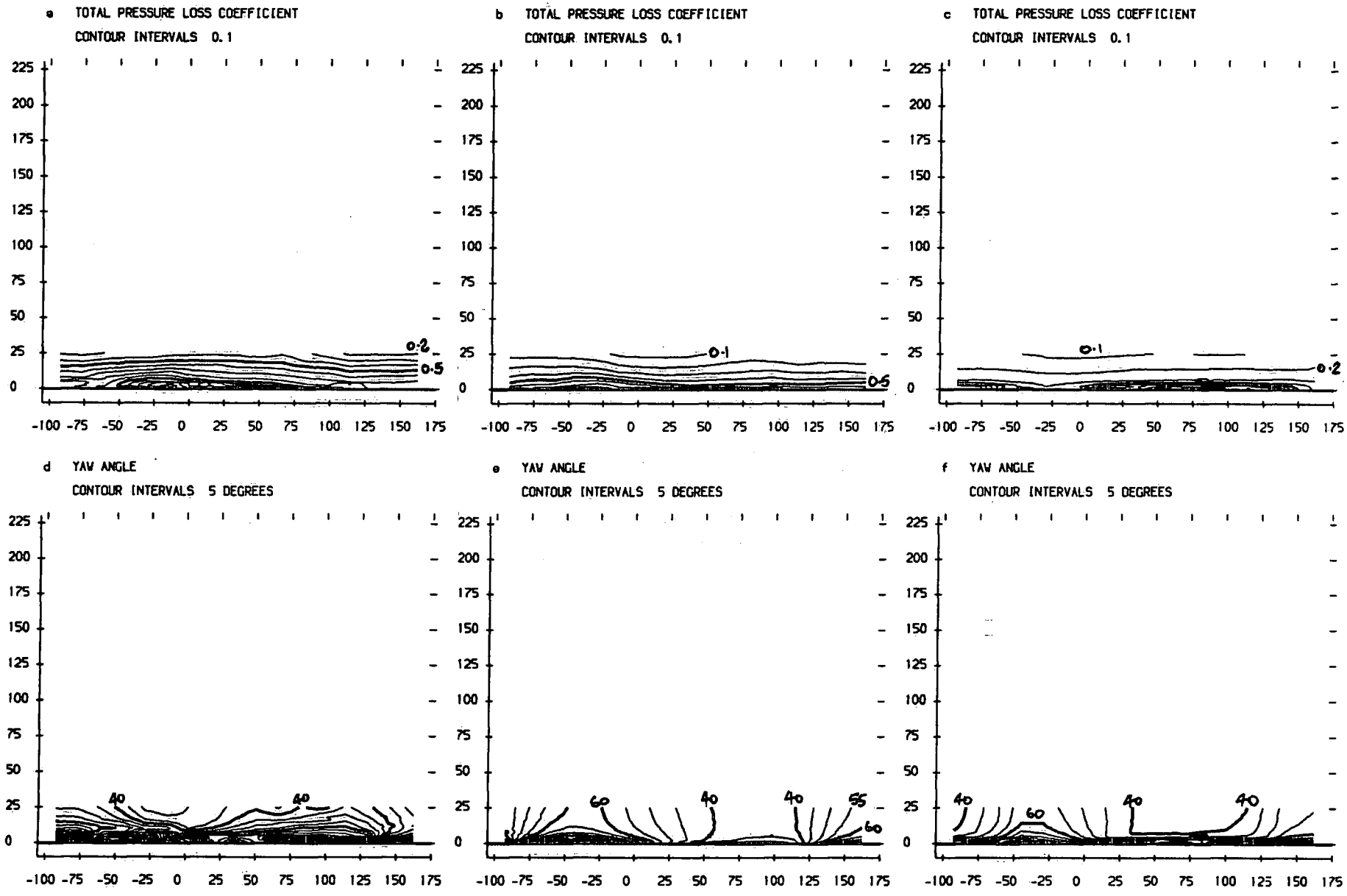

FIGURE 5.3(a-f): Three-Hole Probe Results For Slot 1

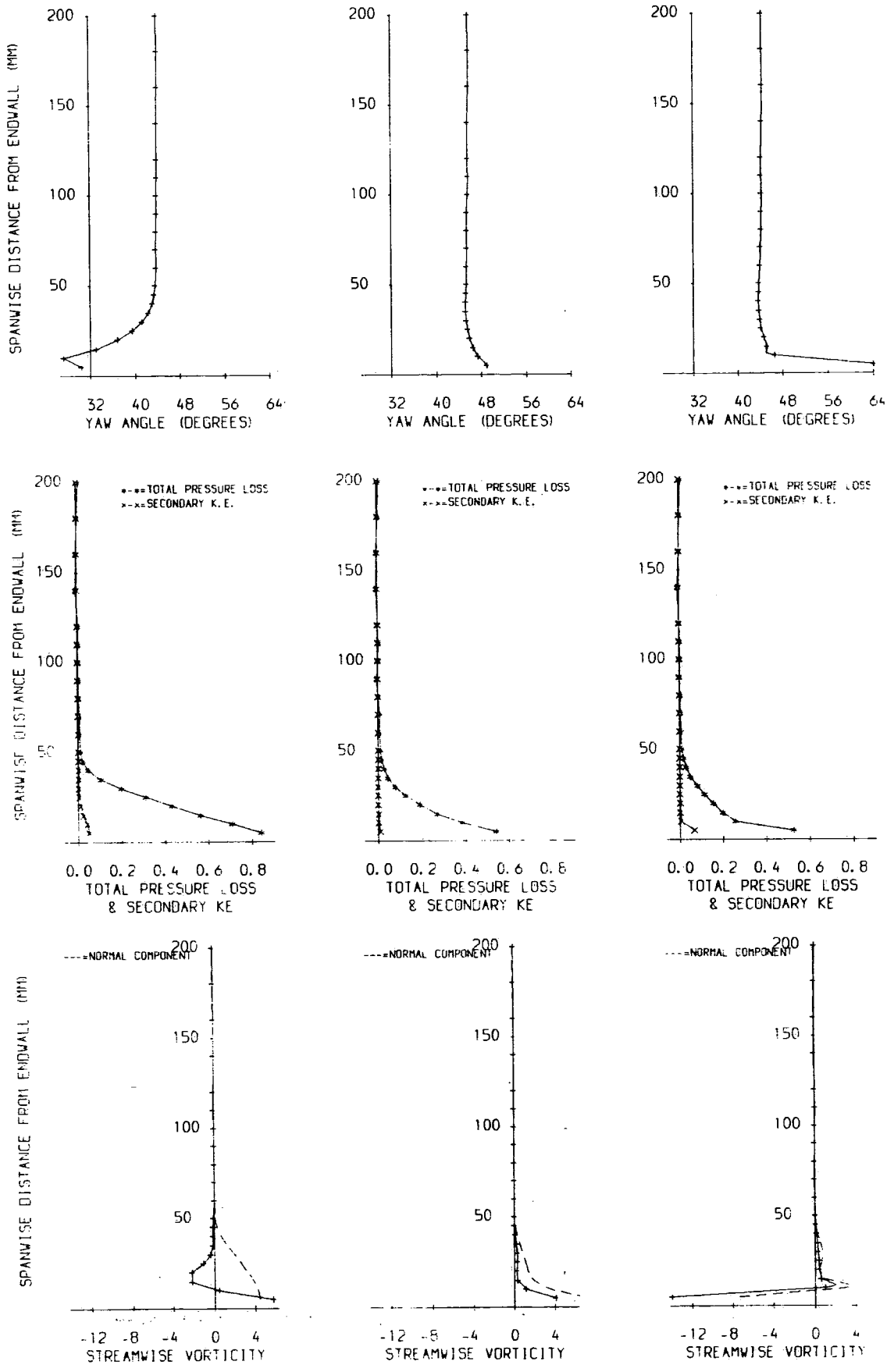

FIGURE 5.4: Pitch Averaged Results For Slot 1

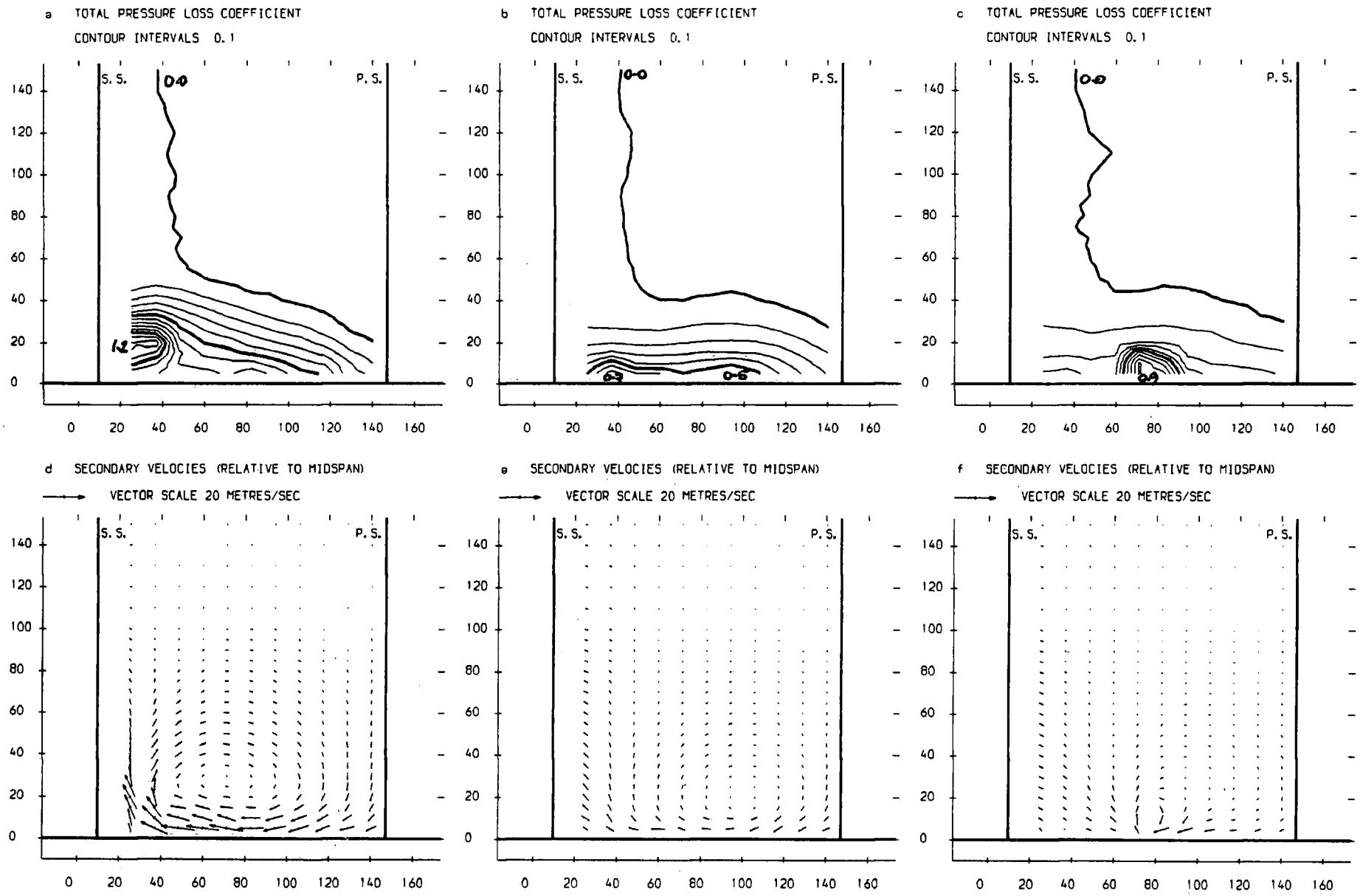

FIGURE 5.5(a-f) : Five-Hole Probe Results For Slot 3

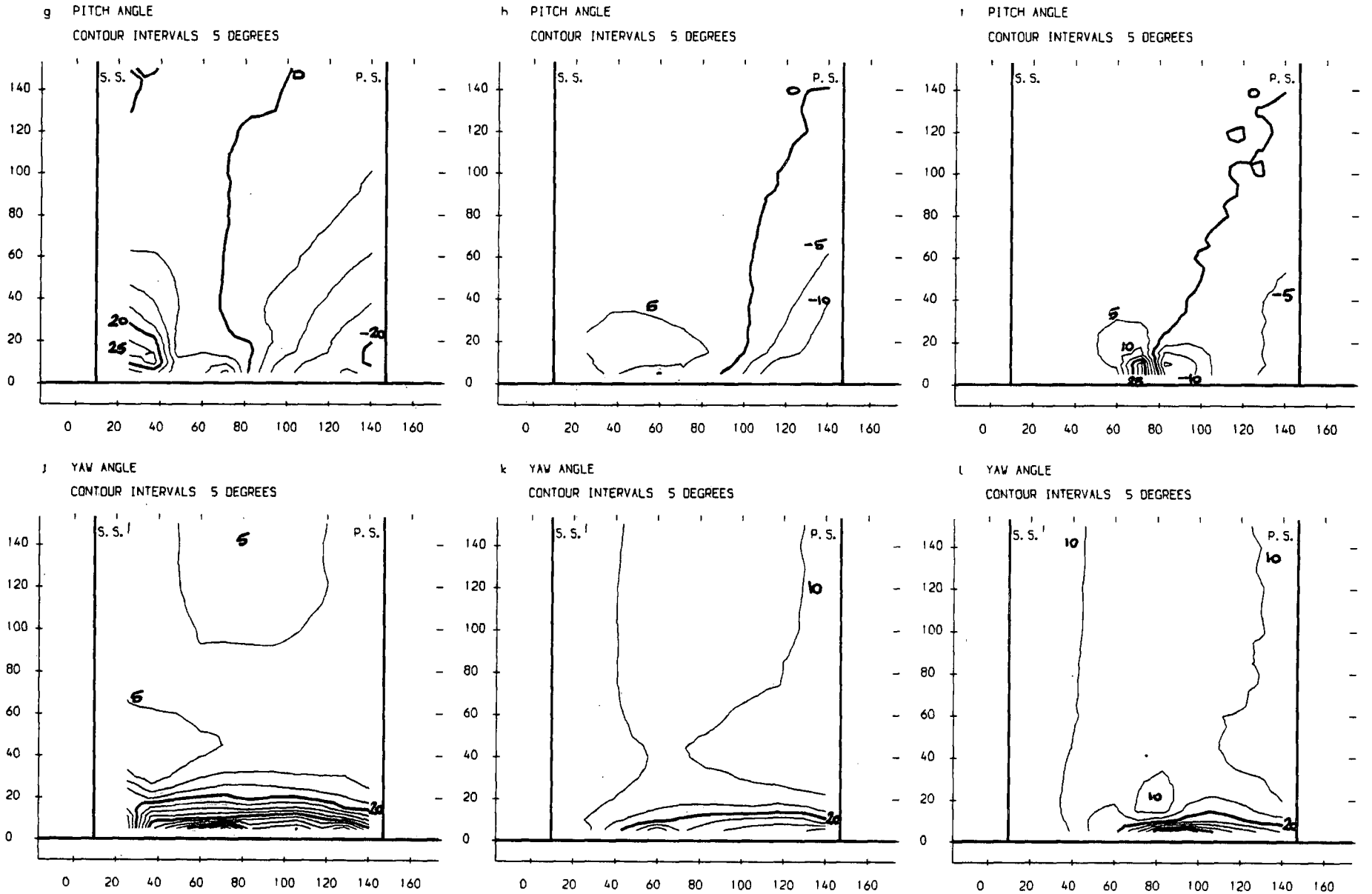

FIGURE 5.5(g-l): Five-Hole Probe Results For Slot 3

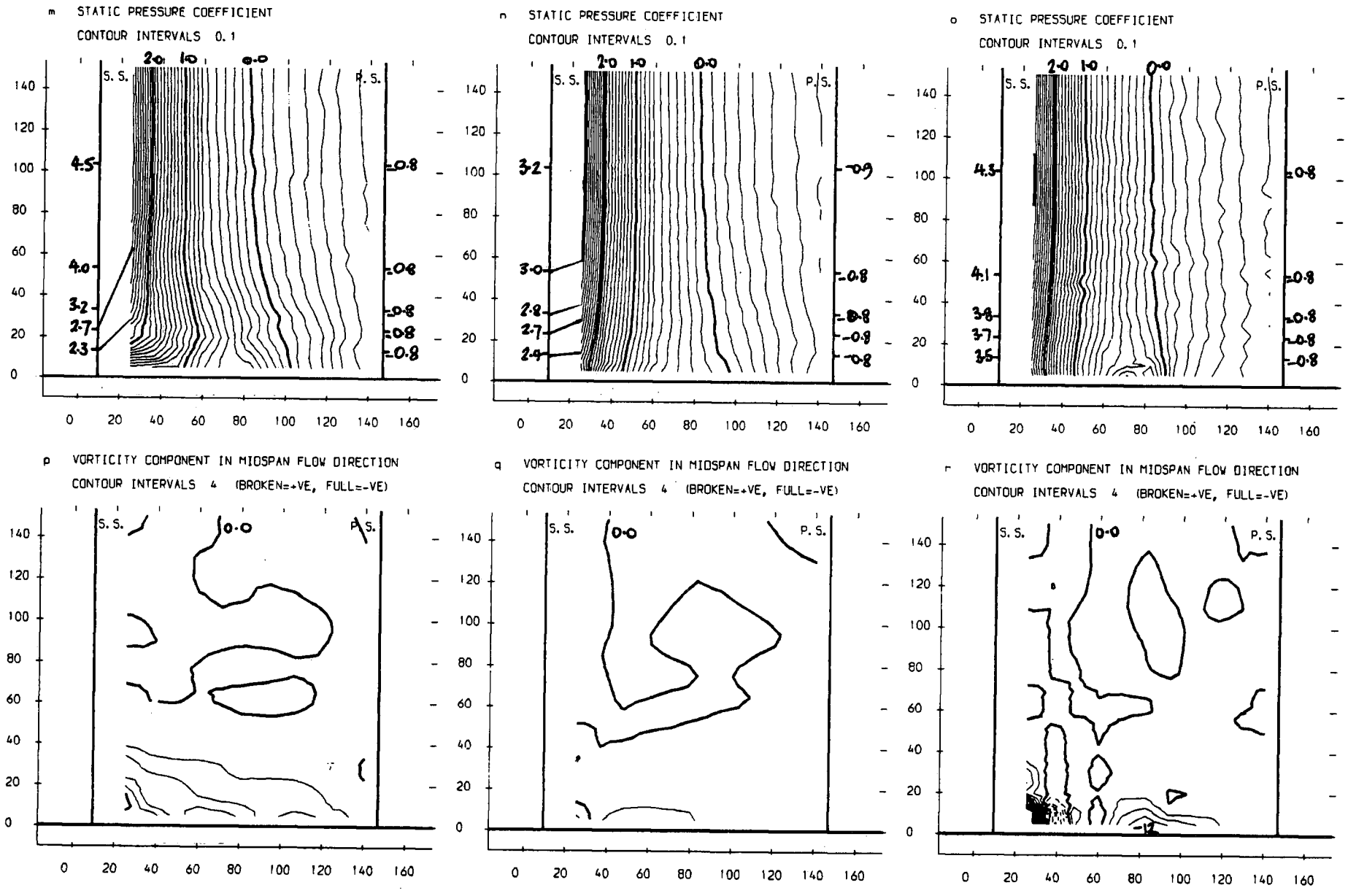

FIGURE 5.5(m-r): Five-Hole Probe Results For Slot 3

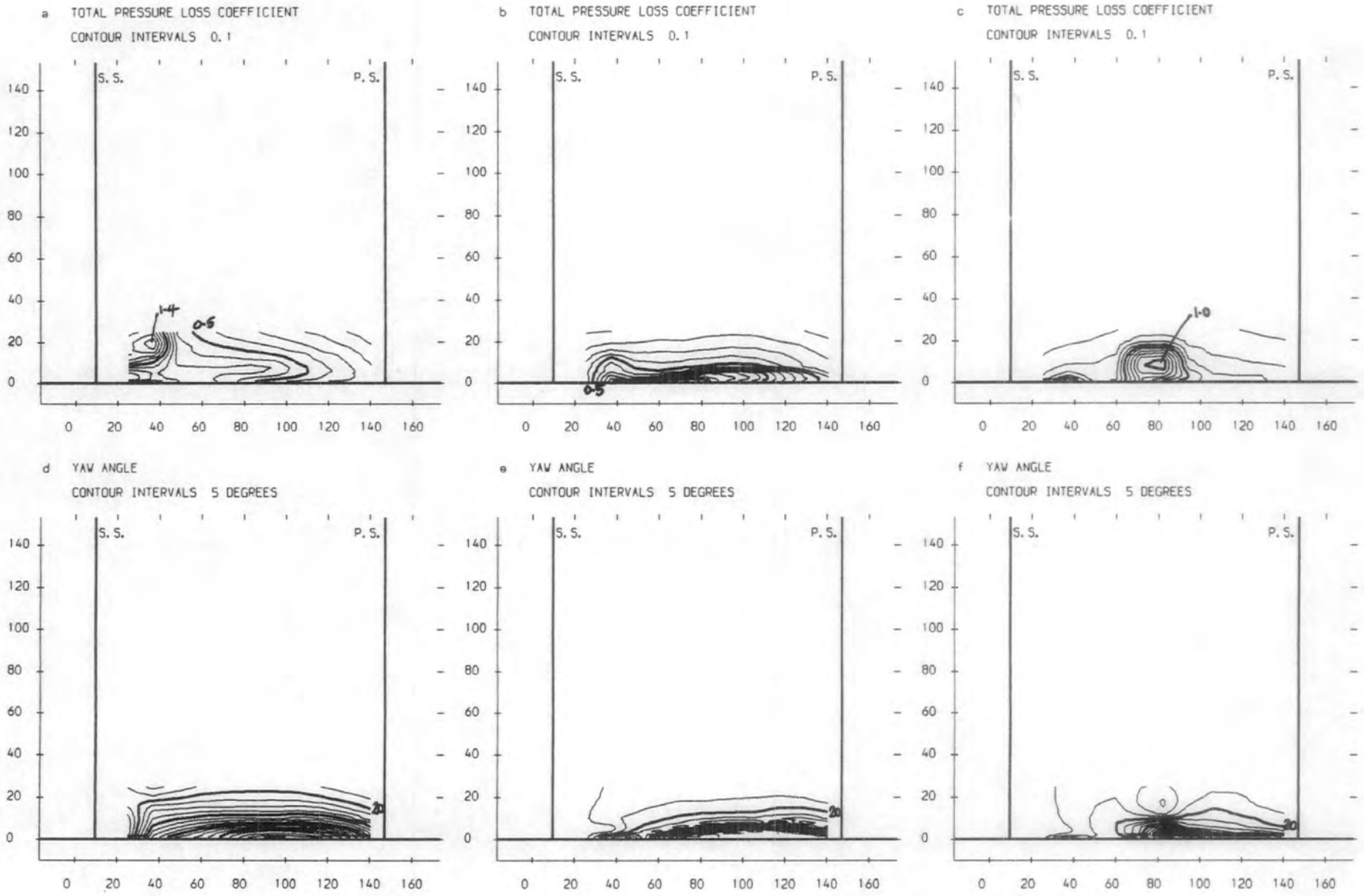

FIGURE 5.6(a-f): Three-Hole Probe Results For Slot 3

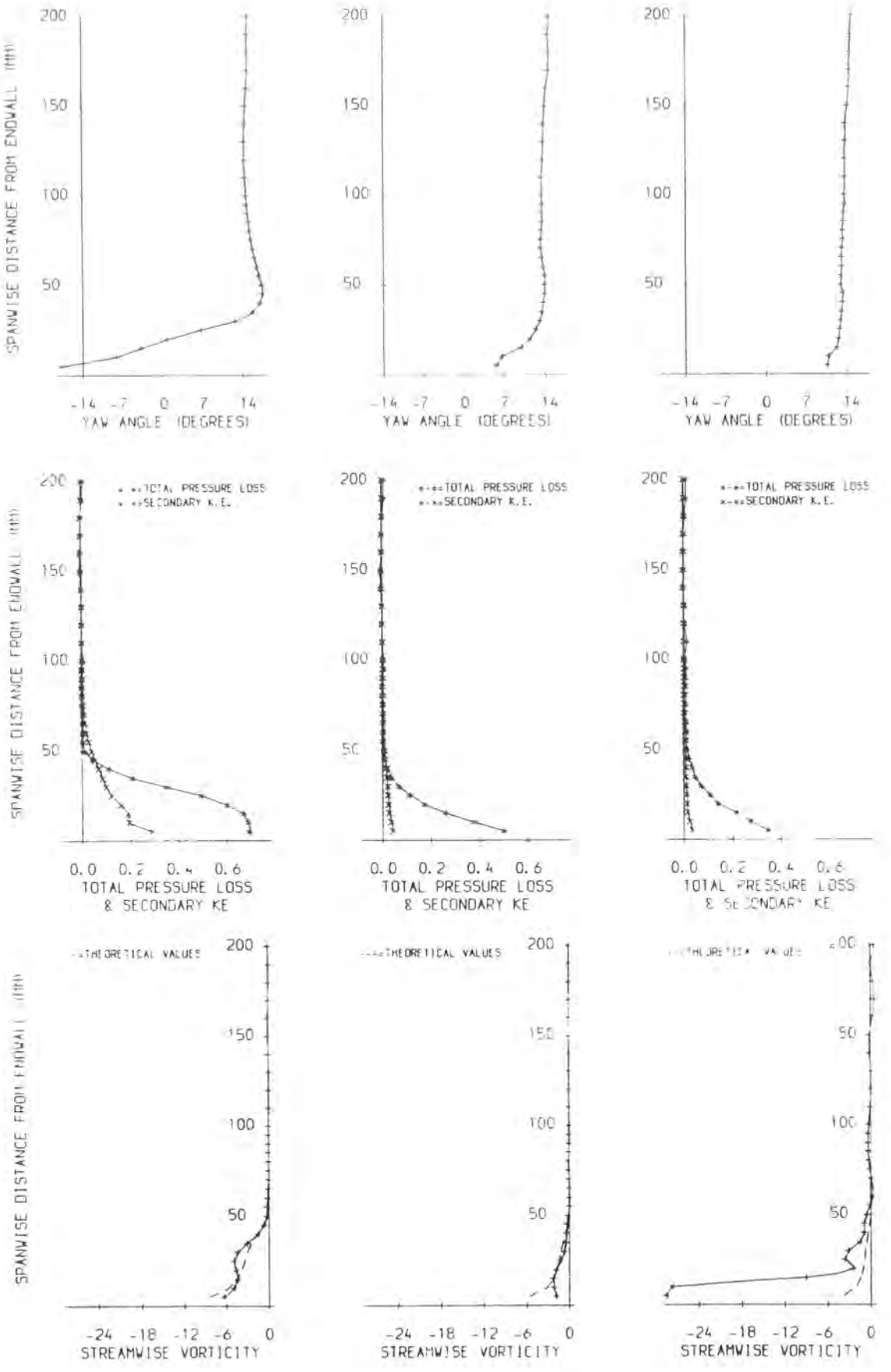

FIGURE 5.7, Pitch Averaged Results For Slot 3

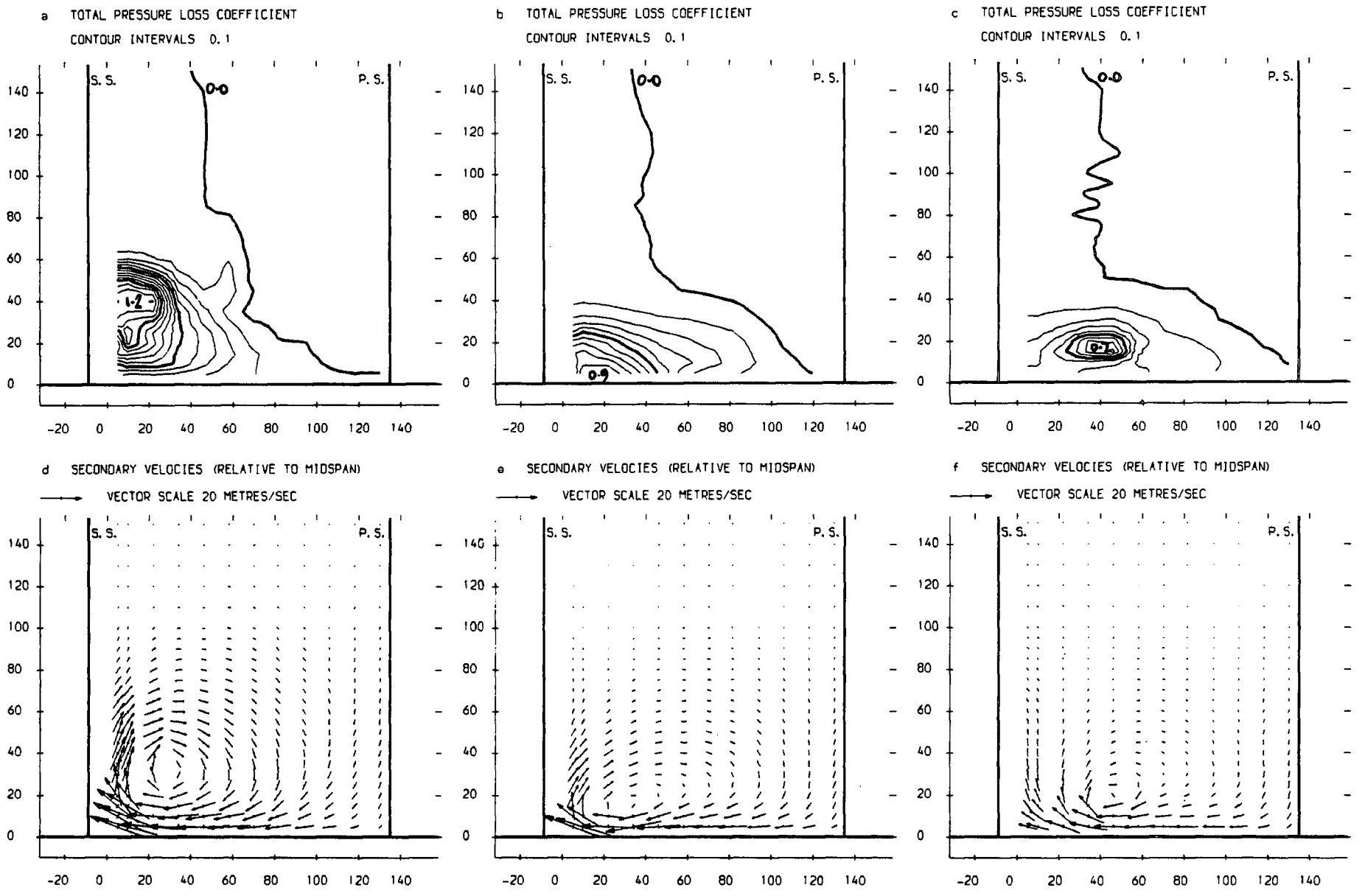

FIGURE 5.8(a-f): Five-Hole Probe Results For Slot 5

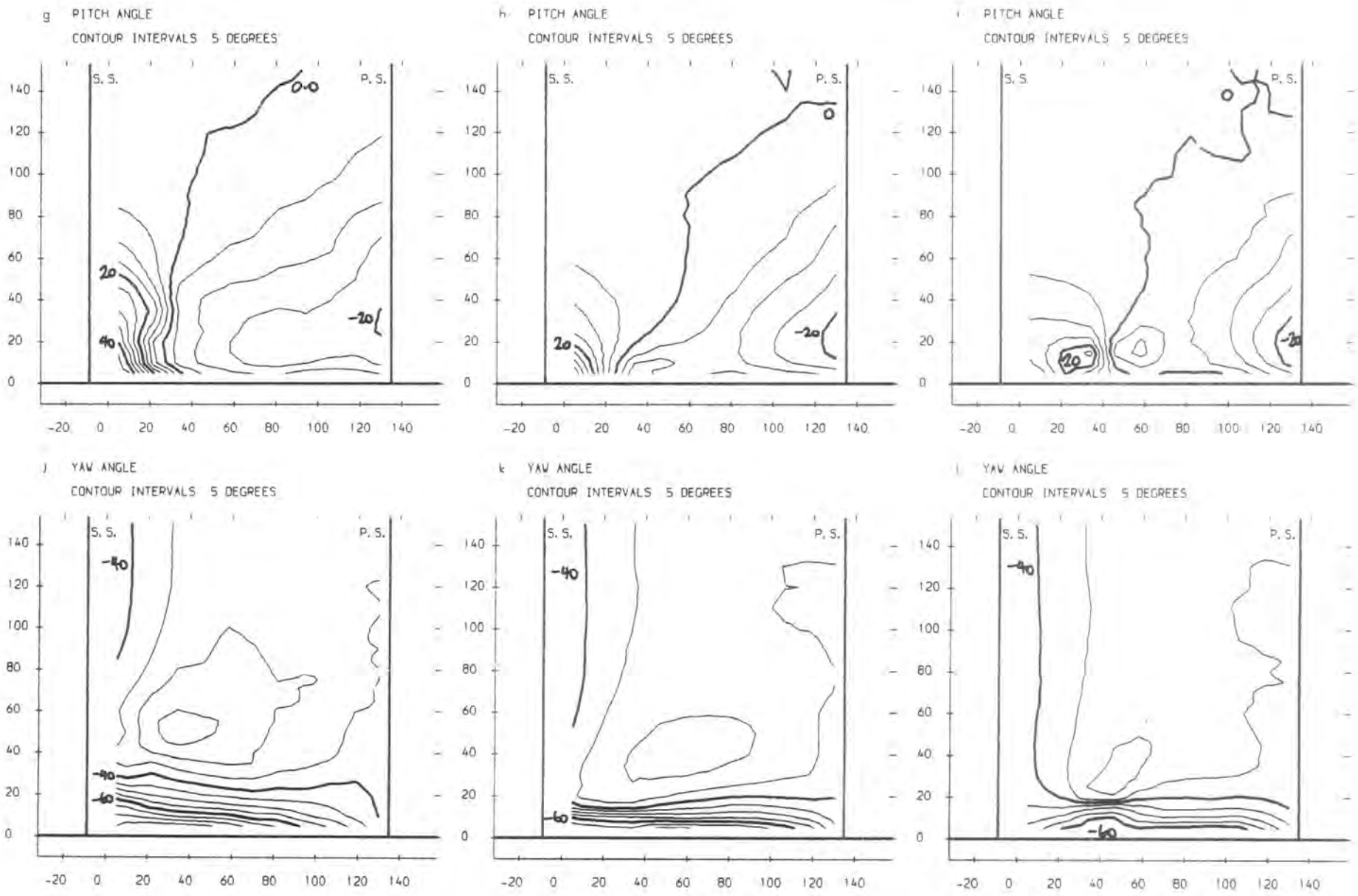

FIGURE 5.8(g-l): Five-Hole Probe Results For Slot 5

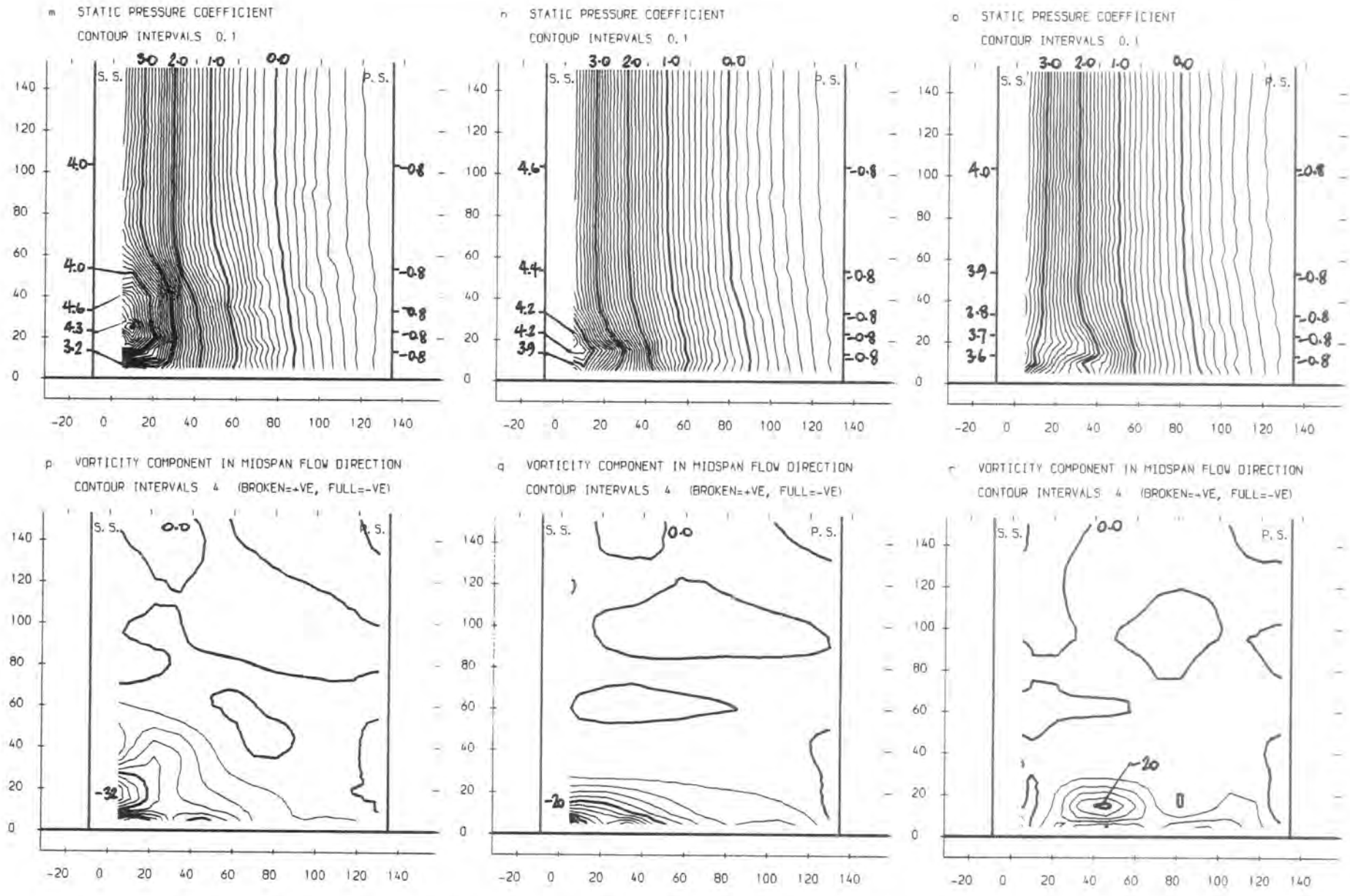

FIGURE 5.8(m-r) : Five-Hole Probe Results For Slot 5

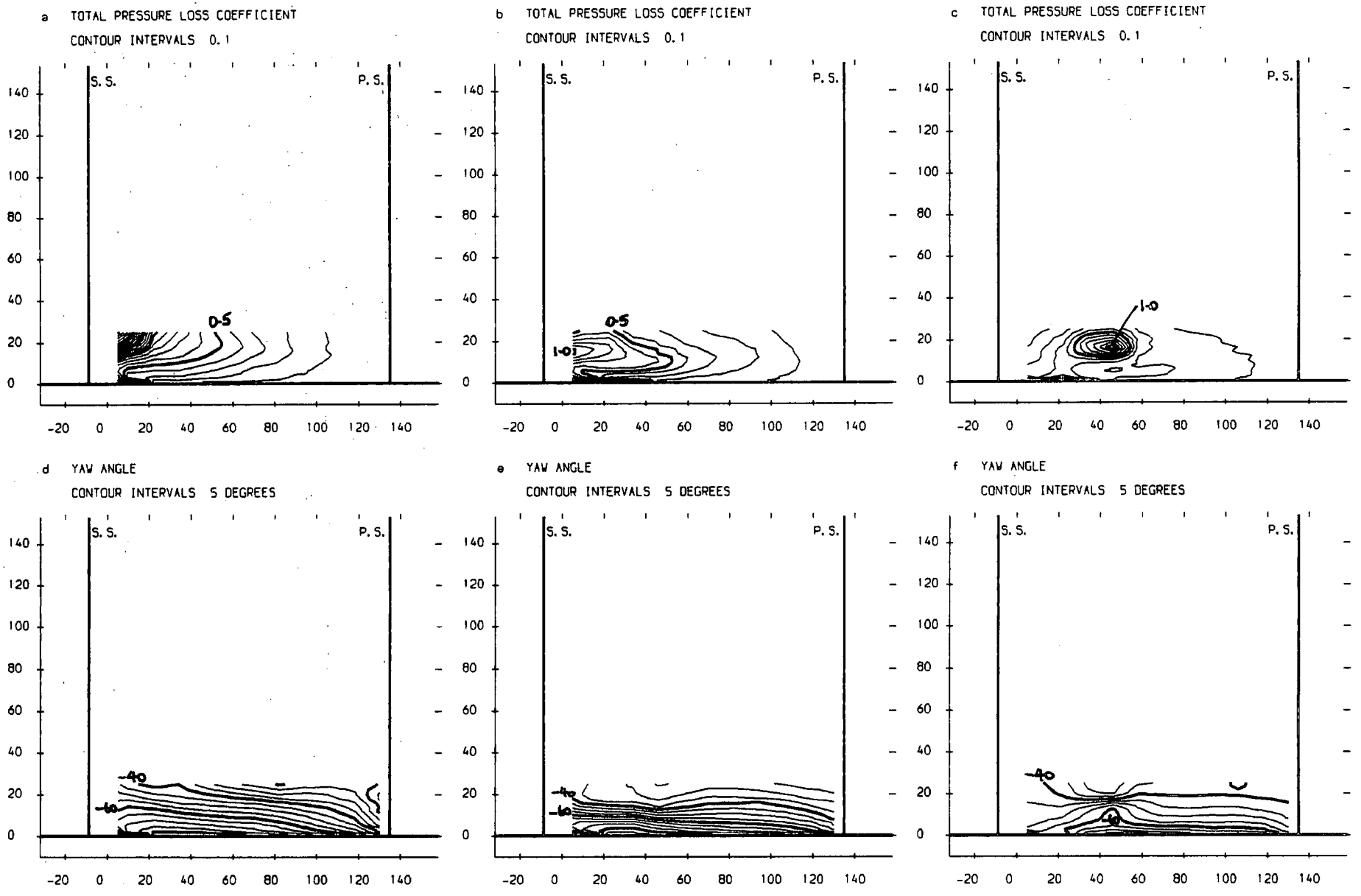

FIGURE 5.9 (a-f) : Three-Hole Probe Results For Slot 5

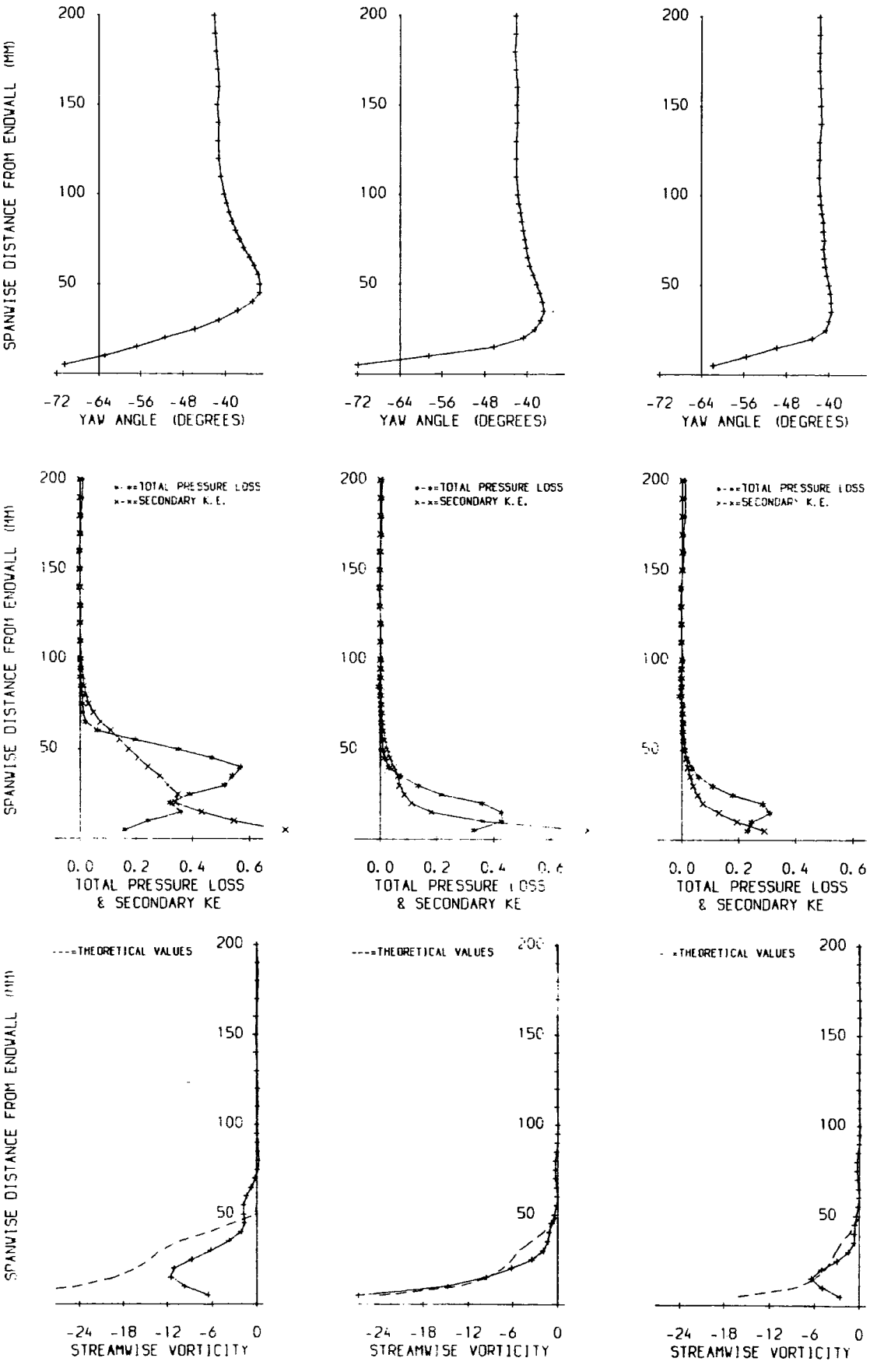

FIGURE 5.10: Pitch Averaged Results For Slot 5

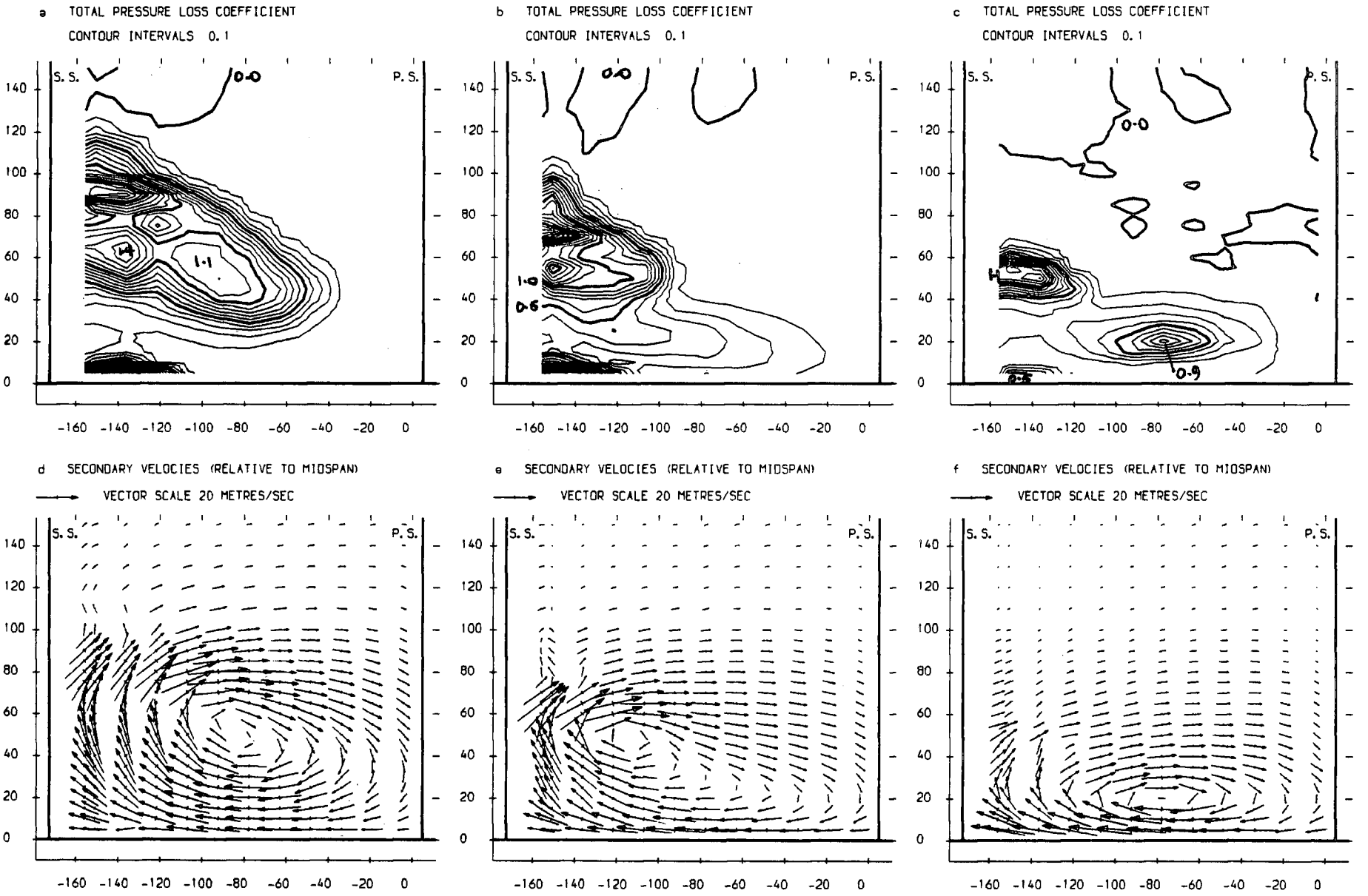

FIGURE 5.11(a-f): Five-Hole Probe Results For Slot 8

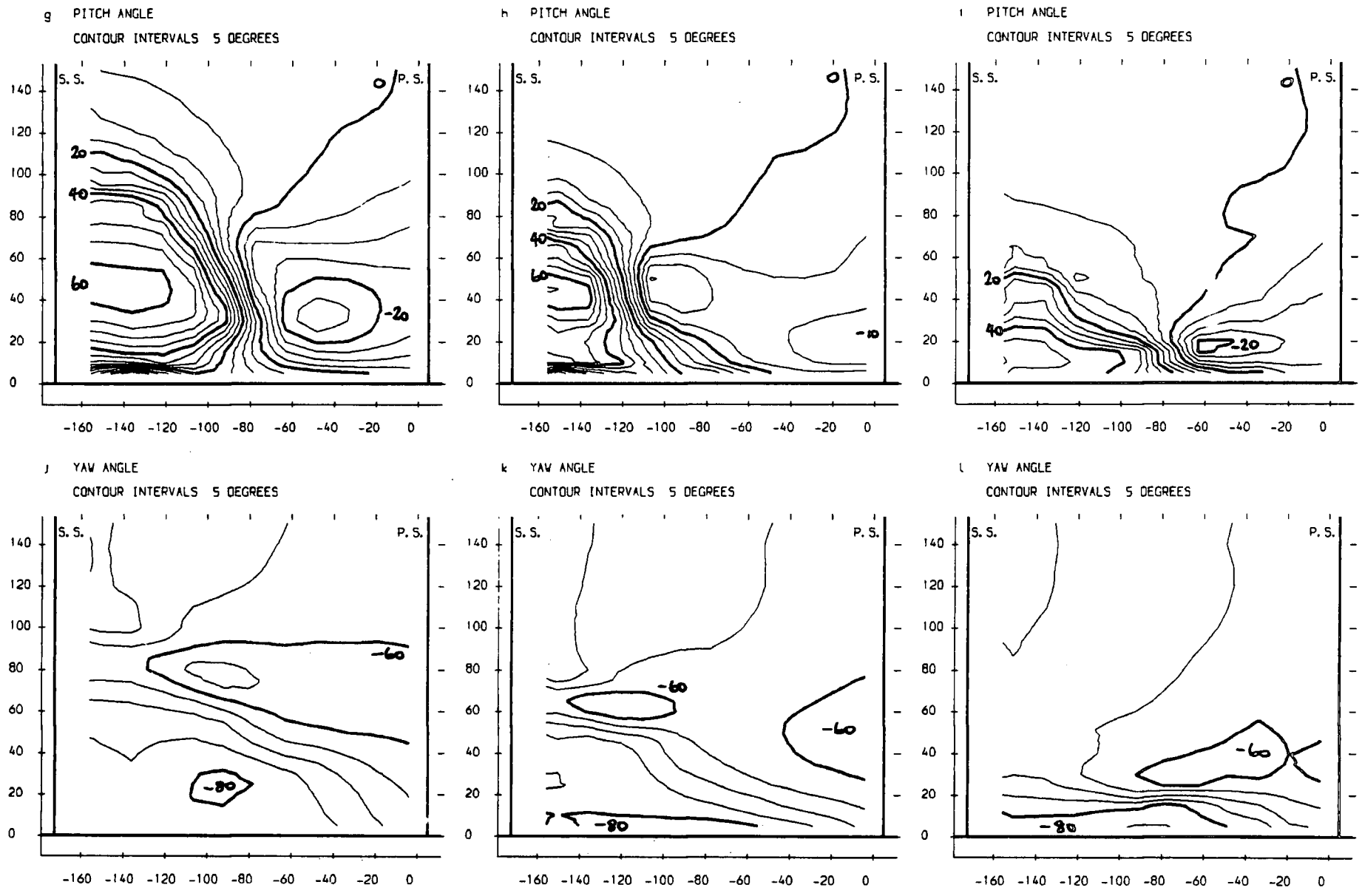

FIGURE 5.11(g-l): Five-Hole Probe Results For Slot 8

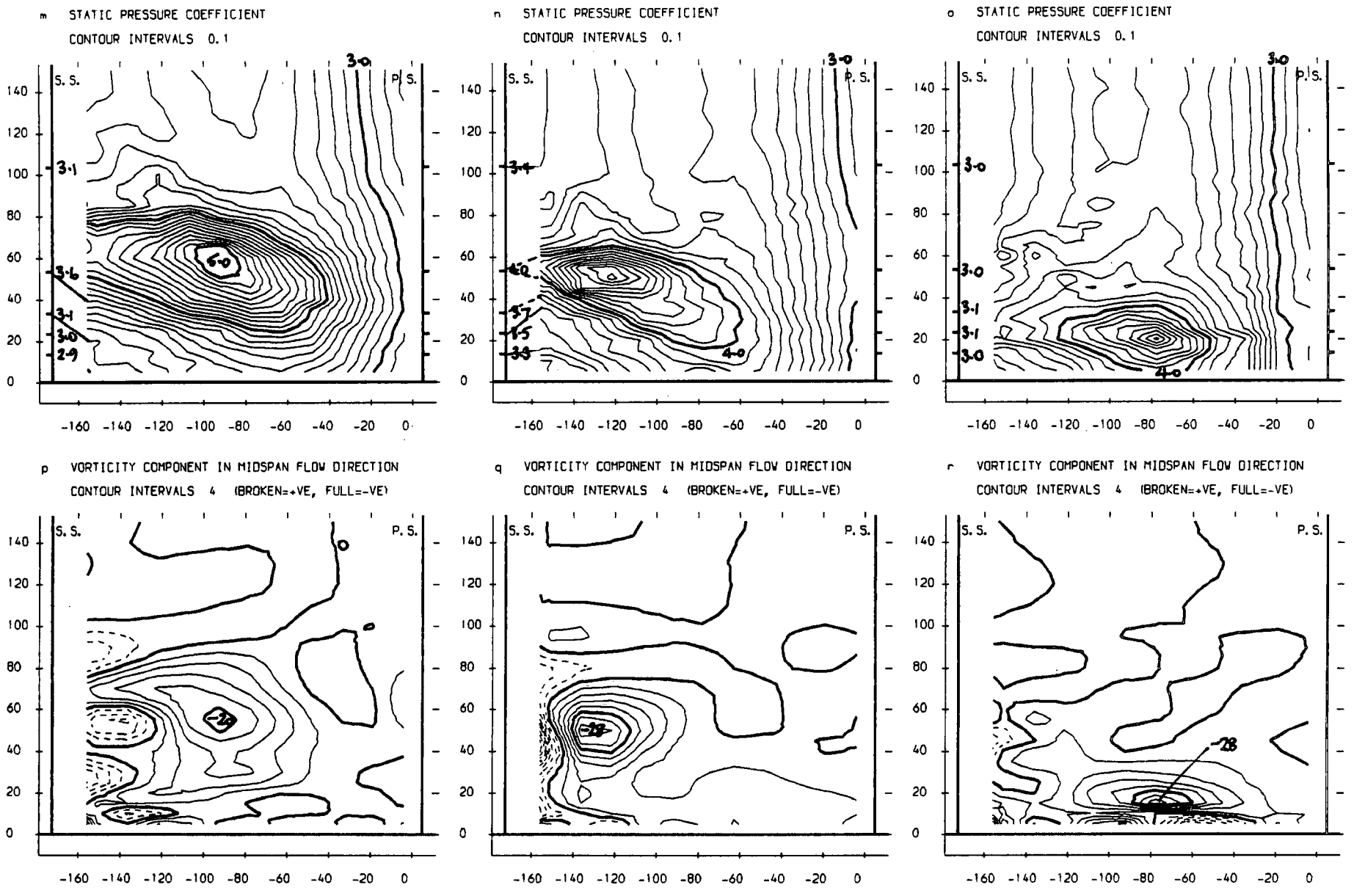

FIGURE 5.11 (m-r) : Five-Hole Probe Results For Slot 8

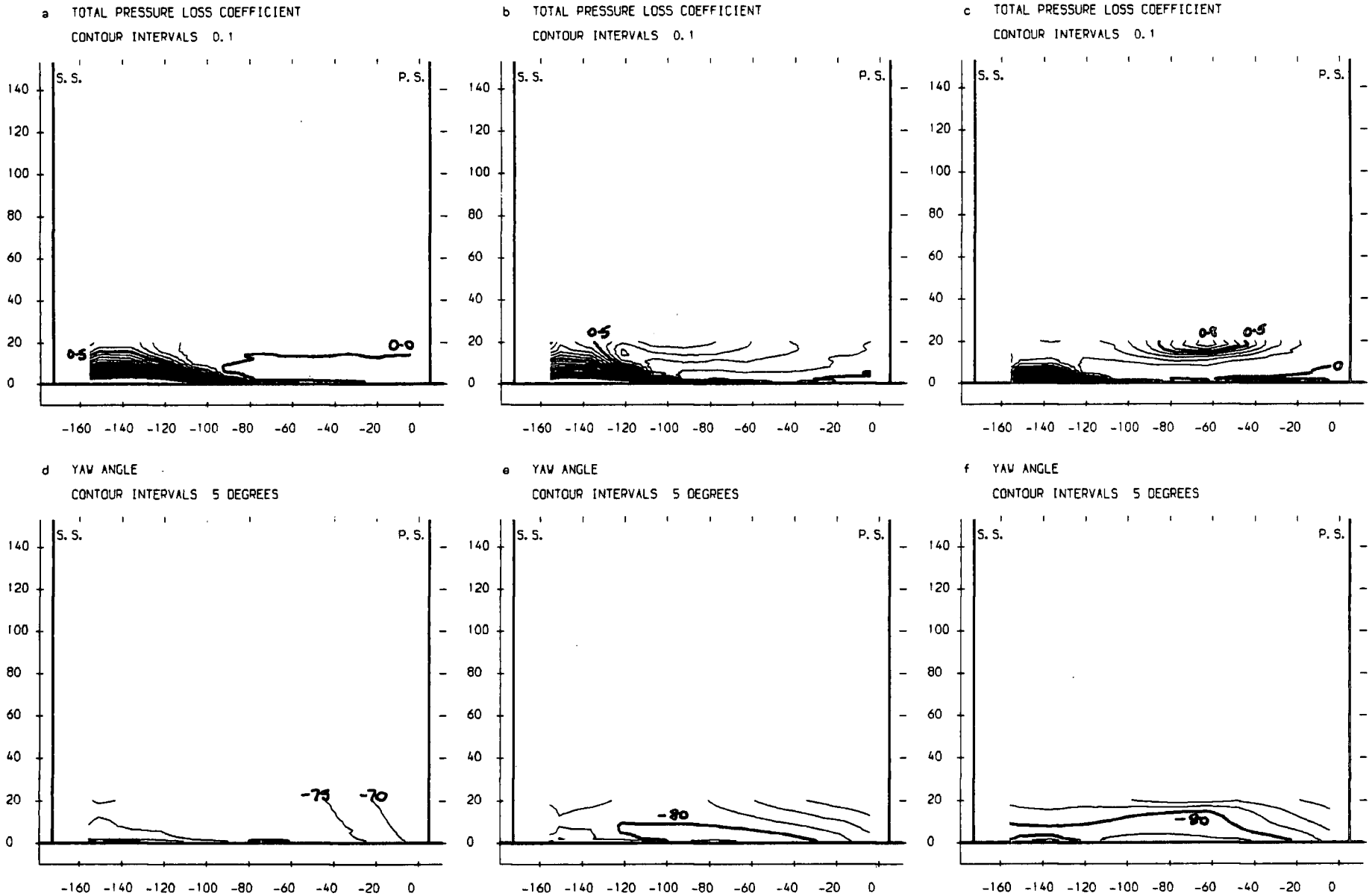

FIGURE 5.12(a-f): Three-Hole Probe Results For Slot 8

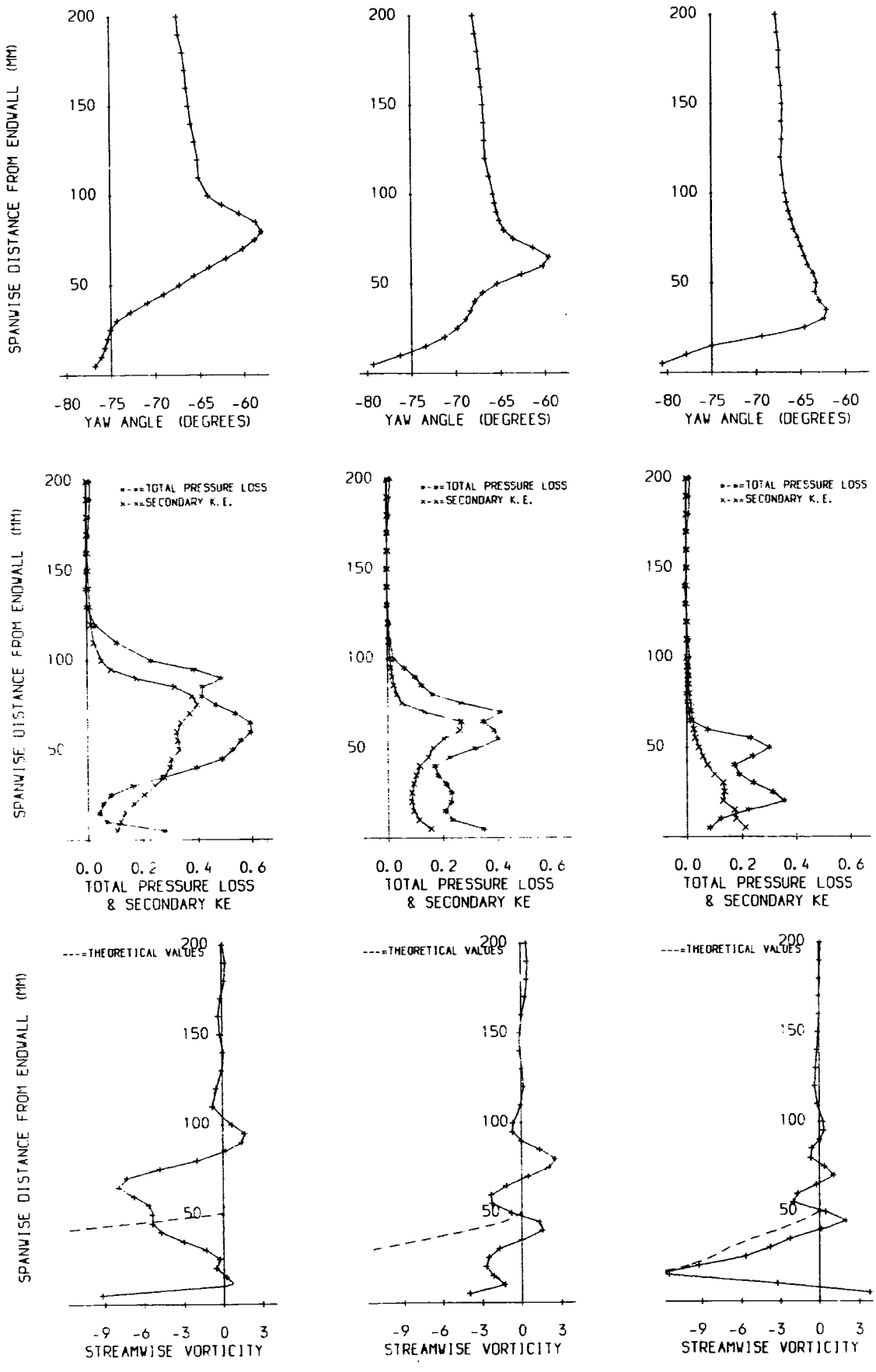

FIGURE 5.13: Pitch Averaged Results For Slot 8

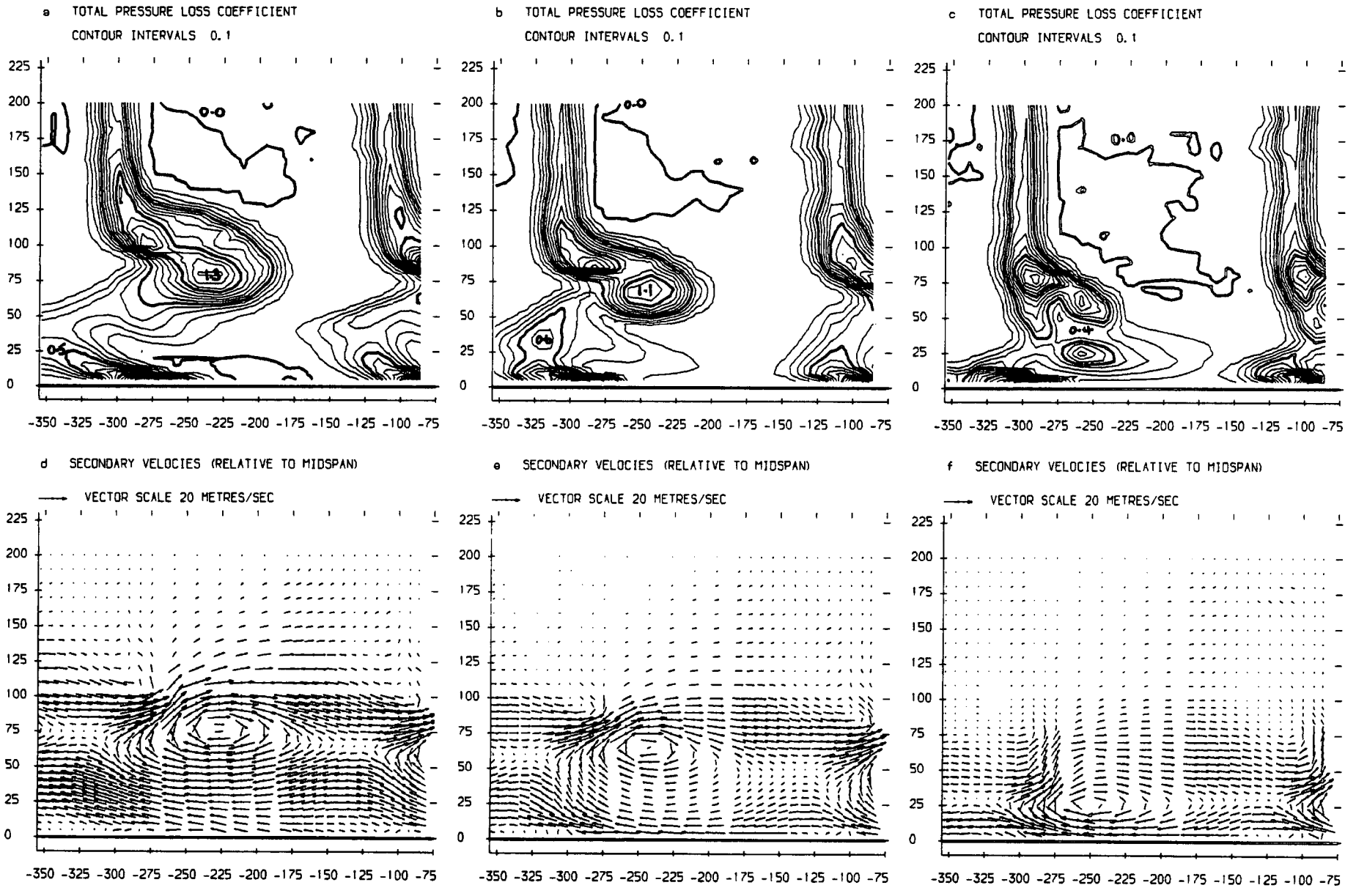

FIGURE 5.14(a-f): Five-Hole Probe Results For Slot 10

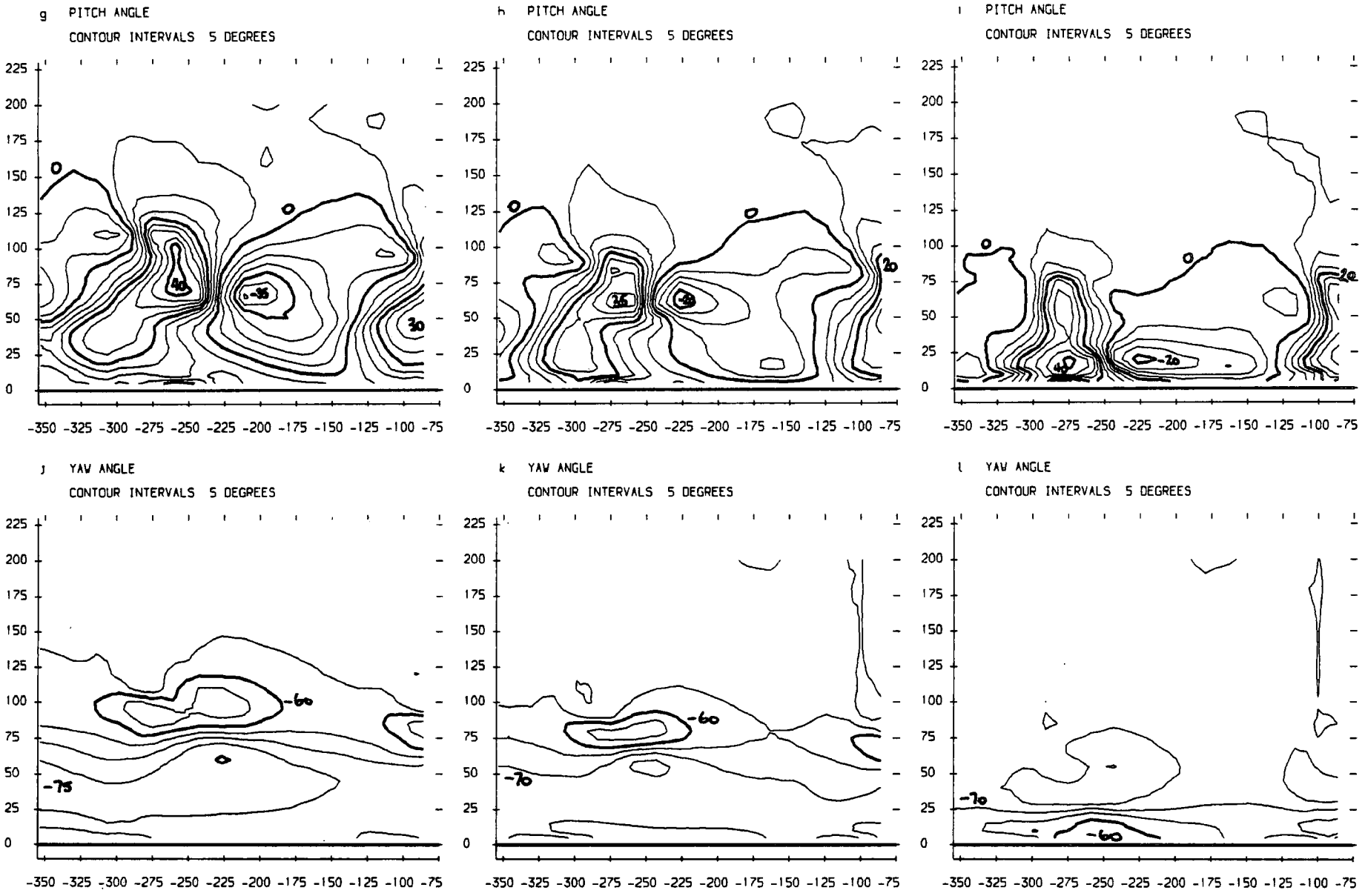

FIGURE 5.14 (g-l): Five-Hole Probe Results For Slot 10

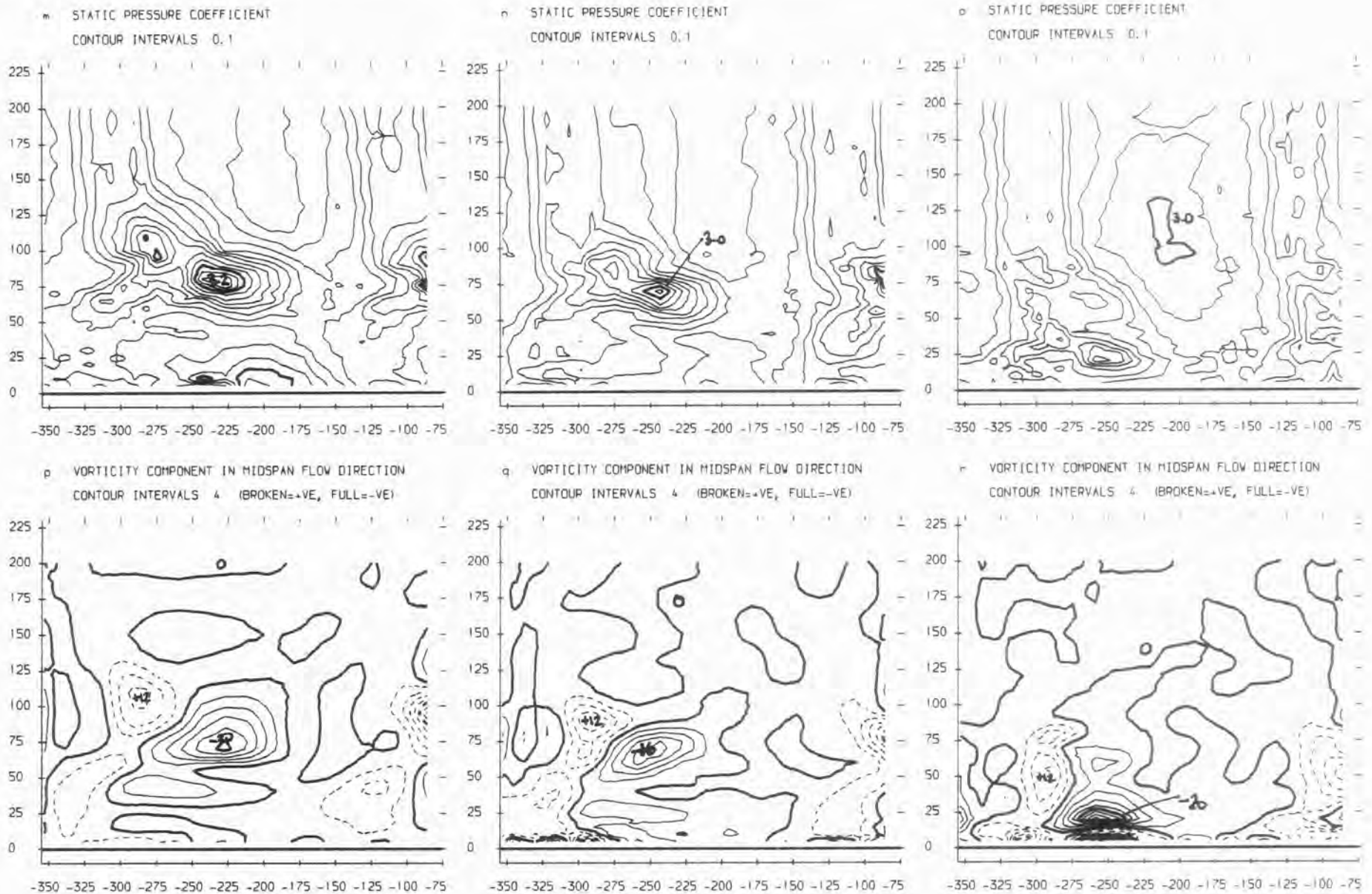

FIGURE 5.14(m-r) : Five-Hole Probe Results For Slot 10

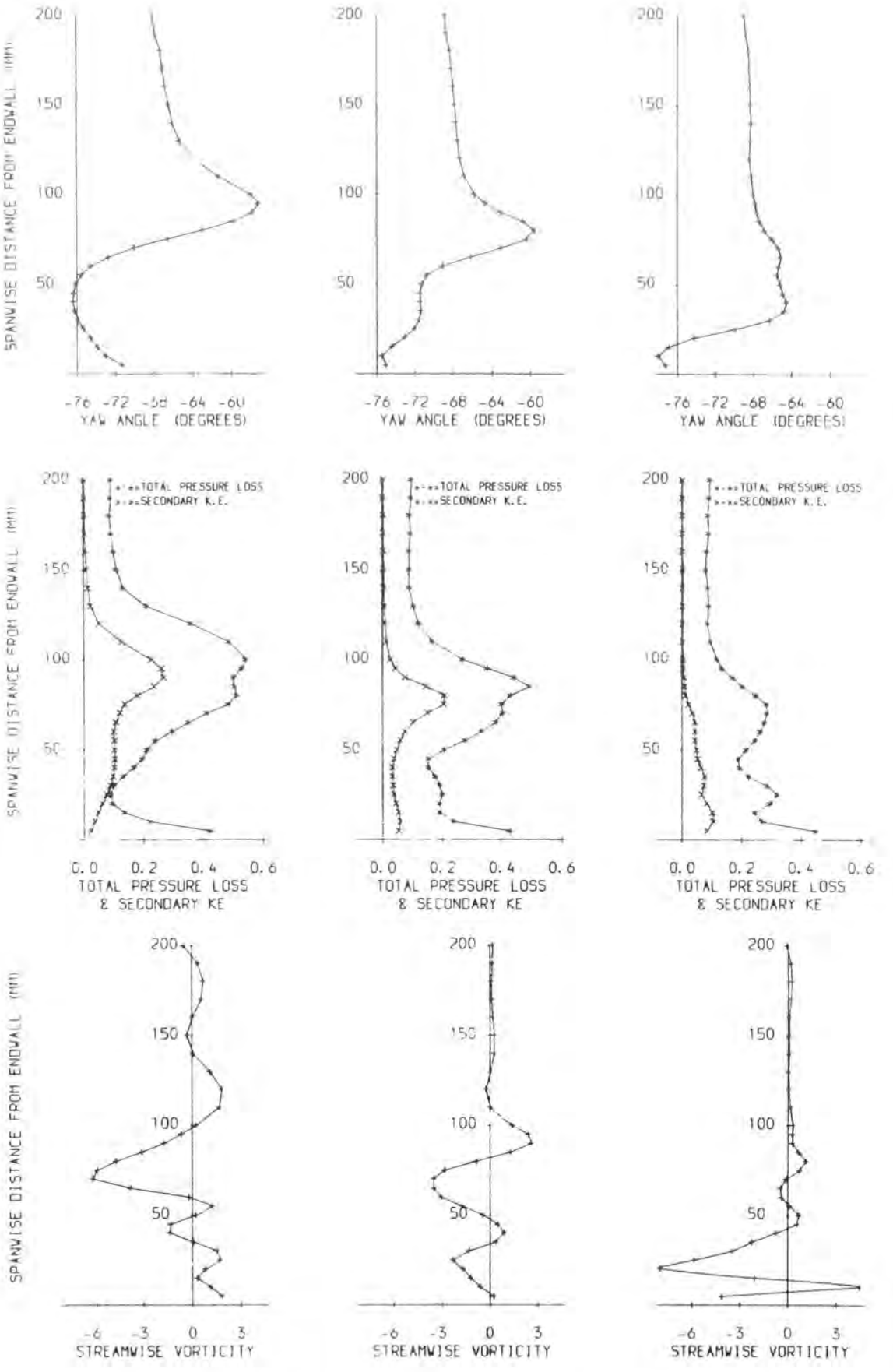

FIGURE 5.15: Pitch Averaged Results For Slot 10

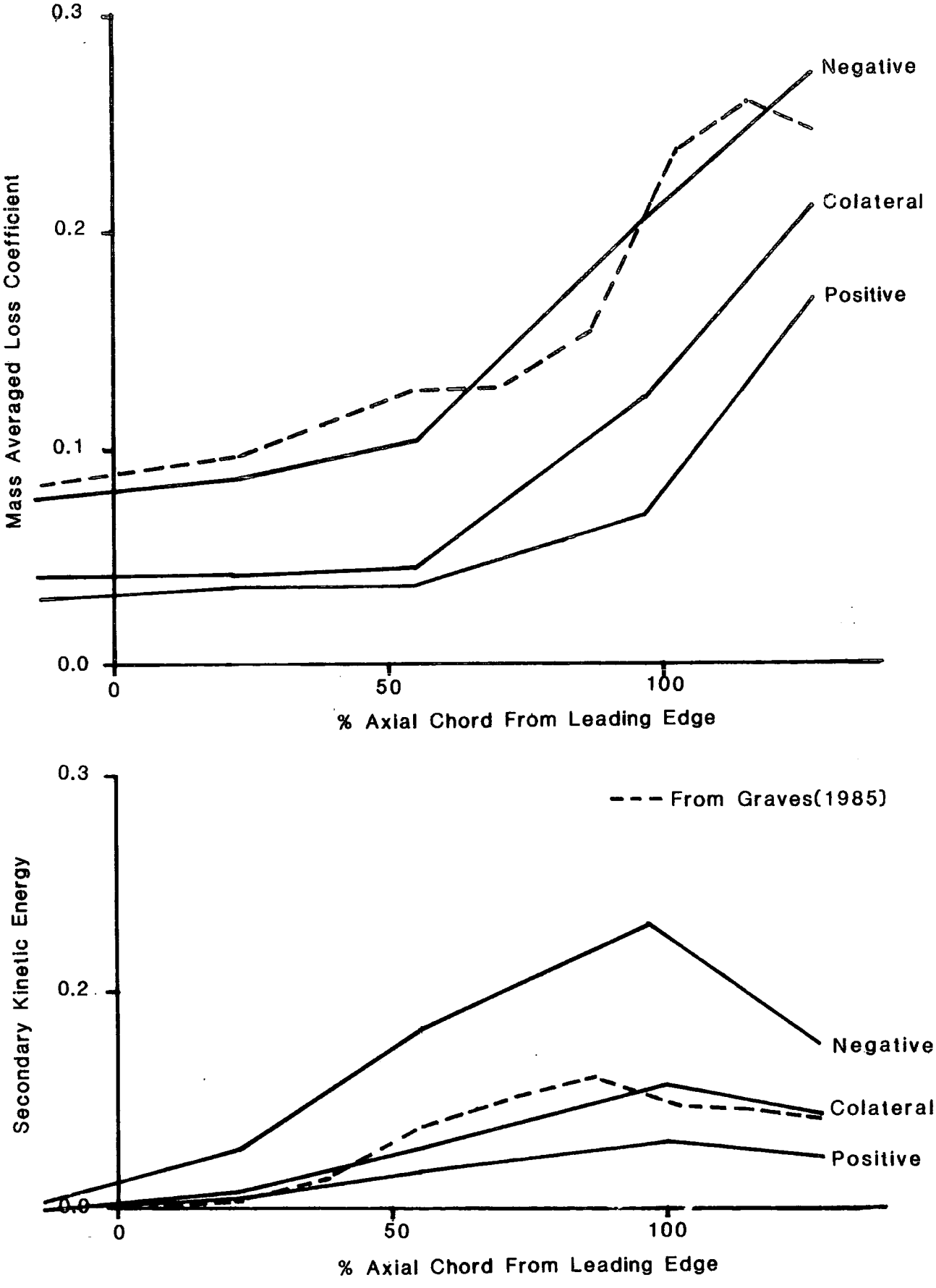

FIGURE 5.16: Development Of Loss

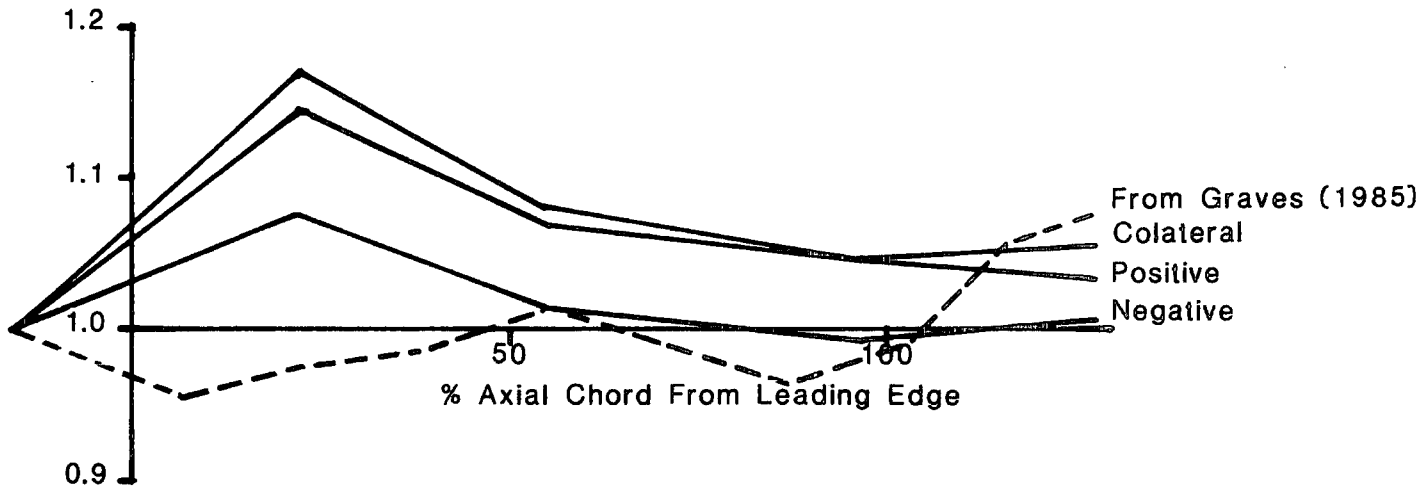

FIGURE 5.17: Normalised Mass Flow

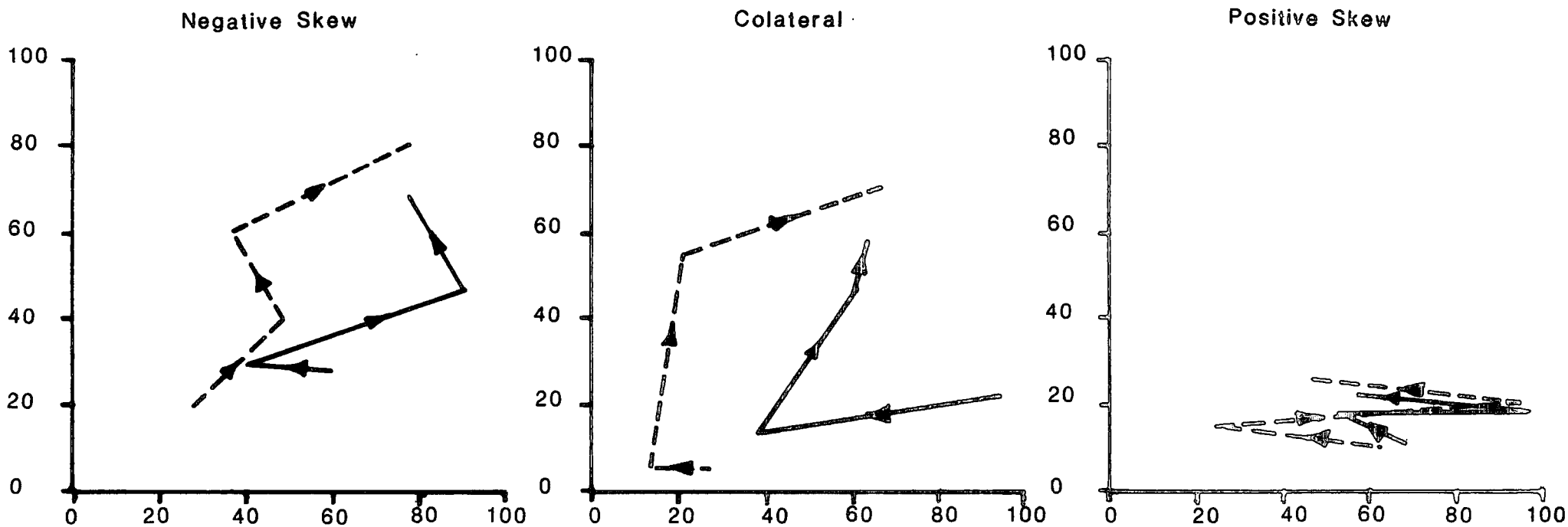

FIGURE 5.18: Passage Vortex Movement

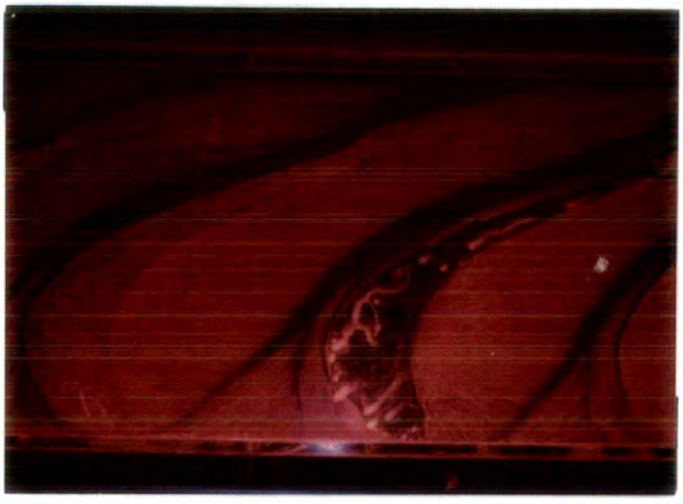

Negative Skew

Colateral

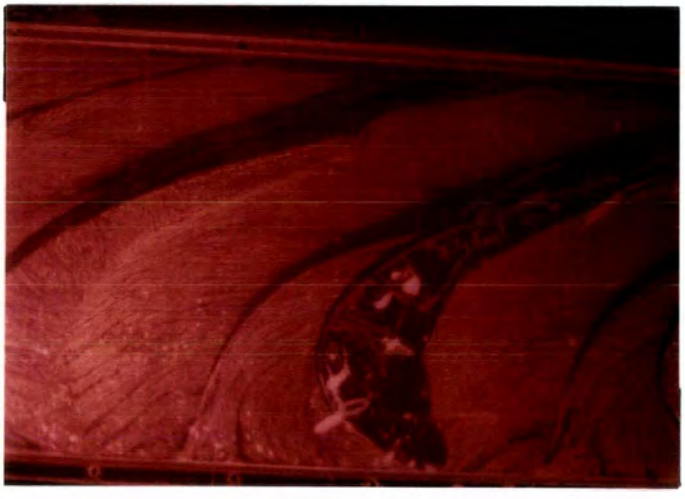

Positive Skew

FIGURE 5.19: Endwall Flow Visualisation Results

Negative Skew

Colateral

Positive Skew

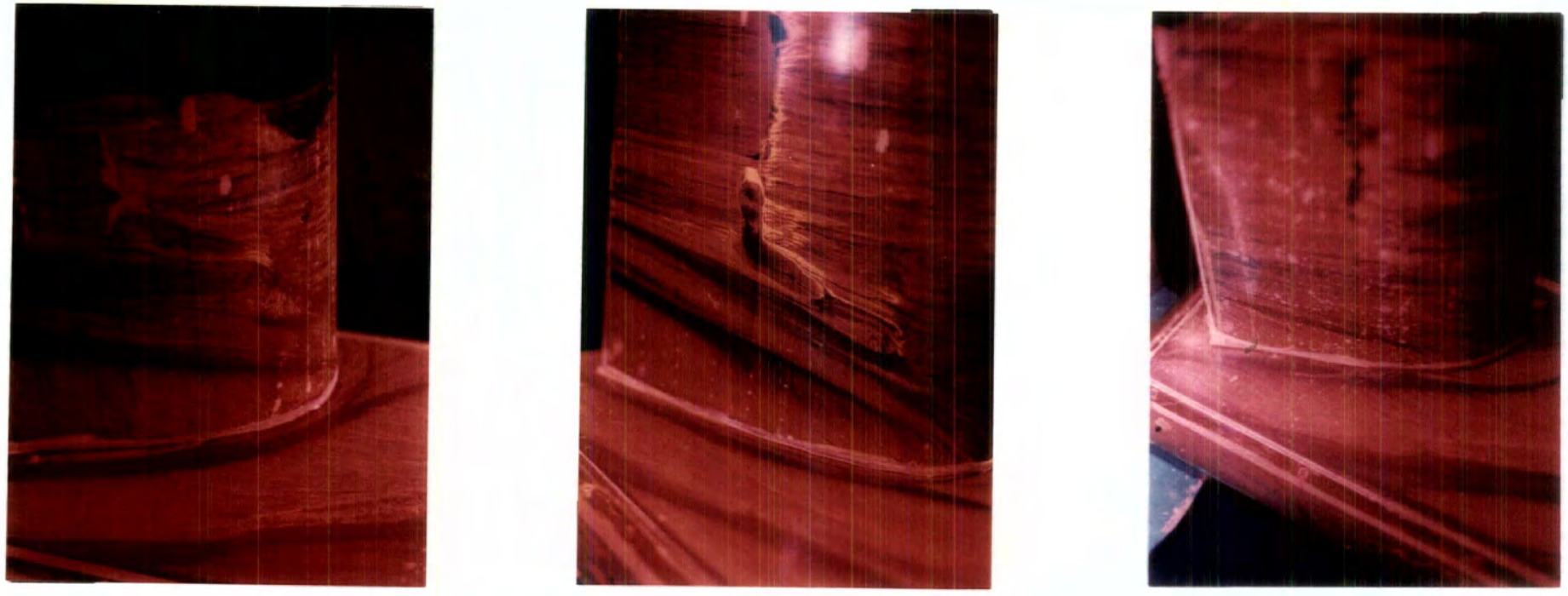

FIGURE 5.20: Suction Surface Flow Visualisation Results

X-Axis: % Axial Chord From Leading Edge
Y-Axis: Static Pressure Coefficient

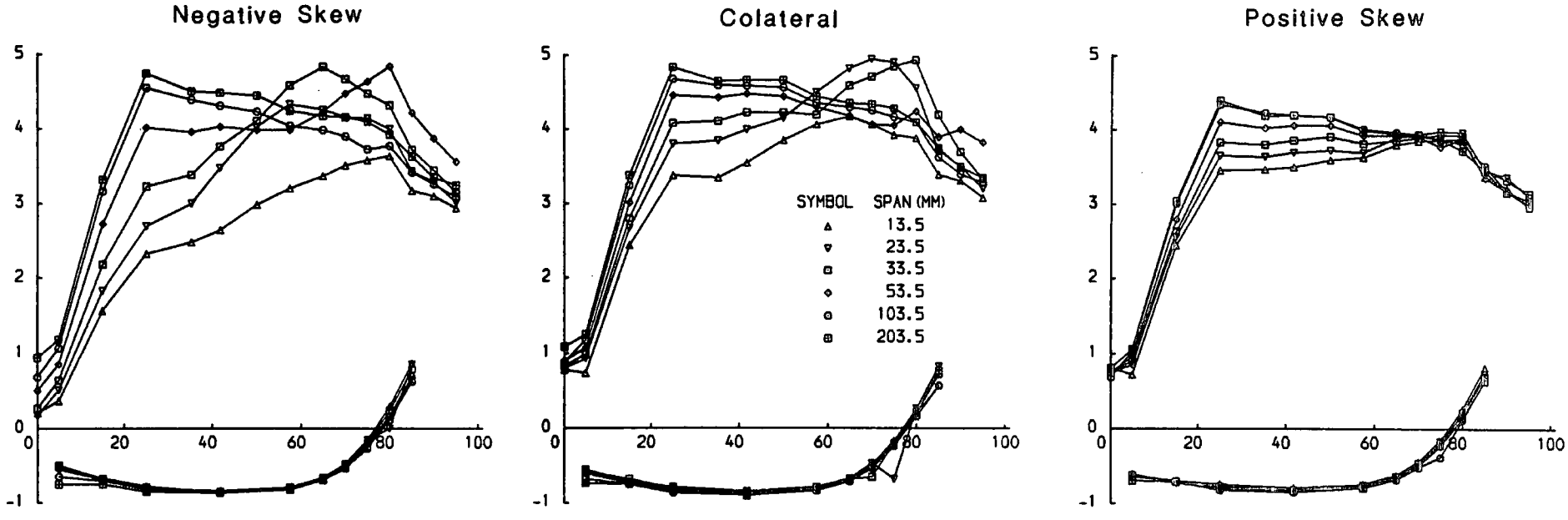

FIGURE 5.21: Static Pressure Coefficient

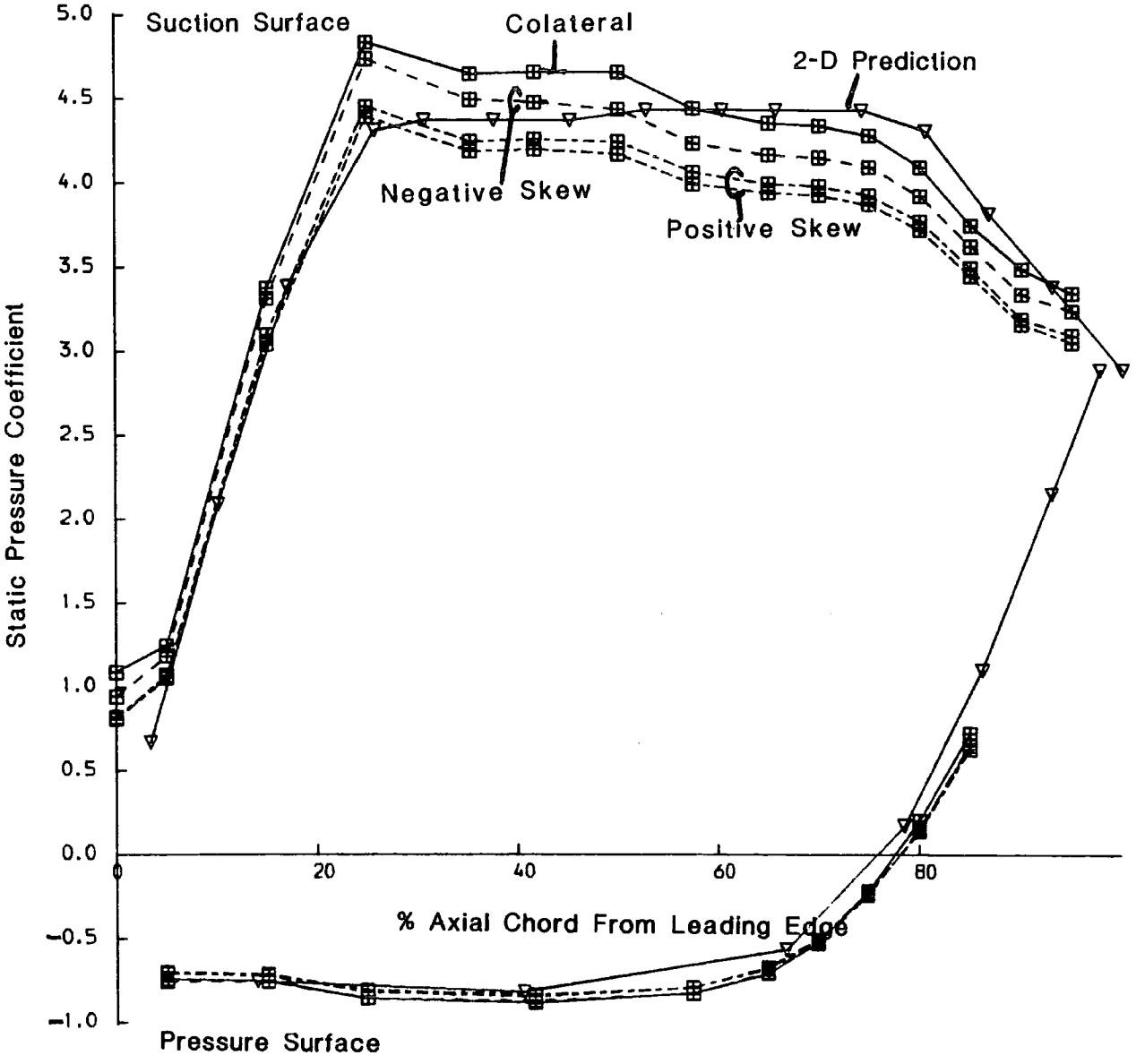

FIGURE 5.22: Midspan Static Pressure Coefficient

CHAPTER 6: MODELLING RESULTS

This chapter reviews the results that have been obtained using models of varying complexity for the JAW cascade. The results were obtained using loss correlations, a theoretical secondary flow model, an inviscid 3-D timemarching model, and a viscous 3-D model.

6.1 SECONDARY LOSS CORRELATIONS

In Chapter 2 reference was made to a number of correlations for the prediction of secondary losses in a cascade. These correlations have been used to calculate the secondary losses for the JAW cascade and the results are given in Table 6.1. In the cases of Dunham (1970) and Dunham and Came (1970) it was assumed that the correlations were for the net secondary loss. The values in Table 6.1 are for the gross secondary loss and where appropriate the correlation was corrected by adding on the inlet loss. The values of inlet boundary layer displacement thickness and momentum thickness were taken from the experimental results for the case of flow relative to the cascade in Table 5.1. Also shown in Table 6.1 are the experimental values for the gross secondary loss taken from Table 5.2.

TABLE 6.1: GROSS SECONDARY LOSS CORRELATIONS

SOURCE	INLET SKEW TYPE		
	NEGATIVE	COLATERAL	POSITIVE
Dunham (1970)	0.130	0.082	0.069
Dunham and Came (1970)	0.151	0.116	0.104
Came (1973)	0.097	0.056	0.049
Morris and Hoare (1975)	0.061	0.042	0.039
Chen and Dixon (1986)	0.095	0.057	0.046
Experimental	0.256	0.147	0.096

These correlations are clearly unable to predict accurately the magnitude of secondary loss for even the baseline case of a colateral inlet flow. In the case of Chen and Dixon (1986) there was no difference between the results obtained using the experimental value for the momentum thickness and the results obtained using their empirical relationship for momentum thickness. It was also found that the downstream distance of the measurement plane had a minimal effect on the value of loss obtained with their correlation. There was a surprising level of agreement between the Chen and Dixon correlation and the Came (1973) correlation. However these correlations gave the worst prediction. In general none of the correlations was able to predict the correct values of loss or even the correct relative change in loss due to the presence of inlet skew. This clearly indicates that all of the correlations need to be applied with caution and should not play an important part in the design process.

6.2 SECONDARY FLOW MODELLING

The gross secondary losses have been modelled using the relatively simple method of Gregory-Smith (1982) that was briefly described in Chapter 2. The secondary losses are assumed to consist of three separate components; a loss core formed from the upstream boundary layer, a loss associated with the growth of a new endwall boundary layer formed downstream of the cross-passage separation line, and an extra secondary loss. The extra secondary loss component was assumed by Gregory-Smith to be proportional to the secondary kinetic energy with a constant of proportionality of unity. However Graves (1985) found that this extra secondary loss more often than not accounted for a major proportion of the total predicted secondary loss. It was suggested that the tangential components of the secondary velocities may produce an incidence variation onto the following blade row and consequently produce a useful contribution to the work done. However, the spanwise components of the secondary velocities could be assumed equal to the extra secondary loss generated. It was therefore assumed that the extra secondary loss was proportional to the kinetic energy of the spanwise velocity component with a constant of proportionality of unity.

The data that was used as the basis for the modelling was that for the colateral case of Chapter 5. The effect of skew on

the inlet flow angle and velocity distribution was calculated with reference to the velocity triangle (Figure 3.6). For the redistribution of the inlet boundary layer the effect of skew on the boundary layer thicknesses was calculated by assuming, in addition to the usual power law assumption, that the displacement thickness remained unchanged.

The results obtained using the model are tabulated below. The extra secondary loss has been calculated using a power law assumption for the velocity profile (PL), and also using the experimental velocity profile.

TABLE 6.2: SECONDARY FLOW MODEL RESULTS

	INLET SKEW TYPE		
	NEGATIVE	COLATERAL	POSITIVE
Loss Core	0.0594	0.0361	0.0187
New Boundary Layer	0.0046	0.0046	0.0046
Extra Sec Loss	0.5001	0.1113	0.0208
Extra Sec Loss (PL)	0.4526	0.1008	0.0188
Total Loss	0.5641	0.1520	0.0441
Total Loss (PL)	0.5166	0.1415	0.0421
Experimental (Slot 8)	0.1979	0.1183	0.0641

It can be seen that the loss is overpredicted in the colateral and negative skew cases and underpredicted for the positive skew case. The main contribution to the error in the results is probably the error in the prediction of the secondary kinetic energy. The table below compares the experimental and predicted values

TABLE 6.3: SECONDARY KINETIC ENERGY

	INLET SKEW TYPE		
	NEGATIVE	COLATERAL	POSITIVE
Predicted	1.239	0.288	0.054
Predicted (PL)	1.202	0.268	0.050
Experimental (Slot 8)	0.130	0.056	0.029

There is clearly an overprediction of the secondary kinetic energy in all of the skew cases.

The model also calculated the distribution of exit angle using classical secondary flow theory. The distributions are plotted in Figure 6.1 along with the corresponding pitch averaged experimental results. It can be seen that the best agreement was obtained in the case of positive skew where the secondary flows were the smallest. The worst agreement was obtained in the case of negative skew where the secondary flows were largest. Classical secondary flow theory was also used to calculate the distribution of streamwise vorticity within the cascade. These results are presented with the corresponding pitch averaged experimental results in Chapter 5. It can be seen that early in the cascade, up to Slot 5 (Figure 5.10), reasonably good results were obtained for the colateral case. The results were worse at Slot 8 (Figure 5.13) due to the presence of large secondary flows. The same comment also applies to the case of negative skew except that the earlier development of the strong secondary flows means that the agreement is worse at slot 5. The case of positive skew shows improvement in agreement on progression though the cascade due to the reduction in prominence of the endwall effects.

Another application of secondary flow theory that was described in Chapter 2 was the prediction of the increase in streamwise vorticity due to the presence of skew using a modified form of Kingcombe's formula. The formula predicts a ratio of 1.10:1:0.82 for the ratio of streamwise vorticity at exit in the skew cases negative:colateral:positive. The area averaged experimental results for Slot 8 give the ratio 5.15:1:2.13. The disagreement is probably due to the presence of shear and large secondary flows.

6.3 THREE-DIMENSIONAL INVISCID MODELLING

It had been intended to present results obtained by modelling the JAW flowfield with the timemarching code of Denton (1983) that has been briefly described in Chapter 2. The aim was to identify the important inviscid effects present in the flowfield with and without the presence of inlet skew. However it was not possible to obtain a fully converged solution using this code. Some work that was done earlier has shown that there is a strong dependence of the convergence of the model on the exit mach number. These results, presented in Figure 6.2, were obtained with a uniform inlet flow for the CPG cascade and they illustrate the difficulty of obtaining a converged solution for exit mach numbers of less than 0.3. This is not a surprising result since the model was written for use in transonic flow regimes. In these regimes density changes are significant and density can therefore be used as the primary variable. For this reason the modelling for the JAW cascade was carried out with a midspan exit mach

number of 0.5. The output routine of the program was modified to produce results compatible with the analysis and plotting programs that were used for the experimental data. The grid that was used had 60 points in the axial direction and 20 points in both of the other two directions. Some results of using the code for the colateral case of the JAW cascade are presented in Figure 6.3. These results are for an unconverged solution after 1000 iterations. Although they show the development of the passage vortex through the cascade the location of the centre of the passage vortex is incorrect at each of the axial locations that correspond to the experimental slots. The model cannot predict total pressure loss and the presence of loss (and therefore error) is an indication of the non-convergence of the solution. The model has an important role in the prediction of inviscid effects but cannot be used as other than a qualitative tool for the study of loss generation mechanisms.

6.4 THREE-DIMENSIONAL VISCOUS MODELLING

The Moore Elliptic Flow Program (Moore and Moore (1985)), that was briefly described in Chapter 2, has been used to model the flowfield of the JAW cascade. The modelling was completed before the start of the experimental programme. This meant that it was necessary to assume, in addition to the assumptions inherent in the model, that the inlet flow was colateral on the surface of the belt. The inlet boundary layer thickness was taken as 35mm and it was assumed that the inlet velocity profile on the belt could be adequately described by a power law relationship

with an index n = 1/7. The experimental results have shown that the power law assumption was reasonable but that the boundary layer should have been assumed to be thicker. A limitation of the Moore model is that transition is not modelled. For this reason the whole of the flowfield was assumed to be turbulent and was modelled by a simple mixing length assumption. The computational grid that was used had 34 points in the axial direction, 19 points in the pitchwise direction, and 13 points in the spanwise direction. The limitation on the grid size was the availability of online computer storage. A run typically required 4 MBytes of storage, and although only 24 iterations were generally required the amount of CPU time (in excess of 4000 seconds on an IBM 370/168) involved using the overnight batch mode. The computational grid that was used for all of the spanwise planes is shown in Figure 6.4. In all three of the coordinate directions the relative spacing of the grid points was reduced as a solid boundary, such as the endwall or blade surface, was approached.

The velocity vectors for a spanwise plane close to the endwall are shown for the three skew cases (corresponding to the experimental cases) in Figure 6.5. In all three cases there was a stagnation region close to the leading edge of the blade and reversed flows due to the presence of the horseshoe vortex. It can also be seen that negative skew increased the strength of the cross-passage flows whereas positive skew reduced them. As the amount of positive skew was increased, to a level produced by the belt moving at the same speed (but in the opposite direction) that was used for negative skew, the cross-passage flows appeared to be

destroyed. The result was an apparently two-dimensional flow through the cascade. For this reason the level of positive skew was approximately halved and all of the subsequent positive skew results (experimental and modelling) were obtained at this lower level. If the vector plots are compared to the endwall flow visualisation results of Chapter 5 (Figure 5.19), the endwall cross-passage separation line can be envisaged in the vector plots albeit in the wrong location.

The results obtained from the model were converted to be in a form that was compatible with the plotting and pitch averaging programs that were used for the experimental data. A selection of plots that correspond to the experimental results of Chapter 5 are presented in Figures 6.6 to 6.10. Only the area plots for total pressure loss coefficient and the secondary velocity vectors are presented.

The results for an axial position corresponding to Slot 1, 14% of an axial chord upstream of the cascade, are presented in Figure 6.6. As expected the total pressure loss coefficient contours, Figure 6.6(a-c), show very little distortion of the Bernoulli surfaces. Close to the endwall there is some distortion of the contours in the non-zero skew cases and this may be an upstream effect of the blade. In the case of negative skew it can be seen that the maximum value of loss was twice that predicted in the colateral case. In the case of positive skew the re-energisation of the boundary layer is evident from the apparent halving of the loss compared to the colateral case. The vector plots, Figure 6.6(d-f), show small secondary flows close to the

endwall. The limitation on the number of grid points has meant that the inlet conditions are effectively described by only four spanwise points. When compared to the experimental results, Figure 5.2, the levels of loss appear very similar apart from in a region very close to the endwall. Also the experimental results had a slightly thicker inlet boundary layer. Both the experimental and modelling vector plots show only very small secondary flows.

The results for an axial position corresponding to Slot 3, inside the blade passage at 22% of an axial chord from the leading edge, are presented in Figure 6.7. In all three skew cases the total pressure loss coefficient contours, Figure 6.7(a-c), show an unrealistically thick boundary layer on the suction surface of the blade. This feature, which is found in the results for all of the subsequent slots, is probably due to the turbulent flow regime and insufficient grid points in the boundary layer. The negative skew case shows a bunching of contours caused by the pressure-side leg of the horseshoe vortex. The positive skew case shows a similar flowfield pattern to the colateral case but with lower levels of loss. The velocity vectors, Figure 6.7(d-f), show very little secondary flow. The flowfield can be seen to be rotating in the passage and the secondary velocities are seen to be largest for the negative skew case. A comparison with the experimental results, Figure 5.5, shows that in the case of negative skew the predicted secondary flows appear less well defined and weaker. The predictions do not show the loss core on the suction surface of the blade and the levels of loss are lower than those measured.

In the colateral case the predicted total pressure loss contours show reasonable agreement with the experimental results apart from in the region close to the endwall. In the case of positive skew the feature detected in the centre of the passage, associated with the pressure-side leg of the horseshoe vortex, is not predicted.

The results for an axial position corresponding to slot 5, inside the blade passage at 55% of an axial chord from the leading edge, are presented in Figure 6.8. In all three skew cases the total pressure loss contours, Figure 6.8(a-c), still show the unrealistically thick boundary layer on the suction surface of the blade. The negative skew case is seen to have the most developed flowfield and the positive skew case the least developed. In the negative skew case the loss core is predicted to have moved away from the endwall. The velocity vectors, Figure 6.8(d-f), show the developing passage vortex. The largest values of secondary velocity are predicted for the case of negative skew. A comparison with the experimental results Figure 5.8, shows that the predicted flow features are less well defined resulting in an apparently less developed flowfield. In the case of negative skew the predicted maximum value of total pressure loss within the loss core is approximately half the measured value. A comparison of the predicted and measured secondary velocity vector plots shows that the magnitude of secondary velocity is underpredicted for the negative skew case. The centre of the passage vortex is predicted as being too close to the centre of the blade passage in the colateral case. The secondary velocities are predicted as being relatively small in the positive skew case.

The results for an axial position corresponding to slot 8, just upstream of the trailing edge of the blade, are presented in Figure 6.9. In all three skew cases the total pressure loss contours, Figure 6.9(a-c), show the unrealistically thick boundary layer on the suction surface of the blade giving the appearance of a wake. The three skew cases show an apparent progression of loss core development. There is no loss core in the case of positive skew and a reasonably well-defined loss core in the negative skew case. In addition the endwall flow appears to be being swept onto the suction surface of the blade. The secondary velocity vectors, Figure 6.9(d-f), show a reasonably developed passage vortex in both the negative skew and the colateral cases. The feature is very weak in the case of positive skew. These results may be compared to the experimental results presented in Figure 5.11. The predicted total pressure loss contours do not appear to be very similar to the experimental contours due to the overpredicted suction surface boundary layer. However the predicted endwall loss may be associated with an endwall counter vortex, although there is no indication of such a feature in the predicted secondary velocity vectors. Compared to the experimental results the predictions for the position of the passage vortex and the strength of the secondary flows are incorrect.

The results for an axial position corresponding to slot 10, 28% of an axial chord downstream of the cascade, are presented in Figure 6.10. In all three skew cases the total pressure loss contours, Figure 6.10(a-c), show that the blade wakes have been thickened due to the overprediction of loss in the suction surface

boundary layer. In the negative skew case, and to a lesser extent the colateral case, the endwall flow appears to be swept into the loss core. In the case of positive skew there is virtually no loss core and the blade wake appears to extend almost to the endwall. The secondary velocity vectors, Figure 6.10(d-f), show the unbounded passage vortex. The secondary velocities appear to be largest in the case of negative skew and smallest in the case of positive skew. In the colateral and negative skew cases there is some indication of counter-rotating flow on the midspan side of the passage vortex. These results may be compared to the experimental results presented in Figure 5.14. The predicted wakes are seen to be much thicker than the measured ones. The endwall is not swept clean in the predictions, as it is in the measurements, and the presence of the endwall counter vortex is not clear. The predictions show two peaks in the loss core for the negative skew case but only one for the colateral case. The experimental results show two peaks in both cases. The predicted levels of loss within the loss core are much higher than the experimental measurements. This is probably due to the high loss fluid from the suction surface boundary layer being swept into the loss core in the predictions. In the positive skew case the prediction shows the loss core structure to be pushed right onto the endwall. In general the predicted secondary velocities appear to be too low, the location of the passage vortex centre is wrongly predicted, and there is no prediction of an endwall counter vortex. The table below presents the mass averaged predicted loss and the results of a mixed out loss calculation.

The secondary losses have been calculated using the method that has been described in Chapter 5 and the table below is directly comparable with Table 5.2.

TABLE 6.4: SLOT 10 PREDICTED SECONDARY LOSS

	INLET SKEW TYPE		
	NEGATIVE	COLATERAL	POSITIVE
Predicted Loss Coefficient	0.472	0.405	0.361
Predicted Profile Loss	0.335	0.318	0.311
Mixed-Out Loss Coefficient	0.533	0.447	0.389
Mixed-Out Profile Loss	0.361	0.344	0.335
Gross Secondary Loss	0.172	0.103	0.054
Inlet Loss	0.040	0.023	0.009
Net Secondary Loss	0.132	0.080	0.045

These results show that inlet skew was predicted to have a very significant effect on the magnitude of the secondary losses. When this table is compared to Table 5.2 it is clear that the losses are overpredicted. In particular the profile losses are predicted to be nearly four times larger than the measured values. What is remarkable is that although the magnitude of net secondary loss is underpredicted, the ratio of net secondary loss between the skew cases is very similar to that obtained for the experimental results.

Some additional area plots are presented in Figure 6.11. Figure 6.11(a) illustrates the predicted effect of high positive skew at slot 8. It can be seen that the skew has effectively caused the endwall boundary layer to be removed and the secondary flows to be completely destroyed. In Figure 6.11(b) the effect of

a mixed flow regime for the colateral case was crudely modelled by assuming that the flowfield was turbulent to within 35mm of the endwall and also downstream of the position of the laminar separation bubble on the suction surface of the blade. The flowfield was assumed to be laminar everywhere else. It can be seen that the suction surface boundary layer is significantly thinner and has allowed the passage vortex to grow larger. Downstream there is less loss in the wake and an apparently smaller loss core. The secondary loss calculations show that hte profile loss is reduced to 0.225, the mixed-out loss is reduced to 0.323 and the inlet loss to 0.019. However it is found that the mixed flow regime makes no difference to the predicted net secondary loss.

The predicted growth of loss and secondary kinetic energy through the cascade can be seen from the area averaged results presented in Figure 6.12. It can be seen that the loss is predicted to grow through the cascade with an increase at the trailing edge. The secondary kinetic energy is predicted to be very small for the colateral and negative skew cases. A value of zero was predicted for the positive skew case. These results may be compared to the experimental results presented in Figure 5.16. It is clear that the loss is overpredicted whilst the secondary kinetic energy is underpredicted.

The predicted distributions of the static pressure coefficient around the blade are presented in Figure 6.13. There is a stagnation point on the pressure surface side of the blade near to the leading edge of the blade. Apart from slightly moving

the stagnation point, skew and distance from the endwall, are predicted to have little effect on the pressure surface distribution. On the suction surface there is a reduction in the loading at the leading edge as the endwall is approached. This effect is most marked in the case of negative skew. There is also a slight loading effect at the trailing edge. These results may be compared to the experimental results presented in Figure 5.21. Although there is reasonably good qualitative agreement there are some slight differences. The loading effects are less marked in the predictions, and the peaks of coefficient on the suction surface are not predicted.

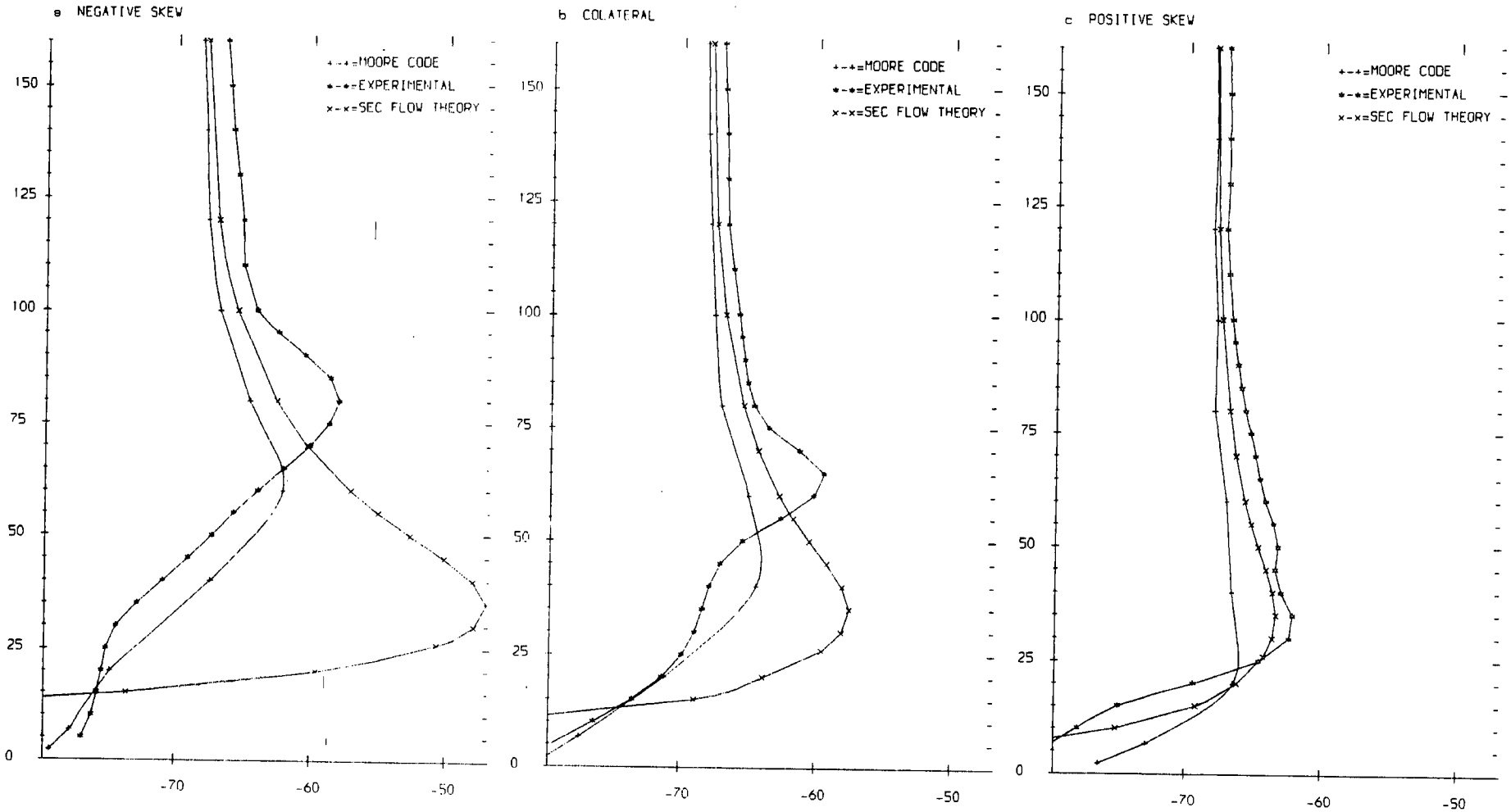

FIGURE 6.1: Pitch Averaged Angle (Slot 8)

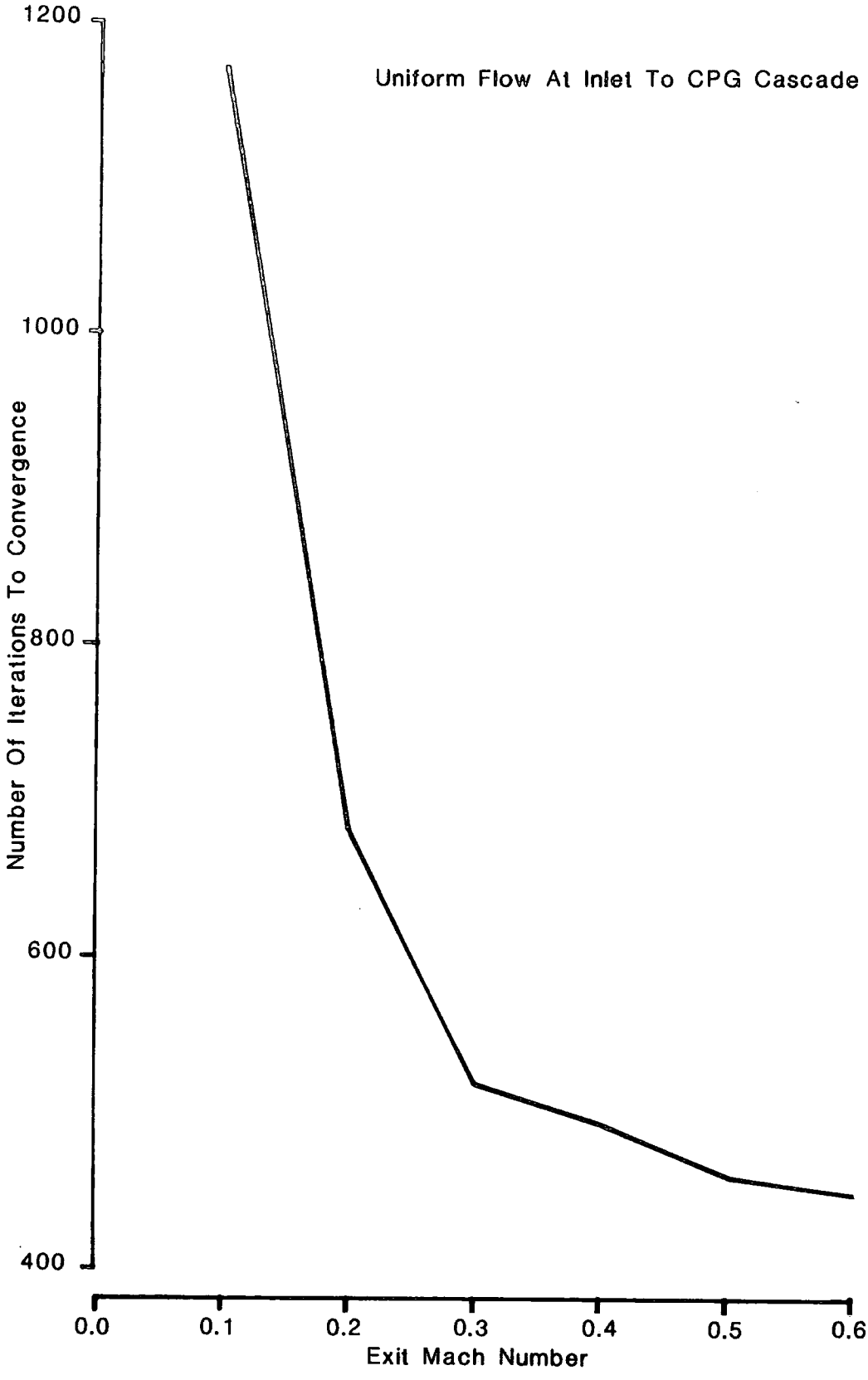

FIGURE 6.2: The Effect Of Mach Number On Convergence

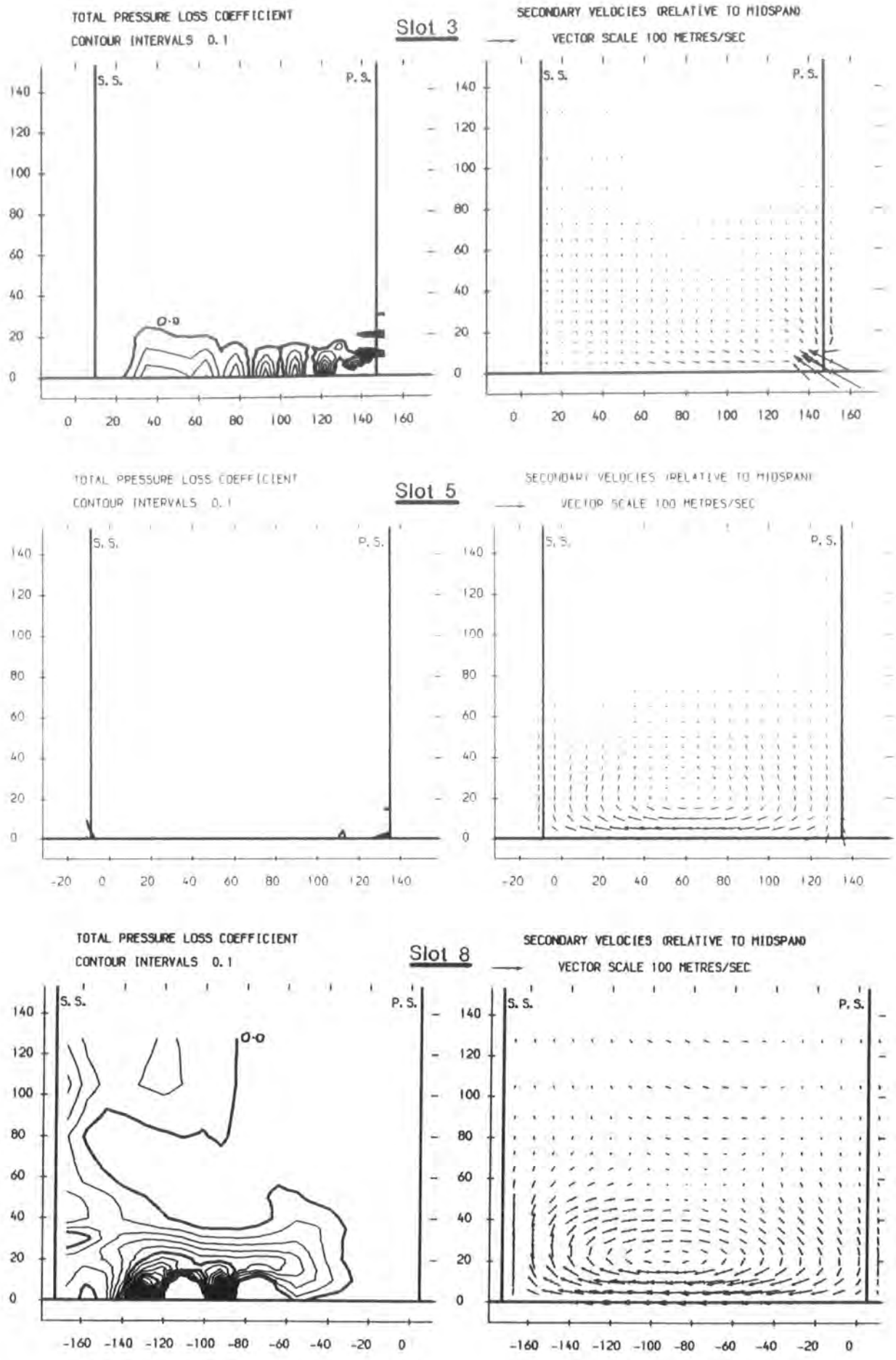

FIGURE 6.3: Denton Code Results

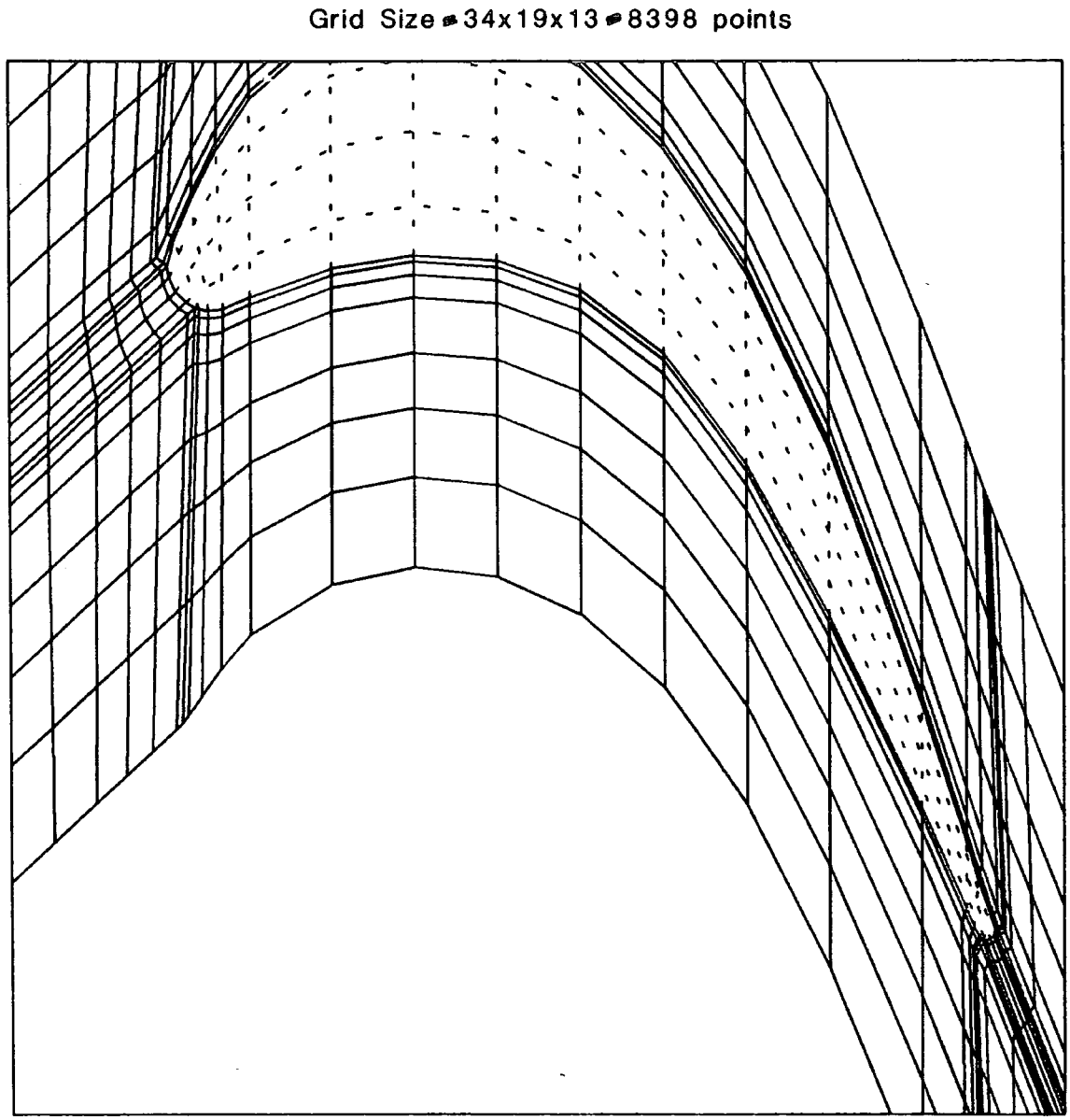

FIGURE 6.4: Moore Code Computational Grid

Negative Skew

Colateral

Positive Skew

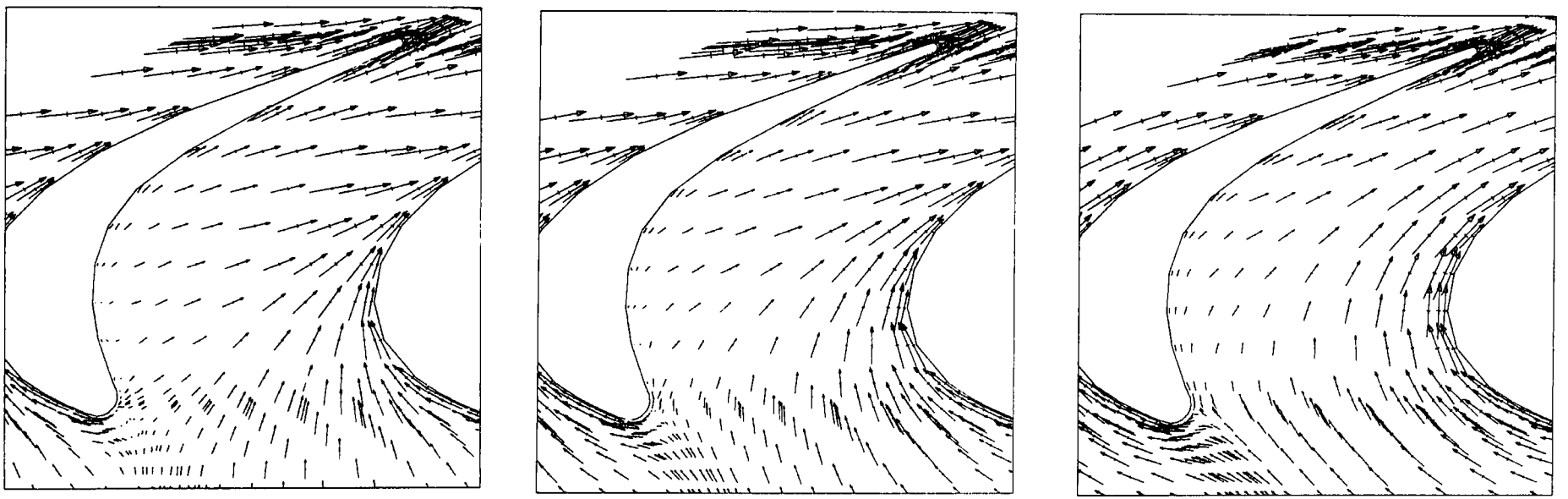

FIGURE 6.5: Predicted Endwall Velocity Vectors

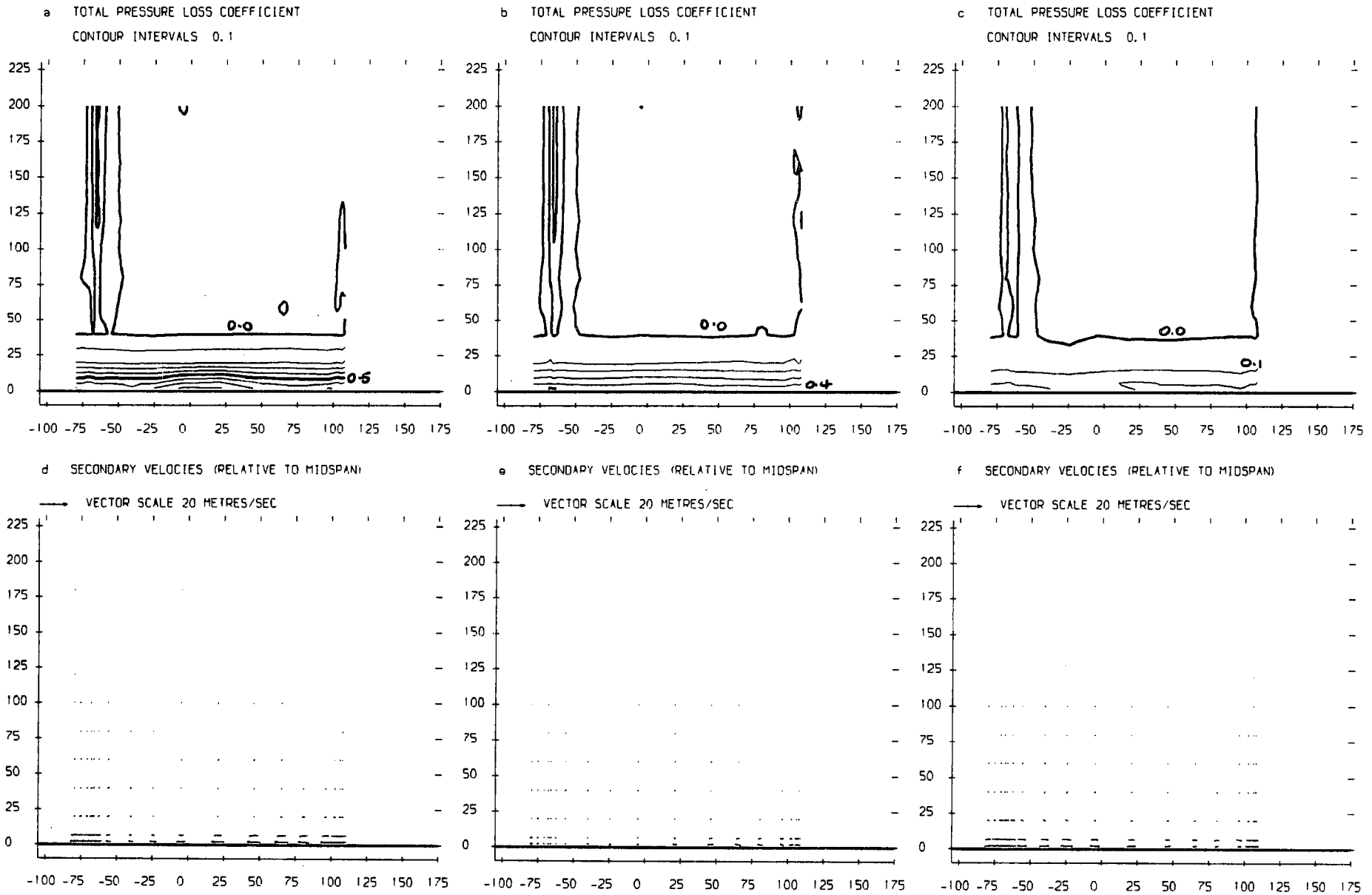

FIGURE 6.6(a-f) : Moore Code Results For Slot 1

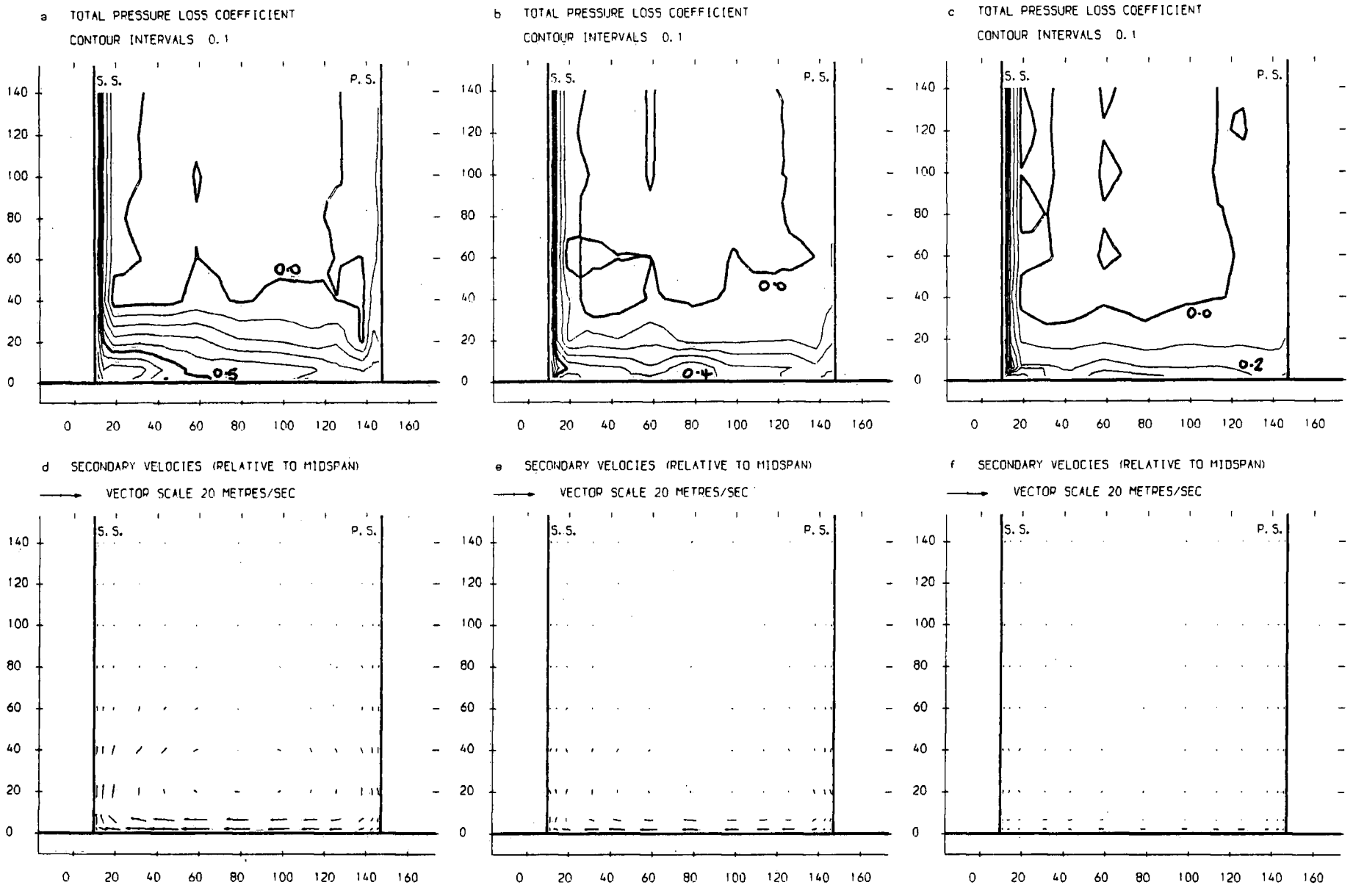

FIGURE 6.7(a-f) : Moore Code Results For Slot 3

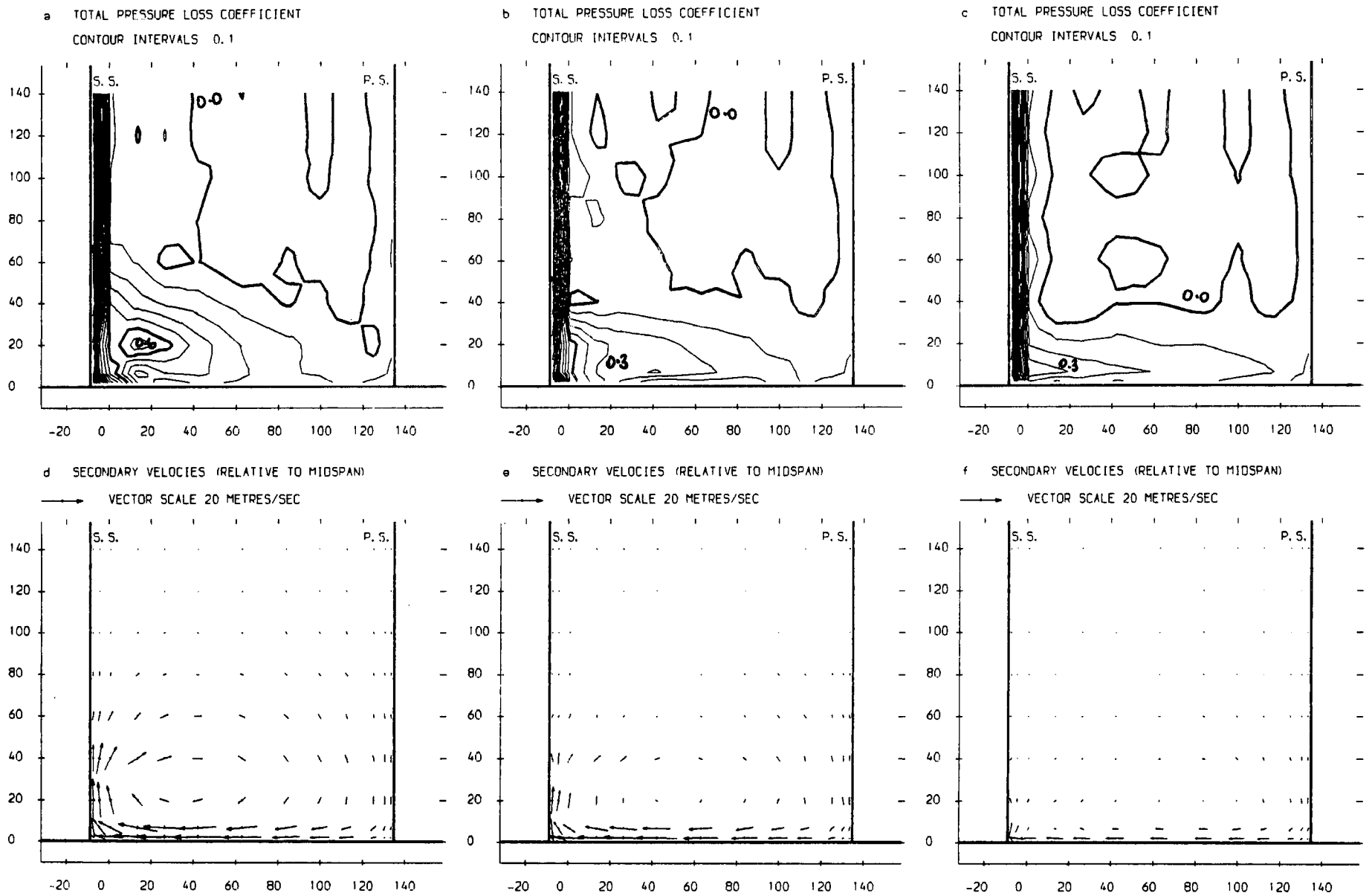

FIGURE 6.8(a-f) : Moore Code Results For Slot 5

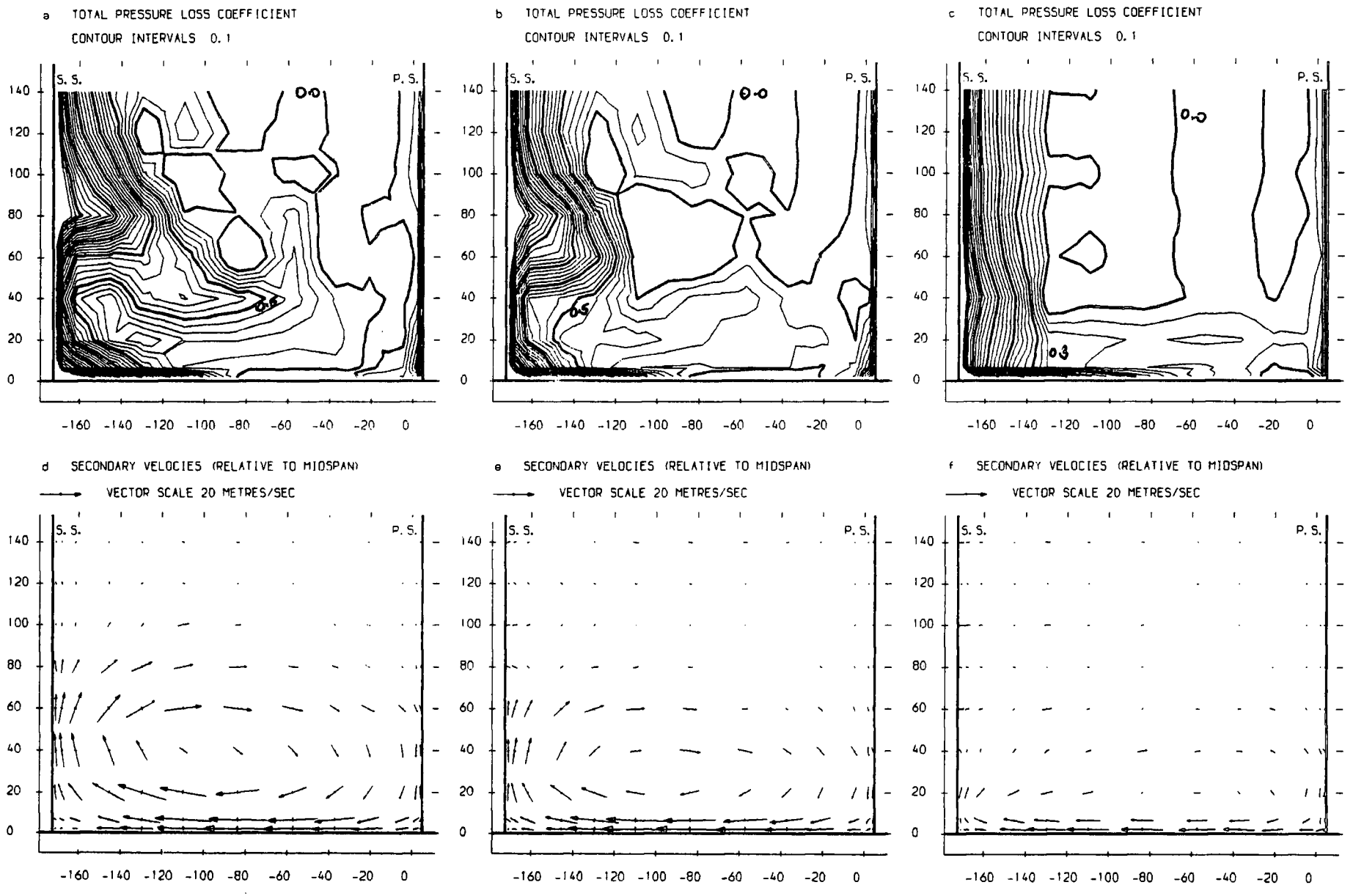

FIGURE 6.9(a-f) : Moore Code Results For Slot 8

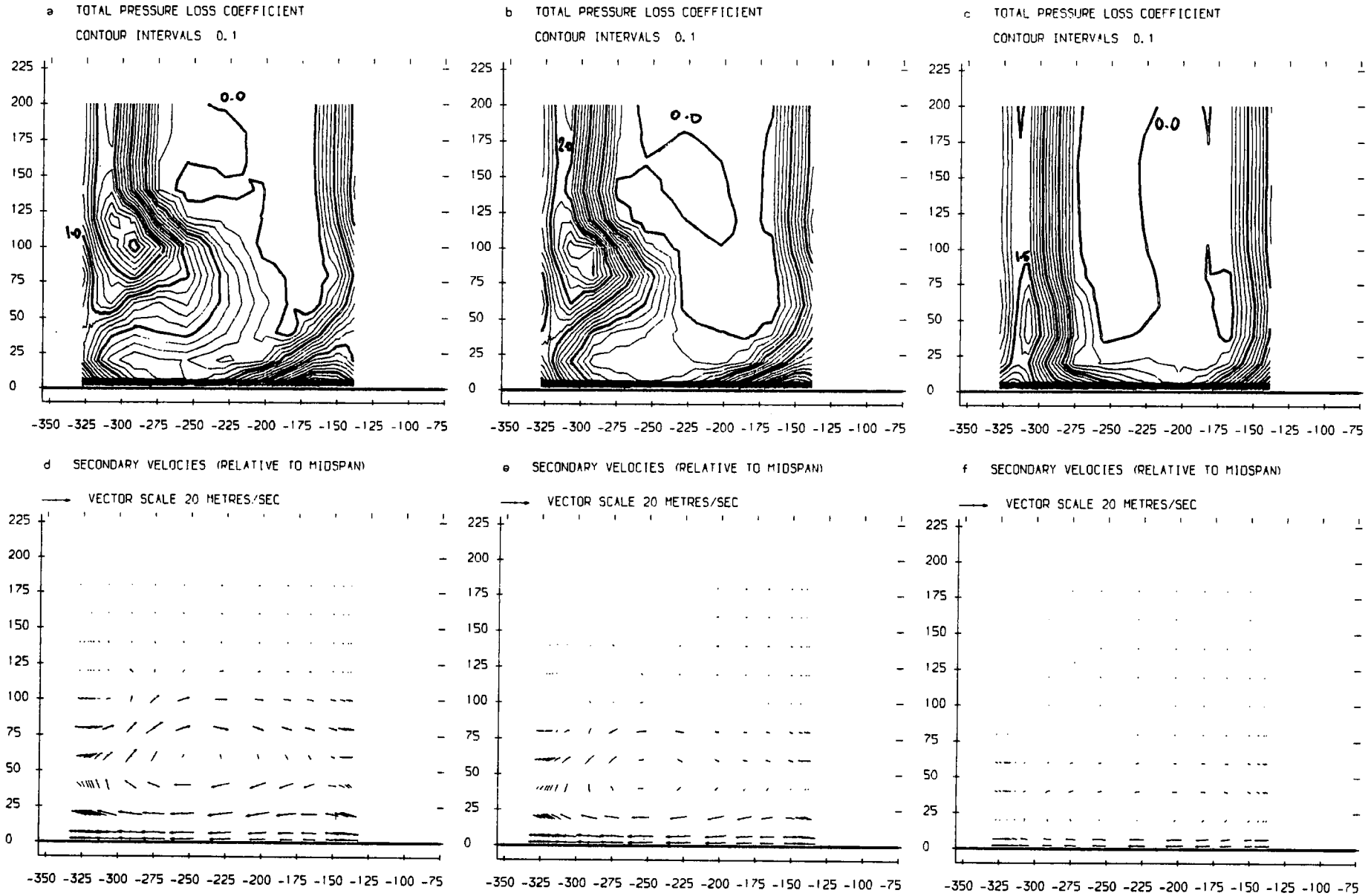

FIGURE 6.10(a-f): Moore Code Results For Slot 10

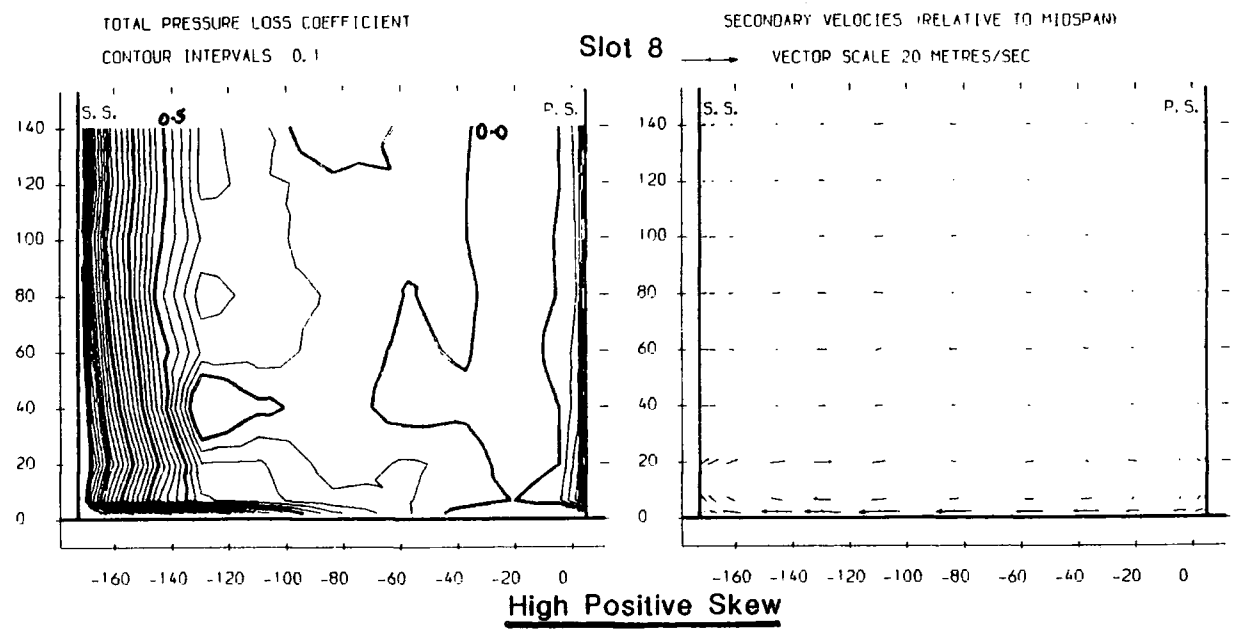

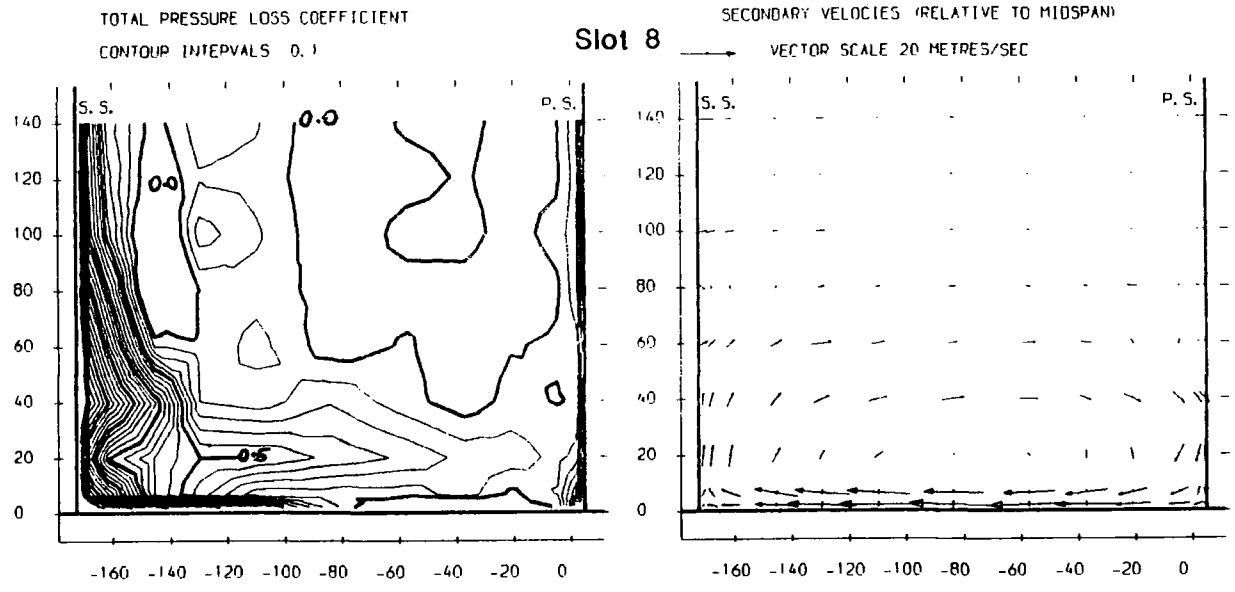

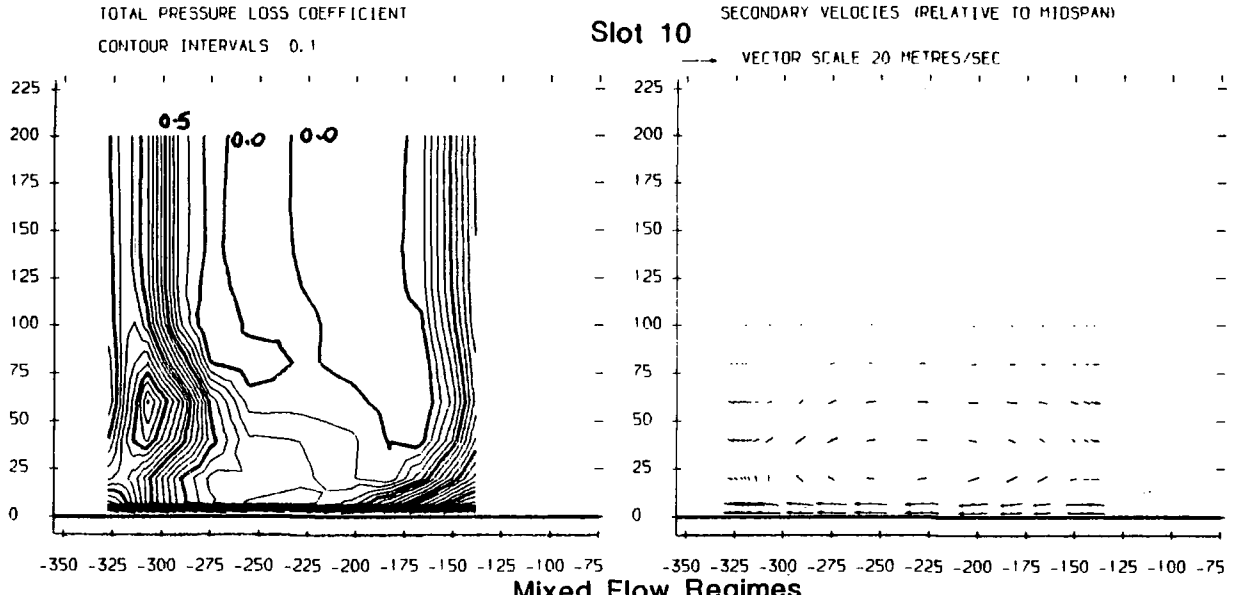

FIGURE 6.11: Additional Moore Code Results

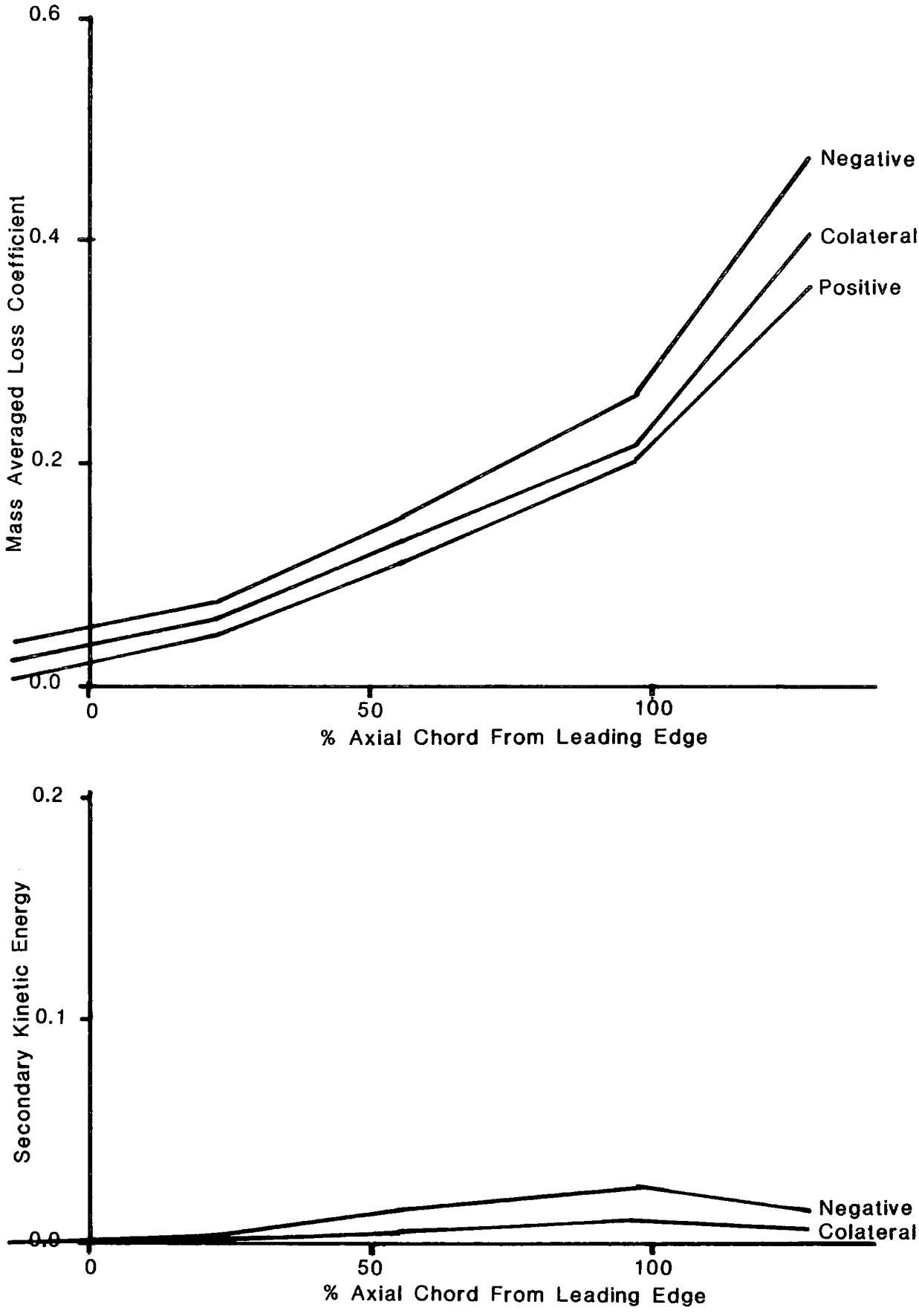

FIGURE 6.12: Predicted Development Of Loss

X-Axis: % Axial Chord From Leading Edge

Y-Axis: Static Pressure Coefficient

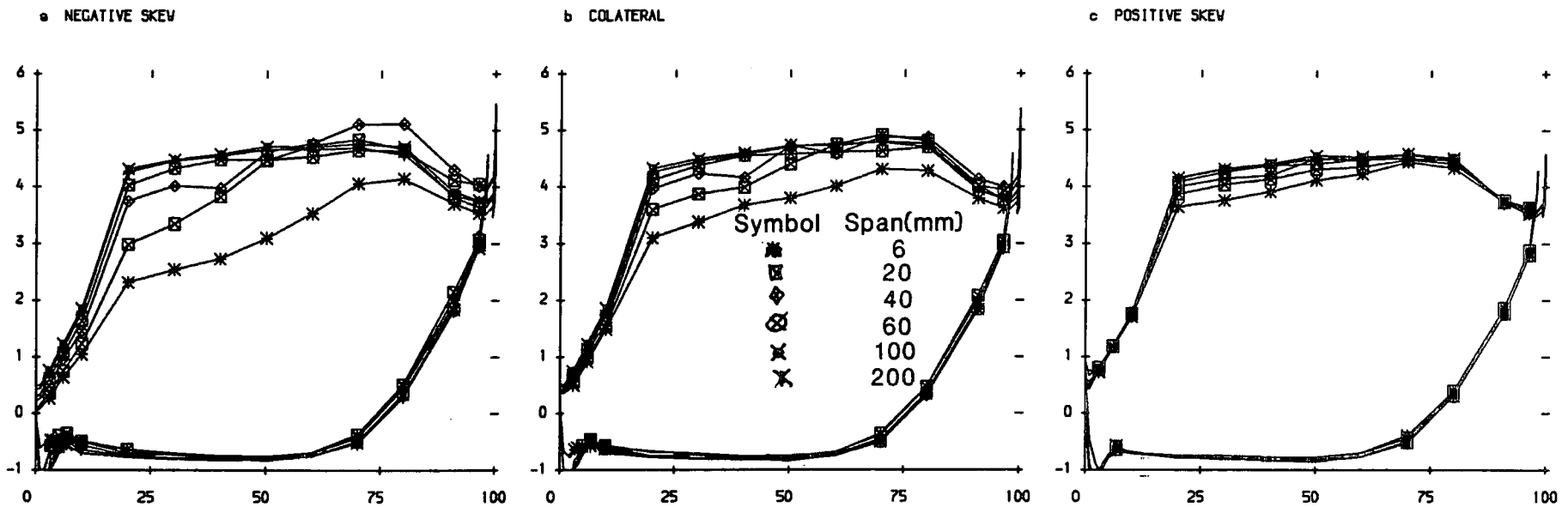

FIGURE 6.13: Predicted Static Pressure Coefficient

CHAPTER 7 : DISCUSSION

This chapter presents a discussion of the experimental and modelling results that form the central core of this thesis with the aim of putting them into context.

7.1 EXPERIMENTAL RESULTS

Further detailed measurements to compliment those obtained by Graves (1985) were obtained downstream of the CPG cascade using a five-hole pressure probe. Extra points were placed within the blade wake regions and these gave a qualitative increase in the flowfield definition and in the blade wake-to-wake repeatability. However the effect on the magnitude of the area averaged losses was relatively minor and this was probably due to the small changes of area that occurred in the regions covered by the extra measurement points. There would therefore be little advantage to be gained by putting even more measurement points into these regions. A reduced number of measurement points may well be adequate if only a qualitative description of the flowfield is required. This result allows a high confidence in the quality of the results obtained.

Extensive flow visualisation has been carried out on both the CPG and JAW cascades using the surface oil flow technique. The results obtained for the CPG cascade and the colateral case of the JAW cascade may be compared to the results of other workers. The endwall flow visualisation results in particular are similar to those presented by other workers and summarised by Sieverding

(1985). Most workers agree that the pressure-side leg of the horseshoe vortex merges in some way with the passage vortex. This result is derived from investigations that show the fluid from the pressure-side leg of the horseshoe vortex is detected within the passage vortex (Moore and Smith (1984) and Pernet (1986)). The result is corroborated by the presence of only a single cross-passage separation line on the endwall. Unfortunately the flow visualisation results presented in this thesis do not extend far enough upstream to detect the stagnation region associated with the horseshoe vortex that was detected by Carrick (1977) and by Langston (1980). It was not possible to detect the secondary separation lines described by Sieverding (1985) for the same reason. There are conflicting views in the literature as to what happens to the suction-side leg of the horseshoe vortex. Sieverding has suggested that the position of the suction-side leg is dependent upon the rotational speed of the passage vortex and on the overall flow conditions. This all-embracing explanation is to take account of the results of Moore and Smith (1984) who found that fluid from the suction-side leg of the horseshoe vortex was convected around the outside of the passage vortex. A similar result was also deduced from the coloured smoke flow visualisation of Sieverding and Van Den Bosch (1983). However the results presented in both of these papers are for low aspect ratio cascades and therefore the passage vortices may have interacted very strongly in the blade passage. The flow visualisation results presented in this thesis do not support the supposition that the suction-side leg of the horseshoe vortex wraps around the

passage vortex as shown in Figure 2.1. A more plausible explanation of the phenomenon may therefore be that as the passage vortex causes the dissipation of the suction-side leg of the horseshoe vortex it entrains some of its fluid. The results for the colateral case of the JAW cascade show that the suction-side leg of the horseshoe vortex is swept onto the suction surface of the blade and then runs up the surface of the blade on the midspan side of the passage vortex. The results for the CPG cascade show that the suction-side leg of the horseshoe vortex is swept onto the suction surface of the blade but then appears to be swallowed by a laminar separation bubble.

We are now able to give a brief qualitative description of the flowfield in a high aspect ratio linear cascade. The flowfield is dominated by several complex three-dimensional flow features. There is a horseshoe vortex that is formed as a result of the blade obstructing the inlet shear flow. This vortex has two legs, one of which goes on each side of the leading edge of the blade. The pressure-side leg moves across the passage and combines with the passage vortex which is formed as a result of the cross-passage pressure gradient and the curvature of the passage. The suction-side leg is swept onto the suction surface of the blade where it remains on the midspan side of the passage vortex. The path of the passage vortex is marked by the cross-passage separation line on the endwall and by a separation line on the suction surface of the blade. The endwall cross-passage separation line is itself separated form the suction surface of the blade by a counter vortex in the suction surface

endwall corner. On the downstream side of the cross-passage separation line a new highly skewed endwall boundary layer is formed. A laminar separation bubble is present on the suction surface of the blade. The presence of the endwall counter vortex was not detected in the low aspect ratio cascade of Moore and Smith (1984) which may explain why the losses were not seen to grow very much downstream of their cascade. The laminar spearation bubble was produced as a result of using a blade designed for a transonic flow regime in an incompressible flow regime. Other workers have used boundary layer trips on the blade surfaces to avoid the formation of the bubble.

The flowfield of the CPG cascade has been traversed with hot-wire probes. The results obtained illustrate the link between total pressure loss growth and the production and dissipation of turbulent kinetic energy. The upstream turbulence intensity level was measured as being approximately 4% by Graves (1985). This is a very high level when compared to the more usual figure of much less than 1% quoted for other wind tunnels. It can be argued that the high level of freestream turbulence is more representative of the conditions that would be found in a real machine. However the reason for such a high level is unclear and a short spectral study did not locate its source. It was originally thought that the cause was associated with the fan that was used to supply the air for the wind tunnel. This theory would have been proved by the presence of the blade passing frequency and its harmonics in the turbulence spectrum. In the absence of these discrete frequencies the cause of the high freestream turbulence intensity is probably

associated with the honeycomb flow straightener. This is located at the exit of the wind tunnel contraction upstream of the working section of the tunnel. Although the source of the turbulence was not located by the spectral study a discrete low frequency component was detected downstream of the cascade that was associated with the passage vortex. The presence of such a frequency may indicate the inappropriateness of treating such gross features as random in nature.

The downstream slot and two slots within the blade passage were traversed in detail with twin hot-wires. The mean flow results showed reasonable agreement with the five-hole pressure probe results which allows added confidence in the results. Worst agreement was for regions of high pitch angle due to an assumption of only small angle variation that was used in the analysis of the hot-wire results. In all of the measurement planes there was a fair degree of isotropy and the regions of high turbulent kinetic energy were associated with regions of high total pressure loss. The levels of turbulence intensity that were measured were significantly higher than those reported by Moore et al (1985) for a downstream plane of their cascade. Their measured total pressure losses were also reported as being significantly lower than those measured in our cascades. It is not clear whether the primary reason for the difference between their cascade and the CPG cascade is their low aspect ratio (where the strong interaction of the passage vortices may have caused the rapid dissipation of the turbulent kinetic energy), or whether the primary reason is the high level of freestream turbulence detected

in the CPG cascade. In their measurements they present results for the v'w' correlation which was found to be the most significant of the Reynolds shear stresses for loss production. It was thought that this shear stress may contribute to the rapid decay of the mean secondary kinetic energy downstream of the cascade. This shear stress component was not measured in the experiments reported in this thesis.

In conjunction with the hot-wire results presented by Graves (1985) and Fulton (1983) for the CPG cascade some interesting comparisons can be made between the total pressure loss and the turbulent kinetic energy. Within the blade passage the location of the peak value of turbulent kinetic energy did not coincide with the centre of the loss core associated with the passage vortex. However the location of the peak value of turbulent kinetic energy appears to be fairly mobile relative to the centre of the loss core. At slot 5 it was located on the suction surface side of the loss core, it was on the pressure surface side at slot 6 and on the midspan side at slot 8. At the downstream slot, slot 10, the centre of the loss core and the location of the peak value of turbulent kinetic energy coincided. The growth through the cascade of the mass averaged total pressure loss and turbulent kinetic energy showed similar trends. Since the growth in total pressure loss in the blade passage is effectively seen as an increase in turbulent kinetic energy it can be deduced that there was only small direct viscous action involved in the loss generation process. Downstream of the cascade the total pressure loss continued to increase due to the

continued growth of the endwall flow features. However the turbulent kinetic energy was seen to decay slightly and this was probably due to the viscous dissipation exceeding the generation from the mean flow.

A new experimental facility was used to investigate the effects of inlet skew. A new blade profile was used in the cascade that was designed to have a reduced level of suction surface diffusion. A laminar separation bubble was detected on the suction surface of the blade but its onset was delayed until later in the blade passage. The moving belt placed upstream of the cascade, that was used to produce the effects of inlet skew, caused a slight thickening of the inlet boundary layer in the non-zero skew cases. Results obtained by Graves (1985) have shown that an even larger variation of inlet boundary layer thickness does not have a significant effect on the downstream secondary flows and losses. Atkins (1985) found that even without an inlet boundary layer, and therefore no horseshoe vortex, a passage vortex and loss core were produced although in a reduced form. Even with only a very thin boundary layer the horseshoe vortex was found to be present. These results appear to indicate that the most important feature of the inlet flow is the presence of streamwise vorticity in the inlet boundary layer. The results of this thesis show that the modification of the distribution of the inlet vorticity by the introduction of skew has a profound effect on the secondary flows and losses in the cascade. The importance of the inlet vorticity, rather than the normal vorticity that is generated within the blade passage, explains why the inviscid

calculation methods are able to predict the exit angle variation for a blade row with a relatively large inlet boundary layer thickness.

Detailed traversing with pressure probes was carried out at five axial locations in the JAW cascade for three levels of inlet skew. The results that were obtained have been discussed in detail in Chapter 5 so only a few major issues will be discussed further at this point. The level of negative skew that was used was chosen to be typical of the conditions that would be found in a modern turbomachine. It was found that the introduction of negative skew intensified the secondary flows by appearing to cause the earlier development of the flowfield. A comparison with the results for the colateral case shows that the whole flowfield was significantly altered by the introduction of the skew. The flow visualisation results show that the suction-side leg of the horseshoe vortex is dissipated before it can be swept onto the suction surface of the blade. The increased vorticity at inlet is seen to cause a larger passage vortex, and associated loss core, in the negative skew case. Even in the absence of the suction-side leg of the horseshoe vortex a region of counter vorticity was detected on the midspan side of the passage vortex on the suction surface of the blade. Another important effect of skew was seen in the static pressure measurements where the blade loading, particularly at the leading edge, was modified. In terms of losses the effect of negative skew was to increase the gross secondary losses by 74%. The increasing of the loss is in agreement with the results of Carrick (1977), who investigated the

effect of skew in a turbine impulse cascade, and the results of Boletis et al (1983) who used a rotating blade row. Atkins (1985) has shown that a judicious choice of endwall profile can be used to slightly reduce the total losses in a cascade, and Graves (1985) has shown that variation of the inlet boundary layer thickness also has a relatively small effect on the losses. This then indicates the relative importance of the effect of inlet skew in the generation of loss in a blade row. The result is of course only valid for the ideal case of linear cascade flow and other factors will be important in annular cascades and in real machines. The work reported by Boletis et al clearly indicates the limitation of the applicability of this work. However even if the absolute magnitude of the effect of skew is not right the relative significance of the results would be expected to remain unchanged.

The case of positive skew at inlet has also been investigated and also found to have a profound effect on the secondary flows and losses. The passage vortex that was formed was much weaker than that detected in the other cases. The reason for its formation may be explained by the results of Atkins (1985) who found that the passage vortex is formed even in the complete absence of an inlet boundary layer, and therefore with no vorticity at inlet. At inlet an effect of positive skew was an apparent re-energisation of the inlet boundary layer. The cross-passage movement of the pressure-side leg of the horseshoe vortex appeared to be delayed until much later in the passage with the result that an intense region of loss was formed in the centre

of the passage close to the endwall. The suction-side leg was not detected on the suction surface of the blade and was probably dissipated by the opposing vorticity at inlet. Downstream of the cascade the loss core associated with the passage vortex appeared to remain separate from the loss core formed from suction surface boundary layer fluid. In the other skew cases these two loss cores tended to coalesce. In terms of loss, the effect of positive skew was to approximately halve the magnitude of the gross secondary loss. Whilst this result appears intuitively reasonable there is no other data to compare it with. The tracking of the paths of the passage vortex and loss core through the cascade revealed the complex nature of their movement. From these results it can be seen that skew has a significant effect on the position of the passage vortex and its associated loss core in the blade passage.

The streamwise vorticity was calculated for each of the measurement planes and the resulting contour plots have proved invaluable in identifying the various flow features. The technique used a bivariate surface fit which is then differentiated using numerical techniques. As long as the absolute values are not required and the contour plots are interpreted with caution the results are acceptable. In regions of high velocity gradient, such as near to the endwall, the results must be treated with caution since the errors associated with the numerical schemes may be significant. The technique has however allowed informative pictures of the growth of streamwise vorticity, and of the trailing vorticity, to be produced. In

particular pitch averaging the results has allowed a comparison of the measured growth of streamwise vorticity and the growth predicted by classical secondary flow theory. Early in the passage there is a reasonable level of agreement but in general classical secondary flow theory is clearly not adequate for this high turning cascade.

An effect of using the new blade profile was that the losses were not seen to grow all the way through the blade passage as had been detected for the CPG cascade. The loss growth was instead seen to be similar in shape to that measured by Langston et al (1977), and others, who used boundary layer trips on the surfaces of the blade. They found that the losses did not start to grow until the latter part of the blade passage. Downstream the flowfield is dominated by the blade wakes and the loss cores associated with the passage vortex and the endwall counter vortex. The pattern of loss growth through the cascade was similar for all of the skew cases.

7.2 MODELLING RESULTS

A series of correlations and three models have been used to model the flowfield of the JAW cascade. A detailed comparison between the experimental results and the modelling results has been presented in Chapter 6. That comparison has shown that the experimental results presented in this thesis provide a severe test case that can be used for any model.

The correlations that were tested are clearly limited in their application but will continue to find use in the design

process. The secondary flow model should provide a useful tool for at least the initial design stages of turbomachinery. The model can run quickly on a microcomputer and therefore be used interactively for systematic investigations in the design process. There are a number of areas of the model that require further work to improve the quality of the results. The loss core shape, which is currently assumed to be triangular, needs to be changed to remove the discontinuity from the resulting loss distribution. The assumption of small Bernoulli surface distortion is clearly inappropriate and the introduction of a method to trace the surfaces may improve the prediction. The role of secondary kinetic energy needs further investigation.

The three-dimensional inviscid code that was used has been formulated for transonic flows and does not appear to be appropriate for low speed flows because of the difficulty in getting a converged solution. Because the inlet vorticity distribution is an important factor some of the flow features appear well modelled. Although the inviscid code is limited by its inability to model loss generating mechanisms it can have a role in the prediction of inviscid effects.

The results obtained with the fully viscous three-dimensional code also indicate some areas for further work. Currently the model can only be used for subsonic flows and a generalisation will be required if the model is to find wide application. The experimental results of this thesis have shown that a good turbulence model will be essential if the accurate prediction of losses is required. Good results have been reported

for the flowfield of Langston's cascade (Moore and Moore (1985)) but this has a totally turbulent flow regime. The lack of a transition model is a major problem but this is clearly due to a suitable model not being available in the literature. More recent results for the flowfield of the JAW cascade (Gregory-Smith and Cleak (1987)) have shown that improvements in the modelling can be made by using a refined calculation grid and by using the experimentally determined inlet conditions. There is a clear need for experimental data to allow a model of transition to be developed. The work will also need to determine the effect of freestream turbulence intensity on transition, and the role of transition in the loss generating processes. In general the model was very time consuming to use in terms of generating the input data, and the interface between the model and the user needs further work.

The three-dimensional codes are likely to be limited in their application both by the expense of running them and the difficulty of using them. Clearly the latter problem is due to the research tool status of the codes and will be resolved with wider availability. Some of the problem areas that will need to be addressed are the input of the geometry of the components and the automatic generation of optimum calculation grids. It is essential to keep the aims of the modelling clear since large numbers of grid points may produce robust predictions but they are no substitute for a thorough understanding of the fundamental physical processes. There will always be a need for simple cheap

methods that can be used interactively in the design processes for quick, systematic investigations.

CHAPTER 8 : CONCLUSIONS AND RECOMMENDATIONS FOR FURTHER WORK

This chapter presents separately the conclusions that are drawn from the experimental and the modelling aspects of the work reported in this thesis. Recommendations are then given for future work using the experimental facilities and also for the continued evaluation of computer codes.

8.1 EXPERIMENTAL CONCLUSIONS

This thesis presents the results of a detailed experimental investigation into the fundamental flow processes of turbomachinery using two large scale, low speed, linear cascades of turbine blades. The results obtained with the original cascade (CPG) have shown that:

(a) the suction surface flow is disrupted by the presence of a laminar separation bubble that appears to be unsteady in nature

(b) the streamwise vorticity grows more negative through the cascade with a jump towards zero at the trailing edge due to the addition of the shed positive streamwise vorticity

(c) the endwall counter vortex is a very significant flow feature particularly downstream of the cascade

(d) regions of high turbulent kinetic energy are associated with regions of high total pressure loss

(e) the growth of turbulent kinetic energy through the cascade follows a similar distribution to that for the growth of total pressure loss

(f) there was a discrete frequency in the turbulence spectrum associated with the passage vortex suggesting that such gross features should not be treated as random in nature.

The second cascade (JAW) was specially built to investigate the effect of inlet skew which is caused by a change in frame of reference as the fluid passes from a stationary hub to a rotating blade row in a real machine. The results obtained with this cascade have shown that:

(a) the redesign of the blade profile to achieve aerodynamic similarity in the low speed conditions was successful in reducing the level of suction surface diffusion

(b) Skew modifies the distributions of both the normal and streamwise components of vorticity at inlet

(c) the presence of inlet skew modifies the whole of the flowfield causing changes, in particular, to features associated with the inlet shear such as the horseshoe vortex

(d) positive skew appears to encourage the regions of loss to remain separate whereas negative skew promotes the mixing of the loss regions

(e) the formation and position of the passage vortex appears to be closely linked to the pressure-side leg of the horseshoe vortex

(f) even when the suction-side leg of the horseshoe vortex is not present on the suction surface of the blade, counter vorticity is developed on the midspan side of the passage vortex to act as a counterbalance

(g) inlet skew has a significant effect on the secondary losses; negative skew increases them and positive skew reduces them

(h) the effect of inlet skew on the secondary losses is more significant than the reported effects due to a change in boundary layer thickness, or due to modifying the endwall profile.

8.2 MODELLING CONCLUSIONS

The flowfield of the JAW cascade has been modelled and detailed comparisons between the experimental results and the predictions have shown that:

(a) the experimental data presents a severe test case

(b) correlations are not able to accurately predict the secondary loss in the cascade or even the relative change in loss due to the presence of inlet skew

(c) the simple secondary flow model is not able to accurately predict the secondary losses due to the inherent secondary flow theory assumptions and the overprediction of the secondary kinetic energy

(d) the secondary flow features are modelled by the inviscid three-dimensional code but the loss generation is not

(e) reasonable results have been obtained with the fully viscous three-dimensional code and although the prediction of the magnitude of the secondary losses was incorrect, the prediction of the relative change due to the presence of skew was nearly right.

8.3 RECOMMENDATIONS FOR FUTURE WORK

There are clearly several areas of experimental work that can be carried out with the existing cascades to provide further useful data. There is further information required on the effect of inlet skew, particularly between slots 5 and 8 since the flowfield appears to change dramatically between these two axial locations. An investigation of the boundary layers on the surfaces of the blades will provide a useful contribution in the development of a model of transition. The effect of variations in the level of freestream turbulence need to be investigated since the role of turbulence in the loss generating process is not fully understood. The effect of freestream turbulence levels on transition is also likely to be important. As it stands the rig can easily be modified to investigate overtip leakage flows. The

linear cascade is a much simplified turbomachinery component that allows the collection of very detailed experimental data. However, the technique of investigating inlet skew, and overtip leakage flows, in such an experimental set up must be seen as an intermediate step between a linear cascade and an annular cascade. Therefore a natural extension of this work would be to develop at the very least an annular cascade and preferably a rotating rig.

There are a number of developments that can be made to the instrumentation that will allow the improved collection of further important data. The pressure and hot-wire probes would be improved by the use of a gimaballed head to allow the approximate nulling of the pitch angle as well as the yaw angle. The automation of the probe traverse mechanism would speed up the traversing. The use of a triple wire hot-wire probe would reduce the tedium of multiple traversing as well as provide data on all of the second order correlations. However, it may be that in the future the measurements may be better made using a non-invasive technique such as Laser Doppler Anemometry.

There is an important on-going need for the validation of the new computer codes as they are developed. One aspect of the validation process must be the collection of very detailed experimental data that can be used as test cases for the models. Another aspect is the provision of data that can be used in the formulation and improvement of the models. It is to be hoped that the results presented in this thesis will at least partially satisfy both of these aspects of the validation process. However, there will still be a need for simple cheap methods that can be

used as a design tool without the need of expensive supercomputers. It is to be hoped that the continued development of simple techniques such as the secondary flow model will result in such a tool.

REFERENCES

AINLEY, D.G. and MATHIESON, G.C.R.

"An Examination of the Flow and Pressure Losses in Blade Rows of Axial-Flow Turbines", ARC R & M, No. 2891, 1951.

ANONYMOUS

"The Jet Engine", Published by Rolls-Royce Ltd., 1973.

ATKINS, M.J.

"Endwall Profiling in Axial Flow Turbines", Ph.D. Thesis, Cambridge University, 1985.

BAILEY, D.A.

"Study of Mean and Turbulent Velocity Fields in a Large-Scale Turbine-Vane Passage", Trans. ASME, J. Eng. Power, 102, p88, 1980.

BARIO, F., LEBOEUF, F. and PAPAILIOU, K.D.

"Study of Secondary Flows in Blade Cascades of Turbomachines", Trans. ASME, J. Eng. Power, 104, p497, 1982.

BELIK, L.

"Secondary Flow in Blade Cascades of Axial Turbomachines and the Possibility of Reducing its Unfavourable Effect", 2nd Int. JSME Symposium on Fluid Mechanics and Fluidics, Tokyo, 1972.

BINDER, A. and ROMEY, R.

"Secondary Flow Effects and Mixing of the Wake Behind a Turbine Stator", Trans. ASME, J. Eng. Power, 105, p40, 1983.

BINDON, J.P.

"The Effect of Hub Inlet Boundary Layer Skewing on the Endwall Shear Flow in an Annular Turbine Cascade", ASME paper no: 79-GT-13, 1979.

"Exit Plane and Suction Surface Flows in an Annular Cascade with a Skewed Inlet Boundary Layer", Int. J. Heat and Fluid Flow, 2, p57, 1980.

BLAKE, W.K.

"Differential Pressure Measurement", (in 'Fluid Mechanics Measurements', Ed. R.J. Goldstein), Published by Hemisphere Publishing Corporation, 1983.

BOLETIS, E.

"Experimental Research on Secondary Flows in Annular Turbine Cascades at VKI", VKI-LS 1984-05, 1984.

BOLETIS, E., SIEVERDING, C.H. and VAN HOVE, W.

"Effects of a Skewed Inlet Endwall Boundary Layer on the 3-D Flow Field in an Annular Turbine Cascade", AGARD-CP-315, 'Viscous Effects in Turbomachines', Paper No. 16, 1983.

BOOTH, T.C.

"An Analysis of the Turbine Endwall Boundary Layer and Aerodynamic Losses", ASME paper no: 75-GT-23, 1975.

BRYCE, J.D. and LITCHFIELD, M.

"Experience of the Denton Blade-Blade Time Marching Programs", NGTE Note no: 1050, 1976.

CAME, P.M.

"Secondary Loss Measurements in a Cascade of Turbine Blades", I.Mech.E. Conf. Publ. no. 3, 'Heat and Fluid Flow in Steam and Gas Turbine Plant', p75, 1973.

CAME, P.M. and MARSH, H.

"Secondary Flow in Cascades: Two Simple Derivations for the Components of Vorticity", J.Mech.Eng.Sci., 16, p391, 1974.

CARRICK, H.B.

"Secondary Flows and Losses in Turbine Cascades with Inlet Skew", AGARD-CP-214, 'Secondary Flows in Turbomachines', Paper no. 9, 1977.

CHAUVIN, J.

"Turbine Cascade Endwall Losses: A Review", VKI-LS-72, 1975.

CHEN, L.D. and DIXON, S.L.

"Growth of Secondary Flow Losses Downstream of a Turbine Blade Cascade", Trans. ASME, J. Eng. Gas Turbines and Power, 108, p270, 1986.

COHEN, H., ROGERS, G.F. and SARAVANAMUTTOO, H.I.

"Gas Turbine Theory", Published by: Longmans, 1972.

DENTON, J.D.

"A Time Marching Method for Two- and Three- Dimensional Blade to Blade Flows", ARC R & M no. 3775, 1975.

"An Improved Time-Marching Method for Turbomachinery Flow Calculation", Trans. ASME, J. Eng. Power, 105, p514, 1983.

DENTON, J.D. and JOHNSON, C.G.

"Measurements of Secondary Loss in a Model Turbine with Variable Inlet Boundary Layer", ARC CP 1335, 1975.

DENTON, J.D. and USUI, S.

"Use of a Tracer Gas Technique to Study Mixing in a Low Speed Turbine", ASME paper no: 81-GT-86, 1981.

DRING, R.P.

"A Momentum-Integral Analysis of the Three-Dimensional Turbine End-Wall Boundary Layer", Trans. ASME, J. Eng. Power, 93, p386, 1971.

DUNCAN, W.J., THOM, A.S. and YOUNG, A.D.

"Mechanics of Fluids", Published by Edward Arnold Ltd., p370, 1960.

DUNHAM, J.

"A Review of Cascade Data on Secondary Losses in Turbines", J. Mech. Eng. Sci., 12, p48, 1970.

DUNHAM, J. and CAME, P.M.

"Improvements to the Ainley Mathieson Method of Turbine Performance Prediction", Trans. ASME, J. Eng. Power, 92, p252, 1970.

FULTON, K.P.

"Turbulence Measurement of Secondary Flows in a Turbine Cascade", Undergraduate Engineering Project Report, Department of Engineering, University of Durham, 1983.

GAUGLER, R.E. and RUSSELL, L.M.

"Comparison of Visualised Turbine Endwall Secondary Flows and Measured Heat Transfer Patterns", Trans ASME, J. Eng. Gas Turbines and Power, 106, p168, 1984.

GLYNN, D.R.

"Calculation of Secondary Flow in Cascades Including Effects of Bernoulli Surface Distortion", Int. J. Heat and Fluid Flow, 3, p73, 1982.

GLYNN, D.R. and MARSH, H.

"Secondary Flow in Annular Cascades", Int. J. Heat and Fluid Flow, 2, p29, 1980.

GOSTELOW, J.P.

"Cascade Aerodynamics", Published by: Pergamon Press, 1984.

GOVARDHAM, M., VENKATRAYULU, N. and PRITHVI RAJ, D.

"Secondary Losses in a Large Deflection Annular Turbine Cascade: Effects of the Entry Boundary Layer Thickness", ASME paper no: 86-GT-171, 1986.

GRAVES, C.P.

"Secondary Flows and Losses in Gas Turbines", Ph.D. Thesis, Durham University, 1985.

GRAZIANI, R.A., BLAIR, M.F., TAYLOR, J.R. and MAYLE, R.E.

"An Experimental Study of the Endwall and Aerofoil Surface Heat Transfer in a Large Scale Turbine Blade Cascade", Trans. ASME, J. Eng. Power, 102, p257, 1980.

GREGORY-SMITH, D.G.

"Secondary Flows and Losses in Axial Flow Turbines", Trans. ASME, J. Eng. Power, 104, p819, 1982.

"Secondary Flow Theory in Straight and Annular Cascades", VKI-LS 1984-05, 1984.

GREGORY-SMITH, D.G. and CLEAK, J.G.

Private Communication, 1987.

GREGORY-SMITH, D.G. and GRAVES, C.P.

"Secondary Flows and Losses in a Turbine Cascade", AGARD-CP-351, 'Viscous Effects in Turbomachines', Paper no. 17, 1983.

GREGORY-SMITH, D.G., GRAVES, C.P. and WALSH, J.A.

"Growth of Secondary Losses and Vorticity in an Axial Turbine Cascade", ASME Paper no: 87-GT-114, 1987.

GREGORY-SMITH, D.G. and MARSH, H.

"The Manufacture of Glass Fibre Rotor Blades with Pressure Tappings", Aero. J., 75, p723, 1971.

HAWTHORNE, W.R.

"Rotational Flow Through Cascades, Part 1: The Components of Vorticity", Q. J. Mech. and Appl. Math., 8, p266, 1955.

HERZIG, H.Z. and HANSEN, A.G.

"Visualisation Studies of Secondary Flows with Applications to Turbomachines", Trans. ASME, 77, p249, 1955.

HERZIG, H.Z., HANSEN, A.G. and COSTELLO, G.R.

"A Visualisation Study of Secondary Flows in Cascades", NACA Report No. 1163, 1953.

HIRCH, C. and DENTON, J.D. (Editors)

"Throughflow Calculations in Axial Flow Turbomachines", AGARD-AR-175, 1981.

HORLOCK, J.H.

"Cross Flows in Bounded Three-Dimensional Turbulent Boundary Layers", J. Mech. Eng. Sci., 15, p274, 1973.

HORLOCK, J.H. and LAKSHMINARAYANA, B.

"Secondary Flows: Theory, Experiment, and Application in Turbomachinery Aerodynamics", Ann. Review Fluid Mech, 5, p247, 1973.

HUNTER, I.H.

"Endwall Boundary Layer Flows and Losses in an Axial Turbine Stage", Trans. ASME, J. Eng. Power, 104, p184, 1982.

ISHII, J. and HONAMI, S.

"A Three-Dimensional Turbulent Detached Flow with a Horseshoe Vortex", Trans. ASME, J. Eng. Gas Turbines and Power, 108, p125, 1986.

JAPIKSE, D.

"Review - Progress in Numerical Turbomachinery Analysis", Trans. ASME, J. Fluids Eng., 98, p592, 1976.

JENNIONS, I.K. and STOW, P.

"A Quasi-Three-Dimensional Turbomachinery Blade Design System: Part I - Throughflow Analysis", Trans. ASME, J. Eng. Gas Turbines and Power, 107, p301, 1985a.

"A Quasi-Three-Dimensional Turbomachinery Blade Design System: Part II - Computerized System", Trans. ASME, J. Eng. Gas Turbines and Power, 107, p308, 1985b.

JILEK, J.

"An Experimental Investigation of the Three-Dimensional Flow within Large Scale Turbine Cascades", ASME paper no: 86-GT-170, 1986.

JOHNSTON, J.P.

"On the Three-Dimensional Turbulent Boundary Layer Generated by Secondary Flow", Trans. ASME, J. Basic. Eng., 82, p233, 1960.

"Experimental Studies in Three-Dimensional Turbulent Boundary Layers", Report MD-34, Department of Mechanical Engineering, Stanford University, 1976.

KINGCOMBE, R.C.

"Skew and Shear in Cascades", Ph.D. Thesis, Cambridge University, 1976.

KLEIN, A.

"Investigation of the Effect of the Entry Boundary Layer on the Secondary Flows in the Blading of Axial-Flow Turbines", Forshung Ing.-Wes., 32, p175, 1966. (Translation: BHRA T1004, 1969).

LAKSHMINARAYANA, B. and HORLOCK, J.H.

"Review: Secondary Flows and Losses in Cascades and Axial-Flow Turbomachines", Int. J. Mech. Eng. Sci., 5, p287, 1963.

"Generalised Expressions for Secondary Vorticity Using Intrinsic Co-ordinates", J. Fluid Mech., 59, p97, 1973.

LANGSTON, L.S.

"Crossflows in a Turbine Cascade Passage", Trans. ASME, J. Eng. Power, 102, p866, 1980.

LANGSTON, L.S., NICE, M.L. and HOOPER. R.M.

"Three-Dimensional Flow within a Turbine Cascade Passage", Trans. ASME, J. Eng. Power, 99, p21, 1977.

LAWRENZ, M.

"Calculation of 3-D Viscous Flows in Annular Cascades using Parabolised Navier Stokes Equations", VKI-LS 1984-05, 1984.

MAGER, A.

"Three-Dimensional Boundary Layer with Small Cross-Flow", J. Aero. Sci., 21, p835, 1954.

MALTBY, R.L. and KEATING, R.F.A.

"The Surface Oil Flow Technique for use in Low Speed Wind Tunnels", AGARDograph 70, 1962.

MARCHAL, Ph. and SIEVERDING, C.H.

"Secondary Flows Within Turbomachinery Bladings", AGARD-CP-214, 'Secondary Flows in Turbomachines', Paper No. 11, 1977.

MARSH, H.

"Secondary Flow in Cascades: The Effect of Axial Velocity Ratio", J. Mech. Eng. Sci., 16, p402, 1974.

"Secondary Flow in Cascades: The Effect of Compressibility", ARC R & M no. 3778, 1976.

McNALLY, W.D. and SOCKOL, P.M.

"Review - Computational Methods for Internal Flows with Emphasis on Turbomachinery", Trans. ASME, J. Fluids Eng., 107, p6, 1985.

MERZKIRCH, W.F.

"Flow Visualisation", Published by Academic Press, 1974.

MOORE, J. and ADHYE, R.Y.

"Secondary Flows and Losses Downstream of a Turbine Cascade", Trans. ASME, J. Eng. Gas Turbines and Power, 107, p961, 1985.

MOORE, J. and MOORE, J.G.

"A Calculation Procedure for Three-Dimensional, Viscous, Compressible Duct Flow, Part I: Inviscid Flow Considerations", ASME paper no: 79-WA/FE-4, 1979.

"Performance Evaluation of Linear Turbine Cascades Using Three-Dimensional Viscous Flow Calculations", Trans. ASME, J. Eng. Gas Turbines and Power, 107, p969, 1985.

MOORE, J. and RANSMAYR, A.

"Flow in a Turbine Cascade, Part 1: Losses and Leading Edge Effects", Trans. ASME, J. Eng. Gas Turbines and Power, 106, p400, 1984.

MOORE, J., SHAFFER, D.M. and MOORE, J.G.

"Reynolds Stresses and Dissipation Mechanisms Downstream of a Turbine Cascade", ASME Paper no: 86-GT-92, 1986.

MOORE, J. and SMITH, B.L.

"Flow in a Turbine Cascade: Part 2 - Measurement of Flow Trajectories by Ethylene Detection", Trans. ASME, J. Eng. Gas Turbines and Power, 106, p409, 1984.

MOORE, R.W. and RICHARDSON, D.L.

"Skewed Boundary Layer Flow Near the Endwall of a Compressor Cascade", Trans. ASME, 79, p1789, 1957.

MORGAN, S.

"Low Aspect Ratio Turbine Design at Rolls-Royce", VKI-LS 1984-05, 1984.

MORRIS, A.W.H. and HOARE, R.G.

"Secondary Loss Measurements in a Cascade of Turbine Blades with Meridional Wall Profiling", ASME paper no: 75-WA/GT-13, 1975.

MOUSTAPHA, S.H., PARON, G.J. and WADE, J.H.T.

"Secondary Flows in Cascades of Highly Loaded Turbine Blades", Trans. ASME, J. Eng. Gas Turbines and Power, 107, p1031, 1985.

PERNET, G.C.

"Secondary Flow Visualisation in a Turbine Cascade", Undergraduate Engineering Project Report, School of Engineering and Applied Science, University of Durham, 1986.

PERRY, A.E.

"Hot-Wire Anemometry", Published by OUP, 1982.

SATO, T., AOKI, S. and NAGAYAMA, T.

"Extensive Verification of the Denton New Scheme from the User's Point of View: Part I - Calibration of Code Control Variables", ASME paper no: 86-GT-57, 1986a.

"Extensive Verification of the Denton New Scheme from the User's Point of View: Part II - Comparison of Calculated and Experimental Results", ASME paper no: 86-GT-58, 1986b.

SCHAUB, U.W., SHARP, C.R. and BASSETT, R.W.

"An Investigation of the Three-Dimensional Flow Characteristics of a Non-Nulling Five-Tube Probe", Report no: LR-393, Division of Mechanical Engineering, National Research Laboratories, Ottawa, Canada.

SENOO, Y.

"The Boundary Layer on the Endwall of a Turbine-Nozzle Cascade", Trans. ASME, 80, p1711, 1958.

SETTLES, G.S.

"Modern Developments in Flow Visualisation", AIAA J., 24, p1313, 1986.

SHARMA, O.P. and BUTLER, T.L.

"Predictions of Endwall Losses and Secondary Flows in Axial Flow Turbine Cascades", ASME paper no: 86-GT-228, 1986.

SHARMA, O.P., BUTLER, T.L., JOSLYN, H.D. and DRING, R.P.

"Three-Dimensional Unsteady Flow in an Axial Flow Turbine", J. Propulsion, 1, p29, 1985.

SIEVERDING, C.H.

"Axial Turbine Performance Prediction Methods", Proceedings NATO ASI, 'Thermodynamics and Fluid Mechanics of Turbomachinery', Paper no. 5.3, 1984.

"Recent Progress in the Understanding of Basic Aspects of Secondary Flow in Turbine Blade Passages", Trans. ASME, J. Eng. Gas Turbines and Power, 107, p248, 1985.

SIEVERDING, C.H. and VAN DEN BOSCH, P.

"The Use of Coloured Smoke to Visualise Secondary Flows in a Turbine Blade Cascade", J. Fluid Mech., 134, p85, 1983.

SIEVERDING, C.H., VAN HOVE, W. and BOLETIS, E.

"Experimental Study of the Three-Dimensional Flow Field in an Annular Turbine Nozzle Guide Vane", Trans. ASME, J. Eng. Gas Turbines and Power, 106, p437, 1984.

SIEVERDING, C.H. and WILPUTTE, P.

"Influence of Mach Number and Endwall Cooling on Secondary Flows in a Straight Nozzle Cascade", Trans. ASME, J. Eng. Power, 103, p257, 1981.

SJOLANDER, S.A.

"The Endwall Boundary Layer in an Annular Cascade of Turbine Nozzle Guide Vanes", Technical Report no. ME/A 75-4, Carlton University, Canada, 1975.

SMITH, L.H.

"Secondary Flows in Axial-Flow Turbomachinery", Trans. ASME, 77, p1065, 1955.

SQUIRE, H.B. and WINTER, K.G.

"The Secondary Flow in a Cascade of Aerofoils in a Nonuniform Stream", J. Aero. Sci., 18, p271, 1951.

TALL, W.A.

"Understanding Turbine Secondary Flow", AGARD-CP-214, 'Secondary Flows in Turbomachines', Paper no. 14, 1977.

TAYLOR, E.S.

"The Skewed Boundary Layer", Trans. ASME, J. Basic Eng., 81, p297, 1959.

TURNER, J.R.

"An Investigation of the End-Wall Boundary Layer of a Turbine-Nozzle Cascade", Trans. ASME, 79, p1801, 1957.

WOLF, H.

"Die Randverluste in Geraden Shaufelgittern", Wiss. Z. Tech. Hochsch. Dresden, 10, 1961.

YAVUZKURT, S.

"A Guide to Uncertainty Analysis of Hot-Wire Data", Trans. ASME, J. Fluids. Eng., 106, p181, 1984.